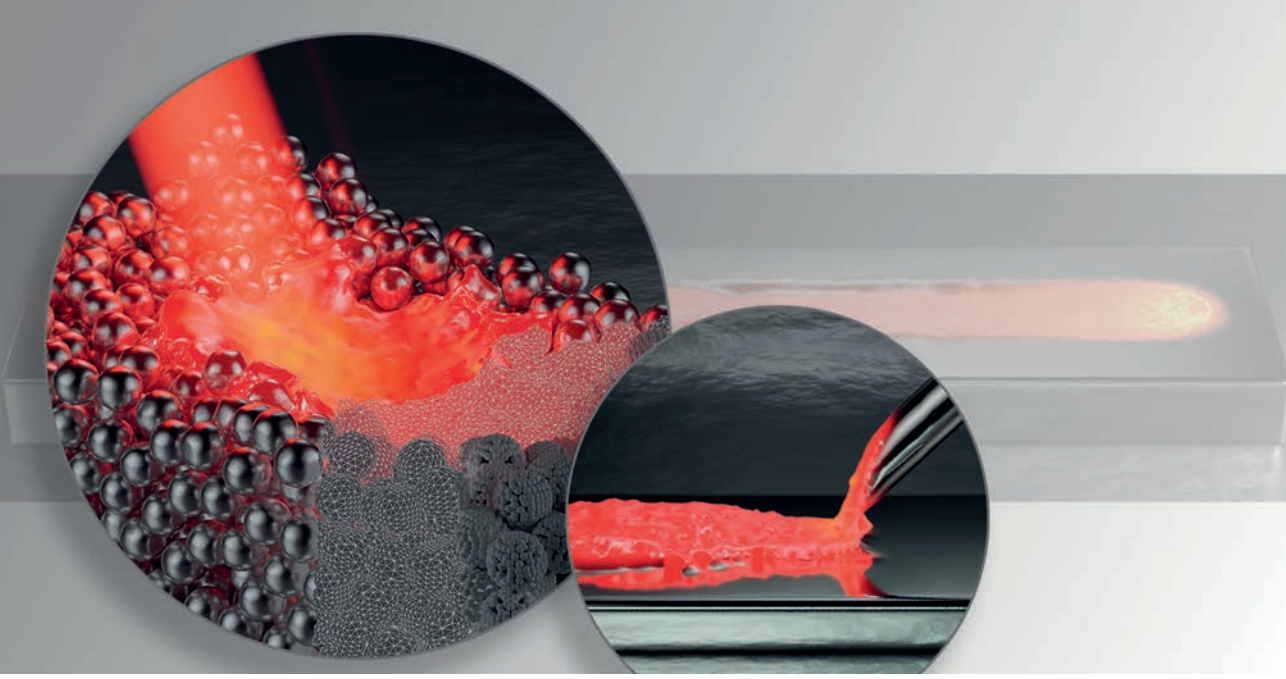

FAU Forschungen, Reihe B, Medizin, Naturwissenschaft, Technik 43

Michael Blank

Simulation of the laser melting process of titanium using Smoothed Particle Hydrodynamics

FAU University Press

Michael Blank

Simulation of the laser melting process of titanium using Smoothed Particle Hydrodynamics

FAU Forschungen, Reihe B
Medizin, Naturwissenschaft, Technik
Band 43

Herausgeber der Reihe:
Wissenschaftlicher Beirat der FAU University Press

Michael Blank

Simulation of the laser melting process of titanium using Smoothed Particle Hydrodynamics

Erlangen
FAU University Press
2023

Bibliografische Information der Deutschen Nationalbibliothek:
Die Deutsche Nationalbibliothek verzeichnet diese Publikation in der Deutschen Nationalbibliografie; detaillierte bibliografische Daten sind im Internet über http://dnb.d-nb.de abrufbar.

Bitte zitieren als
Michael Blank. 2023. *Simulation of the laser melting process of titanium using Smoothed Particle Hydrodynamics.* FAU Forschungen, Reihe B, Medizin, Naturwissenschaft, Technik Band 43. Erlangen: FAU University Press. DOI: 10.25593/ 978-3-96147-648-0.

Der vollständige Inhalt des Buchs ist als PDF über den OPUS-Server der Friedrich-Alexander-Universität Erlangen-Nürnberg abrufbar:
https://opus4.kobv.de/opus4-fau/home

Verlag und Auslieferung:
FAU University Press, Universitätsstraße 4, 91054 Erlangen

Druck: docupoint GmbH

ISBN: 978-3-96147-647-3 (Druckausgabe)
eISBN: 978-3-96147-648-0 (Online-Ausgabe)
ISSN: 2198-8102
DOI: 10.25593/ 978-3-96147-648-0

Simulation of the laser melting process of titanium using Smoothed Particle Hydrodynamics

Simulation des Laserschmelzprozesses von Titan mittels Smoothed Particle Hydrodynamics

Der Technischen Fakultät
der Friedrich-Alexander-Universität
Erlangen-Nürnberg

zur
Erlangung des Doktorgrades Dr.-Ing.

vorgelegt von

Michael Blank

aus Zerbst

Als Dissertation genehmigt
von der Technischen Fakultät
der Friedrich-Alexander-Universität Erlangen-Nürnberg

Tag der mündlichen Prüfung:	19.12.2022
Gutachter:	Prof. Dr. Thorsten Pöschel
	Prof. Dr. Jens Harting
	Prof. Jose Daniel Muñoz Castaño

Abstract

The ability to generate high-energy radiation has made lasers an essential tool in metal processing. Laser welding, selective laser melting, or wire-based laser metal deposition represent joining or additive manufacturing technologies that employ the high material heating rates produced by focused laser beams. Inappropriate processing parameters may lead to material defects that deteriorate the mechanical properties of the weld or the manufactured part. To some extent, this is caused by a lacking understanding of the influence of the process parameters on the governing physical effects in laser-metal processing.

This work presents a three-dimensional numerical model based on the Incompressible Smoothed Particle Hydrodynamics method, which describes heat transfer, phase transitions, and liquid flow simultaneously. The method is embedded into a research software that can be executed on high-performance computers. To reduce the computational cost of the method, the gas phase is not explicitly modeled by particles. Instead, appropriate boundary conditions are applied at free surfaces. To enforce the impermeability of walls, the pressure Poisson equation is modified for particles representing the wall. Subsequently, the velocity field obtained in a plane Poiseuille flow problem is validated against theory.

The interaction of laser radiation with an arbitrarily shaped material surface is modeled using ray tracing, where the laser beam is discretized into many energy portions. The power reflectance of the material surface irradiated by the laser is evaluated using Fresnel equations.

In this work the laser melting process of titanium surrounded by an argon shielding gas is investigated. Due to large the variance in the optical properties of titanium reported in the literature, clean and aged titanium surfaces are distinguished in this work. Surface aging leads to a significantly reduced reflectivity of the material surface for electromagnetic radiation, which can be attributed to oxide layers, contamination, or roughening. The effective absorbtance of a monodisperse and a polydisperse titanium powder bed surrounded by an argon gas at atmospheric pressure is investigated by considering temperature-dependent material properties. It is found that the absorbed laser power by the titanium powder beds increases significantly with increasing temperature. Furthermore, the measured absorptance of aged titanium surfaces is greater than for clean titanium surfaces at all investigated temperatures. In addition, the absorbed laser power is measured as a function

of the propagation depth into a monodisperse and polydisperse titanium powder.

Moreover, this work presents two approaches to model surface tension at free surfaces in Smoothed Particle Hydrodynamics. The first model applies a Young-Laplace pressure boundary condition at the liquid-gas interface. This approach is validated for a range of notoriously difficult test cases and is used to simulate the separation of a liquid cylinder into several drops due to the Plateau-Rayleigh instability. The second approach adapts the continuum surface force model for the application at free surfaces. In addition, an approach to model wetting forces at free surfaces is presented. The robustness and accuracy of the method are shown in several test cases ranging from droplet oscillations and wetting of solids under gravity to thermocapillary flow in a cavity caused by a temperature gradient.

In the central part of this work, the laser melting of titanium surrounded by argon at atmospheric pressure is investigated. For this reason, the absorption of laser radiation in the emerging metal vapor due to evaporation is modeled by reducing the power carried by a ray in the ray tracing algorithm as a function of the evaporation coefficient given by the employed evaporation model. Furthermore, the recoil pressure due to rapid evaporation is modeled as a Dirichlet boundary condition. The effective heat capacity, which includes the latent heat of melting or crystallization in this work, restricts the utilized numerical time step. For this reason, a linear controller adjusts the thermal numerical time step used to solve the energy equation as a function of the heating and cooling rates of the material. Using the small thermal time step, the energy equation is solved multiple times in each numerical time step.

In a series of simulations of single-line laser tracks on titanium metal sheets, the influence of the material's optical properties, laser process parameters, and the emerging vapor on the weld geometry is investigated. The simulated results are compared to experimental measurements provided by the Institute of Photonic Technologies at the Friedrich-Alexander-Universität Erlangen-Nürnberg. In these simulations, a good agreement with the experimentally measured weld shapes is obtained when assuming an aged titanium surface and utilizing process parameters that do not lead to evaporation. Strong fluctuations of the weld geometry can be seen in the experiments with increasing laser intensity and decreasing scanning velocity, which may be caused by phenomena linked to the evaporation process. The simulated weld cross sections agree well with the experiments when accounting for the absorption of laser radiation in the emerging metal vapor. Furthermore, the influence of the wetting force on the welding seam geometry is investigated. High wetting

force at the three-phase contact line leads to a depression along the scan line of the laser, whereas a low wetting force leads to irregular welding seams. By comparing the simulation results with the experiments, the wetting forces are iteratively adjusted for various laser parameters to achieve good agreement of the weld shapes. It is found that the wetting force in laser melting processes can be related to the Stefan number, measured in the melt in the vicinity of the solid-liquid interface. Increasing laser intensity and scanning velocity lead to increasing Stefan numbers and decreasing wetting force, which provokes the humping phenomenon.

In addition, the applicability of wire-based laser metal deposition of titanium in argon atmosphere and in zero-gravity is investigated. It is shown that the absence of gravity has a positive effect on the stability of the formed liquid bridge and, therefore, improves the continuous deposition of molten metal. Finally, the selective laser melting process of a polydisperse titanium powder bed is investigated. The complex morphology of the powder represents a limitation for the presented surface tension model due to erroneous curvature computation. For this reason, surface tension is modeled using pairwise forces among particles in this scenario. It can be seen that the melt coalesces and flows in the same direction as the laser beam, creating a depression in the solidified material behind the laser beam. This behavior may be attributed to the balling phenomenon which should be investigated in conjunction with a comparison of available surface tension models in future work.

Kurzfassung

Die Fähigkeit, Strahlung mit hohen Energiedichten zu erzeugen, hat den Laser zu einem unverzichtbaren Werkzeug in der Metallverarbeitung gemacht. Laserschweißen, selektives Laserschmelzen oder Draht-basiertes Laserauftragschweißen sind Füge-, bzw. additive Fertigungstechnologien, die fokussierte Laserstrahlen nutzen, um hohe Heizraten des Materials zu erzielen. Wenn dabei ungeeignete Prozessparameter verwendet werden, können diese zu Defekten im Material führen, die die mechanischen Eigenschaften der Schweißnaht oder des hergestellten Bauteils verschlechtern. In gewissem Maße ist dies auf ein mangelndes Verständnis des Einflusses der Prozessparameter auf die auftretenden physikalischen Effekte bei der Laser-Metall-Bearbeitung zurückzuführen.

In dieser Arbeit wird ein dreidimensionales numerisches Modell vorgestellt, was auf der Methode Incompressible Smoothed Particle Hydrodynamics basiert, und gleichzeitig die Wärmeübertragung, Phasenübergänge und Flüssigkeitsströmung beschreiben kann. Die Methode ist in eine für Hochleistungscomputersysteme optimierte Forschungssoftware implementiert. Um die Rechenzeit zu senken, wird die Gasphase nicht explizit durch Partikel modelliert. Stattdessen werden geeignete Randbedingungen an freien Oberflächen angewendet. Um die Impermeabilität der Wände zu gewährleisten, wird die Poisson-Gleichung für Wand-Partikel modifiziert. Anschließend wird das Strömungsprofil einer Flüssigkeit zwischen zwei stationären Wänden mithilfe einer analytischen Lösung validiert.

Die Wechselwirkung von Laserstrahlung mit einer geometrisch beliebigen Materialoberfläche wird mit einem Raytracing-Ansatz modelliert, bei dem der Laserstrahl in viele einzelne Strahlen diskretisiert wird. Zur Berechnung der reflektierten Leistung des Lasers an der Materialoberfläche, werden die Fresnel-Gleichungen verwendet.

In dieser Arbeit wird der Laserschmelzprozess von Titan, umgeben von einem Argon-Schutzgas, untersucht. Aufgrund der Varianz der in der Literatur angebenden optischen Eigenschaften von Titan werden in dieser Arbeit reine und gealterte Titanoberflächen unterschieden. Die Alterung der Materialoberfläche führt zu einer deutlich verringerten Reflektivität der elektromagnetischen Strahlung und kann auf die Bildung von Oxidschichten, Verunreinigungen oder der Oberflächenrauigkeit zurückgeführt werden. Die effektive Absorption von Laserstrahlung durch ein monodisperses und ein polydisperses Titanpulverbett, das von Argon bei atmosphärischem

Druck umgeben ist, wird unter Berücksichtigung der temperaturabhängigen Materialeigenschaften untersucht. Es zeigt sich, dass die absorbierte Laserleistung durch die Titanpulverbetten mit steigender Temperatur deutlich zunimmt. Darüber hinaus ist das gemessene Absorptionsvermögen von gealterten Titanoberflächen bei allen untersuchten Temperaturen größer als bei reinen Titanoberflächen. Zusätzlich wird die Absorption der Laserstrahlung in Abhängigkeit der Eindringtiefe in monodisperses und polydisperses Titanpulver untersucht.

Weiterhin werden in dieser Arbeit zwei Ansätze zur Modellierung der Oberflächenspannung an freien Oberflächen für die Anwendung in der Smoothed Particle Hydrodynamics-Methode vorgestellt. Im ersten Modell wird eine Young-Laplace-Druck-Randbedingung an der Flüssig-Gas-Grenzfläche angewendet. Dieser Ansatz wird in einer Reihe von Testfällen validiert und zur Simulation des Zerfalls eines Flüssigkeitszylinders in mehrere Tropfen infolge der Rayleigh-Plateau-Instabilität verwendet. Der zweite Ansatz passt das Continuum Surface Force-Modell für die Anwendung an freien Oberflächen an. Darüber hinaus wird ein Ansatz zur Modellierung der Benetzungskräft an freien Oberflächen vorgestellt. Die Robustheit und Genauigkeit der Methode wird in einer Reihe von Testszenarien überprüft, die von Tropfenoszillationen und der Benetzung von Festkörpern unter Schwerkraft, bis hin zur Marangoni-Konvektion, die durch einen Temperaturgradienten verursacht wird, reichen.

Im zentralen Teil dieser Arbeit wird das Laserschmelzen von Titan, welches von Argon bei Atmosphärendruck umgeben ist, untersucht. Hierzu wird die Absorption der Laserstrahlung im entstehenden Metalldampf modelliert, indem die Leistung eines Strahls im Raytracing-Algorithmus in Abhängigkeit vom Verdampfungskoeffizienten, der durch das verwendete Verdampfungsmodell gegeben ist, reduziert wird. Außerdem wird der Rückstoßdruck, der auf die siedende Flüssigkeitsoberfläche wirkt, als Dirichlet-Randbedingung modelliert. Die effektive Wärmekapazität, die in dieser Arbeit die Schmelz- oder Kristallisationswärme modelliert, schränkt den verwendeten numerischen Zeitschritt ein. Aus diesem Grund wird ein linearer Regler verwendet, um den numerischen Zeitschritt zur Lösung der Energiegleichung in Abhängigkeit der Heiz- und Kühlraten des Materials, adaptiv einzustellen. Unter Verwendung des thermischen Zeitschritts wird die Energiegleichung in jedem numerischen Zeitschritt mehrfach gelöst.

In einer Reihe von Simulationen von geradlinigen Laserspuren auf Titanblechen wird der Einfluss der Oberflächeneigenschaften des Materials, der Laserprozessparameter und des entstehenden Dampfes auf die Schweißgeometrie untersucht. Die simulierten Ergebnisse werden mit experimentellen

Messergebnissen verglichen, die vom Institut für Photonische Technologien der Friedrich-Alexander-Universität Erlangen-Nürnberg bereitgestellt wurden.

Bei Annahme einer gealterten Titanoberfläche und Verwendung von Prozessparametern, die nicht zum Sieden führen, konnte eine gute Übereinstimmung der ermittelten Schweißgeometrie zwischen Simulationen und Experimenten erzielt werden. Starke Schwankungen der Schweißnahtgeometrie sind in den Experimenten mit zunehmender Laserintensität und abnehmender Scangeschwindigkeit zu beobachten. Dies kann möglicherweise auf den Verdampfungsprozess zurückgeführt werden. Die simulierten Schweißnahtquerschnitte stimmen qualitativ mit den Experimenten überein, wenn die Absorption des Laserstrahls im entstehenden Metalldampf berücksichtigt wird. Zusätzlich wird der Einfluss der Benetzungskräfte auf die Schweißnahtgeometrie untersucht. Hohe Benetzungskräfte an der Dreiphasen-Kontaktlinie führen zu einer Vertiefung entlang des Laserpfades, während niedrige Benetzungskräfte zu unregelmäßigen Schweißnähten führen. Durch Vergleich der Simulationsergebnisse mit den Experimenten werden die Benetzungskräfte für verschiedene Laserparameter iterativ angepasst, um eine gute Übereinstimmung der Schweißnahtformen zu erzielen. Es zeigt sich, dass die auftretenden Benetzungskräfte in Laserschmelzprozessen mit der Stefan-Zahl, ermittelt in der Schmelze nahe der Fest-Flüssig-Grenzfläche, in Beziehung gesetzt werden können. Steigende Laserintensitäten und Scangeschwindigkeiten führen zu steigenden Stefan-Zahlen und sinkenden Benetzungskräften, was das Humping-Phänomen begünstigt.

Darüber hinaus wird die Anwendbarkeit des drahtbasierten Laserauftragschweißen von Titan in einer Argon-Atmosphäre und in Schwerelosigkeit untersucht. Es kann gezeigt werden, dass sich die Abwesenheit der Schwerkraft positiv auf die Stabilität der gebildeten Flüssigkeitsbrücke auswirkt und somit die kontinuierliche Ablagerung der Schmelze verbessert. Anschließend wird der selektive Laserschmelzprozess eines polydispersen Titanpulverbettes untersucht. Die komplexe Morphologie des Pulvers verhindert den Einsatz des zuvor verwendeten Oberflächenspannungsmodells, da hier die Berechnung der Krümmung fehlerbehaftet ist. Deshalb wird in diesem Szenario Oberflächenspannung durch paarweise Kräfte zwischen Partikeln modelliert. In der Simulation fließt die Schmelze zusammen und bewegt sich in Scanrichtung des Laserstrahls, wobei eine Vertiefung hinter dem Laserstrahl entsteht. Dieses Verhalten kann eventuell auf das Balling-Phänomen zurückgeführt werden,

was in zukünftigen Arbeiten neben einem Vergleich der verfügbaren Oberflächenspannungsmodelle untersucht werden sollte.

Acknowledgments

First and foremost, I would like to thank my supervisor, Prof. Dr. Thorsten Pöschel, for his support, valuable advice, comments, and the conceded freedom in this project.

I would like to thank Dr. Prapanch Nair for providing snu-SPH, which has been the basis for the numerical investigations in this work, the valuable support and encouragement since the preparation of my master's thesis, and the many SPH-related discussions.

Furthermore, I would like to thank all of my colleagues for the countless constructive scientific discussions and my friends who have contributed substantially to the completion of this thesis.

For providing experimental measurement data, I thank Florian Huber and the Institute of Photonic Technologies of the Friedrich-Alexander-Universität Erlangen-Nürnberg.

I would like to thank my parents from the bottom of my heart, who made this path possible for me and always supported me in all my decisions. Lastly, I thank my family and Monika for their tireless and patient support in the past years.

Funding acknowledgements

The author gratefully acknowledges the Gauss Centre for Supercomputing e.V. (www.gauss-centre.eu) for funding this project by providing computer time through the John von Neumann Institute for Computing (NIC) on the GCS Supercomputer JUWELS at Jülich Supercomputing Centre (JSC).

The author gratefully acknowledges the scientific support and HPC resources provided by the Erlangen National High Performance Computing Center (NHR@FAU) of the Friedrich-Alexander-Universität Erlangen-Nürnberg (FAU). The hardware is funded by the German Research Foundation (DFG).

Funded by the Deutsche Forschungsgemeinschaft (DFG, German Research Foundation)-Project-ID 61375930-SFB 814 “Additive Manufacturing” TP B1.

Contents

Nomenclature

In the following, the nomenclature is introduced. Some variables are not explicitly shown in this list but can be composed of the symbol and the corresponding sub- or superscript. Curve fitting parameters, substitutions used to simplify the handling of long mathematical expressions, or variables used only once are excluded from this list.

Latin symbols

$\mathbf{a}$	acceleration vector
A	surface area
A_{ray}	cross-sectional area of a single ray
B	base radius of a spherical cap
$\mathbf{B}$	magnetic field vector
c	speed of sound
c_p	specific heat capacity at constant pressure
$\tilde{c}_p$	effective heat capacity at constant pressure
$c_p^{\alpha},\ c_p^{\beta},\ c_p^{\mathrm{l}}$	specific heat capacity of α-, β-, or liquid titanium
$c_p^{\alpha\beta},\ c_p^{\beta\mathrm{l}}$	mean specific heat capacity at crystallization temperature between α- and β- phase; mean specific heat capacity at melting temperature between β and liquid phase
$c_{p,\mathrm{D}}^{\alpha}, c_{p,\mathrm{H}}^{\alpha}, c_{p,\mathrm{E}}^{\alpha}$	contributions to molar heat capacity of α-titanium; Debye (D), Hoch (H) and exponential (E)
d	number of dimensions
d^{sl}	normal distance of a liquid SPH particles to the closest solid SPH particle
d^{v}	distance between triangle vertex and the intersection point of a ray with the same triangle
D	depth or diameter
$\mathbf{D}$	displacement of electrons
$D\left(\bar{x}\right)$	Debye function
D_{th}	thermal diffusivity
E_A	energy density

$\mathbf{E}$	electric field vector
$\mathbf{E}_0$	amplitude vector of the electric field
$\mathbf{E}_{\mathrm{ray}}$, $\hat{\mathbf{E}}_{\mathrm{ray}}$	electric field vector and normalized electric field vector of a ray in the ray tracing algorithm
$\mathbf{f}$	acceleration vector
F_{ab}	function including the gradient of the kernel function for a particle pair a and b
F^{-}	dimensionless function accounting for particle collisions within the Knudsen layer
g	body acceleration
G	Green's function
$\tilde{G}$	Fourier transform of Green's function
$\mathbf{G}$	tensor made up from Cartesian basis vectors
h	smoothing length
h_T	smoothing length of a one-dimensional kernel function defined in the temperature domain
h_{cryst}, $\tilde{h}_{\mathrm{cryst}}$	specific enthalpy of crystallization and smoothed specific enthalpy of crystallization
h_{m}, $\tilde{h}_{\mathrm{m}}$	specific enthalpy of melting and smoothed specific enthalpy of melting
h_{vap}	specific enthalpy of vaporization
$h_{\mathrm{vap},0}$	specific enthalpy of vaporization at absolute zero temperature
H	height
i	imaginary unit
I	intensity
$\mathbf{I}$	unity matrix
j^{+}, j^{-}	fluxes of evaporating (+) and condensing (–) particles
j^{net}	net evaporation flux
k	thermal conductivity
k_λ	angular wave number
$\mathbf{k}$	spatial frequency vector
$\mathbf{k}_{\mathrm{ray}}$	propagation direction of a ray in the ray tracing algorithm

$K^{\mathrm{s}},\ K^{\mathrm{l}}$	constant necessary to estimate the electron-phonon collision frequency of a solid (s) or liquid (l) metal
$\mathbf{K}$, $\mathbf{K}'$	curvature tensor in Euclidean or tangent space
L	length
$\mathcal{L}$	linear differential operator
$\mathbf{L}$	normalization tensor
$\mathbf{L}_B$	tensor containing tangent basis vectors
m	mass
m_{A}	atomic mass
m_{e}^*	effective electron mass
$\dot{m}_{\mathrm{vap}}$	evaporation mass flux
M	molar mass
M^2	beam quality factor
$\mathrm{Ma}_{\mathrm{Kn}}$	flow Mach number at outer side of Knudsen layer
$\bar{n}$	complex refractive index, $\bar{n} = n_1 + in_2$
$\underline{n}$	ratio of the complex refractive indices of two adjacent phases (1) and (2), $\underline{n} = \bar{n}^{(1)}/\bar{n}^{(2)}$
$\mathbf{n}$, $\tilde{\mathbf{n}}$	normal and smoothed normal vector
$\hat{\mathbf{n}}$, $\hat{\tilde{\mathbf{n}}}$	normalized normal and normalized smoothed normal vector
n_{e}	number of electrons per unit volume
N_{ints}	total number of ray intersections with a single triangle
n_{ray}	number of rays that statistically hit a single triangle made up from SPH particles
N_{SPH}	total number of SPH particles
$N_{\mathrm{SPH}}^{\mathrm{l}}$	total number of liquid SPH particles
n_{tr}	integer representing the time interval at which the surface mesh is computed
N_{ray}	total number of rays used to discretize the laser beam
p	pressure
p_{a}	ambient pressure
p_{amb}	ambient background pressure in SPH simulations, typically set to $p_{\mathrm{amb}} = 0\,\mathrm{Pa}$

p_{Kn}	pressure at the ambient side of the Knudsen layer
p_{o}	external pressure that acts on SPH particles located in the vicinity of a free boundary
p_{recoil}, $\tilde{p}_{\mathrm{recoil}}$	recoil pressure and smoothed recoil pressure
p_{s}	saturated vapor pressure
P	power
$\mathbf{P}$	polarization density
P_0	total laser power
P_2	second degree Legendre polynomial
P_{ray}	laser power carried by a single ray in the ray tracing algorithm
$\dot{q}_{\mathrm{l}}$	heat flux density due to laser radiation
$\dot{q}_{\mathrm{l,ray}}$	heat flux density due to laser radiation modeled with the ray tracing algorithm
$\dot{q}_{\mathrm{r}}$	heat flux density due to thermal radiation
q_T	temperature difference between the temperature of an SPH particle and the crystallization or melting temperature
$\dot{q}_{\mathrm{vap}}$	volumetric heat flux density due to evaporation
r	radius or radial distance
$\mathbf{r}$	position
$\mathbf{r}'$	position in the neighborhood of $\mathbf{r}$
$\mathbf{r}^*$	intermediate position
r_0	initial or equilibrium radius
r_{ab}	Euclidean distance between particles a and b
$\mathbf{r}_{ab}$	displacement between particles a and b
r_{max}	SPH kernel radius
r_{ray}	radial distance of a ray to the laser beam axis
$r_{\mathrm{ray},0}$	radius of the ray-initialization area
R	reflectivity of an interface for electromagnetic radiation
$R_{\mathrm{g,sp}}$	specific gas constant
S	Shepard filter

$S(0)$	long wavelength limit of the liquid structure factor
S_d	Heat kernel in d spatial dimensions
S_{Kn}	dimensionless velocity at outer edge of Knudsen layer
t	time
$\mathbf{t}$, $\tilde{t}$	tangent and smoothed tangent vector
$\hat{\mathbf{t}}$, $\hat{\tilde{\mathbf{t}}}$	normalized tangent and normalized smoothed tangent vector
$\mathbf{T}$	metric used for changing the bases of the coordinate system
T	temperature
T_0	reference or ambient temperature
T_{boil}	boiling temperature at standard atmospheric pressure
T_{crit}	critical temperature
T_{cryst}	crystallization temperature
T_{Kn}	temperature at the ambient side of the Knudsen layer
T^{l}	mean temperature of liquid SPH particles in the vicinity of the solid-liquid interface
T_{m}	melting temperature
T_{osc}	time for one oscillation, period
T_{s}	surface temperature defined at the vapor side of the condensed phase boundary
T_{t}	target temperature
T_{v}	temperature at which a mass element is completely evaporated
u	scalar velocity
$\mathbf{u}$, $\tilde{\mathbf{u}}$	velocity vector and smoothed velocity vector
$\mathbf{u}^*$	intermediate velocity
	smoothed velocity vector
u_0	initial velocity magnitude
u_{128}	uniformly distributed random number $\in [0,\ 1]$ obtained by the xorshift128 algorithm
u_{feed}	magnitude of the wire-feed velocity
$\bar{u}_{\mathrm{feed}}$	temporal averaged magnitude of the wire-feed velocity

$u_{\mathrm{feed,max}}$	maximum permitted magnitude of the wire-feed velocity
u_{Kn}	vapor velocity at outer side of Knudsen layer
u_{l}	magnitude of the laser scanning velocity
$\mathbf{u}_{\mathrm{l}}$	laser scanning velocity vector
$\mathbf{u}_{\mathrm{s}}$	spreading velocity of a liquid on a solid substrate
$\mathbf{u}_{\mathrm{wire}}$, $\hat{\mathbf{u}}_{\mathrm{wire}}$	velocity vector and normalized velocity vector of the wire in LMD-w
U	characteristic velocity
V	volume
w	mass fraction
w_0	beam waist radius of a Gaussian laser beam
$w\,(z)$	beam radius of a Gaussian laser beam
W	SPH kernel function
$\mathbf{x}$	Cartesian coordinates, $\mathbf{x} = (x, y, z)$
$\bar{x},\ \bar{y}$	integration variables
z_{control}	desired z-position of the wire tip adjusted by a linear controller
z_{e}	number of valence electrons
$z_{\mathrm{wire,min}}$	lowest z-position of the wire tip

Greek letters

α	absorption coefficient
α_{K}	SPH kernel normalization factor for d dimensions
β	SPH penalty term at free boundaries
β^{-}	dimensionless function accounting for particle collisions
γ	specific heat ratio or surface energy
$\gamma_{\perp}$	fraction of the normalized electric field oriented perpendicular to the plane of incidence
Γ	collision frequency
Γ^{l}, Γ^{s}	electron-phonon collision frequency of the liquid (l) or solid (s) phase

δ	Dirac delta function
δ_s	surface delta function
δ_p	penetration depth of electromagnetic radiation
Δp_recoil	pressure difference between recoil and ambient pressure
$\Delta \tilde{p}_\mathrm{recoil}$	smoothed pressure difference between recoil and ambient pressure
Δt	numerical time step
ΔT	half ot the temperature domain in which the latent heat of a phase transition is released or absorbed
Δp_YL, $\Delta p'_\mathrm{YL}$	Young-Laplace pressure difference and scaled Young-Laplace pressure difference
Δx	initial SPH particle spacing on a rectangular lattice
ϵ	permittivity
ϵ_r	complex relative permittivity, $\epsilon_\mathrm{r} = \epsilon_{\mathrm{r},1} + i\epsilon_{\mathrm{r},2}$
ϵ_n	threshold used to discard erroneous surface normal vectors
ϵ_th	thermal emissivity
η	dynamic viscosity
θ_ray	orientation of a unit vector in a circle; used in the ray tracing algorithm
θ	angle between a ray and the surface normal
Θ_∞	equilibrium contact angle
Θ_a	apparent dynamic contact angle
Θ_D	Debye temperature
Θ_H	Heaviside step function
Θ_PY	Percus-Yevick temperature
Θ_s	contact angle of dynamic solidification front
$\bar{\kappa}$	mean curvature
κ_1, κ_2	principal radii of curvature
$\varkappa$	ratio of the number of triangle vertices (SPH particles) which represent the optical properties of aged titanium to the number of vertices that represent the optical properties of clean titanium

λ	wavelength of light
ν	kinematic viscosity
ρ	density
ρ_{e}	electric resistivity
ρ_{Kn}	density at ambient side of Knudsen layer
ρ_{s}	density at vapor side of condensed phase boundary
σ	surface tension coefficient
σ	Cauchy stress tensor
σ_{e}	electric conductivity
τ	deviatoric stress tensor
ϕ	evaporation coefficient
Φ	physical quantity
χ	electric susceptibility
$\psi(z)$	Gouy phase
ω	angular frequency
ω_0	angular resonance frequency
ω_{p}	plasma frequency
Ω	domain which includes all SPH particles
Ω^{l}	domain which includes only liquid SPH particles
$\Omega_{\mathbf{r}}$	domain centered at $\mathbf{r}$
Ω^{s}	domain which includes only solid SPH particles
Ω^{slg}	domain which includes SPH particles that are located in the vicinity of the three-phase contact line
Ω^{v}	domain which includes only interfacial SPH particles
Ω^{w}	domain which includes only wall SPH particles

Subscripts

0	property defined at reference conditions
∞	equilibrium condition
η	property related to viscosity
σ	property related to surface tension
a	central SPH particle whose property is evaluated using kernel weighting
a	property defined in the ambient, undisturbed gas
aged	property related to an oxidized, contaminated or rough titanium surface
ab	evaluation for an SPH particle pair a and b
b	neighboring SPH particle of the central particle a
boil	property related to boiling point
clean	property related to atomically clean titanium surface
crit	property related to critical point
cryst	property related to crystallization point
g	property related to body accelerations
i	property of incident electromagnetic radiation
in	property on the liquid side of a liquid-gas interface
Kn	Knudsen; related to the ambient side of the Knudsen layer
m	related to melting point
max	upper limit of a quantity
min	lower limit of a quantity
o	property defined on the ambient side of a free surface
other	originating from other forces
p	property related to pressure
r	property of reflected electromagnetic radiation
ray	property related to a ray in the ray tracing algorithm
s	property defined at the vapor side of the evaporating surface
t	property of transmitted electromagnetic radiation

th	thermal
tr	property of a triangle
v	related to vapor phase
vap	property of the vapor
wire	property related to the wire in LMD-w
x, y, z	vector oriented in x-, y- or z-direction in Euclidean space

Superscripts

$\perp$	perpendicular
$\parallel$	parallel
$*$	intermediate property in time
1D, 3D	defined in one (1D) or three spatial dimensions (3D)
α	related to α-phase of titanium
β	related to β-phase of titanium
$\alpha\beta$	related to crystallization temperature of titanium
βl	related to melting temperature of titanium
aged	oxidized, polluted or rough titanium surface
anl	analytical value
b	SPH approximation requiring full neighbor particle support
c	SPH approximation applicable to free boundaries
d	spatial dimensions
l	property related to liquid phase
lg	property at liquid-gas interface
n	discrete time in multiples of the numerical time step
other	other contributions to the momentum balance
pf	related to pairwise forces between SPH particles
s	property related to solid phase
sf	property at the solid-fluid interface
sg	property at the solid-gas interface
v	property of an interfacial SPH particle

w	wall
T	transpose of a tensor

Dimensionless numbers

Bo	Bond number = $\frac{\text{gravitational force}}{\text{capillary force}}$
Ca	capillary number = $\frac{\text{viscous force}}{\text{capillary force}}$
Fr	Froude number = $\frac{\text{inertial force}}{\text{gravitational force}}$
Pe	Péclet number = $\frac{\text{convective transport rate}}{\text{diffusive mass transport rate}}$
$\mathfrak{R}$	Reynolds number = $\frac{\text{convective transport rate}}{\text{diffusive momentum transport rate}}$
St	Stefan number = $\frac{\text{sensible heat}}{\text{latent heat}}$
$\overline{\text{St}}$	mean Stefan number
We	Weber number = $\frac{\text{inertial force}}{\text{surface tension force}}$

Constants

c_0	speed of light in vacuum	$299.793 \cdot 10^6\,\mathrm{m\,s^{-1}}$
e	Euler number	2.7183
$\hbar$	reduced Planck constant	$1.05 \cdot 10^{-34}\,\mathrm{J\,s}$
k_B	Boltzmann constant	$1.38 \cdot 10^{-23}\,\mathrm{J\,K^{-1}}$
$L_{\mathrm{e},0}$	Lorenz number	$2.45 \cdot 10^{-8}\,\mathrm{W\,\Omega\,K^{-2}}$
m_e	mass of an electron	$9.109 \cdot 10^{-31}\,\mathrm{kg}$
N_A	Avogadro constant	$6.022 \cdot 10^{23}\,\mathrm{mol^{-1}}$
p_atm	atmospheric pressure	$101325\,\mathrm{Pa}$
q_e	electric charge of an electron	$1.602 \cdot 10^{-19}\,\mathrm{C}$
R_g	ideal gas constant	$8.314\,\mathrm{J\,K^{-1}\,mol^{-1}}$
ϵ_0	electric permittivity of vacuum	$8.854 \cdot 10^{-12}\,\mathrm{F\,m^{-1}}$
σ_SB	Stefan-Boltzmann constant	$5.67 \cdot 10^{-8}\,\mathrm{W\,m^{-2}\,K^{-4}}$
π	circle circumference to diameter ratio	3.1416

Acronyms

BiCGStab	Bi-Conjugate Gradient Stabilized
CAD	Computer Aided Design
CFL	Courant-Friedrichs-Levy
CGAL	Computational Geometry Algorithms Library
CSF	Continuum Surface Force
PPE	Pressure Poisson Equation
FAU	Friedrich-Alexander-Universität Erlangen-Nürnberg
ISPH	Incompressible Smoothed Particle Hydrodynamics
LMD-w	wire-based Laser Metal Deposition
LPT	Institute of Photonic Technologies
MPI	Message Passing Interface
OpenMP	Open Multi-Processing
SLM	Selective Laser Melting
SPH	Smoothed Particle Hydrodynamics
WF	Wiedemann-Franz
YL	Young-Laplace

List of Figures

List of Tables

1 Introduction

Light Amplification by Stimulated Emission of Radiation (LASER) refers to a technology for generating focused light. The energy density of the laser's electromagnetic radiation is sufficient to heat, melt, and vaporize metals with high spatial and temporal precision. For this reason, lasers have become established in numerous fields of application, such as laser cutting [162], laser ablation [169, 232], laser welding [79] or additive manufacturing. Additive manufacturing is an umbrella term for various technologies that allow the fabrication of functional and highly customized components by fusing raw materials layer-by-layer and is promoted as another industrial revolution with a high impact on the established market structures [213]. Selective Laser Melting (Plateau-Rayleigh) of metals [225] and wire-based Laser Metal Deposition (LMD-w) [111] represent two additive manufacturing processes that are being intensively investigated. High demands are placed on the quality and mechanical properties of the manufactured components in metal additive manufacturing in dependence of their intended field of application, e.g., aerospace or automotive. Sub-optimal process conditions can cause material defects such as pores or cracks during the printing process. To avoid such defects, the printing process and the process parameters must be optimized for any feedstock and part geometry, representing a time-consuming and costly trial and error procedure when using traditional experimentation. The interrelationship of physical effects complicates the investigation of isolated process parameters since analytical evaluations are often impossible and experimental measurements are constrained by spatial and temporal resolution. For this reason, this work presents a three-dimensional numerical model for solving laser-metal interaction problems.

In the scope of this work, various numerical models are presented and implemented into an existing research software based on the Smoothed Particle Hydrodynamics (SPH) method. The numerical tool can simulate hydrodynamics, thermodynamics, and laser-matter interaction. The main objective of this work lies in investigating the influence of the material surface properties and the acting wetting forces on the weld geometry in laser welding processes. Furthermore, the process behavior of LMD-w in zero-gravity is investigated, and the applicability of the developed model to SLM is explored. Because of the computational cost of the employed numerical method when solving these problems, the ambient gas phase is not explicitly simulated but modeled using boundary conditions. This is associated with numerical difficulties in the mathematical treatment of SPH particles in the vicinity of free

boundaries. The employed physical models are implemented, ensuring high parallelism of the software using the Open Multi-Processing (OpenMP) interface and the Message Passing Interface (MPI) for use on high-performance computers.

This thesis comprises nine chapters, including the introduction (Chapter 1). Chapter 2 briefly introduces laser welding, LMD-w, and SLM and the governing physical effects of these processes. Furthermore, possible material defects arising in laser-metal processes which deteriorate the product quality, and strategies to avoid them are presented. In this work, laser melting of titanium using an argon shielding gas is investigated. For this reason, Chapter 3 introduces the modeled temperature-dependent material properties of titanium. Diverging data of the optical properties of titanium has been found in the literature. Therefore, this work distinguishes between aged titanium and clean titanium surfaces. An aged titanium surface is characterized by a lower surface reflectivity when compared to a clean titanium surface. The aging of the material surface can be caused by the formation of oxide layers, contamination with other chemicals, or mechanical influences that lead to higher surface roughness.

In Chapter 4, a concise introduction to the employed SPH method is given. Here, an SPH pressure gradient approximation, which allows to apply an ambient pressure on free surfaces, is presented. To ensure stable simulations of laser melting processes of metals, the impermeability condition of walls is met by modifying the pressure Poisson equation for identified wall particles which is solved in Incompressible Smoothed Particle Hydrodynamics (ISPH). By comparing the laminar Poiseuille flow between two semi-infinite plates with the corresponding analytical solution of the velocity field, the impermeability of the wall boundary is validated together with the imposed no-slip boundary condition.

The energy transfer from the laser beam to a material with an arbitrary shaped surface is modeled by ray tracing. Chapter 5 describes the employed ray tracing algorithm and its validation. The effective absorptance of monodisperse and polydisperse titanium powder is subsequently measured as a function of the material's surface properties and temperature. In addition, the propagation depth of laser radiation within the pores of the powder beds is investigated.

Chapter 6 presents an modeling approach for surface tension solely by applying a pressure boundary condition at the liquid-gas interface. In addition, the Continuum Surface Force (CSF) model is adapted for the application to free surface problems using the SPH method. Moreover, wetting forces arise when

a liquid is in contact with a solid. Consequently, a wetting model is presented that can be applied at free boundaries. The accuracy and robustness of the proposed models is verified in a variety of difficult test cases ranging from droplet oscillations, droplet deformations under gravity, to the pinning of drops at surface discontinuities or the simulation of the Plateau-Rayleigh instability.

The central part of this work is presented in Chapter 7. Here, the numerical software is extended by modeling the recoil pressure at the liquid-gas interface via a pressure boundary condition, an absorption model that accounts for the energy lost in the emerging vapor plume, and an adaptive time-stepping scheme for the solution of the energy equation by employing a linear controller. The developed numerical model is subsequently used to investigate the effect of the processing parameters and titanium's surface properties on the weld geometry obtained in single-line laser tracks. The wetting forces are iteratively adjusted for each set of processing parameters to achieve a qualitative agreement between the simulated and the experimental geometries of the welding seams. Consequently, a relationship between the humping phenomenon and the process parameters is established.

In Chapter 8, the developed simulation tool is used to examine LMD-w regarding its applicability to zero-gravity environments, and to investigate the SLM process of a polydisperse titanium powder.

In the last chapter, a concise summary of this work is given.

2 Laser processing of metals

The light emitted by a laser is characterized by its high monochromaticity, coherence, and collimation [165]. Furthermore, laser beams can be focused into small spots which is associated with high energy densities sufficient to rapidly heat, melt, and evaporate metals [173]. This chapter introduces laser welding, LMD-w, SLM, and the accompanied physical phenomena in these processes. In addition, material defects that might arise during laser-metal processing and potential strategies to minimize their formation are presented.

2.1 Process description

Laser welding, LMD-w, and SLM are processes in which a metal is melted by a focused laser beam and subsequently joined with the subjacent or adjacent solid material. Laser welding is the most common, economical, and efficient way to join metals, which is why it is widely applied in the production of aerospace [38] and automotive components [79]. On the contrary, LMD-w and SLM belong to the class of additive manufacturing, which comprises a range of technologies where the building part is designed and sliced into horizontal layers using Computer-Aided Design (CAD) and subsequently manufactured layer-by-layer. Additive manufacturing offers great freedom in designing and producing functional, complex-shaped parts while reducing material wastage, production time, and manufacturing costs and maintaining product quality [103]. During the last decade, intense research, development, and optimization of additive manufacturing processes have led to products that are utilized in the field of aerospace [141], automotive [106], chemical [84] or biomedical industry [122]. The feedstock for these processes ranges from pure metals such as titanium [73], to steel [75], titanium alloys [190], nickel-based superalloys [137], and cobalt-chromium alloys [204]. Since metals are prone to oxidation [54] laser processing must be carried out using a shielding gas such as helium, argon, or nitrogen [69].

2.1.1 Laser welding

In laser welding, the laser is focused and moved along a predefined path on a metal surface where the material is melted. The resultant weld is characterized by a relatively small heat-affected zone, leading to low thermal and mechanical distortions in the workpiece compared to ordinary welding processes such as resistance spot welding [223]. Additionally, the fast and repetitive generation

of long, high-quality welding seams makes laser welding advantageous over conventional joining technologies [191]. Depending on the applied laser intensity, conduction mode laser welding and keyhole laser welding can be distinguished. Figure 2.1 depicts and emphasizes the differences between conduction mode (left) and keyhole laser welding (right). Conduction mode

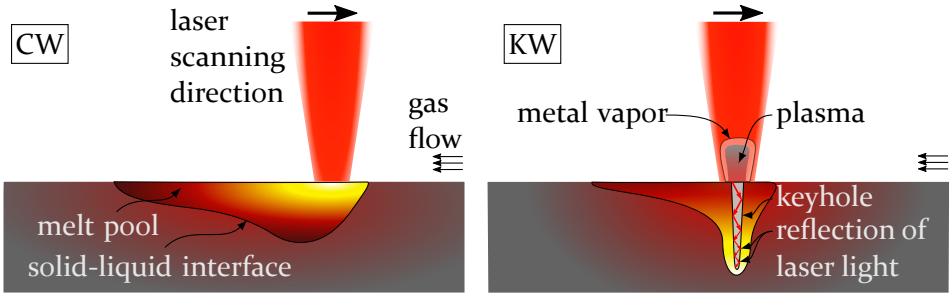

Figure 2.1: Sketch of conduction mode laser welding (CW) and keyhole welding (KW). CW is carried out at laser intensities where the surface temperature of the irradiated material remains below boiling temperature. In contrast, high laser intensities in KW lead to strong evaporation, which is associated with an emerging vapor plume and a forming vapor capillary (keyhole).

laser welding is carried out at laser intensities where the temperature in the heat-affected zone remains below boiling temperature. The heat transfer into the workpiece is limited by heat conduction, and the resultant welding seam has a hemispherical profile. With increasing laser intensity, a transition from conduction mode laser welding to keyhole welding occurs. Keyhole welding, also called deep-penetration laser welding, has a significantly smaller heat-affected zone when compared to heat conduction mode welding. Furthermore, keyhole welding is characterized by rapid evaporation of the molten metal, which leads to high back pressure, also known as recoil pressure, on the liquid surface. As a result, a vapor capillary (keyhole) is formed since the high recoil pressure counteracts the surface tension of the melt, which attempts to close the hole. The ejected metal vapor can not be replenished instantly to sustain the vapor pressure inside the keyhole. For this reason, only a quasi-steady-state can be assumed for the moving keyhole [19]. Moreover, the keyhole allows for multiple reflections of the incident laser irradiation at the solid surface, which increases the fraction of absorbed to reflected laser energy. If the laser intensity is sufficiently high, the vaporized metal ionizes and forms a plasma that absorbs a significant amount of the incident laser energy. For this reason, a shielding gas flow can be used to mechanically push the metal vapor out of the laser interaction zone.

2.1.2 Wire-based laser metal deposition

LMD-w represents an additive manufacturing process where a wire is continuously melted by a laser. Wire and laser move with the same velocity along a predefined path while the wire is continuously fed into the irradiated area by the laser beam as illustrated in Fig. 2.2. Compared to powder-based

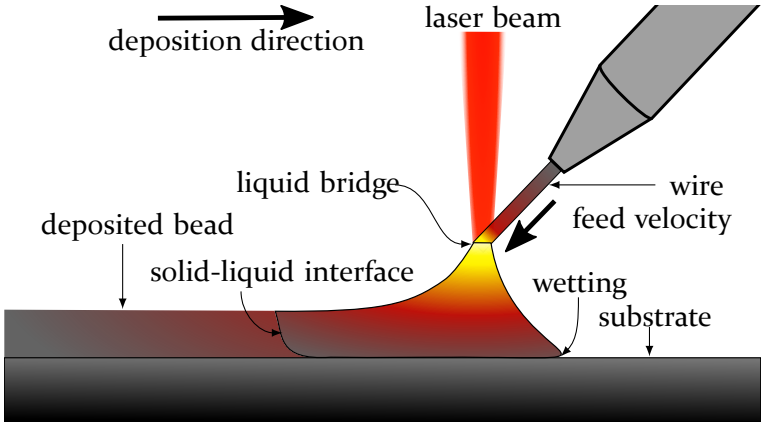

Figure 2.2: Sketch of the LMD-w process. A laser beam melts a wire, and the liquid material is deposited onto a solid substrate by forming a liquid bridge.

processes, a wire offers easier handling, reduced contamination, higher deposition rates, and larger build volumes [111]. Moreover, LMD-w offers lower material wastage and cheaper feedstock compared to powder-based laser metal deposition [148]. A strong metallurgical bond to the subjacent layer is created upon solidification of the melt. Shortcomings of LMD-w are a reduced variety of feedstock material compared to powder-based processes [111], high dependence of the laser absorption on the metal surface quality, or the lack of control of the feed rate of the wire to maintain a stable liquid bridge and to achieve a high quality of the manufactured part [2, 92, 193]. More recent technologies supply the wire coaxially to the melt. Here, the wire is heated from different sides to avoid asymmetric melting of the wire [111].

2.1.3 Selective laser melting

SLM is an additive manufacturing process that allows for building parts with a high degree of freedom and functionality using various powder materials [15, 50]. The SLM process is schematically shown in Fig. 2.3. The metal powder is dispensed from a hopper to the build area with a typical layer thickness between 20 µm and 100 µm [187] using a rake, e.g., a blade or a roller. The

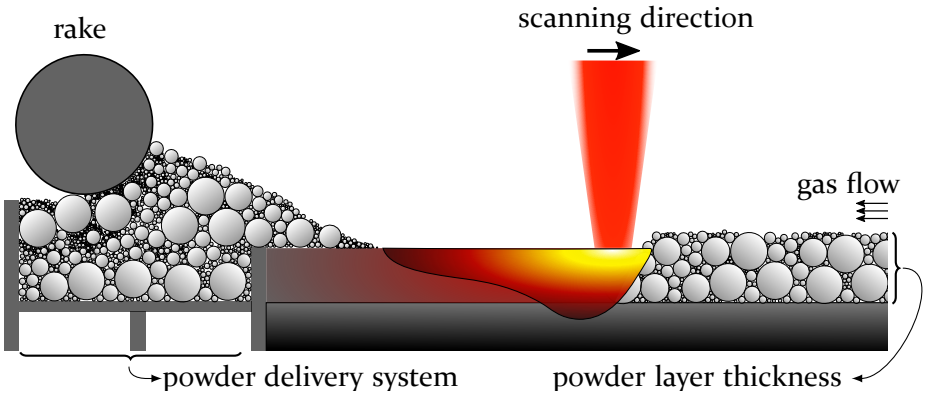

Figure 2.3: Sketch of the SLM process. Metal powder is dispensed using a rake and melted using a laser beam. Layer-by-layer, a three-dimensional object is manufactured due to the fusing of metal powder.

laser beam melts the powder and consolidates it with the subjacent layer according to the path prescribed by the three-dimensional CAD model. The distance between the scan lines of the laser is called hatch spacing and must be chosen so that the molten metal sufficiently overlaps with adjacent scan lines and the subjacent layer. Powder not melted by the laser beam stabilizes the manufactured part mechanically and can be reused in a subsequent printing process. Upon finishing a layer, the building platform is lowered by the powder layer thickness, followed by raking a new layer of fresh powder on top of the previous layer. The raking, melting, and solidification process is repeated until the printing process is completed. Between consecutive layers, the hatching is rotated to ensure a high density of the consolidated metal powder and the fabricated part.

2.2 Physical effects

As sketched in Fig. 2.4, a variety of physical phenomena arise due to the rapid heating and cooling rates of up to $10^8\,\mathrm{K\,s^{-1}}$ [73] in laser-metal processing. The electromagnetic radiation generated by a laser interacts with the superficial atoms of the metal. After that, a fraction of the incident radiation is transmitted, and another part is reflected at the phase boundary. The transmitted radiation is transformed into heat, which is subsequently conducted into the bulk of the material. The generated heat in the material due to laser irradiation leads to rapid melting, solidification, and evaporation rates. Moreover, convection transfers heat within the melt and between the liquid and the gas phase. Furthermore, surface tension leads to capillary and wetting

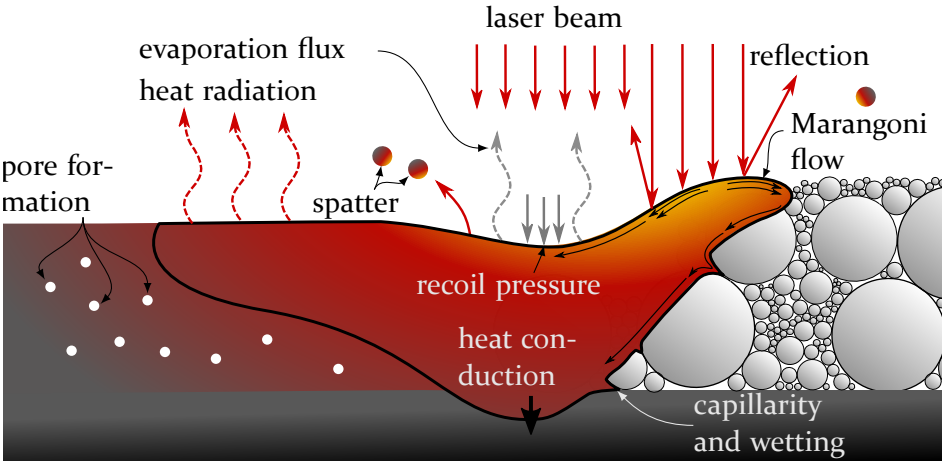

Figure 2.4: Sketch of physical effects that may occur during laser-metal processing.

phenomena as well as thermocapillary motion (Marangoni flow) at the liquid-gas interface. In addition, the material surface loses energy to the ambiance due to thermal radiation. At high laser intensity, the metal evaporates rapidly, which causes a back-pressure on the melt pool surface. This can lead to a depression on the melt surface or, in the case of even higher laser intensity, to the formation of a keyhole, as mentioned in section 2.1.1.

The resulting physical phenomena and their interaction may lead to a complex melt flow, which can induce the formation of pores and spatter, which deteriorates the quality of the fabricated part.

2.2.1 Laser-matter interaction

A laser beam with a Gaussian intensity cross section represents electromagnetic radiation that is characterized by its high ability to be focused into a narrow spot, as depicted in Fig. 2.5. The distance between the focusing optics and the focus spot is called the focal length.

The quality of a laser beam can be characterized by the beam quality factor,

$$M^2 = \frac{\Theta_{\mathrm{real}}}{\Theta_{\mathrm{Gauss}}} \,. \tag{2.1}$$

Here, Θ_{real} and Θ_{Gauss} is the beam divergence angle of a real and a Gaussian beam, respectively. For single mode Gaussian lasers $M^2 = 1$ whereas $M^2 > 1$ for real laser beams [184].

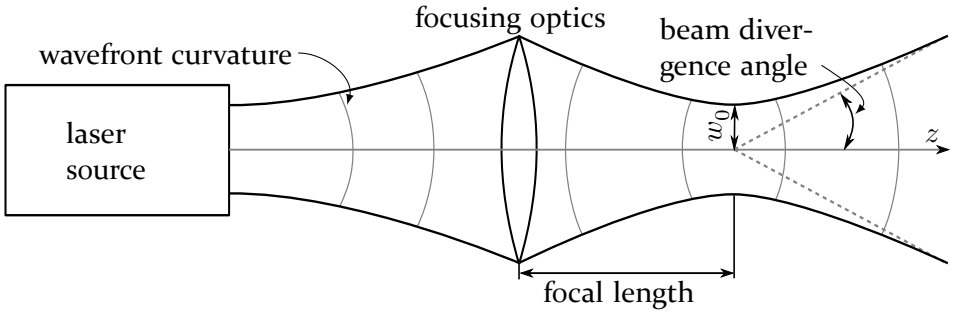

Figure 2.5: Schematic view of a Gaussian laser beam.

Assuming a Gaussian laser beam that propagates in a Cartesian coordinate system in z-direction, the electric field can be obtained as a solution to the Helmholtz equation of paraxial waves given by [165]

$$\mathbf{E} = \mathbf{E}_0 \frac{w_0}{w\left(z\right)} \mathrm{e}^{\frac{-r^2}{w(z)^2}} \mathrm{e}^{-ik_\lambda \frac{r^2}{2R_\mathrm{c}(z)}} \mathrm{e}^{-i(k_\lambda z - \psi(z))} \,. \tag{2.2}$$

Here, $\mathbf{E_0}$ is the amplitude of the electric field, $w(z)$ is the radius where the electric field amplitude decreased to $1/e$ of its value at the beam center axis, w_0 is the beam waist radius, z is the axial distance from the beam waist, r is the radial distance from the beam center axis, k_λ is the angular wave number, R_c is the radius of curvature of the beam wavefront, $\psi\left(z\right)$ is the Gouy-Phase, and i is the imaginary unit. The beam radius is defined by

$$w\left(z\right) = w_0 \sqrt{1 + \left(\frac{\lambda z}{\pi w_0^2}\right)^2} \,, \tag{2.3}$$

where λ is the wavelength emitted by the Gaussian beam, and R_c is given by

$$R_\mathrm{c}\left(z\right) = z \sqrt{1 + \left(\frac{\pi w_0^2}{\lambda z}\right)^2} \,. \tag{2.4}$$

The electric field of the incident laser beam imposes an oscillating force on the charge carriers in the irradiated material, which results in a displacement from their equilibrium position. In the classical Drude-Lorentz model, a material consists of either (i) positive ions and free electrons or (ii) neutral atoms or balanced positive and negative ions, respectively [94]. Case (ii) represents an insulator, whereas (i) represents a metal. By modeling the motion of the electrons as driven damped harmonic oscillators, the Drude-Lorentz model

allows deriving an expression for the material's permittivity, which can be related to the optical properties of the material. The separation of electrons and nuclei due to an electric field results in a polarization given by [94]

$$\mathbf{P} = \epsilon_0 \chi \mathbf{E} \,. \tag{2.5}$$

Here, χ is the material's electric susceptibility, and $\epsilon_0 = 8.854 \cdot 10^{-12}\,\mathrm{F\,m^{-1}}$ is the electric permittivity of vacuum. The higher the susceptibility, the larger the displacement of charges, or the larger the number of dipoles created upon radiation.

The electric susceptibility is given by [94]

$$\chi = \epsilon_\mathrm{r} - 1 \,, \tag{2.6}$$

where ϵ_r is the relative electric permittivity at the frequency of the applied electric field. Substitution of Eq. (2.6) into Eq. (2.5) yields

$$\mathbf{P} = \epsilon_0 \left(\epsilon_\mathrm{r} - 1\right) \mathbf{E} \,. \tag{2.7}$$

Alternatively, the polarization can be given as dipole moment per unit volume [94] by

$$\mathbf{P} = n_\mathrm{e} q_\mathrm{e} \mathbf{D} \,, \tag{2.8}$$

where n_e is the number of electrons per unit volume, $q_\mathrm{e} = 1.602 \cdot 10^{-19}\,\mathrm{C}$ is the charge of an electron, and $\mathbf{D}$ is the displacement of the electrons from their equilibrium position. The polarization of charge carriers results in an electrical field directed opposite to the incident laser radiation.

The Drude-Lorenz model describes the frequency dependence of the dielectric function of solid materials and can be used to describe the optical behavior of materials. Here, electrons are modeled as harmonic oscillators bound to the nucleus of an atom. The force acting on an electron can be described by Newton's second law, according to [94]

$$m_\mathrm{e} \frac{\mathrm{d}^2 \mathbf{D}}{\mathrm{d}t^2} = \mathbf{F}_\mathrm{E} + \mathbf{F}_\mathrm{D} + \mathbf{F}_\mathrm{S} \,, \tag{2.9}$$

where $m_\mathrm{e} = 9.109 \cdot 10^{-31}\,\mathrm{kg}$ is the mass of an electron, $\mathbf{F}_\mathrm{E}$ is a force due to the external electric field, $\mathbf{F}_\mathrm{D}$ is a damping force due to collisions of electrons with other electrons, phonons and lattice imperfections, and $\mathbf{F}_\mathrm{S}$ is a restoration force proportional to the displacement of electrons from their equilibrium position, respectively.

Equation (2.9) can be written as [94]

$$\frac{\mathrm{d}^2\mathbf{D}}{\mathrm{d}t^2} + \Gamma\frac{\mathrm{d}\mathbf{D}}{\mathrm{d}t} + \omega_0^2\mathbf{D} = \frac{q_\mathrm{e}}{m_\mathrm{e}}\mathbf{E}\,, \tag{2.10}$$

where Γ is a damping coefficient, ω_0 is the resonance frequency, and q_e and m_e are the charge and mass of an electron. Substitution of Eq. (2.8) into Eq. (2.10) leads to

$$\frac{\mathrm{d}^2\mathbf{P}}{\mathrm{d}t^2} + \Gamma\frac{\mathrm{d}\mathbf{P}}{\mathrm{d}t} + \omega_0^2\mathbf{P} = \frac{n_\mathrm{e}q_\mathrm{e}^2}{m_e}\mathbf{E}\,. \tag{2.11}$$

The term

$$\omega_\mathrm{p} = \sqrt{\frac{n_\mathrm{e}q_\mathrm{e}^2}{m_\mathrm{e}\epsilon_0}} \tag{2.12}$$

describes the oscillation behavior of the electrons in a solid material and is called plasma frequency. These electron oscillations arise due to the polarization caused by the incident electromagnetic wave of the laser beam, which results in Coulomb forces that attempt to restore the electrons' equilibrium positions. Due to their inertia, the electrons exceed their equilibrium positions, which results in collective electron oscillations at plasma frequency.

By solving the second order ordinary differential equation in Eq. (2.11), the complex polarization of the material is given by

$$\mathbf{P}\,(\omega) = \frac{\epsilon_0\omega_\mathrm{p}^2}{(\omega_0^2 - \omega^2) + i\Gamma\omega}\mathbf{E}\,. \tag{2.13}$$

Here, ω is the angular frequency of light given by

$$\omega = 2\pi c_0/\lambda, \tag{2.14}$$

where $c_0 = 299.793 \cdot 10^6\,\mathrm{m\,s^{-1}}$ is the speed of light in vacuum. Moreover, substituting Eq. (2.7) and the relative permittivity $\epsilon_\mathrm{r} = \epsilon/\epsilon_0$ into Eq. (2.13) leads to

$$\epsilon_\mathrm{r} = 1 + \frac{\omega_\mathrm{p}^2}{(\omega_0^2 - \omega^2) + i\omega\Gamma}\,. \tag{2.15}$$

In metals, the interaction of light occurs primarily with free electrons in the conduction band that are not bound to atoms. Thus, the resonance frequency ω_0 vanishes, and the electric permittivity is [94]

$$\epsilon_\mathrm{r} = 1 - \frac{\omega_\mathrm{p}^2}{\omega^2 + i\omega\Gamma}\,. \tag{2.16}$$

The relative permittivity ϵ_r can be separated into a real and imaginary part according to $\epsilon_\mathrm{r} = \epsilon_{\mathrm{r},1} + i\epsilon_{\mathrm{r},2}$ which yields

$$\epsilon_{\mathrm{r},1} = 1 - \frac{\omega_\mathrm{p}^2}{\omega^2 + \Gamma^2}\,, \qquad \epsilon_{\mathrm{r},2} = -\frac{\omega_\mathrm{p}^2 \Gamma}{(\omega^2 + \Gamma^2)\,\omega}\,. \tag{2.17}$$

Moreover, the real and imaginary parts of the electric permittivity can be related to the real, n_1, and imaginary part, n_2, of the refractive index,

$$\bar{n} = n_1 + i n_2\,, \tag{2.18}$$

by [94]

$$\sqrt{\epsilon_\mathrm{r}} = n_1 + i n_2\,. \tag{2.19}$$

Assuming a relative permeability close to unity, the refractive indices can be expressed as

$$n_1 = \sqrt{\frac{\sqrt{\epsilon_{\mathrm{r},1}^2 + \epsilon_{\mathrm{r},2}^2} + \epsilon_{\mathrm{r},1}}{2}}\,, \qquad n_2 = \sqrt{\frac{\sqrt{\epsilon_{\mathrm{r},1}^2 + \epsilon_{\mathrm{r},2}^2} - \epsilon_{\mathrm{r},1}}{2}}\,. \tag{2.20}$$

Under the assumption of geometrical optics, the Fresnel coefficients describe the ratio of the reflected power to the transmitted power of an electromagnetic wave at a phase boundary. If $\omega < \omega_\mathrm{p}$ a high fraction of the incident wave is reflected. Adversely, for $\omega > \omega_\mathrm{p}$ the reflectivity of the material becomes small, and at $\omega = \omega_\mathrm{p}$ the material's optical properties change from metallic to that of a dielectric material. The Fresnel coefficients depend on the refractive indices and the orientation of the electric field vector with respect to the plane of incidence, as shown in Fig. 2.6.

The plane of incidence is made up of the propagation direction of the incident electromagnetic wave and the surface normal of the phase boundary. In the following, the subscript i denotes the properties of the incident electromagnetic wave, and r denotes the properties of the reflected electromagnetic wave. The Poynting vector gives the propagation direction of the incident electromagnetic wave,

$$\mathbf{S}_\mathrm{i} = \mathbf{E}_\mathrm{i} \times \mathbf{B}_\mathrm{i}\,, \tag{2.21}$$

where $\mathbf{E}_\mathrm{i}$ and $\mathbf{B}_\mathrm{i}$ are the electric and magnetic field vectors of the incident electromagnetic wave.

For specular reflection, the enclosed angle by surface normal and electric field vector of incident, θ_i, and reflected electromagnetic field, θ_r, are equal ($\theta_\mathrm{i} = \theta_\mathrm{r}$). Suppose the electric field of the incident electromagnetic wave is

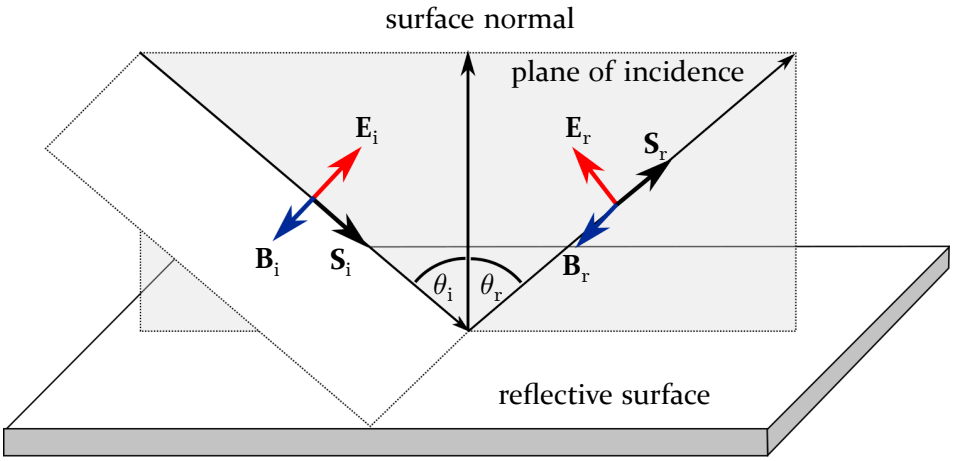

Figure 2.6: Schematic of the reflection of an electromagnetic wave at the interface of two isotropic optical media. The electric field, magnetic field, and the Poynting vector of the incident and reflected electromagnetic waves are oriented perpendicular to each other.

oriented parallel to the plane of incidence, then the electromagnetic wave is said to be p-polarized. In contrast, if the incident electric field is oriented perpendicular to the plane of incidence, the electromagnetic wave is said to be s-polarized. The power reflectance for s- and p-polarization of the incident electromagnetic wave is then given by the squared magnitude of the ratio of incident and reflected electric field vectors. Assuming an interface between a vacuum and a metal with the same magnetic permeability (the relative permeability of commercially pure titanium is 1.00005 [132]), the power reflectance is given by [231]

$$R^\perp = \left| \left(\frac{\mathbf{E}_\mathrm{r}}{\mathbf{E}_\mathrm{i}} \right)^\perp \right|^2 = \left| \frac{\cos\theta_\mathrm{i} - \sqrt{\bar{n}^2 - \sin^2\theta_\mathrm{i}}}{\cos\theta_\mathrm{i} + \sqrt{\bar{n}^2 - \sin^2\theta_\mathrm{i}}} \right|^2 , \tag{2.22}$$

where the superscript $\perp$ denotes s-polarization, and

$$R^\parallel = \left| \left(\frac{\mathbf{E}_\mathrm{r}}{\mathbf{E}_\mathrm{i}} \right)^\parallel \right|^2 = \left| \frac{\bar{n}^2\cos\theta_\mathrm{i} - \sqrt{\bar{n}^2 - \sin^2\theta_\mathrm{i}}}{\bar{n}^2\cos\theta_\mathrm{i} + \sqrt{\bar{n}^2 - \sin^2\theta_\mathrm{i}}} \right|^2 , \tag{2.23}$$

where the superscript $\parallel$ denotes p-polarization. For normal incidence ($\theta_\mathrm{i} = 0°$), $R^\perp = R^\parallel = R$. Since gases have optical properties close to that of vacuum (for instance, $n_1 = 1.00026$, and $n_2 = 0$ for argon at $1\,\mathrm{atm}$ and 298 K [158]),

Eqs. (2.22) and (2.23) are assumed to be valid for the interface between argon and a titanium surface, representing the system investigated in this work. Nonetheless, the more general Fresnel equations shown in Appendix A which describe the reflectivity at an interface between two different optical media, are used. To describe the temperature dependence of the refractive index of metals, the work of Ujihara [205] and Siegel [183] is followed. While Ujihara [205] describes the temperature dependence below the melting point, Siegel [183] extends the theoretical description of the refractive index to the liquid phase beyond melting temperature. According to Eq. (2.15), the optical properties of a metal depend on the plasma frequency, the wavelength of the laser beam, and the damping coefficient. Under quantum-theoretical consideration, the damping coefficient corresponds to the electron-phonon collision frequency, which is proportional to the phonon population in a metal. The phonon population and hence the electron-phonon collision frequency in a metal increase with temperature, affecting the electric permittivity and the refractive index [205]. Ignoring the temperature dependence on the plasma frequency due to volume expansion and assuming that the material's band structure does not change upon temperature rise, the optical properties only depend on the electron-phonon collision frequency. Furthermore, assuming the Debye phonon spectrum model, phonon-phonon scattering mechanisms that preserve the phonon wave vector (N processes) on a spherical Fermi surface and a temperature invariant electron configuration, the electron-phonon collision frequency of the solid, denoted by the superscript s, is given by [205]

$$\Gamma^{\mathrm{s}}\left(T\right) = K^{\mathrm{s}} T^{5} \int_{0}^{\Theta_{\mathrm{D}}/T} \frac{\bar{x}^{4}}{\mathrm{e}^{\bar{x}} - 1} \mathrm{d}\bar{x}\,. \tag{2.24}$$

Here, T is the temperature, $\bar{x}$ is an integration variable and K^{s} is a constant which includes the total scattering cross section of an isolated atom, the Debye temperature, Θ_{D}, the Debye wave number, ion mass, ion density and other constants. To estimate the optical properties of a metal beyond melting temperature, [183] extends the work of [205] using the theory of melting of simple metals by [149] which is based on the collective coordinate theory of simple liquids and the Percus-Yevick concept of liquid phonons [159]. Here, analogous to [205], the damping coefficient of the liquid phase Γ^{l} is considered to be temperature dependent whereas the plasma frequency is assumed to be temperature-independent. The electron-phonon collision frequency of the liquid is given by

$$\Gamma^{\mathrm{l}}\left(T\right) = K^{\mathrm{l}} T^{5} \int_{0}^{\Theta_{\mathrm{PY}}(T)/T} \frac{\bar{x}^{4}}{\mathrm{e}^{\bar{x}} - 1} \mathrm{d}\bar{x}\,. \tag{2.25}$$

Here, K^{l} is a constant analogous to K^{s} for solids and Θ_{PY} is the Percus-Yevick temperature given by [183]

$$\Theta_{\mathrm{PY}}(T) = \left(\frac{k_{\mathrm{B}}T}{m_{\mathrm{A}}S(0)}\right)^{1/2}\left(\frac{18\pi^2\,\rho(T)}{m_{\mathrm{A}}}\right)^{1/3}\frac{k_{\mathrm{B}}}{\hbar}\,, \tag{2.26}$$

where $S(0)$ is the long wavelength limit of the liquid structure factor which describes the scattering of incident radiation, m_{A} is the atomic mass, $\rho(T)$ is the temperature dependent density, $k_{\mathrm{B}} = 1.38 \cdot 10^{-23}\,\mathrm{J\,K^{-1}}$ is the Boltzmann constant, and $\hbar = 1.05 \cdot 10^{-34}\,\mathrm{J\,s}$ is the reduced Planck constant, respectively.

2.2.2 Phase transitions

The generated heat by the laser beam is sufficient to change the metals' aggregate state, which is associated with varying material properties. According to [58], these phase transitions can be classified into first and second order. First-order phase transitions are characterized by discontinuous changes in volume, enthalpy, and entropy. The heat capacity at constant pressure tends infinity and the material temperature remains constant until the required enthalpy, denoted as latent heat, is absorbed or released [12]. Second-order phase transitions do not involve latent heat, and the properties volume, enthalpy, and entropy change continuously [12]. Figure 2.7 sketches the specific enthalpy as a function of temperature at constant pressure in the case of a pure metal. Here, the specific enthalpy of crystallization, h_{cryst}, and melting, h_{m}, are

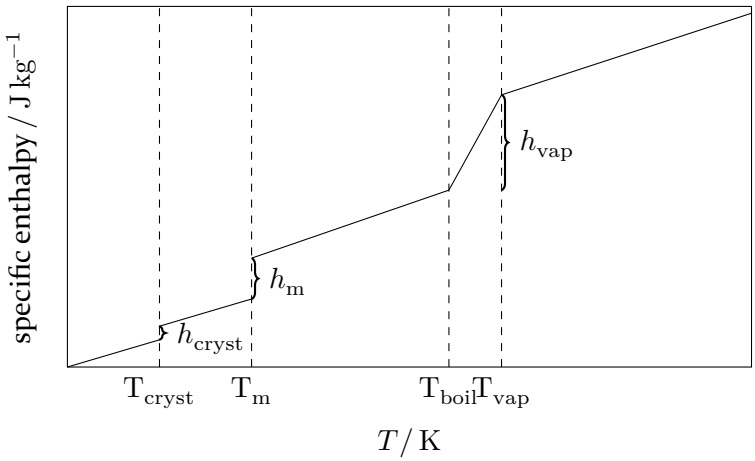

Figure 2.7: Schematic of the change of specific enthalpy with temperature of a material with increasing temperature.

absorbed or released at crystallization, T_{cryst}, or melting temperature, T_{m}, respectively. The evaporation process starts when the material reached boiling temperature, T_{boil}, and is strongly affected by the properties of the ambient gas [101]. Furthermore, the evaporation rate depends on the surface temperature and the flow state of the emerging vapor. In the case of intense laser irradiation, the temperature of the condensed phase can exceed the boiling temperature, which is depicted in Fig. 2.7, where the enthalpy increases linearly within the temperature regime $T_{\mathrm{boil}} \leq T < T_{\mathrm{vap}}$. The evaporation process is completed when T_{vap} is reached.

The discontinuous change of volume and heat capacity at constant pressure at the melting temperature are illustrated in Fig. 2.8. At melting temperature,

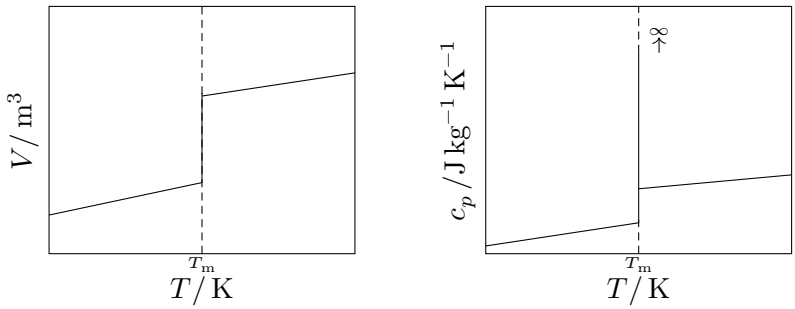

Figure 2.8: Schematic of the change of volume and heat capacity at constant pressure with temperature in a first-order phase transition.

the heat capacity tends to infinity, which is why the temperature remains constant until the latent heat of melting is released or absorbed. Since the energy, mass, and momentum transport change substantially upon melting and solidification, knowing the position of the solid-liquid interface is crucial when modeling phase change processes. Therefore, the effect of latent heat can be incorporated into a numerical method, on the one hand, by adding a source term to the heat conduction equation [157, 209], or, on the other hand, by modifying the heat capacity itself [61, 80, 199]. Such a modified heat capacity, also referred to as effective heat capacity, can be defined by

$$\tilde{c}_p = \begin{cases} c_p^{\alpha} & T < T_{\mathrm{cryst}} \\ c_p^{\alpha\beta} + h_{\mathrm{cryst}}\delta\left(T - T_{\mathrm{cryst}}\right) & T = T_{\mathrm{cryst}} \\ c_p^{\beta} & T_{\mathrm{cryst}} < T < T_{\mathrm{m}} \\ c_p^{\beta\mathrm{l}} + h_{\mathrm{m}}\delta\left(T - T_{\mathrm{m}}\right) & T = T_{\mathrm{m}} \\ c_p^{\mathrm{l}} & T > T_{\mathrm{m}} \end{cases} . \tag{2.27}$$

Here, c_p^{α}, c_p^{β} and c_p^{l} are the heat capacities of the solid with an α- or β-crystal structure, and the liquid material, respectively. For example, the α crystallization of solid titanium is hexagonal close-packed whereas the β-crystallization of solid titanium is body-centered cubic [53]. At crystallization, T_{cryst}, and melting temperature, T_{m}, the latent heat of crystallization, h_{cryst}, and melting, h_{m}, is added to the corresponding heat capacities $c_p^{\alpha\beta}$ and $c_p^{\beta\mathrm{l}}$.

Upon evaporation of a metal due to laser irradiation, the metal vapor expands into the ambient gas at a certain velocity. First theoretical studies on the evaporation process have been carried out by Hertz [76] and Knudsen [102]. The assumption of equilibrium conditions, e.g., a zero net motion of the vapor phase, led to the Hertz-Knudsen equation that approximately describes evaporation and condensation fluxes. In particular, the velocities of the evaporating and condensing particles are assumed to follow a half-range Maxwell-Boltzmann distribution with opposite directions, respectively. The evaporation process has been further elaborated by [10, 101, 229] to account for the case of medium-to-strong evaporation under the assumption that the vapor flow is in the continuum regime. The continuum hypothesis holds for $\mathrm{Kn} \lesssim 0.01$ [98] where the Knudsen number, Kn, is defined as the ratio of the molecular free mean path to the characteristic length scale of the considered problem. This is generally true for laser-based processes conducted at atmospheric pressure. In the regime of net evaporation, inter-particle collisions in the vicinity of the evaporating surface equilibrate the velocity distribution of the expanding gas phase to a full-range Maxwellian. This implies that a fraction of evaporating particles return to the surface and recondenses. According to [216] it can be assumed that all back-scattered particles condense in the case of monoatomic metal vapor. The transition region where the particle behavior changes from free-molecular (half-range Maxwellian) to continuum flow (full-range Maxwellian) is called the Knudsen layer and has a thickness in the order of a few molecular mean free paths [181]. In a macroscopic context, the change of thermodynamic properties across the Knudsen layer represents a gas-dynamic discontinuity that must be modeled using analytical jump conditions. The stationary Knudsen layer is followed by an expanding layer of vapor that is separated by a contact discontinuity from the compressed ambient gas. Both layers have identical velocity and pressure fields but distinct densities and temperatures. The emerging vapor may move at a subsonic or supersonic speed depending on the pressure ratio of the vapor at the metal surface to the ambient atmosphere. Lastly, the hydrodynamic compressed ambient gas evolves into the undisturbed ambient gas with a shock wave. In this work, the simulations of laser welding, SLM, or LMD-w processes are carried out at laser energies that lead to vapor flows in the subsonic regime

with the corresponding flow structure depicted in Fig. 2.9. Each transition

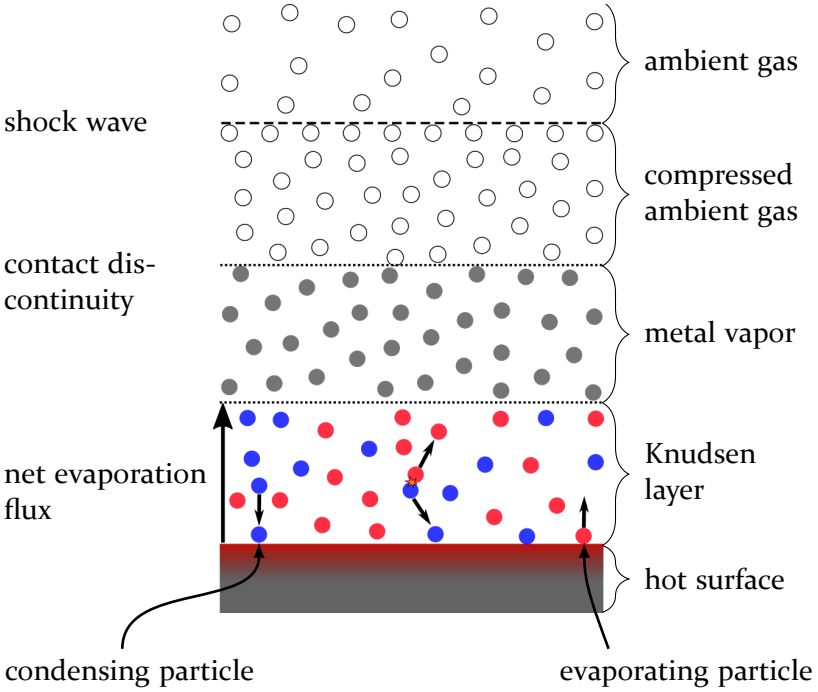

Figure 2.9: Sketch of the flow structure caused by expanding vapor due to evaporation into an ambient, undisturbed gas.

layer represents a gas-dynamic discontinuity that propagates with constant velocity into the half-space beyond the stationary Knudsen layer, as sketched in Fig. 2.10.

The net evaporation mass flux is determined by the difference between the particle flux leaving the condensed phase, j^+, and the flux of particles returning to the evaporating surface due to inter-particle collisions, j^-. The net flux of evaporating particles per square meter and per second is given by [101]

$$j^{\text{net}} = j^+ - j^- = \left(\frac{j^+ - j^-}{j^+} \right) \cdot j^+ = \phi \cdot j^+ \,, \tag{2.28}$$

where ϕ is the evaporation coefficient representing the ratio of evaporating to condensing particles. When the liquid and gas phases are in equilibrium,

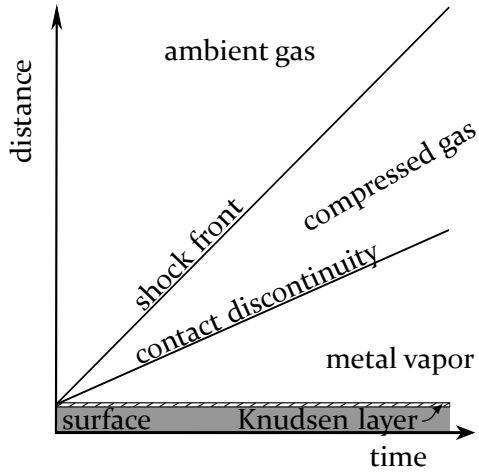

Figure 2.10: Temporal evolution of the contact boundaries for subsonic flow in one dimension. Metal vapor, compressed ambient gas, and shock front propagates with constant velocity into the ambient gas, whereas the Knudsen layer is stationary.

$\phi = 0$. In the case of net evaporation, $\phi > 0$, and in the case of net condensation, $\phi < 0$. Thus, the net evaporated mass flux is given by

$$\dot{m}_{\mathrm{vap}} = A j^{\mathrm{net}}\,, \tag{2.29}$$

where A is the evaporating surface area. According to [76, 102], the evaporation flux of a single-component substance is given by

$$j^{+} = p_{\mathrm{s}} \sqrt{\frac{m_{\mathrm{A}}}{2\pi k_{\mathrm{B}} T_{\mathrm{s}}}}\,. \tag{2.30}$$

Here, T_{s} and p_{s} are the temperature and pressure of the vapor with atom mass m_{A} directly at the vapor side of the liquid-gas interface. Assuming thermodynamic equilibrium between vapor and condensed phase prior to vaporization, p_{s} can be understood as the saturated vapor pressure at temperature T_{s}. The relation between saturated vapor pressure and temperature in equilibrium, is given by the Clausius-Clapeyron equation

$$\frac{1}{p}\mathrm{d}p = \frac{m_{\mathrm{A}} \cdot h_{\mathrm{vap}}\,(T)}{k_{\mathrm{B}}} \cdot \frac{1}{T^2}\mathrm{d}T. \tag{2.31}$$

Upon integration of Eq. (2.31) from $T = T_{\mathrm{boil}}$ to $T = T_{\mathrm{s}}$ and $p = p_{\mathrm{atm}}$ to $p = p_{\mathrm{s}}$ by employing the temperature-dependent heat of vaporization [227],

$$h_{\mathrm{vap}}\left(T\right) = h_{\mathrm{vap},0} \cdot \sqrt{1 - \left(\frac{T}{T_{\mathrm{crit}}}\right)^2}\,, \tag{2.32}$$

the following expression for the ratio of the saturated vapor pressure to the ambient pressure reads [99]

$$\begin{aligned}\frac{p_{\mathrm{s}}}{p_{\mathrm{a}}} = \frac{p_{\mathrm{atm}}}{p_{\mathrm{a}}} \cdot \exp\Bigg(- \frac{h_{\mathrm{vap},0} \cdot m_{\mathrm{A}}}{k_{\mathrm{B}}} \cdot \Bigg[& \frac{1}{T_{\mathrm{s}}} \sqrt{1 - \left(\frac{T_{\mathrm{s}}}{T_{\mathrm{crit}}}\right)^2} \\ & - \frac{1}{T_{\mathrm{boil}}} \sqrt{1 - \left(\frac{T_{\mathrm{boil}}}{T_{\mathrm{crit}}}\right)^2} \\ & - \frac{1}{T_{\mathrm{crit}}} \left(\arcsin\left(\frac{T_{\mathrm{s}}}{T_{\mathrm{crit}}}\right) - \arcsin\left(\frac{T_{\mathrm{boil}}}{T_{\mathrm{crit}}}\right) \right) \Bigg] \Bigg)\,.\end{aligned} \tag{2.33}$$

Here, T_{crit} is the critical temperature at standard atmospheric pressure ($p_{\mathrm{atm}} = 101325\,\mathrm{Pa}$), and $h_{\mathrm{vap},0}$ is the specific heat of vaporization at absolute zero temperature. The mass flux of condensing particles is given by [230]

$$j^{-} = p_{\mathrm{Kn}} \sqrt{\frac{m_{\mathrm{A}}}{2\pi \cdot k_{\mathrm{B}} T_{\mathrm{Kn}}}} \beta^{-} \cdot F^{-}\,, \tag{2.34}$$

when assuming non-equilibrium effects within the Knudsen layer. Here, p_{Kn} and T_{Kn} are the pressure and temperature at the ambient side of the Knudsen layer, and the dimensionless functions, β^{-} and F^{-}, that account for particle collisions within the Knudsen layer, are given by

$$\beta^{-}\left(S_{\mathrm{Kn}}^2\right) = \left(2S_{\mathrm{Kn}}^2 + 1\right) - \sqrt{\pi} \cdot S_{\mathrm{Kn}} \cdot \sqrt{\frac{T_{\mathrm{s}}}{T_{\mathrm{Kn}}}} \tag{2.35}$$

and

$$F^{-}\left(S_{\mathrm{Kn}}\right) = \exp\left(-S_{\mathrm{Kn}}^2\right) - \sqrt{\pi} \cdot S_{\mathrm{Kn}} \cdot \mathrm{erfc}\left(S_{\mathrm{Kn}}\right)\,. \tag{2.36}$$

Here, erfc is the complementary error function and S_{Kn} is the dimensionless gas velocity at the ambient side of the Knudsen layer [98],

$$S_{\mathrm{Kn}} = \frac{\gamma_{\mathrm{v}}}{2} \cdot \mathrm{Ma}_{\mathrm{Kn}}\,, \tag{2.37}$$

where γ_v is the specific heat ratio of the vapor ($\gamma_\mathrm{v} = 5/3$ for monoatomic vapor [12]) and Ma_Kn is the flow Mach number. The abrupt change of temperature and density across the Knudsen layer is determined by the jump conditions [101]

$$\sqrt{\frac{T_\mathrm{Kn}}{T_\mathrm{s}}} = \sqrt{1 + \pi \left(\frac{\gamma_\mathrm{v} - 1}{\gamma_\mathrm{v} + 1} \cdot \frac{S_\mathrm{Kn}}{2} \right)^2} - \sqrt{\pi} \cdot \frac{\gamma_\mathrm{v} - 1}{\gamma_\mathrm{v} + 1} \cdot \frac{S_\mathrm{Kn}}{2} \tag{2.38}$$

and

$$\begin{aligned} \frac{\rho_\mathrm{Kn}}{\rho_s} = \sqrt{\frac{T_\mathrm{S}}{T_\mathrm{Kn}}} \cdot \left[\frac{1}{2} \left(2S_\mathrm{Kn}^2 + 1 \right) \cdot \exp\left(S_\mathrm{Kn}^2 \right) \operatorname{erfc}\left(S_\mathrm{Kn} \right) - \frac{S_\mathrm{Kn}}{\sqrt{\pi}} \right] \\ + \frac{1}{2} \frac{T_\mathrm{s}}{T_\mathrm{Kn}} \cdot \left[1 - \sqrt{\pi} \cdot S_\mathrm{Kn} \cdot \exp\left(S_\mathrm{Kn}^2 \right) \cdot \operatorname{erfc}\left(S_\mathrm{Kn} \right) \right]. \end{aligned} \tag{2.39}$$

Moreover, the thermodynamic conditions on both sides of the emerging pressure wave are determined by the Rankine-Hugoniot jump conditions [101]. Together with the Knudsen layer jump conditions in Eqs. (2.38) and (2.39), the vapor pressure at the evaporating surface can be related to the undisturbed ambient gas by [98]

$$\begin{aligned} \frac{p_\mathrm{s}}{p_\mathrm{a}} = \Bigg[1 + \gamma_\mathrm{a} \cdot \mathrm{Ma}_\mathrm{Kn}\left(T_\mathrm{s} \right) \cdot \frac{c_\mathrm{Kn}}{c_\mathrm{a}} \cdot \Bigg[\frac{\gamma_\mathrm{a} + 1}{4} \cdot \mathrm{Ma}_\mathrm{Kn}\left(T_\mathrm{s} \right) \cdot \frac{c_\mathrm{Kn}}{c_\mathrm{a}} \\ + \sqrt{1 + \left(\frac{\gamma_\mathrm{a} + 1}{4} \cdot \mathrm{Ma}_\mathrm{Kn}\left(T_\mathrm{s} \right) \cdot \frac{c_\mathrm{Kn}}{c_\mathrm{a}} \right)^2} \Bigg] \Bigg] \cdot \left[\frac{\rho_\mathrm{Kn}}{\rho_\mathrm{s}} \frac{T_\mathrm{Kn}}{T_\mathrm{s}} \right]^{-1}, \end{aligned} \tag{2.40}$$

where $c_\mathrm{Kn}/c_\mathrm{a}$ is the ratio of the local speed of sounds at the ambient side of the Knudsen layer to the ambient gas defined by

$$\frac{c_\mathrm{Kn}}{c_\mathrm{a}} = \sqrt{\frac{m_\mathrm{A,a} \gamma_\mathrm{v} T_\mathrm{Kn}}{m_\mathrm{A,v} \gamma_\mathrm{a} T_\mathrm{a}}}. \tag{2.41}$$

The speed of sound is defined by

$$c_l = \sqrt{\frac{\gamma_l k_\mathrm{B} T_l}{m_{\mathrm{A},l}}}, \tag{2.42}$$

where the subscript l represents the corresponding transition layer, Knudsen (Kn) or ambient gas (a). In Eq. (2.41) $\gamma_\mathrm{v} = \gamma_\mathrm{Kn}$ and $m_\mathrm{A,v} = m_\mathrm{A,Kn}$. The

flow Mach number at the ambient side of the Knudsen layer characterizes the vapor flow state specified by the pressure ratio $p_\mathrm{s}/p_\mathrm{a}$ and is defined by

$$\mathrm{Ma}_\mathrm{Kn} = \frac{u_\mathrm{Kn}}{c_\mathrm{Kn}}\,, \tag{2.43}$$

where u_Kn is the velocity of the vapor phase at the ambient side of the Knudsen layer. The maximum value of the flow Mach number at the ambient side of the Knudsen layer is $\mathrm{Ma}_\mathrm{Kn} = 1$, which was proven by [229] using Boltzmann's H-theorem. Due to the limitation of the vapor flow velocity, the evaporation coefficient converges towards a maximum value given in literature between $\phi = 0.8$ and $\phi = 0.85$ [9, 62, 101, 181]. The evaporation coefficient in Eq. (2.28) can be derived using Eqs. (2.28), (2.42), (2.43), as well as Eqs. (B.11), (B.12) and (B.13) provided in Appendix B, and is given by [99, 101]

$$\phi = \sqrt{2\pi\gamma_\mathrm{v}} \cdot \mathrm{Ma}_\mathrm{Kn} \cdot \frac{\rho_\mathrm{Kn}}{\rho_\mathrm{s}} \sqrt{\frac{T_\mathrm{Kn}}{T_\mathrm{s}}}\,. \tag{2.44}$$

The evaporation coefficient, Φ, given by Eq. (2.44) has a maximum value of $\phi_\mathrm{max} = 0.82$, as shown in Fig. 2.11, and is valid in the case of steady state

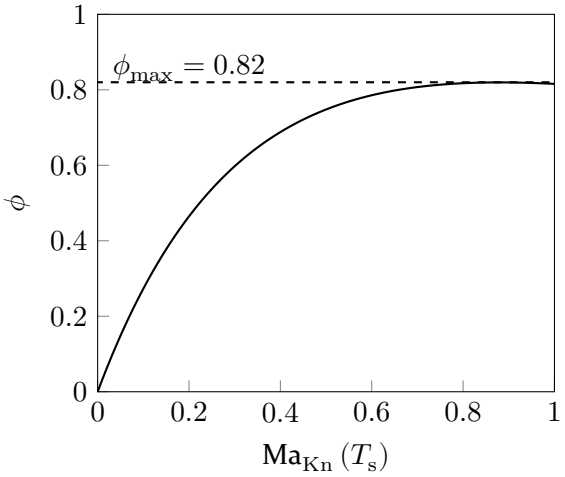

Figure 2.11: Evaporation coefficient as a function of the flow Mach-number measured at the ambient side of the Knudsen layer.

evaporation when a stable Knudsen layer has been formed. According to [9] the formation of the Knudsen layer takes approximately 20 times the mean collision time, which is in the order of $10^{-8}\,\mathrm{s}$ to $10^{-7}\,\mathrm{s}$ in case of metals at boiling temperature [98].

The flow Mach number is now determined for a given surface temperature, T_s, by

$$\left(\frac{p_\mathrm{s}}{p_\mathrm{a}}\right)_{\text{R-H}} = \left(\frac{p_\mathrm{s}}{p_\mathrm{a}}\right)_{\text{C-C}} , \tag{2.45}$$

where $(p_\mathrm{s}/p_\mathrm{a})_{\mathrm{C-C}}$ represents the saturated-to-ambient pressure ratio given in Eq. (2.33), and $(p_\mathrm{s}/p_\mathrm{a})_{\mathrm{R-H}}$ is the vapor-to-ambient pressure ratio given in Eq. (2.40), derived from the Rankine-Hugoniot and Knudsen layer jump conditions.

The allowed flow states of the evaporation flux as a function of the ambient pressure and the surface temperature can be determined by the intersections of the sets of curves corresponding to the pressure ratios of $(p_\mathrm{s}/p_\mathrm{a})_{\text{R-H}}$ and $(p_\mathrm{s}/p_\mathrm{a})_{\text{C-C}}$. Graphically, Eq. (2.45) can be represented by flow state diagrams [101]. The flow state diagram for the system titanium-argon, which is employed in this work, is introduced in section 3.1. The expanding vapor generates a recoil pressure on the evaporating surface due to the conservation of momentum. Under equilibrium conditions, the flux of evaporating particles equals the flux of condensing particles, and the net evaporation flux is zero. The pressure acting on the surface consists of equal contributions from the recoil of evaporating particles and collisions of condensing particles with the surface by [76]

$$p_\mathrm{recoil} = 0.5 p_\mathrm{s} + 0.5 p_\mathrm{Kn} . \tag{2.46}$$

In case of net evaporation, $j^\mathrm{net} > 0$, the contribution of condensing particles to the recoil pressure decreases and is governed by the evaporation coefficient. Klassen et al. [99] assumed a linear decrease in the vapor pressure from the evaporating surface to the exit plane of the Knudsen layer. The pressure contribution of the evaporation, $\bar{p}^+$, and condensation, $\bar{p}^-$, particle fluxes is given by [99]

$$\bar{p}^+ = 0.5 p_\mathrm{s} , \qquad \bar{p}^- = 0.5 \frac{p_\mathrm{Kn} + p_\mathrm{s}}{2} . \tag{2.47}$$

Thus, the recoil pressure that acts on the surface is given by [99]

$$\begin{aligned} p_\mathrm{recoil} &= \bar{p}^+ + (1-\phi)\,\bar{p}^- \\ &= \frac{1}{2} \cdot \left[1 + \frac{1}{2} \cdot (1-\phi) \cdot \left(1 + \frac{\rho_\mathrm{Kn}}{\rho_\mathrm{s}} \sqrt{\frac{T_\mathrm{Kn}}{T_\mathrm{s}}} \right) \right] . \end{aligned} \tag{2.48}$$

In the case of rapid evaporation this results in $p_\mathrm{recoil} = 0.56 p_\mathrm{s}$ as maximum value. Likewise, the emerging vapor plume of the metal absorbs a fraction of the incident laser irradiation. At sufficiently high energy input by the laser, the electric field can create a discharge in the metal vapor if the ionization

energy of the metal vapor is reached. This plasma or plume propagates from the evaporating surface towards the laser source and may absorb a significant fraction of the incident laser energy. Additionally, the plasma may defocus the laser beam, displace the focal point of the laser beam from its original position, and acts as another heat source emitting energy in all directions.

2.2.3 Heat transfer

The intensity of an electromagnetic wave is given by the magnitude of the time-averaged magnitude of the Poynting vector [173]. For a Gaussian laser beam propagating in vacuum, the intensity can be written as [175]

$$\dot{q}_\mathrm{l} = I_0 \left(\frac{w_0}{w(z)} \right)^2 \mathrm{e}^{-\frac{2r^2}{w(z)^2}} , \tag{2.49}$$

where I_0 is the axial intensity given by

$$I_0 = \frac{2P_0}{\pi w(z)^2} . \tag{2.50}$$

Here, P_0 is the total power of the laser beam. If the laser beam propagates into an absorbing material ($n_2 > 0$), the intensity decreases exponentially according to Beer-Lambert's law [173, 231]:

$$I_0 \cdot \mathrm{e}^{-\alpha \cdot z}, \quad \alpha = \frac{4\pi n_2}{\lambda} . \tag{2.51}$$

Here, α is the absorption coefficient whose reciprocal is the penetration depth, δ_p, which describes the distance at which the intensity decreased to $1/e$ of its surface value. At room temperature, δ_p is given by

$$\delta_\mathrm{p} = \frac{\lambda}{4\pi n_2} . \tag{2.52}$$

At constant pressure and volume, the total energy of a system can be described by the enthalpy, which is generated by the continuous molecular motion caused by the vibration of atoms in solids and liquids [7]. In a material, heat can be transported by conduction, convection, or radiation. Heat conduction transfers heat without mass transport through the exchange of kinetic energy between neighboring atoms, e.g., via collisions. Convection is caused by the transport of particles, such as in liquids, and electromagnetic waves cause the transport of heat by radiation.

Assuming an incompressible material at constant pressure, the heat equation can be derived from Fourier's law assuming isotropic material properties, leading to [18]

$$\rho \tilde{c}_p \frac{\partial T}{\partial t} = \nabla \cdot (k \nabla T) \ , \tag{2.53}$$

where ρ is the density, ∇T is the temperature gradient, k is the material's thermal conductivity, and $\tilde{c}_p$ is the effective heat capacity at constant pressure which includes the latent heat of melting or crystallization. Moreover, the Stefan-Boltzmann law describes the heat transfer due to radiation by [18]

$$\dot{q}_\mathrm{r} = \sigma_\mathrm{SB} \epsilon_\mathrm{th} \left(T^4 - T_0^4\right) \ , \tag{2.54}$$

where $\sigma_\mathrm{SB} = 5.67 \cdot 10^{-8}\,\mathrm{W\,m^{-2}\,K^{-4}}$ is the Stefan-Boltzmann constant, ϵ_th is the emissivity, and T_0 the temperature of the ambient environment.

The heat loss due to evaporation is given by the product of the net evaporation flux, j^net, and the latent heat of vaporization according to Eq. (2.32), by

$$\dot{q}_\mathrm{vap} = j^\mathrm{net} h_\mathrm{vap}\left(T\right) \ . \tag{2.55}$$

2.2.4 Fluid dynamics

The motion of the forming melt in laser-metal processing can be described using continuum mechanics. According to Newton's second law, the temporal change of velocity of a fluid element is proportional to the sum of all forces acting on it. The momentum balance can be given in the Lagrangian description by [208]

$$\frac{\mathrm{D}\mathbf{u}}{\mathrm{D}t} = \frac{1}{\rho} \left(\nabla \cdot \sigma\right) + \mathbf{f}_\mathrm{other} \, , \tag{2.56}$$

where $\mathbf{u}$ is the velocity, σ is the Cauchy stress tensor, and $\mathbf{f}_\mathrm{other}$ are other forces, such as gravitational or surface tension forces. Moreover, $\mathrm{D}\mathbf{u}/\mathrm{D}t$ is the material or substantial derivative of velocity. For an arbitrary physical property Φ the material derivative is defined as

$$\frac{\mathrm{D}\Phi}{\mathrm{D}t} = \frac{\partial \Phi}{\partial t} + \mathbf{u} \nabla \Phi \, . \tag{2.57}$$

Assuming an incompressible, Newtonian fluid, where the viscous stress is proportional to the strain-rate, σ can be written as [208]

$$\sigma = -p\mathbf{I} + \tau, \tag{2.58}$$

where $\mathbf{I}$ is the identity matrix and τ is the deviatoric stress tensor given by

$$\tau = \lambda(\nabla \cdot \mathbf{u})\mathbf{I} + 2\eta\mathbf{D}\,. \tag{2.59}$$

Here, η is the dynamic viscosity, λ is the bulk viscosity, and $\mathbf{D}$ is the strain rate tensor given by

$$\mathbf{D} = \frac{1}{2}\left(\nabla\mathbf{u} + (\nabla\mathbf{u})^{\mathrm{T}}\right)\,, \tag{2.60}$$

where the superscript T denotes the transpose of a tensor. The continuity equation

$$\frac{\partial\rho}{\partial t} = -\rho\,(\nabla \cdot \mathbf{u}) = 0, \tag{2.61}$$

implies

$$\nabla \cdot \mathbf{u} = 0\,. \tag{2.62}$$

Thus, the second term on the right-hand side of Eq. (2.59) is zero and the Navier-Stokes equation for an incompressible material is

$$\frac{\mathrm{D}\mathbf{u}}{\mathrm{D}t} = \frac{1}{\rho}\left(-\nabla p + \nabla \cdot (\eta\nabla\mathbf{u})\right) + \mathbf{f}_{\mathrm{other}}\,. \tag{2.63}$$

At the micro-scale, the dynamics of a liquid are significantly influenced by surface tension. The origin of surface tension lies in attractive forces, e.g., Van der Waals forces or ionic or covalent bonds among liquid molecules [12]. In the bulk of a fluid, the net force acting on a molecule is zero since it is attracted equally from all sides by neighboring molecules. In contrast, a molecule in the vicinity of a liquid-gas interface experiences an inward oriented net force due to the smaller interaction forces between liquid and gas molecules. As a result, normal and tangential forces arise at the liquid-gas interface, attempting to minimize the surface area associated with increased pressure inside the liquid with a convex surface [12]. The surface stress balance for a surfactant-free interface between two immiscible fluids is given by [18]

$$\hat{\mathbf{n}}_1\,(p_1 - p_2) + \hat{\mathbf{n}}_1 \cdot (\sigma_1 - \sigma_2) = \hat{\mathbf{n}}_1\,(\nabla_{\mathrm{s}} \cdot \hat{\mathbf{n}}_1)\,\sigma + \nabla_{\mathrm{s}}\sigma\,, \tag{2.64}$$

where the subscripts 1 and 2 denote the fluids on both sides of the interface, ∇_{s} is the surface gradient, $\hat{\mathbf{n}}$ is the unit surface normal vector pointing from phase 1 to phase 2, and $\nabla_{\mathrm{s}} \cdot \hat{\mathbf{n}}$ is the surface curvature. The pressure difference across the interface of a spherical droplet in equilibrium is given by the Young-Laplace equation [167]

$$\Delta p_{\mathrm{YL}} = p_{\mathrm{in}} - p_{\mathrm{o}} = \frac{2\sigma}{r_0}\,, \tag{2.65}$$

where r_0 is the radius of the drop, p_{in} is the pressure inside the drop, and p_{o} is the pressure of the ambient phase, respectively. Figure 2.12 illustrates the molecular origin of surface tension.

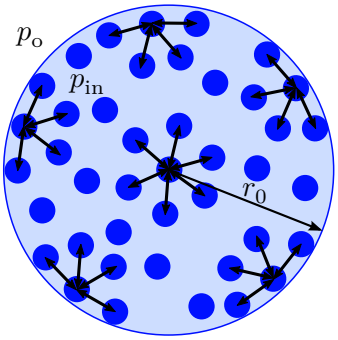

Figure 2.12: Schematic of surface tension caused by attractive forces among molecules. Molecules near the phase boundary are pulled to the interior of the droplet due to the stronger attractive forces among liquid molecules compared to the attraction between liquid and gas molecules.

Another phenomenon caused by surface tension is the spreading behavior of a liquid on a solid substrate. The wettability of a solid substrate with a liquid describes the ability of the phases to remain in contact or to repel each other, denoted as wetting or non-wetting behavior, respectively.

According to Young's equation [228], the equilibrium contact angle of a droplet resting on an ideal, plane solid substrate, depends on the ratio of surface tension between liquid and gas phase, σ, and the surface energy between solid and gas, γ^{sg}, as well as solid and liquid phase, γ^{sl}, given by

$$\gamma^{\mathrm{sg}} = \gamma^{\mathrm{sl}} + \sigma \cdot \cos\left(\Theta_{\infty}\right) , \tag{2.66}$$

where Θ_{∞} is the equilibrium contact angle. The contact angle is defined as the enclosed angle between the tangent defined by the liquid and gas phase, and the tangent between the solid and liquid phase, originating at the three-phase contact point as illustrated in Fig. 2.13. Wetting and non-wetting behavior is associated with $\Theta_{\infty} < 90^{\circ}$ or $\Theta_{\infty} > 90^{\circ}$, respectively.

In the industry, wetting is of interest in applications where surface tension dominates inertial, viscous, or gravitational forces and, thus, leads to surface tension flows. This applies to the fields of microfluidics [174, 198], oil recovery [13, 14], two-phase heat transfer [57], discrete wetting processes such as ink-jet printing [33, 188] or continuous wetting processes [168, 212]. In laser additive manufacturing applications where a single pure metal is processed,

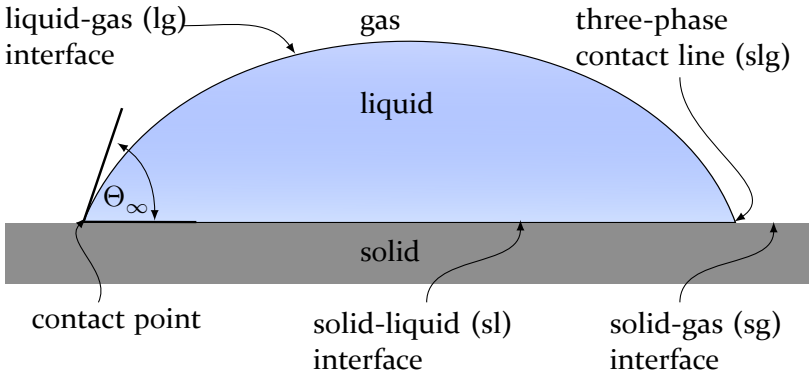

Figure 2.13: Isothermal wetting of a liquid on a solid substrate.

the melt wets a colder, solid substrate of its kind. As a result, the solid-liquid interface is not fixed in space but moves due to the solidification of the melt or melting of the solid phase. This is called homologous wetting and represents a non-equilibrium phenomenon due to the simultaneous effects of heat transfer, moving solid-liquid interfaces, and liquid spreading. In contrast to isothermal wetting, which is well investigated, homologous wetting is subject to research [170, 171, 172]. According to [170, 171, 172], the spreading of a molten droplet on a solid of its kind arrests if the apparent dynamic contact angle, Θ_a, reaches a critical value, Θ_s, which represents the contact angle of the dynamic solidification front. An advancing contact line is only possible if $\Theta_\mathrm{a} > \Theta_\mathrm{s}$. According to [170, 171, 172], Θ_s is a function of the Stefan number which can be determined empirically for any material and which is given by

$$\mathrm{St} = c_p \frac{T - T_\mathrm{m}}{h_\mathrm{m}} \,. \tag{2.67}$$

Here, $T - T_\mathrm{m}$ is the difference between the temperature of the liquid and a target temperature, e.g. the melting temperature. Figure 2.14 shows a sketch of homologous wetting where $\mathbf{u}_\mathrm{s}$ is the spreading velocity of the liquid on the solid substrate.

2.2.5 Further effects

Due to the temperature change of the material irradiated by the laser, volume expansion and shrinkage occur. Thermal stress may lead to the initiation and propagation of cracks in the material. Moreover, temperature gradients in the molten metal result in buoyancy forces affecting the melt flow. The motion of solid particles must also be considered in some laser-metal processes, such

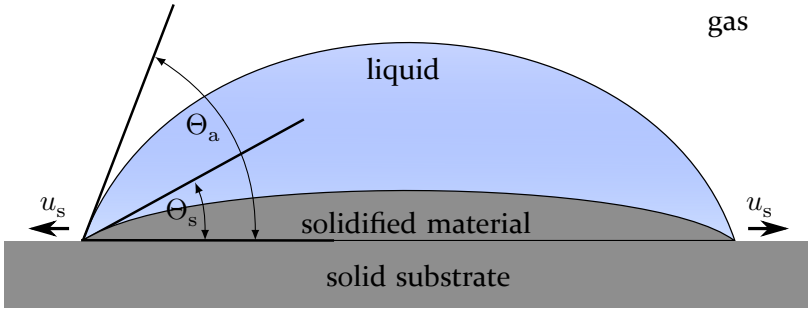

Figure 2.14: Homologous wetting of a liquid on a solid substrate of the same material.

as SLM and laser metal deposition. For instance, in SLM, rapid evaporation leads to recoil pressure on the condensed surface. As a result, powder particles can be carried away or drawn into the melt pool due to the high gas velocities in the vicinity of the heat-affected zone.

2.3 Material defects

Defects in laser metal processing can increase production time, deteriorate the mechanical properties of the manufactured part, or lead to premature termination of the manufacturing process. The origin of these defects can be related to complex physical phenomena involved in laser-metal processing. Choosing material-specific, appropriate processing conditions can reduce or avoid these material defects. Common defects in laser-metal processing are:

- residual stresses and cracks
- pores
- spheroidization of the melt
- oxidation

2.3.1 Residual stress and cracks

The large heating and cooling rates ($10^3\,\mathrm{K\,s^{-1}}$ to $10^8\,\mathrm{K\,s^{-1}}$ [73]) in laser-metal processing lead to high temperature gradients in the processed metal [187]. A consequence of the thermal cycle (the repeated heating and cooling of the material according to the laser scanning path) is the repeated thermal expansion and contraction of the material [72] in additive manufacturing processes, which causes residual stress in the built structure. In particular, the contact areas between melt and solid material are affected by high residual stresses,

which may initiate and propagate cracking, delamination, fatigue failure, or thermal deformation [85, 112, 196] and, henceforth, affect the mechanical properties of the produced part [224]. In SLM, the occurring stresses can be classified into thermal and structural stresses [34]. Anisotropic heating associated with thermal expansion of the material as well as differences in the shrinkage behavior of the material as a function of the distance to the molten metal [52, 123] induces thermal stress that is a primary cause of crack initiation [115]. In contrast, phase transition and the associated expansion and contraction of volume are related to structural stresses [96]. If the stress inside a manufactured part exceeds the yield strength, plastic deformations such as cracks or geometric distortions form to release stress [153]. Often, finite element simulations are carried out to predict residual stress in a manufactured part due to the difficulty of experimental measurements in additive manufacturing processes [234].

In SLM, cracking can be categorized into liquation and solidification cracking [146]. Liquation cracking occurs due to precipitation of low melting point eutectics in the processing of alloys [35, 83]. Solidification cracking, also referred to as hot cracking, is related to the temperature range of solidification in alloys and arises due to the solidification of the residual liquid film between crystals [59].

The residual stresses in the manufactured part can be reduced by lowering the cooling rate, by preheating or remelting the metal [52, 93, 124], or by adjusting the laser energy so that the molten metal has sufficient time to fill and heal cracks during the manufacturing process [37]. For instance, in selective electron beam melting of titanium-aluminides, the surrounding powder must be preheated to about $1000°C$ to avoid the crack formation during material cooling [192]. Furthermore, aluminum alloys are commonly preheated to $50°C$ to $200°C$ [234]. Nevertheless, preheating to too high temperatures can lead to other defects, such as the formation of agglomerates, referred to as balling phenomenon [219].

2.3.2 Porosity

During laser-metal processing, the formation of persistent spherical or aspherical pores deteriorates the mechanical properties of the manufactured part [218]. In SLM, pores can be classified into gas pores, shrinkage pores, and lack-of-fusion pores [46, 73, 90]. Gas pores cannot escape from the molten metal due to high solidification rates and are randomly distributed in the manufactured part [233]. The development of gas pores can be

attributed to surface turbulence at the liquid-gas interface that leads to the entrapment of metal vapor or inert gas from the protective atmosphere into the melt, gas which is located in between the gaps of metal powder in SLM processes, or the evaporation of low melting compounds in the case of feedstock contamination or the processing of alloys [29, 70, 97, 217, 233]. If the volume of the melt insufficient to fill pores during the solidification process, shrinkage porosity occurs [145, 218]. These pores related to the gas phase are typically small, spherical [3, 217], and can result in intensified residual stresses and crack densities [23, 67].

If the laser energy density is too low, a disordered solidification front and an insufficient overlap of adjacent scan lines and subjacent layers may arise. This promotes balling and the formation of lack-of-fusion pores [67, 145, 196]. Lack-of-fusion is one of the most severe defects in laser additive manufacturing and a significant reason for the structural failure of the manufactured part [196]. Lack-of-fusion pores are irregularly shaped and can propagate in the building direction, so multiple layers are affected by this defect. This also leads to reduced heat conductivity, further enhancing this effect. An additional effect is the increased appearance of balling due to insufficient wetting on the solid substrate, which enhances the surface roughness.

2.3.3 Balling and humping

A liquid tends to spheroidize to minimize its surface energy. The occurrence of this behavior in powder-based processes is called balling [225, 234] and can be related to poor wetting of the solid substrate [75] or droplet splashing during the manufacturing process. Large liquid spheres occur due to incomplete wetting of the substrate when using insufficient laser energies [74]. Upon translation of the laser along the predefined path, a cylindrical-shaped melt pool occurs, which fragments into several coarsened spheres which can have the diameter of the laser beam or even exceed its size [201]. The occurrence of discontinuous scan lines may prevent overlapping of the melt with adjacent scan lines and the subjacent layer [74]. This impairs the uniform deposition of fresh powder, which favors the formation of pores and thermal stresses, delamination due to weak interlayer bonding, and deteriorates the part geometry [186, 236]. Additionally, many pores can be formed between disconnected metal balls [114]. The formation of relatively large metal spheres can also prevent the recoating device from moving [5, 236], or even damage the device in SLM [225]. Increasing the laser power, reducing the laser scan speed, or reducing the powder layer thickness are strategies to mitigate balling [74].

If the laser energy is too high, excessive liquid metal will lead to smaller micrometer-scaled droplets [74, 201] which lead to a rough surface accompanied by many pores that reduce the density and quality of the manufactured part [75, 234]. In keyhole welding, high recoil pressure can lead to the ejection of a liquid jet that can break into metal balls [221]. Moreover, in SLM, the formation of metal vapor may disperse solid metal powder or liquid splashes sideways [117]. Nevertheless, the high temperature reduces the liquid's viscosity and increases its fluidity, which assists in mitigating balling [234].

Figure 2.15 shows a computer tomography reconstruction of titanium spatter formed in an SLM process [S166]. The agglomerates formed can reach

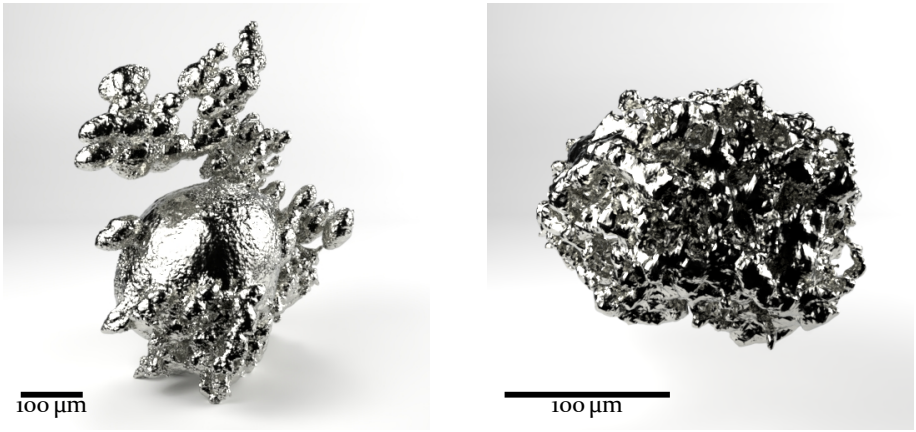

Figure 2.15: Computer tomography reconstruction of titanium spatter obtained from SLM experiments [S166].

significantly larger dimensions than the initial powder. For example, the left particle in Fig. 2.15 has an extent of 652 µm. Droplets with diameters of 920 µm have been reported in the literature [39].

In welding processes, inappropriate process conditions can lead to the spheroidization of the welding seam. Figure 2.16 shows a simulation snapshot of this phenomenon also referred to as humping. A variety of theories have been developed to explain the humping phenomenon [211] ranging from Raleigh's capillary instability [28, 71], Kelvin-Helmholtz instability [105, 203], hydraulic jump [180], to the fluid flow, e.g., due to Marangoni forces [125].

2.3.4 Oxidation

Most metals form an oxide layer on their surface when exposed to air [54]. In laser-metal processing, oxide inclusion is caused by utilizing oxidized

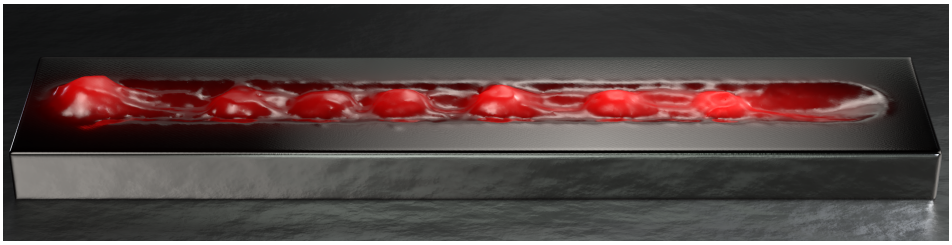

Figure 2.16: Humping in laser melting simulations performed in this work (see Section 7.4).

feedstock or by the oxygen concentration in the ambient atmosphere which can be entrapped into the molten metal due to the turbulent flow [97, 217]. Oxide films can form on all sides of a melt pool in laser processing [118]. The surface energy of oxide layers is smaller than the corresponding liquid-gas surface tension of pure metals and can enhance balling due to the weak wetting forces between oxides and molten metal [49, 54, 154]. This can reduce the density and induce crack initiation, which degrades the mechanical properties of the fabricated parts [89, 90]. Furthermore, oxide layer increase the absorption of laser energy by the underlying pure metal [173]. Reducing the oxygen content in the atmosphere below 0.1% can alleviate balling [113]. Therefore, sufficiently low oxygen partial pressure and clean metal powder in SLM must be ensured. The use of deoxidizing agents added to the metal powder can also be attempted [104].

2.4 Process control

Process control aims to achieve the best possible material properties by avoiding the formation of defects and minimizing the required manufacturing time of parts. Due to the variety of the involved physical phenomena, adjusting the free parameters of the processes requires time-consuming trial and error procedures. In the following, a summary of possible parameters is given. The adjustable process parameters include laser power, beam diameter, and focal length to control the laser's intensity and scanning velocity. High scanning velocity and a controlled inert gas flow to mechanically push the induced vapor plume out of the heat affected zone [173] can be used to minimize the interaction of the laser beam with the emerging metal vapor. The focal point can be placed on the surface of the processed material but also at a certain height above or below the material surface to optimize, for instance, the welding process of thick materials ($> 10\,\mathrm{mm}$). The main purpose of the inert gas, e.g. argon or helium, is to avoid oxidation of the metal. Due to the higher ionization potential of helium compared to argon ($24.46\,\mathrm{eV}$ compared

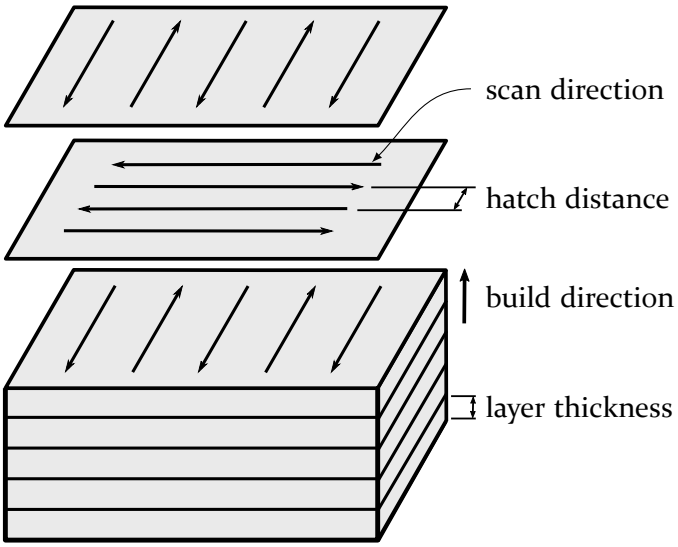

Figure 2.17: Rotation of the scan direction among layers in additive manufacturing processes.

to $15.68\,\mathrm{eV}$), deeper penetration welds can be achieved in laser welding [173] when using helium as an inert gas. The laser beam can also be tailored to optimize the melt geometry and final product quality, e.g., by beam shaping. Furthermore, preheating the substrate aims to reduce the thermal gradient and the formation of cracks. The packing fraction in powder-based processes is essential to reduce the formation of pores. Moreover, smart scanning strategies of the laser beam are necessary to maximize the compactness of the manufactured part. For instance, the direction of laser scan lines can be varied between consecutive layers, as sketched in Fig. 2.17, to increase the material density.

3 Modeling material properties of titanium

This work investigates the melting process of pure titanium surrounded by an argon atmosphere due to laser irradiation. Titanium is a lightweight material with a high strength-to-weight ratio and corrosion resistance and is thus widely used in the aerospace [11] and chemical plant industry [156]. Due to its good bio-compatibility, it is also used for biomedical implants [182, 206]. Its mechanical properties are strongly influenced by its oxygen concentration [152]. In the following, the temperature-dependent material properties of titanium are introduced. If no experimental data are available, appropriate models are employed instead. As an exception, the dynamic viscosity of liquid titanium is considered temperature-independent with $\eta = 3.3 \cdot 10^{-3} \mathrm{Pa\,s}$ [87] and the thermal emissivity of titanium is $\epsilon_{\mathrm{th}} = 0.5$ [27] in this work.

3.1 Phase transitions

As temperature rises, titanium undergoes several phase transitions. At $T_{\mathrm{cryst}} = 1166\,\mathrm{K}$ titanium changes its crystalline structure from hexagonal close-packed to body-centered cubic [53]. These transformations of titanium are called α-titanium or β-titanium, respectively, and are denoted as Ti^{α} and Ti^{β} in this work. The latent heat of this transformation is $h_{\mathrm{cryst}} = 87.12\,\mathrm{kJ\,kg^{-1}}$. Furthermore, at $T_{\mathrm{m}} = 1943\,\mathrm{K}$, titanium undergoes a solid-liquid phase transition where the latent heat of melting is $h_{\mathrm{m}} = 303.97\,\mathrm{kJ\,kg^{-1}}$ [53]. The phase transition from liquid to gaseous titanium at atmospheric pressure takes place at $T_{\mathrm{boil}} = 3558\,\mathrm{K}$ [30]. The latent heat of vaporization varies with temperature as given by Eq. (2.32) and the latent heat of vaporization at absolute zero temperature is $h_{\mathrm{vap},0} = 9700\,\mathrm{kJ\,kg^{-1}}$ [86]. Moreover, titanium's critical temperature, atomic mass, and specific heat ratio are $T_{\mathrm{crit}} = 11790\,\mathrm{K}$ [65], $m_{\mathrm{A,v}} = 47.87\,\mathrm{Da}$, and $\gamma_{\mathrm{v}} = 5/3$.

Using Eqs. (2.33) and (2.40), argon's atomic mass, $m_{\mathrm{A,a}} = 39.95\,\mathrm{Da}$, and specific heat ratio, $\gamma_{\mathrm{a}} = 5/3$ [12], the flow states of evaporating titanium propagating into the ambient argon atmosphere at atmospheric pressure, can be computed as introduced in Section 2.2.2. The flow state diagram of the system titanium-argon is shown in Fig. 3.1, where the dashed lines are obtained by the Clausius-Clapeyron equation (2.33) and the solid lines correspond to Eq. 2.40 which is based on the Rankine-Hugoniot and Knudsen layer jump conditions. By connecting the intersection of the two sets of curves with a linear function

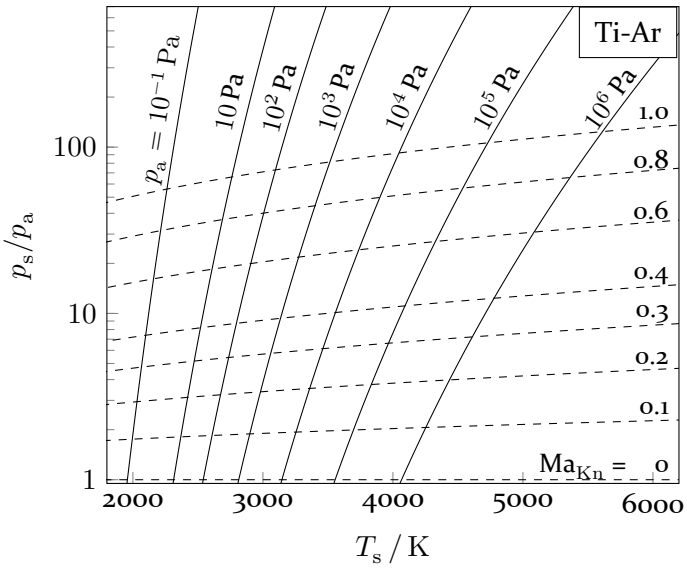

Figure 3.1: Flow state diagram of evaporating titanium vapor into an ambient argon atmosphere as a function of temperature and ambient pressure, p_a. Dashed curves are given by the Clausius-Clapeyron equation (2.33), and solid lines are provided by Eq. 2.40 based on the Rankine-Hugoniot and Knudsen layer jump conditions.

at $\mathrm{Ma_{Kn}} = 0$ and $\mathrm{Ma_{Kn}} = 1$, the surface temperature can be related to the flow Mach number and constant ambient pressure [98].

3.2 Density

According to [200, 220], the temperature dependence of the density of titanium is

$$\rho(T) = A_0 + A_1 T + A_2 T^2 + A_3 T^3 \,. \tag{3.1}$$

Here, the coefficients A_0, A_1, A_2, and A_3 are given in Tab. 3.1 for Ti^{α} ($200\,\mathrm{K} < T \leq T_{\mathrm{cryst}}$), Ti^{β} ($T_{\mathrm{cryst}}\,\mathrm{K} < T \leq T_{\mathrm{m}}$) and liquid titanium Ti^{l} ($T > T_{\mathrm{m}}$), respectively. Figure 3.2 shows titanium's density as a function of temperature, which decreases from $4512\,\mathrm{kg\,m^{-3}}$ at $T = 300\,\mathrm{K}$ to $3776\,\mathrm{kg\,m^{-3}}$ at T_{boil}. All simulations carried out in this work assume a density invariant material. Nevertheless, Eq. (3.1) is required to model the temperature dependence of the optical properties of titanium introduced in Section 3.6.

Table 3.1: Polynomial fit parameters for the temperature-dependent density of titanium [200].

	$200\,\mathrm{K} < T \leq T_{\mathrm{cryst}}$	$T_{\mathrm{cryst}} < T \leq T_{\mathrm{m}}$	$T > T_{\mathrm{m}}$
A_0	4546.26	4471.86	4580.00
A_1	$-1.05568 \cdot 10^{-1}$	$4.06497 \cdot 10^{-2}$	-0.2260
A_2	$-3.47491 \cdot 10^{-5}$	$-1.14497 \cdot 10^{-4}$	0
A_3	$8.16976 \cdot 10^{-9}$	$2.03179 \cdot 10^{-8}$	0

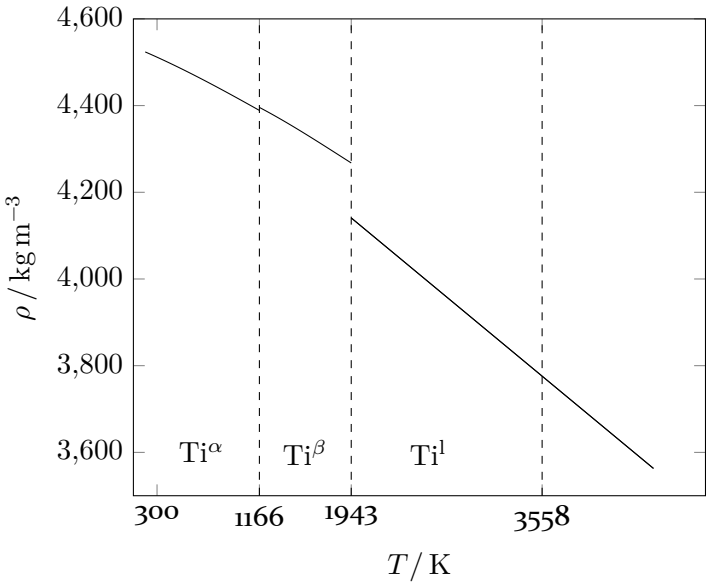

Figure 3.2: Density of titanium as a function of temperature.

3.3 Heat capacity

The temperature dependence of the specific heat capacity at constant pressure is modeled for three different temperature regimes that correspond to Ti^{α}, Ti^{β} and liquid titanium, Ti^{l} according to [200]

$$c_p\,[\mathrm{J\,kg^{-1}\,K^{-1}}] = \begin{cases} c_p^{\alpha} & T < T_{\mathrm{cryst}} \\ c_p^{\beta} & T_{\mathrm{cryst}} \leq T \leq T_{\mathrm{m}} \\ c_p^{\mathrm{l}} & T > T_{\mathrm{m}} \end{cases}. \tag{3.2}$$

The heat capacity of Ti^{α} is composed of different contributions depending on the temperature regime and can be described by [200]

$$c_p^{\alpha} = \frac{c_{p,\mathrm{D}}^{\alpha} + c_{p,\mathrm{H}}^{\alpha} + c_{p,\mathrm{E}}^{\alpha}}{M}\,. \tag{3.3}$$

Here, $M = 47.87 \cdot 10^{-3}\,\mathrm{kg\,mol^{-1}}$ [12] is the molar mass of titanium, $c_{p,\mathrm{D}}^{\alpha}$ is heat capacity estimated by the Debye model, and $c_{p,\mathrm{H}}^{\alpha}$ represents a polynomial that describes the electronic and vibrational contributions to the heat capacity [78]. The heat capacity of some transition metals shows a sharp increase in the temperature regime where their magnetic state changes. This is accounted by the last term on the right-hand side of Eq. (3.3), $c_{p,\mathrm{E}}^{\alpha}$, in the case of titanium.

For the low-temperature regime, the molar heat capacity $c_{p,\mathrm{D}}^{\alpha}$ is given by the Debye model

$$c_{p,\mathrm{D}}^{\alpha}\left[\mathrm{J\,mol^{-1}\,K^{-1}}\right] = 3R_{\mathrm{g}}C\left(\bar{x}\right), \quad \bar{x} = \Theta_{\mathrm{D}}/T, \tag{3.4}$$

where R_{g} is the ideal gas constant, $\Theta_{\mathrm{D}}(298\,\mathrm{K}) = 375\,\mathrm{K}$ [200] is the Debye temperature of titanium, and $C\left(\bar{x}\right)$ is given by

$$C\left(\bar{x}\right) = 4D\left(\bar{x}\right) - \frac{3\bar{x}}{\mathrm{e}^{\bar{x}} - 1}\,. \tag{3.5}$$

Here, $D\left(\bar{x}\right)$ is the Debye function defined by

$$D\left(\bar{x}\right) = \frac{3}{\bar{x}^3}\int_0^{\bar{x}} \frac{\bar{y}^3}{e^{\bar{y}} - 1}\mathrm{d}\bar{y}\,. \tag{3.6}$$

The second term on the right hand side of Eq. (3.3) accounts for electronic and vibrational contributions to the heat capacity [78, 200] and is given by

$$c_{p,\mathrm{H}}^{\alpha}\left[\mathrm{J\,mol^{-1}\,K^{-1}}\right] = 6.40 \cdot 10^{-3}T. \tag{3.7}$$

Finally, the sharp increase in the heat capacity in the vicinity of T_{cryst} is defined by

$$c_{p,\mathrm{E}}^{\alpha}\left[\mathrm{J\,mol^{-1}\,K^{-1}}\right] = \exp\left(-9.21 + 10.23T\right)\,. \tag{3.8}$$

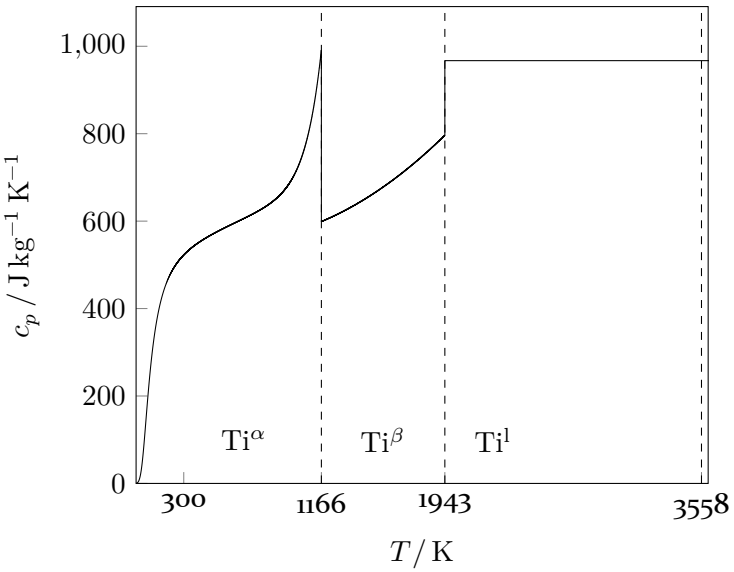

Figure 3.3: Specific heat capacity of titanium as a function of temperature.

For the temperature regime $T_{\mathrm{cryst}} \leq T \leq T_{\mathrm{m}}$ the polynomial expression by [200] for the data of [53] is used

$$c_p^{\beta}\left[\mathrm{J\,kg^{-1}\,K^{-1}}\right] = \frac{1}{M}\left(28.66 - 7.28 \cdot 10^{-3} T + 6.25 \cdot 10^{-6} T^2\right), \quad T_{\mathrm{cryst}} \leq T \leq T_{\mathrm{m}}. \tag{3.9}$$

Because the temperature dependence of the heat capacity at temperatures far below the critical temperature is generally small for liquid titanium ($T > T_{\mathrm{m}}$), a constant heat capacity of

$$c_p^{\mathrm{l}}\left[\mathrm{J\,kg^{-1}\,K^{-1}}\right] = 46.29, \qquad T > T_{\mathrm{m}} \tag{3.10}$$

is assumed [86, 200]. The modeled specific heat capacity as a function of temperature is shown in Fig. 3.3.

3.4 Thermal conductivity

Metals are characterized by their high electrical and thermal conductivity, which can be attributed to freely moving electrons in the conduction band.

The Wiedemann-Franz (WF) law relates thermal conductivity to electric resistivity by [94]

$$\frac{k}{\sigma_\mathrm{e} T} = L_\mathrm{e} \,. \tag{3.11}$$

Here, σ_e is the electric conductivity and L_e is the Lorenz number. The inverse of the electric conductivity is the electric resistivity, $\sigma_\mathrm{e} = \rho_\mathrm{e}^{-1}$, which is given for titanium by [176]

$$\begin{aligned} \rho_\mathrm{e}\,[\Omega\,\mathrm{m}] =& 1.672 + 1.589 \cdot 10^{-4}\,(T - T_\mathrm{m}) \\ &+ 6.776 \cdot 10^{-9}\,(T - T_\mathrm{m})^2 \end{aligned} \quad , \quad T_\mathrm{m} \leq T \leq 5000\,\mathrm{K}\,. \tag{3.12}$$

According to the Drude theory, the theoretical (Sommerfeld) Lorenz number is $L_{\mathrm{e},0} = 2.45 \cdot 10^{-8}\,\mathrm{W}\,\Omega\,\mathrm{K}^{-2}$ [94]. Nevertheless, the experimental Lorenz number for titanium differs from its theoretical value and is given at melting temperature by the Wiedemann-Franz ratio $L_\mathrm{e}/L_{\mathrm{e},0} = 1.1$ according to [126]. Thus, the thermal conductivity is given by

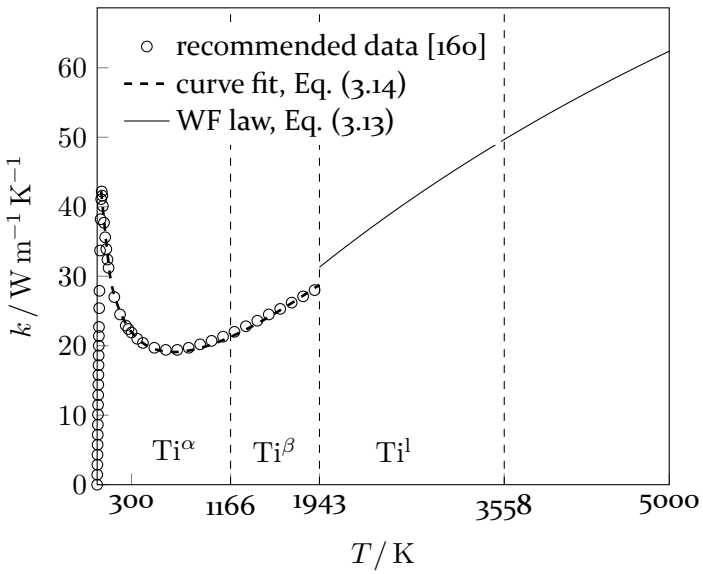

Figure 3.4: Thermal conductivity of titanium as a function of temperature.

$$k = 1.1 L_{\mathrm{e},0} T \rho_\mathrm{e}^{-1} \,. \tag{3.13}$$

For temperatures $T < T_\mathrm{m}$, the recommended data given by [160] are interpolated using

$$k\left[\mathrm{W\,m^{-1}\,K^{-1}}\right] = \big(2.279 \cdot \mathrm{T}^{-\frac{5.195}{1000}} + 1.716 \cdot 10^{-2} T - 2.196 \cdot 10^{3}\big)\mathrm{W\,m^{-1}\,K^{2}} \quad T > T_\mathrm{m}\,. \tag{3.14}$$

In this work, the thermal conductivity is described as shown in Fig. 3.4, using Eqs. (3.14) and (3.13). Moreover, the recommended thermal conductivity by [160] is shown by hollow circles.

3.5 Surface tension

The temperature dependence of the surface tension coefficient is given by [235]

$$\sigma = \sigma_0 + \sigma_T (T - T_\mathrm{m})\ , \tag{3.15}$$

where $\sigma_0 = 1.64\,\mathrm{N\,m^{-1}}$ and $\sigma_T = -2.38 \cdot 10^{-4}\,\mathrm{K^{-1}}$. Figure 3.5 shows the linear decrease of titanium's surface tension with increasing temperature. The temperature dependence of the surface tension is required for modeling Marangoni forces as shown in Chapter 6. However, the normal component of surface tension is modeled assuming a constant surface tension coefficient of $\sigma_0 = 1.64\,\mathrm{N\,m^{-1}}$ in the simulations that are presented in Chapters 7 and 8.

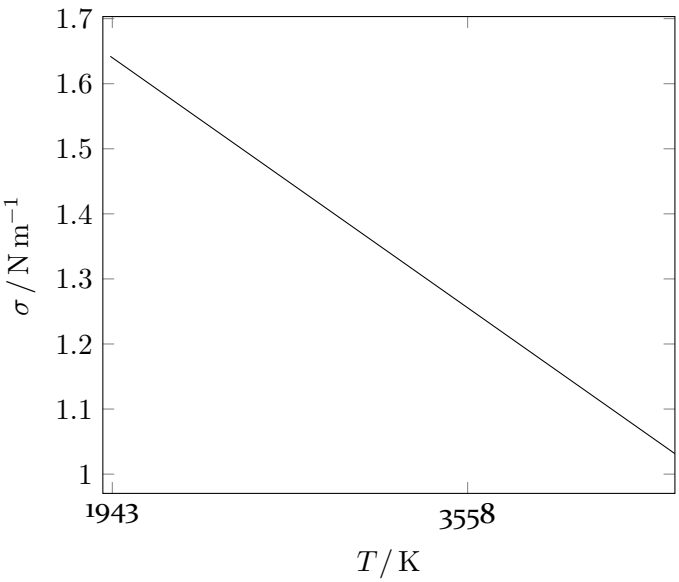

Figure 3.5: Surface tension of titanium as a function of temperature.

3.6 Optical properties

In the following, the temperature-dependent complex refractive index of titanium for laser irradiation with a wavelength of $\lambda = 1.08\,\mu\mathrm{m}$ is introduced. Therefore, K^s in Eq. (2.24) can be computed by

$$K^\mathrm{s} = \Gamma_0^\mathrm{s} \left(T_0^5 \int_0^{\Theta_\mathrm{D}/T_0} \frac{\bar{z}^4}{\mathrm{e}^{\bar{z}} - 1} \mathrm{d}\bar{z} \right)^{-1} . \tag{3.16}$$

Here, Γ_0^s is the collision frequency at reference temperature T_0. The relation [205]

$$2 n_{1,0} n_{2,0} = \frac{\omega_p^2}{\omega^2 + \Gamma_0^2} \frac{\Gamma_0}{\omega} , \tag{3.17}$$

where $n_{1,0}$ and $n_{2,0}$ are the real and imaginary components of the refractive index at T_0, gives the collision frequency at T_0. Solving Eq. (3.17) yields

$$\Gamma_0 = \frac{\omega_\mathrm{p} - \sqrt{\omega_\mathrm{p}^4 - 16 n_{1,0}^2 n_{2,0}^2 \omega^4}}{4 n_{1,0} n_{2,0} \omega} . \tag{3.18}$$

Here, the plasma frequency is computed using the effective electron mass, m_e^*, by

$$\omega_\mathrm{p} = \sqrt{\frac{n_\mathrm{e} q_\mathrm{e}^2}{\epsilon_0 m_\mathrm{e}^*}} , \tag{3.19}$$

and the electron density is given by

$$n_\mathrm{e} = \frac{z_\mathrm{e} N_\mathrm{A} \rho_0}{M} , \tag{3.20}$$

where $N_\mathrm{A} = 6.022 \cdot 10^{23}\,\mathrm{mol}^{-1}$ is the Avogadro constant and z_e is the number of valence electrons of titanium.

The complex permittivity at the reference temperature is obtained from experimental measurements as shown in Tab. 3.2. The permittivity is used to compute the real and imaginary parts of the refractive index according to Eq. (2.20). Furthermore, the corresponding reflectivity at normal incidence is computed by Eq. (2.22) or (2.23). As can be seen in Tab. 3.2, a variety of measured optical properties exist for a wavelength of $\lambda = 1.08\,\mu\mathrm{m}$ which correspond to reflectivity values between 49.33 % and 96.99 % for normal incidence. Surface roughness, contamination with chemicals, or the formation of a passive layer can drastically increase the absorbtance of the material [173]. Titanium is prone to oxidation even for low exposure times to air [54]. There-

Table 3.2: Real and imaginary parts of the refractive index and permittivity of titanium for $\lambda = 1.08\,\mu\mathrm{m}$.

$n_{1,0}$	$n_{2,0}$	$\epsilon_{1,0}$	$\epsilon_{2,0}$	$R\,/\,\%$	reference
3.49	4.02	-3.96	28.02	61.53	[91]
3.48	3.33	1.02	23.18	55.33	[150]
3.37	3.63	-188	24.46	58.28	[121]
0.67	9.30	-86.07	12.50	96.99	[215]
2.92	2.76	0.91	16.15	49.22	[155]

fore, special care must be spent on examining the surface quality of titanium in these experiments. The data by [215] were obtained by reflection electron energy-loss spectroscopy using ultra-high vacuum conditions (pressure $< 1.33 \cdot 10^{-9}\,\mathrm{mbar}$). Moreover, a clean titanium surface was ensured using Ar^+ bombardment to remove any contamination on the sample, which was verified via Auger-electron spectroscopy.

Another experimental study on the optical properties of titanium, using ultra-high vacuum conditions (pressure $< 1.33 \cdot 10^{-8}\,\mathrm{mbar}$) and ensuring an atomically clean titanium surface to the detection limit of Auger-spectroscopy, was obtained by Wall et al. [210]. Though Wall et al. [210] provide only experimental data in the wavelength range from $49.6\,\mathrm{nm}$ to $0.62\,\mu\mathrm{m}$, their results indicate a sharp increase in reflectivity for a wavelength $> 0.25\,\mu\mathrm{m}$. This is why the highest confidence is put into the data by [215], which is used to compute the reflectivity of a clean titanium surface.

Consequently, he plasma and collision frequency at reference temperature in Eqs. (3.18) and (3.19) can be computed using the data provided in Tab. 3.3. It is assumed that the experimental data are measured at a reference temperature of $T_0 = 300\,\mathrm{K}$. Subsequently, K^s in Eq. (3.16) can be computed and $\Gamma^\mathrm{s}\,(T)$ is given by Eq. (2.24) up to the melting temperature.

Accordingly, the constant K^l must be found for the liquid phase. Therefore, the plasma frequency, which is assumed to be temperature independent, is given by Eq. (3.19). Moreover, the collision frequency at the melting point, $\Gamma^\mathrm{l}_\mathrm{m}(T_\mathrm{m})$, is obtained from Eq. (2.24) and the constant K^l is provided by

$$K^\mathrm{l}\,(T_\mathrm{m}) = \Gamma^\mathrm{l}(T_\mathrm{m}) \left(T_\mathrm{m}^5 \int_{\bar{y}=0}^{\Theta_\mathrm{PY}(T_\mathrm{m})/T_\mathrm{m}} \frac{\bar{y}^4}{\mathrm{e}^{\bar{y}} - 1} \mathrm{d}\bar{y} \right)^{-1} . \tag{3.21}$$

Table 3.3: Material properties that are required to model the temperature dependence of the real and imaginary parts of the refractive index of titanium.

property	value	reference
$S(0)$	0.02	[140]
z_e	4	[88]
$m_\mathrm{e}^*/m_\mathrm{e}$	3.2	[88]
Θ_D	380 K	[88]

Here, Θ_PY can be computed using Eq. (2.26) by employing the temperature-dependent density given in Eq. (3.1). The collision-frequency, $\Gamma^\mathrm{l}(T)$, is now given by Eq. (2.25) and is assumed to be valid for material temperatures larger than the boiling temperature.

For the experimentally measured optical properties of titanium, the temperature-dependent complex permittivity and refractive index can be computed by Eqs. (2.17) and (2.20) for an angular frequency of $\omega = 1.74 \cdot 10^{15}\,\mathrm{s}^{-1}$ according to Eq. (2.14) and $\lambda = 1.08\,\mu\mathrm{m}$. Using the data by [215] ($n_1 = 0.67$ and $n_2 = 9.30$), the real and imaginary parts of the complex refractive index are shown as solid blue lines in Fig. 3.6 as a function of temperature. In addition, the corresponding reflectivity for radiation at normal incidence is shown as a solid black line. Since the evaluation of n_1 and n_2 using the proposed models by Ujihara [205] and Siegel [183] is numerically too expensive, the following fit functions are used for the solid ($T \leq T_\mathrm{m}$)

$$n_{1,\mathrm{clean}}^\mathrm{s} = A_0 T^{0.5} + A_1 T + A_2\,, \tag{3.22}$$

$$n_{2,\mathrm{clean}}^\mathrm{s} = A_0 T^{3} + A_1 T^{2} + A_2\,, \tag{3.23}$$

and the liquid phase ($T > T_\mathrm{m}$)

$$n_{1,\mathrm{clean}}^\mathrm{l} = A_0 T^{2} + A_1 T + A_2\,, \tag{3.24}$$

$$n_{2,\mathrm{clean}}^\mathrm{l} = A_0 T^{-0.5} + A_1 T + A_2\,, \tag{3.25}$$

as shown by the blue dashed lines in Fig. 3.6. The coefficients A_0, A_1 and A_2 are given in Tab. 3.4. In this work, it is assumed that Eqs. (3.22) to (3.25) describe the optical properties of a clean titanium surface. Using Eqs. (3.22) to (3.25), the reflectivity as a function of the angle of incidence is given by Eqs. (2.22) and (2.23). Figure (3.7) shows the reflectivity for parallel and per-

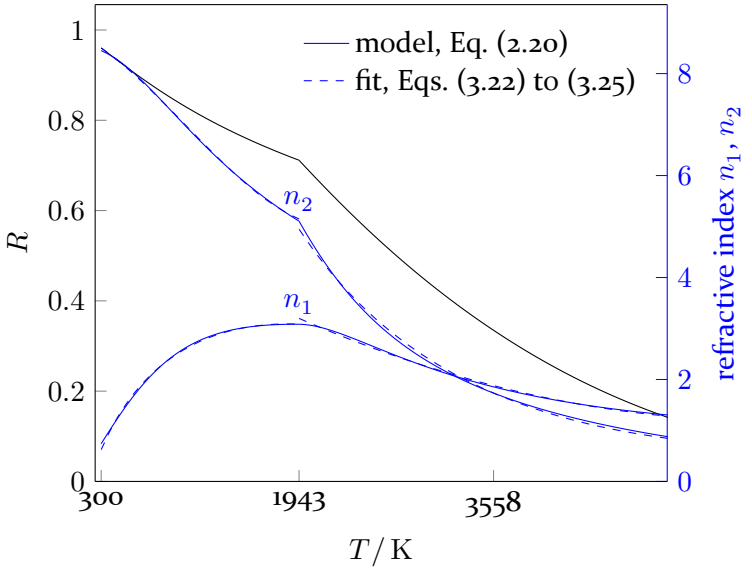

Figure 3.6: Temperature dependence of the real and imaginary parts of the refractive index of a clean titanium surface as well as the corresponding reflectivity of light with a wavelength of $\lambda = 1.08\,\mu\mathrm{m}$ at normal incidence according to Eqs. (2.22) and (2.23).

pendicular polarized light with respect to the plane of incidence for $T = 300\,\mathrm{K}$, $T = 1943\,\mathrm{K}$ (melting temperature) and $T = 3558\,\mathrm{K}$ (boiling temperature at atmospheric pressure) depending on the incident angle.

In the following, the second set of fit formulas that describe the temperature dependence of the real and imaginary parts of the refractive index of an aged titanium surface is introduced. Elimination of ω_p by substitution of the

Table 3.4: Fitting coefficients used to model the real and imaginary parts of the refractive index of a clean titanium surface that is irradiated by a laser beam with a wavelength of $1.08\,\mu\mathrm{m}$.

	A_0	A_1	A_2	regime
$n^\mathrm{s}_{1,\mathrm{clean}}$	0.32	$-3.72 \cdot 10^{-3}$	-3.81	$300\,\mathrm{K} \leq T \leq T_\mathrm{m}$
$n^\mathrm{s}_{2,\mathrm{clean}}$	$5.30 \cdot 10^{-10}$	$-1.59 \cdot 10^{-6}$	8.88	$300\,\mathrm{K} \leq T \leq T_\mathrm{m}$
$n^\mathrm{l}_{1,\mathrm{clean}}$	$1.31 \cdot 10^{-7}$	$-1.54 \cdot 10^{-3}$	-5.69	$T_\mathrm{m} < T \leq 5000\,\mathrm{K}$
$n^\mathrm{l}_{2,\mathrm{clean}}$	$7.44 \cdot 10^{2}$	$7.37 \cdot 10^{-4}$	-13.36	$T_\mathrm{m} < T \leq 5000\,\mathrm{K}$

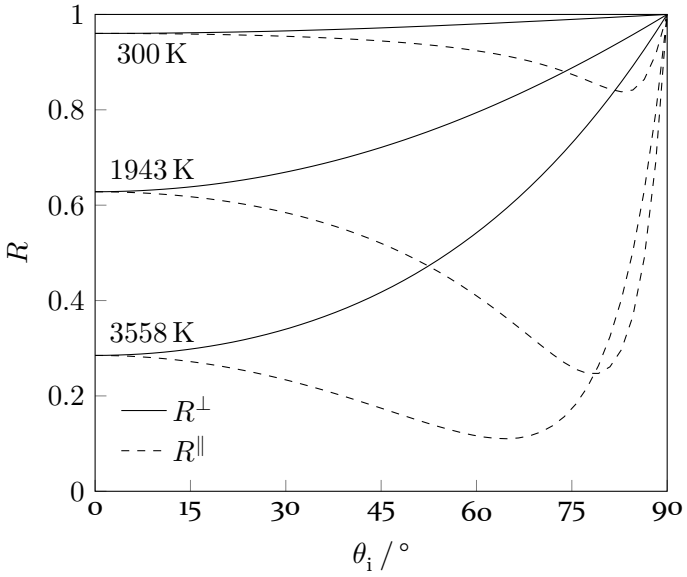

Figure 3.7: Reflectivity of a clean titanium surface for light with a wavelength of $\lambda = 1.08\,\mu\mathrm{m}$. The reflectivity depends on the temperature as well as the orientation of the electric field with respect to the plane of incidence.

imaginary part of the complex permittivity into the real part of the permittivity, given in Eq. (2.17), leads to the following expression for the collision frequency:

$$\Gamma_0 = \frac{\epsilon_{\mathrm{r},2}\omega}{1-\epsilon_{\mathrm{r},1}}\,. \tag{3.26}$$

Moreover, substitution of Eq. (3.26) into the real part of the permittivity in Eq. (2.17) yields

$$\omega_\mathrm{p} = \sqrt{(1-\epsilon_1)\,(\omega^2+\Gamma_0^2)}\,. \tag{3.27}$$

Using Eq. (3.27) to estimate the plasma frequency and Eq. (3.26) to calculate the collision frequency at reference temperature, T_0, eliminates the need to compute ω_p in Eq. (3.19), which requires knowledge of titanium's electron density and effective electron mass.

Employing the permittivity provided by [91] in Tab. 3.2 as input parameter to Eqs. (3.26), (3.27), (3.16), (3.21), (2.24), (2.25), and (2.17), leads to the temperature-dependent real and imaginary part of the refractive index given by (2.20), shown as solid blue lines in Fig. 3.8. The set of fitting equations

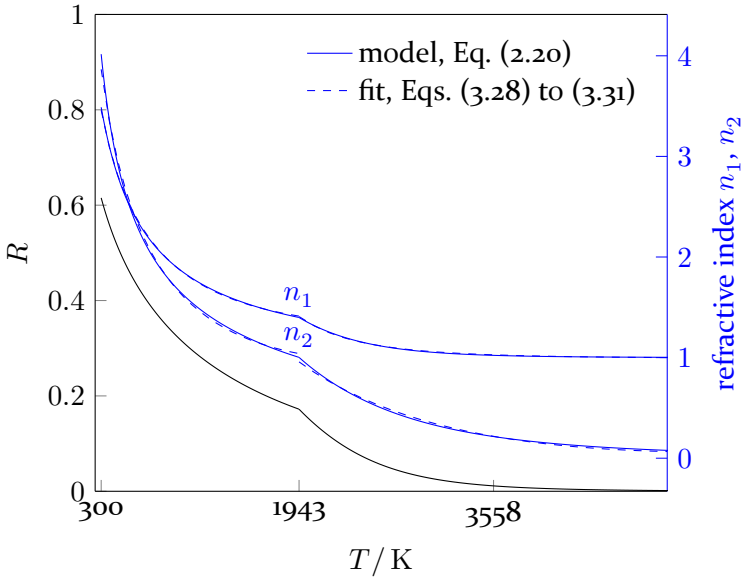

Figure 3.8: Temperature dependence of the real and imaginary parts of the refractive index as well as the corresponding reflectivity of an aged titanium surface for light with a wavelength of $\lambda = 1.08\,\mu\mathrm{m}$ at normal incidence according to Eqs. (2.22) and (2.23).

describing the refractive indices of the solid and liquid phase with aged surfaces are given by

$$n^{\mathrm{s}}_{1,\mathrm{aged}} = A_0 T^{-0.5} + A_1 T + A_2\,, \tag{3.28}$$

$$n^{\mathrm{s}}_{2,\mathrm{aged}} = A_0 T^{-0.5} + A_1 T + A_2\,, \tag{3.29}$$

$$n^{\mathrm{l}}_{1,\mathrm{aged}} = A_0 T^{-0.5} + A_1 T + A_2\,, \tag{3.30}$$

$$n^{\mathrm{l}}_{2,\mathrm{aged}} = A_0 T^{-0.5} + A_1 T + A_2\,, \tag{3.31}$$

where the corresponding coefficients are provided in Tab. 3.5. Eqs. (3.28) to (3.31) are shown as dashed blue lines in Fig. 3.8. Furthermore, the reflectivity for normal incidence is shown as a solid black line in Fig. 3.8. In addition, Fig. 3.9 shows the reflectivity of an aged titanium surface as a function of the angle of incidence at 300 K, 1943 K (melting temperature) and 3558 K (boiling temperature at atmospheric pressure).

Table 3.5: Fitting coefficients used to model the real and imaginary parts of the refractive index of an aged titanium surface that is irradiated by light with a wavelength of $1.08\,\mu\mathrm{m}$.

	A_0	A_1	A_2	regime
$n^{\mathrm{s}}_{1,\mathrm{aged}}$	48.29	$1.44 \cdot 10^{-4}$	-0.15	$300\,\mathrm{K} \leq T \leq T_{\mathrm{m}}$
$n^{\mathrm{s}}_{2,\mathrm{aged}}$	80.46	$2.84 \cdot 10^{-4}$	-1.61	$300\,\mathrm{K} \leq T \leq T_{\mathrm{m}}$
$n^{\mathrm{l}}_{1,\mathrm{aged}}$	51.49	$8.55 \cdot 10^{-5}$	-0.16	$T_{\mathrm{m}} < T \leq 5000\,\mathrm{K}$
$n^{\mathrm{l}}_{2,\mathrm{aged}}$	144.52	$1.94 \cdot 10^{-4}$	-2.97	$T_{\mathrm{m}} < T \leq 5000\,\mathrm{K}$

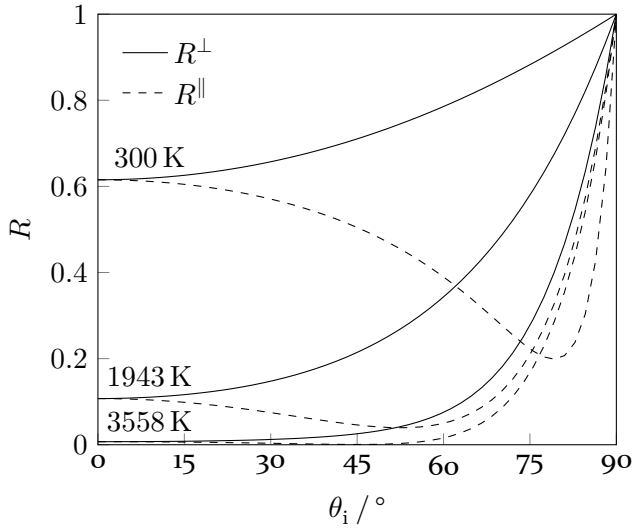

Figure 3.9: Reflectivity of an aged titanium surface for light with a wavelength of $\lambda = 1.08\,\mu\mathrm{m}$. The reflectivity depends on the temperature as well as the orientation of the electric field with respect to the plane of incidence.

3.7 Concluding remarks

This chapter introduced the temperature dependence of density, heat capacity, thermal conductivity, and surface tension of titanium used in this work. Moreover, the optical properties of a titanium surface for light with a wavelength of $1.08\,\mu\mathrm{m}$ are presented. A literature review revealed a surface reflectivity for normal incidence of laser irradiation between $49\,\%$ [155] and $97.0\,\%$ [215] of titanium when employing Fresnel laws. The variance of the reported complex refractive index and permittivity may be caused by the sensitivity of these properties to the surface quality of the material. The formation of an oxidation layer, contamination with other chemicals, or a rough titanium surface can

significantly affect the measured optical properties. For this reason, clean and aged titanium surfaces are distinguished in this work. The thermal emissivity and viscosity of titanium are assumed to be temperature-independent in this work.

4 Smoothed Particle Hydrodynamics

This chapter deals with the mathematical principles of SPH, a Lagrangian numerical method to solve continuum mechanical problems. SPH was developed by Gingold and Monaghan [68], and Lucy [119] separately in 1977. Initially, it was used to investigate astrophysical problems and gas dynamics. Apart from its original field of application, it has been used to simulate numerous other problems, including hemodynamics in blood vessels and aneurysms [135, 161], sloshing and granular cargo behavior in transport vehicles [63, 64], friction between tire and wet surfaces [17], or extrusion and forging processes [24, 41, 164]. Thus, SPH has been demonstrated to be a reliable and robust numerical method for simulating complex problems involving numerous concurrent physical phenomena.

4.1 Idea and mathematical formulation

SPH is a Lagrangian method in which nodal points discretize the domain. Unlike lattice-based methods with fixed vertices, these points, commonly referred to as SPH particles, are mobile in space and do not preserve their neighborhood. Physical properties such as density, ρ, pressure, p, and velocity, $\mathbf{u}$, are defined at these positions. Additionally, each SPH particle carries a fraction of the total fluid mass corresponding to a certain volume. To obtain a discrete formulation of the governing equations that describe the motion and energy of an SPH particle, the concept of integral interpolation is used. Therefore, an arbitrary scalar field, Φ, can be represented by a spatial convolution product with the Dirac delta distribution, δ, by

$$\Phi(\mathbf{r}) = \int_{\Omega} \Phi(\mathbf{r}') \, \delta(\mathbf{r} - \mathbf{r}') \, \mathrm{d}\mathbf{r}' \,, \tag{4.1}$$

where Ω denotes the whole continuous medium, $\mathbf{r}$ is a position in Ω where δ is centered, $\mathbf{r}' \neq \mathbf{r}$ is a position in the neighborhood of $\mathbf{r}$ in Ω and $\mathrm{d}\mathbf{r}'$ is an infinitesimal volume element. The Dirac delta distribution, δ, is given by

$$\delta(\mathbf{r} - \mathbf{r}') = \begin{cases} \infty & \mathbf{r} = \mathbf{r}' \\ 0 & \mathbf{r} \neq \mathbf{r}' \end{cases} \,, \tag{4.2}$$

whereas its integral is defined as $\int_{\Omega} \delta(\mathbf{r} - \mathbf{r}') \, \mathrm{d}\mathbf{r}' = 1$.

In the SPH method, δ is replaced by an appropriate kernel function, $W(\mathbf{r}-\mathbf{r}', h)$, whose radius of influence is determined by the smoothing length, h. Equation (4.1) can now be written as

$$\Phi(\mathbf{r}) \approx \int_{\Omega_\mathbf{r}} \Phi(\mathbf{r}')\, W(\mathbf{r}-\mathbf{r}', h)\, \mathrm{d}\mathbf{r}' \,, \tag{4.3}$$

where $\Omega_\mathbf{r}$ denotes the neighborhood of $\mathbf{r}$ defined by h. By discretizing the simulation domain using SPH particles with constant mass and volume, the integrand in Eq. (4.3) vanishes everywhere except at the positions of the SPH particles. Consequently, the integral can be replaced by a sum, particularly at the position $\mathbf{r}_a$ of the central SPH particle, which gives

$$\Phi(\mathbf{r}_a) \approx \sum_b \frac{m_b}{\rho_b} \Phi(\mathbf{r}_b)\, W(\mathbf{r}_a - \mathbf{r}_b, h) \,, \tag{4.4}$$

where b runs over all SPH particles that are located within the kernel radius, $r_{\max}$. The factor m_b/ρ_b describes the volume assigned to particle b of mass m_b and density ρ_b. These quantities characterize the simulated material. In the following, the shorthand notation

$$\Phi_a = \sum_b \frac{m_b}{\rho_b} \Phi_b W_{ab} \tag{4.5}$$

is used instead of Eq. (4.4). Here, the subscripts a and b denote the central and a neighbor particle, respectively. Figure 4.1 illustrates the used notation. Par-

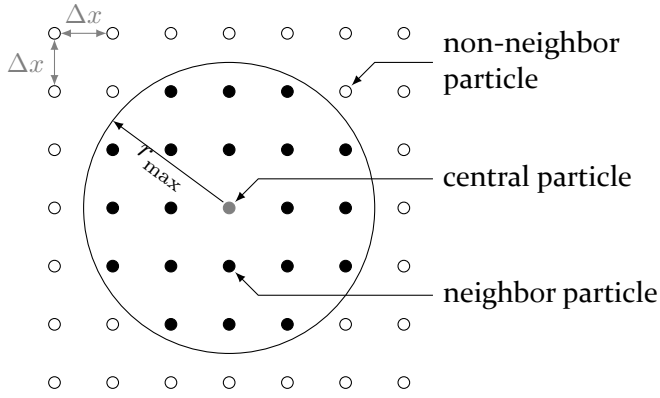

Figure 4.1: Sketch of the compact support of a kernel function in two spatial dimensions. The SPH particles are placed on a rectangular lattice with spacing Δx. The central particle (gray circle) is only affected by neighboring SPH particles (black circles) and not by SPH particles located outside the support radius (hollow circles).

ticles located outside of the kernel radius are not included into the summation in Eq. (4.5).

The spatial gradients that occur in the governing equations in Section 4.2 shall be approximated analogous to Eq. (4.5). Applying the gradient operator to a scalar field Φ followed by integration by parts results in [208]

$$\begin{aligned}\nabla\Phi\left(\mathbf{r}\right) &= \int_{\Omega_\mathbf{r}} \frac{\partial\Phi\left(\mathbf{r}'\right)}{\partial\mathbf{r}'} W\left(\mathbf{r}-\mathbf{r}',h\right)\mathrm{d}\mathbf{r}' \\ &= \int_{\Omega_\mathbf{r}} \frac{\partial}{\partial\mathbf{r}'}\left(\Phi\left(\mathbf{r}'\right)W\left(\mathbf{r}-\mathbf{r}',h\right)\right)\mathrm{d}\mathbf{r}' \\ &\quad - \int_{\Omega_\mathbf{r}} \Phi\left(\mathbf{r}'\right)\frac{\partial W\left(\mathbf{r}-\mathbf{r}',h\right)}{\partial\mathbf{r}'}\mathrm{d}\mathbf{r}' \,.\end{aligned} \tag{4.6}$$

Using the Gauß theorem, the first term on the right-hand side of Eq. (4.6) can be transformed into a surface integral carried out over the domain boundary $\partial\Omega_\mathbf{r}$. Moreover, taking advantage of the symmetry of the kernel function,

$$\frac{\partial W\left(\mathbf{r}-\mathbf{r}',h\right)}{\partial\mathbf{r}'} = -\frac{\partial W\left(\mathbf{r}-\mathbf{r}',h\right)}{\partial\mathbf{r}} \,, \tag{4.7}$$

Eq. (4.6) can be written as

$$\begin{aligned}\nabla\Phi\left(\mathbf{r}\right) &= \oint_{\partial\Omega_\mathbf{r}} \Phi\left(\mathbf{r}\right)W\left(\mathbf{r}-\mathbf{r}',h\right)\hat{\mathbf{n}}\left(\mathbf{r}'\right)\mathrm{d}s \\ &\quad + \int_{\Omega_{\mathbf{r}'}} \Phi\left(\mathbf{r}\right)\frac{\partial W\left(\mathbf{r}-\mathbf{r}',h\right)}{\partial\mathbf{r}}\mathrm{d}\mathbf{r}' \,,\end{aligned} \tag{4.8}$$

where $\hat{\mathbf{n}}$ is the unit normal vector to $\partial\Omega_\mathbf{r}$ at point $\mathbf{r}'$ oriented outwards from the surface s of the area of integration. The surface integral becomes zero if the domain of integration is located completely within the continuum represented by particles. Thus, the gradient of Φ at the position of particle a is given by

$$\nabla\Phi_a = \sum_b m_b \frac{\Phi_b}{\rho_b}\nabla W\left(\mathbf{r}_a-\mathbf{r}_b,h\right) \,, \tag{4.9}$$

which is written in the following by the shorthand notation

$$\nabla\Phi_a = \sum_b m_b \frac{\Phi_b}{\rho_b}\nabla W_{ab} \,. \tag{4.10}$$

This expression for $\nabla\Phi_a$ does not become zero for disordered particle distributions and constant Φ_b, which violates the normalization condition of the SPH kernel function. This is why Monaghan [128] proposed the identities

$$\rho\nabla\Phi = \nabla(\rho\Phi) - \Phi\nabla\rho \tag{4.11}$$

and

$$\frac{\nabla\Phi}{\rho} = \nabla\left(\frac{\Phi}{\rho}\right) + \frac{\Phi}{\rho^2}\nabla\rho \tag{4.12}$$

for higher accuracy. The corresponding SPH discretizations of Eqs. (4.11) and (4.12) are given by

$$\begin{aligned}\rho_a\nabla\Phi_a &= \sum_b \frac{m_b}{\rho_b}\rho_b\Phi_b\nabla W_{ab} - \Phi_a\sum_b \frac{m_b}{\rho_b}\rho_b\nabla W_{ab} \\ &= -\sum_b m_b\left(\Phi_a - \Phi_b\right)\nabla W_{ab}\end{aligned} \tag{4.13}$$

and

$$\begin{aligned}\frac{\nabla\Phi_a}{\rho_a} &= \sum_b \frac{m_b}{\rho_b}\frac{\Phi_b}{\rho_b}\nabla W_{ab} + \frac{\Phi_a}{\rho_a^2}\sum_b \frac{m_b}{\rho_b}\rho_b\nabla W_{ab} \\ &= \sum_b m_b\left(\frac{\Phi_a}{\rho_a^2} + \frac{\Phi_b}{\rho_b^2}\right)\nabla W_{ab}\end{aligned}, \tag{4.14}$$

which represent a non-conservative and a conservative form of the gradient approximation, respectively.

The second derivative of a scalar field can be expressed by two-time differentiation of the kernel function, analogous to the first derivative according to

$$\nabla\Phi_a^2 = \sum_b m_b\frac{\Phi_b}{\rho_b}\nabla^2 W_{ab}\,. \tag{4.15}$$

However, this form is known to be sensitive to particle disorder and does not conserve thermal energy in heat conduction problems with insulating walls [129]. Hence, the second order approximations [32, 40]

$$\nabla\cdot\left(\frac{\kappa_a}{\rho_a}\nabla\Phi_a\right) = \sum_b \frac{m_b}{\rho_a\rho_b}\left(\kappa_a + \kappa_b\right)\left(\Phi_a - \Phi_b\right)F_{ab}\,, \tag{4.16}$$

$$\nabla\cdot\left(\frac{\kappa_a}{\rho_a}\nabla\Phi_a\right) = \sum_b \frac{m_b}{\rho_a\rho_b}\left(\frac{4\kappa_a\kappa_b}{\kappa_a + \kappa_b}\right)\left(\Phi_a - \Phi_b\right)F_{ab}\,, \tag{4.17}$$

and

$$\nabla \cdot \left(\frac{1}{\rho_a} \nabla \Phi_a \right) = \sum_b \frac{m_b}{\rho_b} \frac{4}{\rho_a + \rho_b} \left(\Phi_a - \Phi_b \right) F_{ab} \tag{4.18}$$

are used in this work. Here, κ is a scalar constant and F_{ab} is defined as

$$F_{ab} = \frac{\mathbf{r}_{ab} \cdot \nabla W_{ab}}{r_{ab}^2 + 0.01h^2}, \qquad \mathbf{r}_{ab} = \mathbf{r}_a - \mathbf{r}_b, \tag{4.19}$$

where r_{ab} is given by

$$r_{ab} = |\mathbf{r}_a - \mathbf{r}_b| \tag{4.20}$$

and $0.01h^2$ is a small number to avoid division by zero if $r_{ab} \to 0$.

The smoothing kernel weights the contribution of neighboring particles to a property computed at the location of the central particle depending on their radial distance. Moreover, the kernel is responsible for the stability and accuracy of the SPH method and has to satisfy the following properties [116]:

1. Normalization: $\int_{\Omega_\mathbf{r}} W(\mathbf{r} - \mathbf{r}', h)\, \mathrm{d}\mathbf{r}' = 1$
2. Compact support: $W(\mathbf{r} - \mathbf{r}', h) = 0$ for $|\mathbf{r} - \mathbf{r}'| > r_{\max}$
3. Positivity: $W(\mathbf{r} - \mathbf{r}', h) \geq 0$
4. Delta function behavior: $\lim_{h \to 0} W(\mathbf{r} - \mathbf{r}', h) = \delta(\mathbf{r} - \mathbf{r}')$
5. Radial symmetry: $W(\mathbf{r} - \mathbf{r}', h) = W(\mathbf{r}' - \mathbf{r}, h)$

Moreover, the smoothing function has to monotonically decrease with increasing distance to the central particle and must be continuous, as shown in Fig. 4.2.

In this work, the Wendland C2 kernel, function [214]

$$W_{ab} = \begin{cases} \alpha_\mathrm{K} \left(1 - \frac{r_{ab}}{2h}\right)^4 \left(\frac{2r_{ab}}{h} + 1\right) & r_{ab} \leq 2h \\ 0 & r_{ab} > 2h \end{cases}, \tag{4.21}$$

with a maximum radius of support $r_{\max} = 2h$ is used due to its stabilizing properties against the pairing instability [51]. Here, $\alpha_\mathrm{K} \in \{\frac{3}{4h}, \frac{21}{16\pi h^3}\}$ is the

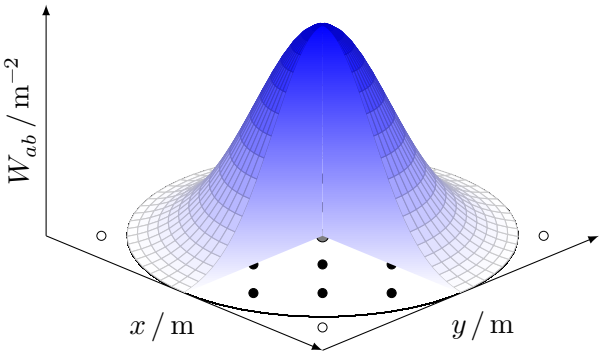

Figure 4.2: SPH kernel function in two dimensions. The kernel function takes a zero value for all SPH particles located outside of the support radius of the kernel function, $r_{ab} > r_{\max}$.

normalization constant for one or three dimensions, respectively. Moreover, the kernel gradient at position $\mathbf{r}_b$ is given by

$$\nabla W_{ab} = \frac{\mathbf{r}_a - \mathbf{r}_b}{r_{ab}} \frac{\alpha_{\mathrm{K}}}{h} \begin{cases} -5 \frac{r_{ab}}{h} \left(1 - \frac{r_{ab}}{2h}\right)^3 & r_{ab} \leq 2h \\ 0 & r_{ab} > 2h \end{cases} . \tag{4.22}$$

Figure 4.3 shows the Wendland kernel and its gradient in one dimension as a function of the x-coordinates of two particles a and b in Euclidean space.

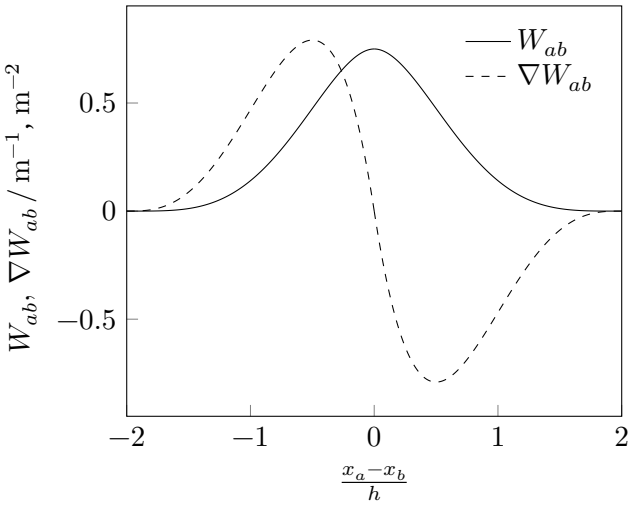

Figure 4.3: One-dimensional Wendland kernel and gradient of the Wendland kernel function for $h = 1\,\mathrm{m}$ depending on the relative position of the central, x_a, and neighboring SPH particle, x_b.

In this work, appropriate phenomenological models, such as the evaporation and recoil pressure models presented in Chapter 3, are used to describe the influence of the ambient gas on the liquid phase. For this reason, the gas phase is not explicitly represented by SPH particles to minimize the required computational time of the numerical model. This leads to the truncation of the smoothing kernel of a central particle located in the vicinity of the free surface due to an insufficient number of neighboring SPH particles. Figure 4.4 shows a schematic representation of the kernel truncation of SPH particles near a free boundary. The hatched area denotes the neighboring SPH particles' missing contribution to ensure the kernel function's normalization condition. Therefore, the normalization condition for the kernel function is not satisfied,

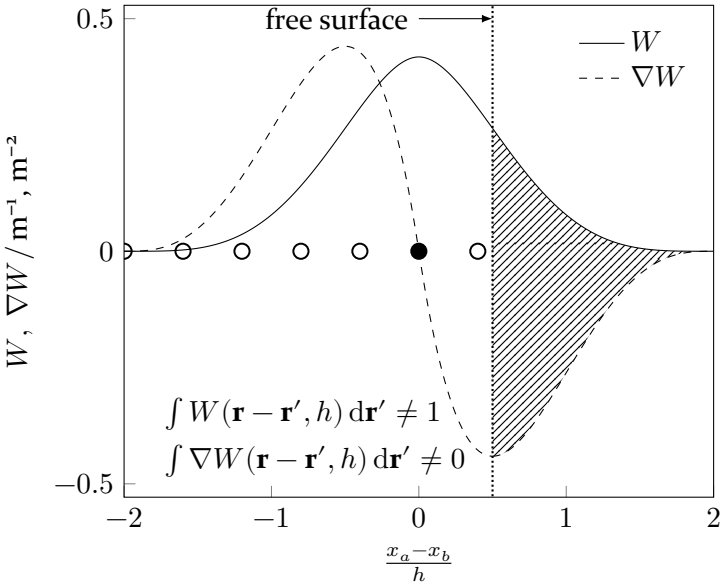

Figure 4.4: Schematic of the truncation of the SPH kernel integral in the vicinity of a domain boundary. The black circle denotes the central SPH particle, whereas the hollow circles denote neighboring SPH particles. The missing contribution of neighboring SPH particles to the kernel integral, shown by the hatched areas, leads to a violation of the kernel and kernel gradient normalization conditions.

and appropriate schemes to restore this property must be applied. To identify SPH particles in the vicinity of a free boundary, the Shepard filter [178], given by

$$S_a = \sum_b \frac{m_b}{\rho_b} W_{ab}, \tag{4.23}$$

is used in this work. For an SPH particle with constant mass and volume, $S_a \approx 1$ if the particle has full neighbor support, or $S_a < 1$ if an SPH particle

is located near the free surface. A threshold of $S_a \leq 0.95$ is used to identify all SPH particles that require a correction of the truncated smoothing kernel. To ensure the normalization condition of the kernel function, the Shepard filter can be applied to any quantity obtained by Eq. (4.5) according to

$$\Phi_a = \frac{1}{S_a} \sum_b \frac{m_b}{\rho_b} \Phi_b W_{ab} \,. \tag{4.24}$$

Similarly, the first derivative of a quantity can be normalized by scaling the kernel gradient using a correction matrix [25, 144] which ensures that the condition

$$\sum_b \frac{m_b}{\rho_b} (\mathbf{r}_b - \mathbf{r}_a) \otimes \nabla W_{ab} = \mathbf{I} \tag{4.25}$$

is met. Therefore, the corrected kernel gradient is given by

$$\hat{\nabla} W_{ab} = \mathbf{L} \nabla W_{ab} \,, \tag{4.26}$$

where the correction matrix, $\mathbf{L}$, is given by

$$\mathbf{L} = \left(\sum_b \frac{m_b}{\rho_b} (\mathbf{r}_b - \mathbf{r}_a) \otimes \nabla W_{ab} \right)^{-1} . \tag{4.27}$$

An alternative approach attempts to provide the truncated part of the kernel integral analytically. For example, the summation in Eq. (4.14) can be decomposed into independent summations over neighboring particles inside, b_i, and outside, $\mathrm{b_o}$, of the phase boundary ($\sum_b = \sum_{b_\mathrm{i}} + \sum_{b_\mathrm{o}}$) according to

$$\begin{aligned} \frac{\nabla \Phi_a}{\rho_a} = &- \sum_{b_i} m_b \left(\frac{\Phi_a}{\rho_a^2} + \frac{\Phi_b}{\rho_b^2} \right) \nabla W_{ab} \\ &- \sum_{b_\mathrm{o}} m_b \left(\frac{\Phi_a}{\rho_a^2} + \frac{\Phi_\mathrm{o}}{\rho_b^2} \right) \nabla W_{ab} \,, \end{aligned} \tag{4.28}$$

Here, Φ_o represents a scalar quantity which prevails in the ambiance near the free boundary. Since the contribution of the (absent) pseudo particles to

the left-hand side of Eq. (4.28) is unknown, Eq. (4.28) can be expressed using $\sum_{b_o} = \sum_b - \sum_{b_i}$ according to

$$\begin{aligned}\frac{\nabla\Phi_a}{\rho_a} = &-\sum_{b_i} m_b \left(\frac{\Phi_a}{\rho_a^2} + \frac{\Phi_b}{\rho_b^2}\right) \nabla W_{ab} \\ &-\sum_{b} m_b \left(\frac{\Phi_a}{\rho_a^2} + \frac{\Phi_o}{\rho_b^2}\right) \nabla W_{ab} \\ &+\sum_{b_i} m_b \left(\frac{\Phi_a}{\rho_a^2} + \frac{\Phi_o}{\rho_b^2}\right) \nabla W_{ab}\,.\end{aligned} \tag{4.29}$$

Since the gradient of any constant scalar field is zero, the second term on the right-hand side of Eq. (4.29) becomes zero and the gradient of Φ_a is given by

$$\frac{\nabla\Phi_a}{\rho_a} = \sum_{b_i} m_b \left(\frac{\Phi_o - \Phi_b}{\rho_b^2}\right) \nabla W_{ab} \tag{4.30}$$

for particles near the free boundary. Analogously, second order derivatives can be decomposed as shown in Eq. (4.28) and Eq. (4.29). For example, the summation of neighboring particles in Eq. (4.18) can be decomposed into [138],

$$\nabla \cdot \left(\frac{1}{\rho_a}\nabla\Phi_a\right) = \sum_b \frac{m_b}{\rho_b}\frac{4}{\rho_a + \rho_b}\Phi_a F_{ab} - \sum_b \frac{m_b}{\rho_b}\frac{4}{\rho_a + \rho_b}\Phi_b F_{ab}\,. \tag{4.31}$$

The second term on the right-hand side of Eq. (4.31) can be decomposed into summations over b_i and b_o which results in

$$\begin{aligned}\nabla \cdot \left(\frac{1}{\rho_a}\nabla\Phi_a\right) = &\sum_b \frac{m_b}{\rho_b}\frac{4}{\rho_a + \rho_b}\Phi_a F_{ab} - \sum_{b_i} \frac{m_b}{\rho_b}\frac{4}{\rho_a + \rho_b}\Phi_b F_{ab} \\ &- \sum_{b_o} \frac{m_b}{\rho_b}\frac{4}{\rho_a + \rho_b}\Phi_o F_{ab}\,.\end{aligned} \tag{4.32}$$

Finally, using $\sum_{b_o} = \sum_b - \sum_{b_i}$, Eq. (4.32) yields:

$$\begin{aligned}\nabla \cdot \left(\frac{1}{\rho_a}\nabla\Phi_a\right) = \quad & (\Phi_a - \Phi_o)\sum_b \frac{m_b}{\rho_b}\frac{4}{\rho_a+\rho_b}F_{ab} \\ & - \sum_{b_i} \frac{m_b}{\rho_b}\frac{4}{\rho_a+\rho_b}\Phi_b F_{ab} \\ & + \sum_{b_i} \frac{m_b}{\rho_b}\frac{4}{\rho_a+\rho_b}\Phi_o F_{ab}\,.\end{aligned} \tag{4.33}$$

4.2 SPH formulation of conservation laws

In the following, conservation of mass, momentum, and energy, assuming an incompressible material, is presented.

4.2.1 Conservation of momentum

The terms on the right-hand side of Eq. (2.63) can be discretized using the SPH integral interpolation introduced in Section 4.1. To simplify the handling and manipulation of the contributions to the momentum equation, Eq. (2.63) is written as

$$\frac{\mathrm{D}\mathbf{u}_a}{\mathrm{D}t} = \mathbf{f}_{\mathrm{p},a} + \mathbf{f}_{\eta,a} + \mathbf{f}_{g,a} + \mathbf{f}_{\mathrm{other},a}\,. \tag{4.34}$$

Here, the acceleration of a particle a with full kernel support caused by pressure forces, $\mathbf{f}_{\mathrm{p},a}$, viscous forces, $\mathbf{f}_{\eta,a}$, and body forces, $\mathbf{f}_{g,a}$, is denoted in the following using the subscripts p, η and g. Accelerations due to surface tension or other forces are represented by $\mathbf{f}_{\mathrm{other},a}$ and will be introduced in the relevant sections in the course of this work. The employed conservative pressure gradient approximation is obtained by using the derivation rule in Eq. (4.14) which yields:

$$\mathbf{f}^{\mathrm{b}}_{\mathrm{p},a} = -\left(\frac{\nabla p_a}{\rho_a}\right) = -\sum_b m_b \left(\frac{p_a}{\rho_a^2} + \frac{p_b}{\rho_b^2}\right)\nabla W_{ab}\,. \tag{4.35}$$

The expression in Eq. (4.35) is valid for full kernel support ($S_a > 0.95$). At free surfaces, where the insufficient number of neighboring particles leads to a violation of the normalization condition of the kernel function, Eq. (4.35) is written as

$$\mathbf{f}^{\mathrm{c}}_{\mathrm{p,a}} = -\sum_b m_b \left(\frac{p_b - p_o}{\rho_b^2}\right)\nabla W_{ab} \quad \text{if } S_a \leq 0.95 \tag{4.36}$$

which is obtained by using Eq. (4.30) and assuming an external pressure p_{o}. Thus, the acceleration due to pressure is given by

$$\mathbf{f}_{\mathrm{p},a} = \begin{cases} \mathbf{f}^{\mathrm{c}}_{\mathrm{p,a}} & \text{if } S_a \leq 0.95 \\ \mathbf{f}^{\mathrm{b}}_{\mathrm{p},a} & \text{else} \end{cases} . \tag{4.37}$$

The viscous force approximation for a Newtonian fluid is derived using the integral approximation for second order derivatives in Eq. (4.16) [134], leading to

$$\mathbf{f}_{\eta,a} = \nabla \cdot \left(\frac{\eta_a}{\rho_a} \nabla \mathbf{u}_a \right) = \sum_b m_b \frac{\eta_a + \eta_b}{\rho_a \rho_b} F_{ab} \mathbf{u}_{ab} \,, \tag{4.38}$$

where the velocity difference between particles a and b is given by

$$\mathbf{u}_{ab} = \mathbf{u}_a - \mathbf{u}_b \,. \tag{4.39}$$

The contribution of the gas phase to the viscous acceleration of particles near the free surface in Eq. (4.38) becomes zero if $\mathbf{u}_a = \mathbf{u}_b$. This represents a reasonable approximation since it assumes that the gas flow follows the liquid phase's motion. Nonetheless, some works employ a numerical density,

$$\rho_a = S_a \rho_0 \,, \tag{4.40}$$

where ρ_0 is the reference density, which dampens the motion of particles near a free surface [66]. The corresponding viscous force approximation utilizing the numerical density can be given for particles near the free boundary ($S_a \leq 0.95$) by

$$\mathbf{f}^{\mathrm{c}}_{\eta,a} = \nabla \cdot \left(\frac{\eta_a}{\rho_a} \nabla \mathbf{u}_a \right) = \sum_b m_b \frac{\eta_a + \eta_b}{S_a \rho_a S_b \rho_b} F_{ab} \mathbf{u}_{ab} \,. \tag{4.41}$$

Equation (4.41) is only applied in Section 6.1 in this work and is not required otherwise. The momentum balances relevant for a particular simulation problem are introduced in the respective sections.

4.2.2 Conservation of mass

Conservation of mass is enforced by employing the projection method presented in [45], which couples the pressure to the divergence of velocity to achieve strict incompressibility in the simulation domain. Using this approach, the numerical method is termed ISPH in the literature.

According to the Helmholz-Hodge decomposition, any vector field can be decomposed into a divergence-free and an irrotational part. Furthermore, the

irrotational part of the vector field can be represented by a scalar potential, which is given in the case of the incompressible Navier-Stokes equation by

$$\frac{\mathrm{D}\mathbf{u}_a}{\mathrm{D}t} = -\frac{1}{\rho_a}\nabla p_a \,. \tag{4.42}$$

Replacing the time derivative, $\mathrm{D}\mathbf{u}_a/\mathrm{D}t$, with a finite difference and taking the divergence of Eq. (4.42) yields a Poisson equation for pressure,

$$\nabla \cdot \frac{\mathbf{u}_a^{n+1} - \mathbf{u}^*}{\Delta t} = \nabla \cdot \left(-\frac{1}{\rho_a}\nabla p_a \right) \,, \tag{4.43}$$

where $\mathbf{u}^{n+1}$ is the velocity at time $n+1$ and $\mathbf{u}^*$ is an intermediate velocity field that can be obtained from

$$\frac{\mathbf{u}_a^* - \mathbf{u}^n}{\Delta t} = \frac{1}{\rho_a}\nabla \cdot (\eta_a \nabla \mathbf{u}_a) + \mathbf{f}_{\mathrm{other},\,a} \tag{4.44}$$

upon temporal integration.

Since the divergence of $\mathbf{u}^{n+1}$ shall be divergence-free, Eq. (4.43) leads to a Pressure Poisson Equation (PPE):

$$\nabla \cdot \left(\frac{\nabla p_a^*}{\rho_a} \right) = \frac{\nabla \cdot \mathbf{u}_a^*}{\Delta t} \,. \tag{4.45}$$

Applying the discretization rule given in Eq. (4.18) to the left-hand side of the PPE in Eq. (4.45) leads to

$$\nabla \cdot \left(\frac{\nabla p_a^*}{\rho_a} \right) = \sum_b \frac{m_b}{\rho_b} \frac{4}{\rho_a + \rho_b} \left(p_a^* - p_b^* \right) F_{ab} \,, \tag{4.46}$$

whereas the divergence of velocity on the right-hand side of Eq. (4.45) is given by

$$\frac{\nabla \cdot \mathbf{u}_a^*}{\Delta t} = \sum_b -\frac{m_b}{\rho_a} \frac{\mathbf{u}_{ab}^* \cdot \nabla W_{ab}}{\Delta t} \,, \qquad \mathbf{u}_{ab}^* = \mathbf{u}_a^* - \mathbf{u}_b^* \,, \tag{4.47}$$

using the discretization rule in Eq. (4.13). The corresponding SPH approximation of Eq. (4.45) is obtained by Eq. (4.46) and (4.47) according to

$$\sum_b \frac{m_b}{\rho_b} \frac{4}{\rho_a + \rho_b} \left(p_a^* - p_b^* \right) F_{ab} = \sum_b -\frac{m_b}{\rho_a} \frac{\mathbf{u}_{ab}^* \cdot \nabla W_{ab}}{\Delta t} \,, \tag{4.48}$$

which represents a linear system of equations that is solved using the Bi-Conjugate Gradient Stabilized (BiCGSTAB) [189] method in this work. The

divergence of velocity approximation on the right-hand side of Eq. (4.48) requires no further correction for free surfaces since $\mathbf{u}_a^* = \mathbf{u}_b^*$ is implicitly assumed for the contribution of the absent ambient particles.

To correct the Laplacian of pressure in Eq. (4.46) for SPH particles in the vicinity of a free boundary, the formulation in Eq. (4.33) is employed, which results in

$$\begin{aligned}(p_a^* - p_\mathrm{o}) \underbrace{\sum_b \frac{m_b}{\rho_b} \frac{4}{\rho_a + \rho_b} F_{ab}}_{\beta} - \sum_b \frac{m_b}{\rho_b} \frac{4p_b^*}{\rho_a + \rho_b} F_{ab} \\ = \sum_b \frac{m_b}{\rho_b} \left(-\frac{\mathbf{u}_{ab}^* \cdot \nabla W_{ab}}{\Delta t} - \frac{4p_\mathrm{o}}{\rho_a + \rho_b} F_{ab} \right) .\end{aligned} \tag{4.49}$$

Here, β remains constant throughout the simulation for a density invariant material.

4.2.3 Conservation of energy

In this work, the energy balance of the considered incompressible material is composed of various contributions introduced in Eqs. (2.53), (2.49), (2.54) and (2.55), which correspond to heat conduction, including the effect of latent heat (crystallization, melting, and solidification), absorption of laser irradiation, heat loss due to thermal radiation, as well as heat loss due to evaporation. Equation (2.53) is discretized using the approximation rule given in Eq. (4.17), leading to

$$\rho_a c_{p,a} \frac{\mathrm{D}T_a}{\mathrm{D}t} = \sum_b \frac{m_b}{\rho_b} \frac{4k_a k_b}{k_a + k_b} (T_a - T_b) F_{ab} \,. \tag{4.50}$$

The remaining contributions to the energy equation (laser source term, heat loss due to radiation and evaporation) are transformed into volumetric terms using the discretization length Δx which yields

$$\rho_a \tilde{c}_{p,a} \frac{\mathrm{D}T_a}{\mathrm{D}t} = \sum_b \frac{m_b}{\rho_b} \frac{4k_a k_b}{k_a + k_b} (T_a - T_b) F_{ab} + \frac{\dot{q}_{\mathrm{l},a} + \dot{q}_{\mathrm{r},a} + \dot{q}_{\mathrm{vap},a}}{\Delta x} \,, \tag{4.51}$$

where the term $\left(\dot{q}_{\mathrm{l},a} + \dot{q}_{\mathrm{r},a}\right)/\Delta x$ is applied to a single layer of interfacial particles, and $\dot{q}_{\mathrm{vap},a}/\Delta x$ is applied to all SPH particles exceeding boiling temperature. In the case of the laser source term, it is assumed that an interfacial layer of SPH particles absorbs all the laser energy. This assumption is justified if $\Delta x > \delta_\mathrm{p}$, which generally holds for the discretization lengths used in this work, a laser wavelength of $\lambda = 1.08\,\mu\mathrm{m}$, and the temperature-

dependent extinction coefficients of clean or aged titanium surfaces presented in Section 3.6.

The interfacial SPH particles are identified by the surface meshing algorithm, which is required by the ray-tracing algorithm and which will be introduced in Chapter 5. In particular, particles that represent a vertex of a surface triangle are identified as interface particles. The latent heat of crystallization, melting and solidification is included into Eq. (4.51) by substituting the heat capacity with an effective heat capacity, $\tilde{c}_{p,a}$ [60]. In this work, the effective heat capacity is defined as

$$\tilde{c}_{\mathrm{p},a} = \begin{cases} c_p^{\alpha} & T < T_{\mathrm{cryst}} - \Delta T \\ c_p^{\alpha} + \tilde{h}_{\mathrm{cryst}} & T_{\mathrm{cryst}} - \Delta T \leq T \leq T_{\mathrm{cryst}} \\ c_p^{\beta} + \tilde{h}_{\mathrm{cryst}} & T_{\mathrm{cryst}} < T \leq T_{\mathrm{cryst}} + \Delta T \\ c_p^{\beta} & T_{\mathrm{cryst}} + \Delta T < T \\ c_p^{\beta} + \tilde{h}_{\mathrm{m}} & T_{\mathrm{m}} - \Delta T \leq T \leq T_{\mathrm{m}} \\ c_p^{\mathrm{l}} + \tilde{h}_{\mathrm{m}} & T_{\mathrm{m}} < T \leq T_{\mathrm{m}} + \Delta T \\ c_p^{\mathrm{l}} & T > T_{\mathrm{m}} + \Delta T \end{cases}, \tag{4.52}$$

where c_p^{α} and c_p^{β} denote the heat capacity of a solid with α- or β-crystallization, and c_p^{l} represents the heat capacity of the liquid. Moreover, T_{cryst} and T_{m} are the phase transition temperatures at which the crystal structure changes or the material transits from the solid to liquid phase. Moreover, $\tilde{h}_{\mathrm{cryst}}$ and $\tilde{h}_{\mathrm{m}}$ represent the smoothed latent heat which is gradually released within a narrow temperature range of $2\Delta T$ centered at the transition temperatures, T_{cryst} and T_{m}, according to

$$\begin{cases} \tilde{h}_{\mathrm{cryst}} & \text{if} \quad T_{\mathrm{cryst}} - \Delta T \leq T_{\mathrm{cryst}} \leq T_{\mathrm{cryst}} + \Delta T \\ \tilde{h}_{\mathrm{m}} & \text{if} \quad T_{\mathrm{m}} - \Delta T \leq T_{\mathrm{m}} \leq T_{\mathrm{m}} + \Delta T \end{cases}. \tag{4.53}$$

Here, the latent heat of crystallization and melting of a particle a undergoing a phase transition is given by [60]

$$\tilde{h}_{\mathrm{cryst},a} = \sum_b \frac{m_b}{\rho_b} h_{\mathrm{cryst}} W_T\left(|T_b - T_{\mathrm{cryst}}|, h_T\right) \frac{W_{ab}}{S_a} \tag{4.54}$$

and

$$\tilde{h}_{\mathrm{m},a} = \sum_b \frac{m_b}{\rho_b} h_{\mathrm{m}} W_T\left(|T_b - T_{\mathrm{m}}|, h_T\right) \frac{W_{ab}}{S_a}, \tag{4.55}$$

where W_T and h_T is the one-dimensional Wendland C2 kernel and the corresponding smoothing length, defined in the temperature domain. The Shepard filter, S_a, is applied to Eqs. (4.54) and (4.55) to correct the truncation of the kernel integral of SPH particles located in the vicinity of free boundaries. The one-dimensional Wendland C2 kernel defined in the temperature domain is given by

$$W_T = \begin{cases} \frac{3}{4h_T}\left(1-\frac{q_T}{2h_T}\right)^4\left(\frac{2q_T}{h_T}+1\right) & q_T \leq 2h_T \\ 0 & q_T > 2h_T \end{cases}, \tag{4.56}$$

where, $q_T = |T_b - T_{\mathrm{cryst}}|$ or $q_T = |T_b - T_{\mathrm{m}}|$ depending on the temperature of the SPH particle, respectively. Half of the temperature range of the mushy region is given by

$$\Delta T = 2h_T\,, \tag{4.57}$$

where h_T is the smoothing length of the one-dimensional Wendland C2 kernel which can be chosen freely but should be as small as possible when modeling pure metals with sharp phase transition temperatures [60]. Figure 4.5 shows a schematic of the effective heat capacity, which includes the latent heat. To

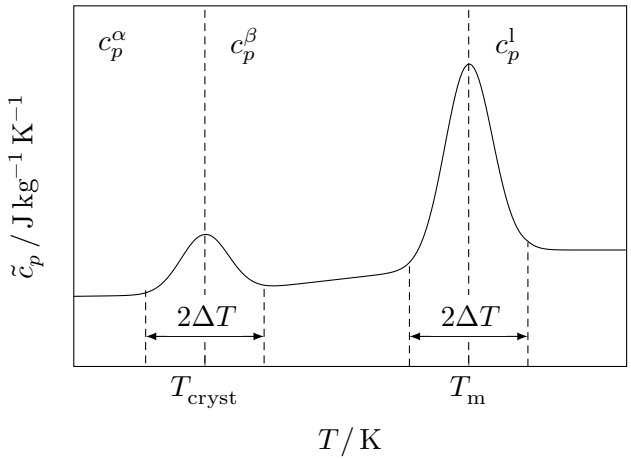

Figure 4.5: Schematic of the smoothed effective heat capacity as a function of temperature. The latent heat is distributed within a narrow temperature region of $2\Delta T$ centered at the phase transition temperature.

approximate the latent heat with sufficient accuracy, the time step must be chosen so that the temperature change per time step is smaller than $2\Delta T$. The approach used in the current work to overcome the imposed restriction of the numerical timestep size will be presented in Chapter 7.

4.3 Integration scheme

In this work, the predictor-corrector time integration scheme presented in [45] is employed to advance particles in space. Therefore, the SPH particles are translated with their current velocity, $\mathbf{u}^n$, at time n by

$$\mathbf{r}_a^* = \mathbf{r}_a^n + \mathbf{u}_a^n \Delta t \,, \tag{4.58}$$

where $\mathbf{r}_a^*$ is an intermediate position of particle a. At these new particle positions, the intermediate velocity $\mathbf{u}_a^*$ of an SPH particle a is computed from all contributing forces, except for the pressure forces, by

$$\mathbf{u}_a^* = \mathbf{u}_a^n + \left(\frac{1}{\rho_a} \nabla \cdot (\eta_a \nabla \mathbf{u}_a^n) + \mathbf{f}_{\text{other},a} \right) \Delta t \,. \tag{4.59}$$

At these particle positions, the PPE in Eq. (4.48), Eq. (4.49) or Eq. (4.68) is solved. Subsequently, the gradient of the resultant pressure field is computed by Eq. (4.35) or Eq. (4.36), respectively, and subtracted from the current velocity field according to

$$\mathbf{u}_a^{n+1} = \mathbf{u}_a^* - \frac{1}{\rho_a} \nabla p_a^* \Delta t \,. \tag{4.60}$$

The obtained velocity field is finally used to predict the particle positions, $\mathbf{r}^{n+1}$, at time $n+1$ by

$$\mathbf{r}_a^{n+1} = \mathbf{r}_a^n + \left(\frac{\mathbf{u}_a^n + \mathbf{u}_a^{n+1}}{2} \right) \Delta t \,. \tag{4.61}$$

Moreover, the temperatures of the SPH particles are obtained using the explicit or implicit Euler integration scheme applied to Eq. (4.51). The explicit Euler integration scheme is given by

$$T_a^{n+1} = T_a^n + \left(\frac{\mathrm{D}T_a}{\mathrm{D}t} \right)^n \Delta t \,, \tag{4.62}$$

whereas the implicit Euler integration scheme reads

$$T_a^{n+1} = T_a^n + \left(\frac{\mathrm{D}T_a}{\mathrm{D}t} \right)^{n+1} \Delta t \,. \tag{4.63}$$

Here, T_a^{n+1} is the temperature of a particle a at time $n+1$ and T_a^n is the temperature at time n. Applying these integration schemes to Eq. (4.51) yields

$$T_a^{n+1} = T_a^n + \frac{\Delta t}{\rho_a \tilde{c}_{p,a}} \Bigg(\sum_b \frac{m_b}{\rho_b} \frac{4k_a k_b}{k_a + k_b} (T_a^n - T_b^n) F_{ab} + \frac{\dot{q}_{\mathrm{l},a} + \dot{q}_{\mathrm{r},a} + \dot{q}_{\mathrm{vap},a}}{\Delta x} \Bigg) \tag{4.64}$$

and

$$\begin{aligned} T_a^{n+1} - \Delta t \sum_b \frac{m_b}{\rho_b} \frac{4k_a k_b}{k_a + k_b} (T_a^{n+1} - T_b^{n+1}) F_{ab} \\ = T_a^n + \frac{\Delta t}{\rho_a \tilde{c}_{p,a}} \left(\frac{\dot{q}_{\mathrm{l},a} + \dot{q}_{\mathrm{r},a} + \dot{q}_{\mathrm{vap},a}}{\Delta x} \right) , \end{aligned} \tag{4.65}$$

respectively. Whether Eq. (4.64) or Eq. (4.65) is used to compute the temperature of particle a at time $n+1$, will be mentioned in the corresponding chapters. Note that $\dot{q}_{\mathrm{r},a}$ will be substituted with $\dot{q}_{\mathrm{r,ray},a}$ in Chapter 5 to emphasize the usage of the developed ray-tracing algorithm and which is used in all investigated problems involving a laser beam in this work.

The numerical time step, Δt, has to satisfy the Courant-Friedrichs-Levy (CFL) condition in order to maintain a stable simulation [110]. As a result, the chosen numerical time step depends on the CFL conditions for acceleration [128], velocity [45], viscosity [134], surface tension [133], and thermal diffusion [131], according to

$$\Delta t = 0.25 \cdot \min \left(\sqrt{\frac{h}{|\mathbf{a}_a|}}, \frac{h}{|\mathbf{u}_a|}, \frac{h^2 \rho_a}{2\eta_a}, \sqrt{\frac{h^3 \rho_a}{2\pi\sigma_a}}, \frac{\rho_a \tilde{c}_{p,a} \Delta x^2}{k_a} \right) . \tag{4.66}$$

Note that the time step restriction due to thermal diffusion is omitted when using the implicit integration scheme in Eq. (4.65).

4.4 Solid wall boundary

A solid wall represents an impermeable boundary for which the condition [208]

$$\mathbf{u}\left(\mathbf{r} = \mathbf{r}_{\mathrm{wall}}\right) = \mathbf{u}_{\mathrm{wall}}\left(\mathbf{r}_{\mathrm{wall}}\right) \tag{4.67}$$

must be satisfied. Here, $\mathbf{r}_{\mathrm{wall}}$ is the position and $\mathbf{u}_{\mathrm{wall}}$ the velocity of the solid wall. Satisfying this condition is necessary to obtain accurate and robust simulations in problems that involve solid boundaries. Various methods have

been proposed to model solid boundaries in SPH, ranging from the usage of repulsive forces [130] or dummy particles [44], employing mirror boundary [134] or immersed boundary methods [142], or utilizing semi-analytical approaches [108]. This section presents a simple and reliable wall boundary model which employs dummy particles in ISPH. The Poisson equation for pressure that must be solved in the ISPH method is modified so that the pressure of a wall SPH particle is computed by considering only liquid SPH particle neighbors in the linear system of equations. Furthermore, the modeling approach of the no-slip boundary condition is shown in the subsequent section.

4.4.1 SPH formulation

To prevent the penetration of liquid SPH particles into a solid wall, the PPE in Eq. (4.48) is modified for SPH wall particles ($a \in \Omega^{\mathrm{w}}$) according to

$$\sum_{b\in\Omega^{\mathrm{l}}} \frac{m_b}{\rho_b} \frac{4}{\rho_a + \rho_b} \left(p_a - p_b\right) F_{ab} = \sum_{b\in\Omega^{\mathrm{l}}} -\frac{m_b}{\rho_b} \frac{\mathbf{u}_{ab} \cdot \nabla W_{ab}}{\Delta t} \,. \tag{4.68}$$

Here, the summation index on the left- and right-hand side runs only over neighboring liquid SPH particles ($b \in \Omega^{\mathrm{l}} \subseteq \Omega$). The particle species (solid or liquid) is defined and assigned to the SPH particles in the beginning of the simulation. Wall particles are a subset of solid particles ($\Omega^{\mathrm{w}} \subseteq \Omega^{\mathrm{s}} \subseteq \Omega$) and are identified by the particle species (solid phase) as well as the criterion $S_a^{\mathrm{l}} > 0$. Here, S_a^{l} is the Shepard filter computed exclusively from liquid SPH particles by

$$S_a^{\mathrm{l}} = \sum_{b\in\Omega^{\mathrm{l}}} \frac{m_b}{\rho_b} W_{ab} \,. \tag{4.69}$$

The condition $S_a^{\mathrm{l}} > 0$ is used to identify solid particles which have at least one liquid SPH particle in their neighborhood. Nevertheless, in this work, a solid SPH particle is identified as a wall particle if $S_a^{\mathrm{l}} > 10^{-3}$ to exclude potential wall particles with a minor contribution to the computed pressure field and to ensure a fast convergence of the BiCGSTAB method [189].

Note that Eq. (4.68) does not impose a Dirichlet boundary condition to SPH wall particles as done by (4.49) for the contribution of missing neighboring SPH particles. Instead, the truncation of the kernel integral is modeled with a Neumann boundary condition which is automatically applied [45].

To ensure the no-slip boundary condition at walls, the proposed approach by [4] is employed. In a first step, the smoothed velocity field of the liquid phase is projected to the position of SPH wall particles with $S_a^{\mathrm{l}} > 10^{-3}$ by

$$\tilde{\mathbf{u}}_{\mathrm{l},a}^{\mathrm{w}} = \frac{1}{S_a^{\mathrm{l}}} \sum_{b \in \Omega^{\mathrm{l}}} \frac{m_b}{\rho_b} \mathbf{u}_b W_{ab} \,. \tag{4.70}$$

Now, the velocity of an SPH wall particle is given by

$$\tilde{\mathbf{u}}_a^{\mathrm{w}} = 2\mathbf{u}_a - \tilde{\mathbf{u}}_{\mathrm{l},a}^{\mathrm{w}} \,, \tag{4.71}$$

and can be used in Eq. (4.38) to ensure the no-slip boundary condition.

4.4.2 Poiseuille flow

To verify if the employed approaches in Eqs. (4.68) and (4.71) satisfy Eq. (4.67), the plane Poiseuille flow between two stationary, infinite planes, located at $x = \pm L$ in Euclidean space, is simulated and validated against the time-dependent analytical solution given by [134]

$$\begin{aligned} u_y(x,t) = \frac{g_y}{2\nu} x\,(x-L) + \sum_{n=0}^{\infty} \frac{4 g_y L^2}{\nu \pi^3 \left(2n+1\right)^3} \\ \sin\left(\frac{\pi x}{L}\left(2n+1\right)\right) \exp\left(-\frac{\left(2n+1\right)^2 \pi^2 \nu}{L^2} t\right) \end{aligned} \,. \tag{4.72}$$

Here, ν is the kinematic viscosity given by

$$\nu = \frac{\eta}{\rho} \,. \tag{4.73}$$

For this simulation scenario, periodic boundary conditions are applied in the y- and z-directions. Thus, the liquid phase is not exposed to a free boundary. The momentum balance of the liquid phase is given by Eq. (4.34) and the PPE that is solved for the pressure of liquid SPH particles is given by Eq. (4.48). The PPE of the solid SPH particles is given by Eq. (4.68) if $S_a^{\mathrm{l}} > 0.001$, by Eq. (4.49) if $S_a \leq 0.95$, and by Eq. (4.48) otherwise. Employing Eq. (4.49) and applying an ambient pressure of $p_{\mathrm{o}} = 0\,\mathrm{Pa}$ is required to obtain a solvable PPE. Furthermore, the solid SPH particles are fixed in space and their velocities are not updated. The kinematic viscosity and the density of all SPH particles is $\nu = 0.01\,\mathrm{m^2\,s^{-1}}$ and $\rho = 1\,\mathrm{kg\,m^{-3}}$, respectively. Moreover, liquid SPH particles are accelerated in the y-direction by a body force $\mathbf{f}_{g,a} = \left[0,\ g_y,\ 0\right]$ with $g_y = 0.1\,\mathrm{m\,s^{-2}}$. According to Eq. (4.72) this leads to a maximum velocity in

the y-direction of $u_y(x/L = 0) = u_{y,\max} = 1.25\,\mathrm{m\,s^{-1}}$ for the given parameters in equilibrium. The corresponding Reynolds number characterizing the flow is $\mathfrak{R} = 2Lu_{y,\max}/\nu = 125$. The SPH particles representing the liquid phase are initially placed on a rectangular lattice within $\mathbf{x} \in (-L,\, L)^3$ in all spatial directions with $L = 0.5\,\mathrm{m}$. In addition, the wall at $x = \pm L$ is approximated by SPH wall particles that are placed at $L \leq x \leq L + 2r_{\max}$ as well as $L - 2r_{\max} \leq x \leq L$. The thickness of the walls is twice the Wendland kernel radius ($r_{\max} = 2h$) to apply the zero pressure Dirichlet boundary condition to solid SPH particles that satisfy $S_a^1 \leq 10^{-3}$ and $S_a < 0.95$ via Eq. (4.49). Furthermore, the smoothing length of the kernel function is adjusted to $h = 2\Delta x$. The liquid phase is discretized with $L/\Delta x \in \{10, 20, 40\}$ in each dimension which leads to {8 000, 64 000, 512 000} liquid SPH particles being simulated.

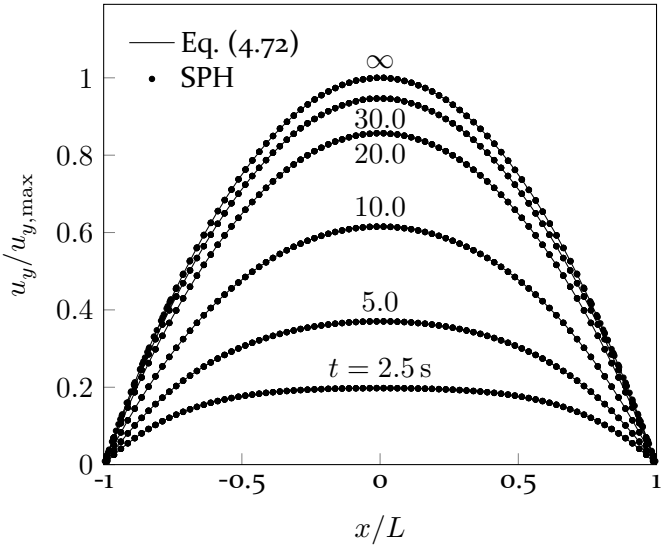

Figure 4.6: Transient velocity fields of an accelerated liquid between two infinite plates. The fluid flows in the y-direction in Euclidean space, and its velocity is measured within the range $-\Delta x \leq y \leq \Delta x$ and $-\Delta x \leq z \leq \Delta x$ is computed as a function of the x-position of the SPH particles.

Figure 4.6 shows a comparison of the transient velocity fields obtained by Eq. (4.72) and SPH simulation using $L/\Delta x = 40$ SPH particles in each dimension at different times. The relative error of the SPH particles' velocities to the corresponding analytical values is computed for SPH particles located within $-\Delta x \leq y \leq \Delta x$ and $-\Delta x \leq z \leq \Delta x$ as a function of their x-position. The mean relative error is $1.6\,\%$ at $t = 100\,\mathrm{s}$ for $L/\Delta x = 40$. Moreover, utilizing a

spatial discretization of $L/\Delta x = 10$ leads to a mean relative error between simulated and analytical velocity of $3.8\,\%$ at $t = 100\,\mathrm{s}$.

4.5 Concluding remarks

In this chapter, the fundamentals of the employed ISPH method have been presented. In addition, an implicit pressure boundary condition that ensures the impermeability of solid walls for liquid SPH particles has been presented. The reliability and accuracy of the impermeability and no-slip boundary condition in SPH has been investigated in a plane Poiseuille flow problem. Here, the mean relative error between the equilibrium velocity field obtained by SPH simulations to the corresponding analytical velocity varies between $3.8\,\%$ and $1.6\,\%$ for the lowest and highest simulated spatial resolution, respectively.

5 Modeling laser-metal interaction

The accurate modeling of the transfer of energy of electromagnetic waves into a material with complex geometry, such as metal powder or the keyhole in welding processes, is very challenging. Depending on the wavelength of the laser light, only a small fraction of the incident energy may be transmitted into a metal, which is why subsequent reflections must be considered to describe the energy transfer accurately.

There are two approaches for modeling laser-material interaction. Electromagnetic field simulations attempt to solve Maxwell's equations and have been used to study the interaction of laser-metal interaction in mesh-based simulation methods [6, 43]. Nevertheless, the requirement that the spatial discretization must be smaller than the wavelength of the laser restricts this approach to two-dimensional simulations [6, 43]. In this work, the spatial discretization length, Δx, would have to be smaller than $1.08\,\mu\mathrm{m}$, resulting in extreme spatial resolution, which is neither required in the simulations performed in this work nor computational economical.

The second method discretizes the laser into discrete energy portions, which can be motivated by Maxwell's equation as shown in [237] and is called ray tracing. In ray tracing, the plane wavefront is represented by many discrete rays that contain certain energy portions. The Fresnel equations dictate the trajectories of these rays and the absorption and reflection of energy at the material surface. This method is frequently used, for instance, to model laser welding or SLM processes in mesh-based simulation methods [36, 48, 107, 226] but is less pronounced in particle-based simulation methods [81, 82, 177] due to its computational cost. Figure 5.1 shows a schematic of a ray tracing approach. Each ray carries a discrete amount of energy, which is a fraction of the total energy provided by a laser beam. This work employs a Gaussian intensity distribution, I, as illustrated in Fig. 5.1. In this chapter, the ray tracing algorithm implemented into the utilized SPH software is presented. Moreover, the ray tracing approach is validated against derived analytical expressions of the forced heat equation in a bounded domain using the concept of Green's functions and the method of images. The influence of smoothing length, spatial resolution, and ray density on the simulated temperature fields is investigated and compared to theory. After that, the effective absorbtance of laser irradiation by a deposited monodisperse and polydisperse titanium powder bed is investigated depending on the powder bed temperature. Finally, the absorbed laser power by the monodisperse and the polydisperse powder is

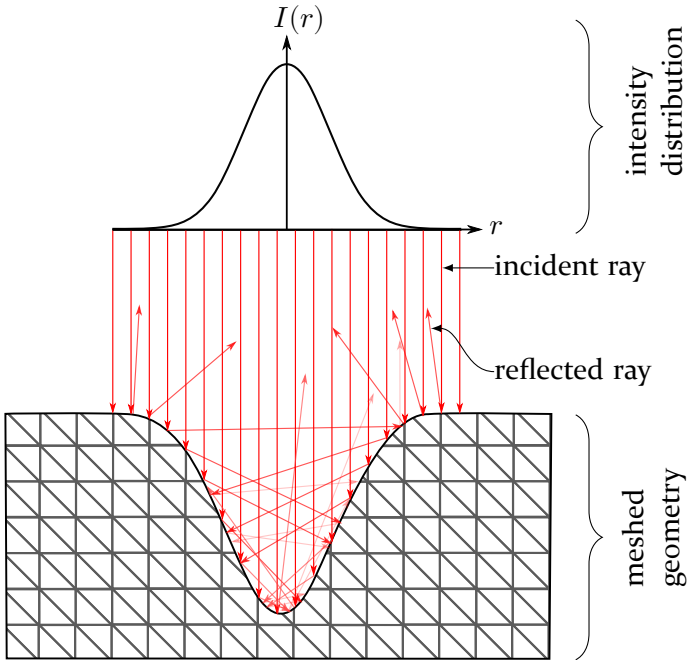

Figure 5.1: Schematic of the ray tracing method. The laser is discretized into energy portions, "rays". Each ray carries a fraction of the total laser power as a function of its radial distance to the beam axis. Multiple successive reflections of the rays at the surface of the meshed geometry lead to a high amount of energy being transferred into the material.

measured as a function of the propagation depth of the rays into the powder and the powder temperature.

5.1 Ray tracing algorithm

The developed ray tracing algorithm can be subdivided into the following parts:

- surface mesh generation
- ray initialization
- reduction of intersection candidates
- ray-triangle intersection
- compute power reflectance

According to the Fresnel equations, the absorption of light depends on the incident angle of the laser beam on the material surface. To calculate this angle efficiently, the material surface is represented by a polygon mesh composed of triangles. The SPH particles serve as nodal points on which a Delaunay triangulation is applied using the Computational Geometry Algorithms Library (CGAL) [197] which leads to a tetrahedralized volume mesh in a first step. Subsequently, the volume mesh is reduced to a surface mesh by applying an alpha shape algorithm.

The SPH particles are classified into different subsets to obtain distinct surface meshes for each set of particles. For example, every titanium particle is represented by several SPH particles which have the same index. Particles that belong to the liquid phase represent another set of particles with a unique identification number, which may change upon phase transition. For instance, a particle that changes from a solid to a liquid phase is subsequently assigned to the subset of liquid particles. Conversely, a solidifying SPH particle obtains the identification number of the closest solid SPH particle in the immediate neighborhood with a distance $< \Delta x$. Alternatively, if there are no particles in the neighborhood to which a solidifying particle can be assigned, it receives a new, unique identification number.

Figure 5.2 shows the result of the meshing procedure on different sets of SPH particles. The left image shows the initial SPH particle configuration on a rectangular lattice. In contrast, the right image shows the corresponding surface meshes computed by including all SPH particles with the same identification number. As a result, each titanium particle is represented by a distinct surface mesh. The SPH particles, which constitute a triangle of the computed surface mesh, represent the subset of interfacial particles, $\Omega^{\mathrm{v}} \subseteq \Omega$.

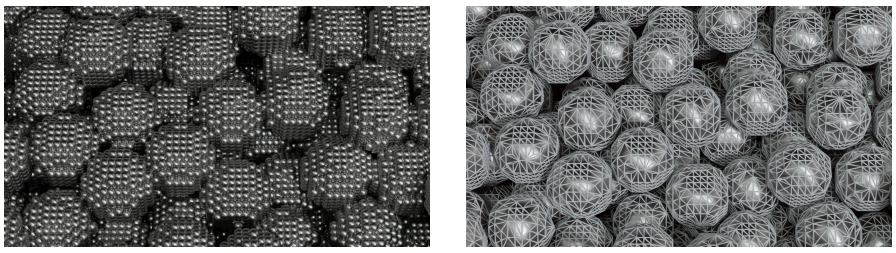

(a) SPH particle representation of deposited metal powder.

(b) Surface mesh representation of deposited metal powder.

Figure 5.2: Simultaneous representation of SPH particles and surface meshes computed using the CGAL library [197]. The surface mesh is required to efficiently compute line-triangle intersections to model the laser-metal interaction.

In each numerical timestep, the laser beam is discretized into a finite number of rays and their intersections with the previously computed surface meshes are calculated. For this purpose, each ray carries its own properties, such as origin, propagation direction, current amount of energy, and the orientation of the electric field.

This work assumes a non-divergent Gaussian laser beam with a transverse electromagnetic mode and random polarization. This means that the electric and magnetic fields, as well as the propagation direction of the laser beam, are oriented perpendicular to each other. The laser beam is oriented towards the material surface in a negative z-direction in Euclidean space. The electric field vectors of the rays are initially oriented randomly in the x-y-plane. Consequently, the initial ray positions and electric field orientation can be determined by drawing uniformly distributed numbers according to

$$\begin{pmatrix} r_{\mathrm{ray}} \\ \theta_{\mathrm{ray}} \\ \theta_E \end{pmatrix} = \begin{pmatrix} r_{\mathrm{ray},0}\sqrt{u_{128}} \\ 2\pi u_{128} \\ 2\pi u_{128} \end{pmatrix} . \tag{5.1}$$

Here, $u_{128} \in [0,\ 1]$ denotes a uniformly distributed random number obtained using the "xorshift128" algorithm [120, 207], r_{ray} is the radial distance of a ray to the center axis of the beam, and $r_{\mathrm{ray},0}$ is the radial distance up to which rays are initialized. Moreover, θ_{ray} and θ_{E} denote the polar angle within the unit circle used to initialize the orientation of the ray as well as its electric field. Finally, the ray positions are translated in positive z-direction so that the origin of the rays is located above the surface of the material. Furthermore, assuming a non-divergent laser beam ($w(z) = w_0$), the individual intensity of each ray is computed as a function of its radial distance to the beam center, r_{ray}, by

$$I_{\mathrm{ray}} = \dot{q}_{\mathrm{l}} = \frac{2P_0}{\pi w_0^2} \exp\left(\frac{-2r_{\mathrm{ray}}^2}{w_0^2}\right) . \tag{5.2}$$

Here, P_0 is the total power of the laser, and w_0 is the waist radius of the laser beam, which includes 86.5 % of the total laser energy. The total laser power is given by the sum of the individual power carried by each ray according to

$$\dot{q}_{\mathrm{l,ray}} = \sum_{i=0}^{N_{\mathrm{ray}}} \frac{2P_0}{\pi w_0^2} \exp\left(-\frac{2r_{\mathrm{ray},i}^2}{w_0^2}\right) , \tag{5.3}$$

where N_{ray} is the total number of initialized rays.

Accordingly, the power carried by a single ray is given by

$$P_{\mathrm{ray}} = I_{\mathrm{ray}} A_{\mathrm{ray}} \,, \tag{5.4}$$

where $A_{\mathrm{ray},i}$ is the area of a ray given by

$$A_{\mathrm{ray}} = \frac{\pi r_{\mathrm{ray},0}^2}{N_{\mathrm{ray}}} \,. \tag{5.5}$$

The ray area depends on the total number of initialized rays, N_{ray}, and is identical for all initialized rays. Due to the usage of random numbers to initialize the rays, the total energy of the rays is normalized to satisfy the condition

$$\sum_{i=0}^{N_{\mathrm{ray}}} I_{\mathrm{ray},i} A_{\mathrm{ray}} = \frac{4P_0}{w_0^2} \int_{r=0}^{r_0} \exp\left(-\frac{2r^2}{w_0^2}\right) r \mathrm{d}r \,. \tag{5.6}$$

To reduce the computational cost of the ray tracing procedure, the domain is partitioned using a grid. All cells have identical dimensions, and the maximum triangle edge length determines their box length in the simulated domain. The maximum edge length of the triangles may vary for disordered particle configurations (e.g., due to the liquid flow) in the order of a few Δx and depending on the employed alpha-radius that is used as an input parameter to the alpha shape algorithm. For this reason, the grid is updated in each meshing procedure to ensure that no triangle edge exceeds the cell length. The cells are used, on the one hand, to find for each ray the traversed cells in chronological order; on the other hand, to sort the triangle vertices (SPH particles) into these cells. Therefore, the algorithm's complexity is reduced since only triangles located in cells that are traversed by a ray are considered as intersection candidates. Upon melting in laser metal processing, the geometry of the meshed surface changes. For this reason, only those bodies that have changed their geometry are remeshed, whereas the unchanged surface meshes are kept for the ray tracing computation in the next time step. For this purpose, the cell traversal algorithm presented in [8] is used to identify the traversed cells in chronological order, illustrated by the gray-filled boxes in Fig. 5.3. In addition, vertices and the corresponding triangles located in the adjacent cells in each spatial dimension are also checked for line-triangle intersections to avoid ray-triangle misses. For instance, such a missed ray-triangle intersection could be caused by a triangle whose vertices are located in different adjacent cells but not in the cell where the area segment of the intersected triangle is located. To compute the intersections of the rays with the triangulated surface mesh, the Möller-Trumbore algorithm [127] is employed. In the case

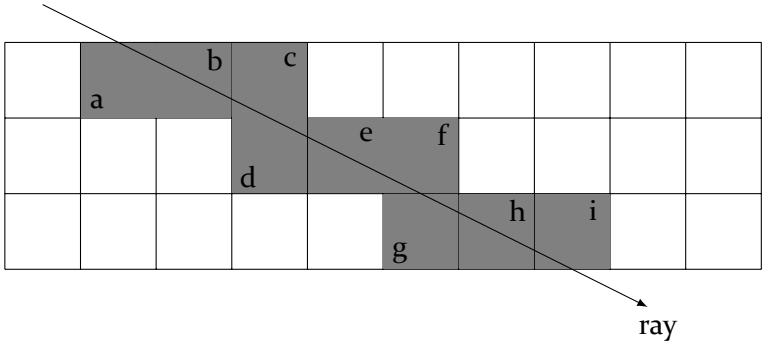

Figure 5.3: Schematic of the employed ray-cell traversal algorithm by [8] in two dimensions. The cells are traversed in chronological order.

of multiple possible intersections of a ray with triangles located in the same cell, the position of the ray-triangle intersection with the smallest distance to the ray origin is chosen. Once the minimum distance of a ray-triangle intersection is identified, the reflected direction of the reflected ray as well as the reflected power must be computed. The fraction of the transmitted and reflected energy depends on the orientation of the electric field to the plane of incidence, which is defined as the plane that contains the surface normal vector and the propagation vector of the incident electromagnetic wave. The incident ray with propagation direction $\mathbf{k}_{\mathrm{ray,i}}$, electric field $\mathbf{E}_{\mathrm{ray,i}}$ and magnetic field $\mathbf{B}_{\mathrm{ray,i}}$ is reflected at the two-phase interface, and the reflection angle, $\theta_{\mathrm{ray,r}}$, between reflected ray and surface normal is equal to the angle, $\theta_{\mathrm{ray,i}}$, enclosed by incident ray and surface normal. This type of reflection is called specular reflection. The direction of the reflected ray $\mathbf{k}_{\mathrm{ray,r}}$ is given by

$$\mathbf{k}_{\mathrm{ray,r}} = \mathbf{k}_{\mathrm{ray,i}} - 2\left(\hat{\mathbf{n}}_{\mathrm{tr}} \cdot \mathbf{k}_{\mathrm{ray,i}}\right)\hat{\mathbf{n}}_{\mathrm{tr}}\,, \tag{5.7}$$

where $\hat{\mathbf{n}}_{\mathrm{tr}}$ is normal vector of the triangle. Similar, $\mathbf{E}_{\mathrm{ray,i}}$ is rotated by

$$\mathbf{E}_{\mathrm{ray,r}} = -\mathbf{E}_{\mathrm{ray,i}} + 2\mathbf{E}_{\mathrm{ray,i}}\left(\mathbf{E}_{\mathrm{ray,i}} \cdot \hat{\mathbf{n}}_{\mathrm{tr}}\right) \tag{5.8}$$

to obtain the direction of the reflected electric field vector of the ray. The orientation of the magnetic field vector is not considered since it is not required by the Fresnel coefficients for s- and p-polarization as given in Eqs. (2.22) and (2.23). For any ray-triangle intersection, the reflected power can be described as a superposition of a wave with parallel and perpendicular polarization by

$$P_{\mathrm{ray,r}} = P_{\mathrm{ray,i}}\left(\gamma^{\perp}_{\mathrm{ray,i}} R^{\perp}_{\mathrm{tr}} + \left(1 - \gamma^{\perp}_{\mathrm{tr,i}}\right) R^{\parallel}_{\mathrm{tr}}\right)\,, \tag{5.9}$$

where $R^{\perp}$ and $R^{\parallel}$ is the reflectivity of the intersected triangle for s- and p-polarized light, as a function of the angle of incidence as well as the temperature-dependent optical properties of the material given by Eqs. (2.22) and (2.23), and $\gamma^{\perp}_{\mathrm{ray,i}}$ denotes the fraction of the incident, normalized electric field vector, $\hat{\mathbf{E}}_{\mathrm{ray,i}}$, that is oriented perpendicular to the plane of incidence, given by

$$\gamma^{\perp}_{\mathrm{ray,i}} = \hat{\mathbf{E}}_{\mathrm{ray,i}} \cdot \hat{\mathbf{n}}_{\mathrm{tr}} \,. \tag{5.10}$$

Since the reflectivity and the corresponding real and imaginary parts of the refractive index is temperature-dependent, the temperature of the triangle is given by the mean temperature of the three SPH particles which constitute the triangle. The transmitted power is given by

$$P_{\mathrm{ray,t}} = P_{\mathrm{ray,i}} - P_{\mathrm{ray,r}} \,. \tag{5.11}$$

Seeing that any triangle is made up of three vertices, the power from the intersecting rays is transmitted to every SPH particle a by a weighted average given by

$$P_a = \frac{P_{\mathrm{ray,t}}/d_a^{\mathrm{v}}}{\sum_{i=1}^{3} 1/d_i^{\mathrm{v}}} \,, \tag{5.12}$$

where d_a is the distance between the vertex corresponding to the position of particle a and the intersection point of the ray and the intersected triangle, and d_i^{v} is the distance between the ray-triangle intersection point and a vertex v of the triangle. Thus, the heat flux absorbed by a surface SPH particle is given by the sum of the transmitted power of all ray intersections with the same triangle, N_{ints}, according to

$$\dot{q}_{\mathrm{l,ray},a} = \sum_{i=1}^{N_{\mathrm{ints}}} \frac{P_{a,i}}{\Delta x^2} \,, \tag{5.13}$$

where particle a is a vertex SPH particle of the corresponding triangle and Δx^2 is the cross-sectional area of an SPH particle with constant volume. The rays are traced until the power carried by the ray is below a threshold of $1\,\%$ of the initial power of the ray due to multiple reflections, or the ray has left the simulation domain.

5.2 Validation

To validate the implemented ray tracing approach, two analytical expressions for the forced heat equation,

$$\rho c_p \frac{\partial T}{\partial t} = \nabla \cdot k \nabla T + \dot{q}_\mathrm{l} \,, \tag{5.14}$$

are derived. Therefore, two sets of boundary conditions representing a bounded domain are applied, as shown in the Appendix C. The corresponding SPH approximation of Eq. (5.14) is obtained by removing the contributions due to phase transitions and thermal radiation from Eq. (4.51), which yields:

$$\rho_a c_{p,a} \frac{\mathrm{D}T_a}{\mathrm{D}t} = \sum_b \frac{m_b}{\rho_b} \frac{4 k_a k_b}{k_a + k_b} (T_a - T_b) F_{ab} + \frac{\dot{q}_{\mathrm{l,ray},a}}{\Delta x} \,. \tag{5.15}$$

Equation (5.15) is solved using the explicit time integration scheme introduced by Eq. (4.62) and neglecting the terms for thermal radiation, evaporation, and latent heat. SPH particles whose temperature has to remain constant to ensure the Dirichlet boundary conditions are not updated using Eq. (4.62). The thermodynamic properties of the simulated material for all subsequent validation cases are given by $\rho = 1\,\mathrm{kg\,m^{-3}}$, $c_p = 1\,\mathrm{J\,kg^{-1}\,K^{-1}}$ and $k = 1\,\mathrm{W\,m^{-1}\,K^{-1}}$. Moreover, $w_0 = 1\,\mathrm{m}$ and $r_{\mathrm{l},0} = 7\mathrm{m}$.

The first configuration depicts a cube located in the origin of Euclidean space. Moreover, its edges with a length of $2L$ are aligned with the x-, y-, and z-axes. The extent of the cube is $\mathbf{x} \in [-L,\ L]^3$, where $\mathbf{x}$ is a vector containing the x, y, and z coordinates. Moreover, $L = 10\,\mathrm{m}$. The following boundary conditions are imposed

$$T|_{\mathbb{R}^3 \times \{0\}} = 0\,\mathrm{K} \qquad \lim_{|\mathbf{x}| \to L} T = 0\,\mathrm{K}\ \forall\ t \,. \tag{5.16}$$

All sides of the cube are kept at a constant temperature, whereas the initial temperature of the cube is $T = 0\,\mathrm{K}$. The laser source term is placed in the origin of Euclidean space at $x/L = y/L = z/L = 0$ in the x-y-plane of the cube. Using the boundary conditions given by Eq. (5.16), an analytical expression for Eq. (5.14) is derived using the concept of Green's functions and

the method of images. The derivation is shown in the Appendix C and leads to the following expression

$$
\begin{aligned}
T(\mathbf{x}, \mathbf{x}', t, t') = \frac{2P_0}{\pi w_0^2} \int_{t'=0}^{t_1} \int_{y'=-L}^{L} \int_{x'=-L}^{L} \frac{1}{\left(4\pi D_{\mathrm{th}} \left(t - t'\right)\right)^{3/2}} \\
\cdot \exp\left(-\frac{2\left(x'^2 + y'^2\right)}{w_0^2} \right) \sum_{m=-\infty}^{\infty} \sum_{n=-\infty}^{\infty} \sum_{o=-\infty}^{\infty} (-1)^{m+n+o} \\
\cdot \exp\left(\frac{\left(x - x' + 2mL\right)^2 + \left(y - y' + 2nL\right)^2 + \left(z + 2oL\right)^2}{4D\left(t - t'\right)} \right) \\
\mathrm{d}x' \mathrm{d}y' \mathrm{d}t' \, .
\end{aligned}
\tag{5.17}
$$

Here, $D_{\mathrm{th}} = k/(\rho c_p)$ is the thermal diffusivity, the variables x, y, z represent Cartesian coordinates at which the temperature is computed, and the variables x', y', z' represent the position of the laser source term at time t'. The temperature at position $\mathbf{x}$ and at time t depends on the spatial and temporal distance to the localized laser source. Equation (5.17) can be solved numerically. The corresponding SPH simulations are carried out by placing SPH particles on a rectangular lattice representing a cube centered in the origin of Euclidean space with dimensions $-L \leq \mathbf{x} \leq L$. Wall particles are placed around the cube with a thickness of $2h$. The temperature of these particles is kept constant throughout the simulation, ensuring Dirichlet boundary conditions.

Figure 5.4 shows the arrangement of SPH particles with $2L/\Delta x = 101$ and $h = 2.5\Delta x$. One-quarter of the simulation domain is removed in the image to uncover a fraction of the x-y-plane where the rays of the laser beam intersect the material surface. SPH particles located at $z/L > 0$ are transparent to the laser irradiation in this test case, whereas SPH particles located at $z/L \leq 0$ have a reflectivity of $0\,\%$. This setup is chosen to avoid inaccuracies that could arise due to the presence of a free boundary, which would lead to a truncation of the kernel integral of SPH particles near the free boundary.

In the following, the influence of the number of rays discretizing the laser laser beam, spatial discretization of the domain, and smoothing length of the kernel function on the obtained temperature field in the x-y-plane at $z/L = 0$ is examined.

Due to the computational costs inherent in ray tracing approaches, the number of rays necessary to achieve sufficient accuracy with respect to the analytical prediction by Eq. (5.17), and the computational cost necessary to achieve

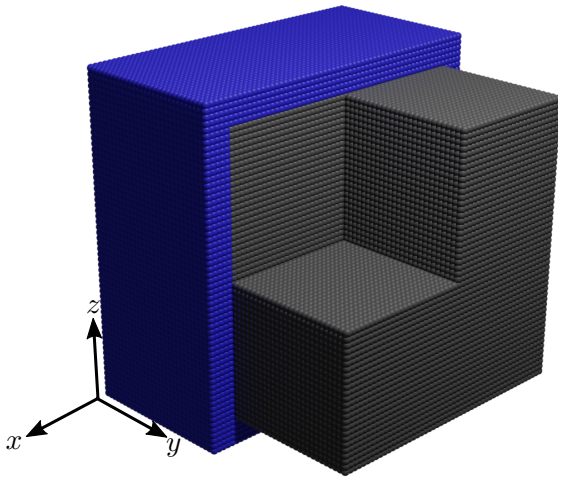

Figure 5.4: SPH particle arrangement for the validation of the ray tracing algorithm. A fraction of the domain is removed and not visualized in order to expose a segment of the x-y plane at $z/L = 0$, where the laser interacts with the perfectly absorbing material. Blue particles are wall particles that are fixed at a constant temperature, whereas black particles are SPH particles whose temperature changes due to the laser energy applied.

that result must be balanced. Therefore, the accuracy of the simulations is investigated as a function of the ray density by

$$n_{\mathrm{ray}} = N_{\mathrm{ray}} \frac{\Delta x^2}{2\pi r_{\mathrm{ray},0}^2} \,. \tag{5.18}$$

The ray density statistically represents the number of rays intersecting a single triangle made up of SPH particles that are placed on a regular lattice. The ray density is varied between $n_{\mathrm{ray}} = 0.1$ and $n_{\mathrm{ray}} = 1000$. Moreover, the particle spacing is given by $2L/\Delta x = 101$, which results in 1 030 301 SPH particles (excluding wall particles) used to discretize the domain. The smoothing length is set to $h = 1.5\Delta x$, which implies a wall thickness of $3\Delta x$, respectively, using the Wendland kernel. The analytical expression in Eq. (5.17) demands that the laser source term is placed within the x-y-plane at $z/L = 0$. This is achieved by excluding particles located at $z/L > 0$ from the meshing procedure to obtain a surface mesh for the layer of SPH particles at $z/L = 0$. The temperature in the center of the laser beam at $x/L = y/L = z/L = 0$ is shown in Fig. 5.5 over time. The black line shows the analytical solution of Eq. (5.17) at $x/L = y/L = z/L = 0$ over time. The temperature increases and converges from $0\,\mathrm{K}$ at $t = 0\,\mathrm{s}$ to a constant equilibrium temperature

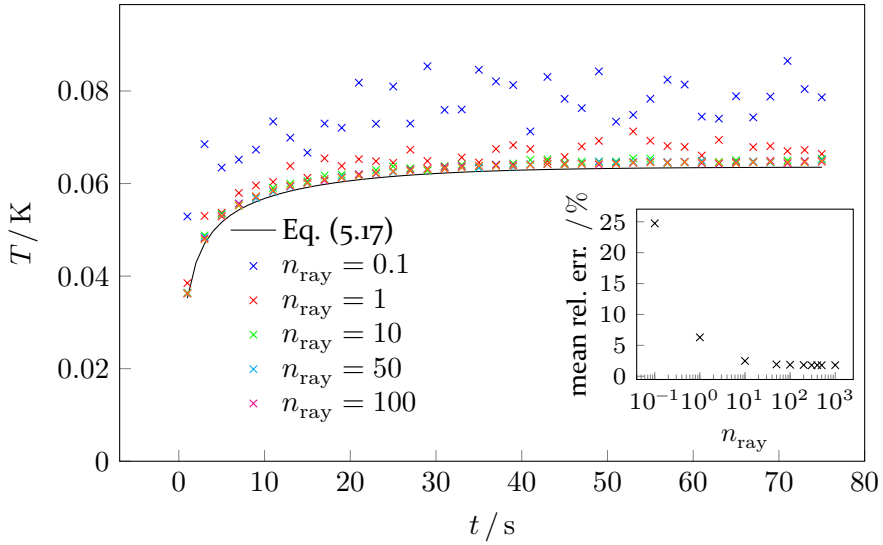

Figure 5.5: Simulated peak temperature as a function of the ray density and computed mean relative errors. The mean relative error is computed from the simulated temperatures and the corresponding analytical prediction in Eq. (5.17) in the range $0\,\mathrm{s} \leq t \leq 75\,\mathrm{s}$ for varying ray density.

of $0.064\,\mathrm{K}$ for $t > 40\,\mathrm{s}$ due to the applied Dirichlet boundary conditions at the walls. The colored crosses mark the SPH simulation results for the temperature and a ray density of $n_{\mathrm{ray}} \in \{0.1,\ 1,\ 10,\ 50,\ 100\}$. For low ray densities $n_{\mathrm{ray}} \leq 1$, the temperature does not reach equilibrium but fluctuates. This is caused by the insufficient approximation of the Gaussian intensity distribution due to the low number of rays. With increasing ray density, the temporal fluctuation of temperature decreases and converges towards the predicted peak temperature given by Eq. (5.17) for $n_{\mathrm{ray}} > 10$. To estimate the accuracy of the ray tracing approach as a function of the ray density, the mean relative error is computed for the temperatures obtained by SPH simulations and the analytical prediction in Eq. (5.17). The time-averaged mean relative error is shown over n_{ray} in Fig. 5.5 as a subgraph. The error decreases from 24.74 % for $n_{\mathrm{ray}} = 0.1$ to 1.86% for $n_{\mathrm{ray}} \geq 100$. Increasing the ray density to $n_{\mathrm{ray}} = 1000$ leads to a slightly improved accuracy with a mean relative error of 1.80 %.

Furthermore, the radial temperature field at $z/L = 0$, $y/L = 0$ and $t = 75\,\mathrm{s}$ is shown in Fig. 5.6. It can be seen that the highest absolute deviation from the predicted temperature by Eq. (5.17) occurs close to the center of the beam. In addition, the mean relative error computed from the temperature of all

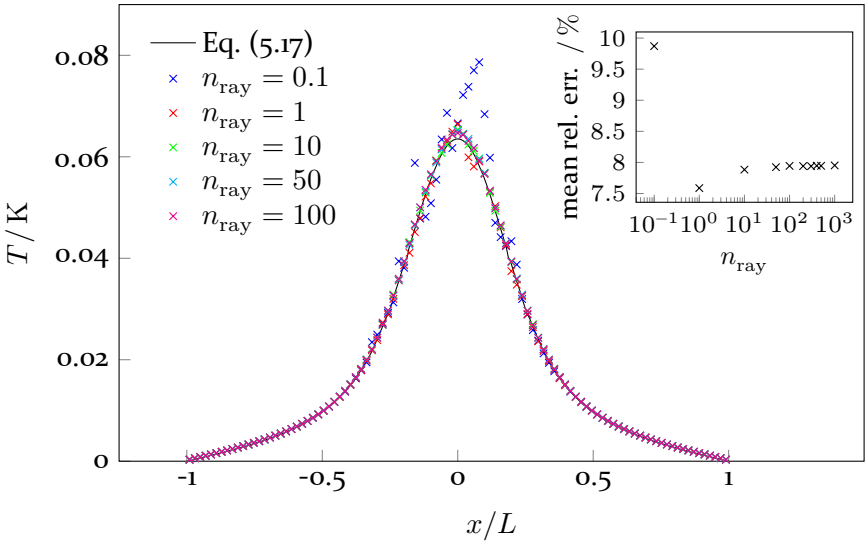

Figure 5.6: Radial temperature field at $z/L = y/L = 0$ obtained by Eq. (5.17) and SPH simulations as a function of the ray density at $t = 75\,\mathrm{s}$. In addition, the corresponding mean relative errors are shown as a function of the ray density.

SPH particles that are located in the x-y-plane at $z/L = 0$ is shown as a supplementing graph in Fig. 5.6. The highest mean relative error is 9.9 % for $n_{\mathrm{ray}} = 0.1$ and the lowest is 7.6 % for $n_{\mathrm{ray}} = 1$. For larger ray densities, the mean relative error converges to 7.9 %. Since the ray tracing algorithm initializes the rays at random positions, the lower relative error at $n_{\mathrm{ray}} = 1$ may be caused by stochastic fluctuations. A ray density of $n_{\mathrm{ray}} = 100$ is considered a good balance between accuracy and computational cost of the presented ray tracing algorithm since $n_{\mathrm{ray}} > 100$ does not lead to a significant reduction of the computed mean relative error.

In addition, the influence of the spatial discretization on the obtained temperature field is investigated by varying Δx and keeping the dimensions of the simulated domain constant. A smoothing length of $h = 1.5\Delta x$ is employed, and each dimension of the domain is discretized by $2L/\Delta x \in \{25, 51, 101\}$ particles. This results in {15 625, 132 651, 1 030 301} SPH particles being simulated. Additionally, the domain is surrounded by three layers of wall particles determined by the smoothing length. The ray density is adjusted to $n_{\mathrm{ray}} = 2000$ to minimize errors arising from the discretization of the laser beam.

Figure 5.7 shows the temperature field at $z/L = y/L = 0$ and $t = 75\,\mathrm{s}$ predicted by Eq. (5.17) and the corresponding SPH simulation results. Moreover,

the computed mean relative error is shown as a graph in the upper right corner of Fig. 5.7. The mean relative error decreases from 18.4 % for $2L/\Delta x = 25$ to

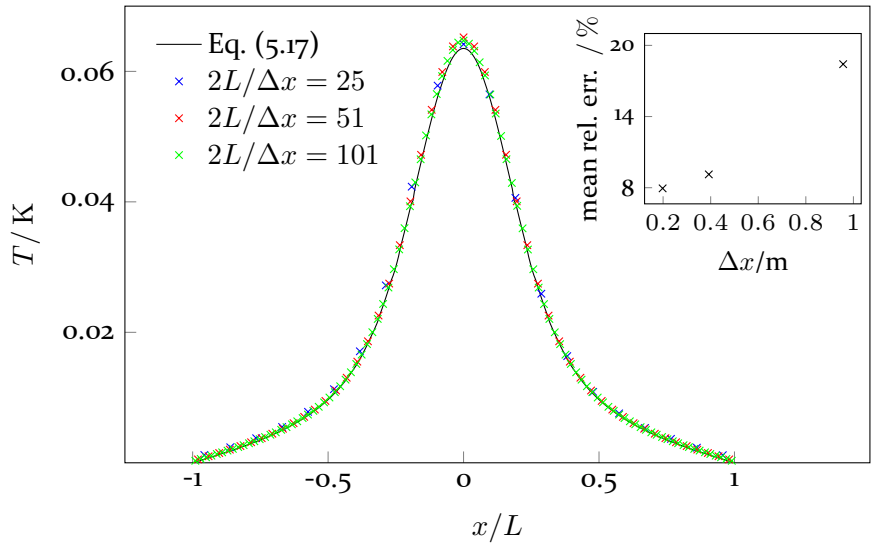

Figure 5.7: Radial temperature field at $z/L = y/L = 0$ obtained by Eq. (5.17) and SPH simulations as a function of the spatial discretization at $t = 75\,\mathrm{s}$. In addition, the corresponding mean relative errors are shown as a function of the discretization length.

7.9 % for $2L/\Delta x = 101$.

The last parameter investigated regarding its influence on the obtained temperature field is the smoothing length. Therefore, the smoothing length is set to $h/\Delta x \in \{1.5,\ 2.0,\ 2.5\}$. The domain is discretized in each spatial dimension by $2L/\Delta x = 101$ SPH particles (1030301 SPH particles) and, in addition, by $\{3\Delta x,\ 4\Delta x,\ 5\Delta x\}$ layers of SPH wall particles depending on the smoothing length. Furthermore, the ray density is adjusted to $n_{\mathrm{ray}} = 2000$. Figure 5.8 shows the obtained temperature field at $z/L = 0$, $y/L = 0$ and $t = 75\,\mathrm{s}$ as well as the corresponding mean relative errors of all particles included inside the laser radius when compared to Eq. (5.17).

The mean relative error decreases from 10.6 % for $h = 2.5\Delta x$ to 7.9 % for $h = 1.5\Delta x$. The result states that the approximation of the Gaussian intensity distribution becomes more accurate with decreasing smoothing length, $h \to 0$.

In the second test case, a cuboid with the same dimensions as in the previous test case ($\mathbf{r} \in [-L,\ L]^3$) is placed in the origin of Euclidean space. To provide a more realistic scenario with respect to laser processing of metals,

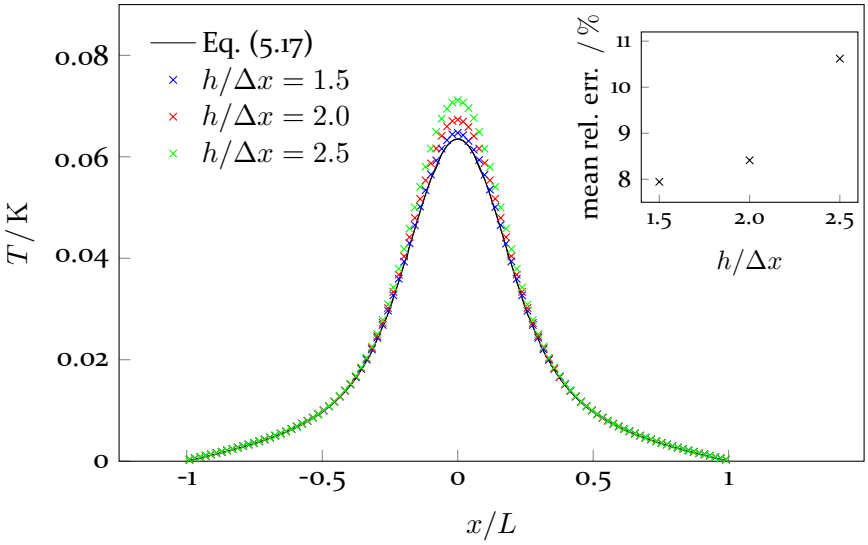

Figure 5.8: Radial temperature field at $z/L = y/L = 0$ obtained by Eq. (5.17) and SPH simulations as a function of the smoothing length at $t = 75\,\mathrm{s}$. In addition, the corresponding mean relative errors are shown as a function of the smoothing length.

a Neumann boundary condition is applied at $z/L = 0$. This represents a thermally insulated surface which is also considered and used in the laser melting simulations performed in this work. All other sides of the cuboid are kept at a constant temperature using Dirichlet boundary conditions. The initial temperature at $t = 0\,\mathrm{s}$ is $T = 0\,\mathrm{K}$. The initial and boundary conditions are defined by

$$\begin{aligned} T|_{\mathbb{R}^n \times \{0\}} &= 0\,\mathrm{K} \\ \lim_{z \to 0} \frac{\mathrm{d}T}{\mathrm{d}t} &= 0\,\mathrm{K\,s^{-1}} \\ \lim_{|x| \to L} T = 0\,\mathrm{K} \quad \lim_{|y| \to L} T = 0\,\mathrm{K} \quad \lim_{z \to -L} T &= 0\,\mathrm{K}\,. \end{aligned} \tag{5.19}$$

The corresponding analytical expression to Eq. (5.14) using the boundary conditions shown in Eq. (5.19) is given by

$$
\begin{aligned}
T(\mathbf{x},t) = \frac{4P_0}{\pi w_0^2} \int_{t'=0}^{t_1} \int_{y'=-L}^{L} \int_{x'=-L}^{L} \frac{1}{\left(4\pi D_{\mathrm{th}}\left(t-t'\right)\right)^{3/2}} \\
\cdot \exp\left(-\frac{2\left(x'^2+y'^2\right)}{w_0^2}\right) \sum_{m=-\infty}^{\infty} \sum_{n=-\infty}^{\infty} \sum_{o=-\infty}^{\infty} (-1)^{m+n+o} \\
\cdot \exp\left(\frac{\left(x-x'+2mL\right)^2+\left(y-y'+2nL\right)^2+\left(z+2oL\right)^2}{4D\left(t-t'\right)}\right) \\
\mathrm{d}x'\mathrm{d}y'\mathrm{d}t' \, .
\end{aligned}
\tag{5.20}
$$

The corresponding derivation of the expression in Eq. (5.20) is presented in Appendix C.

Figure 5.9 shows the arrangement of SPH particles with $2L/\Delta x = 101$ along the x and y-axis and a height H discretized by $H/\Delta x = 51$ SPH particles. The

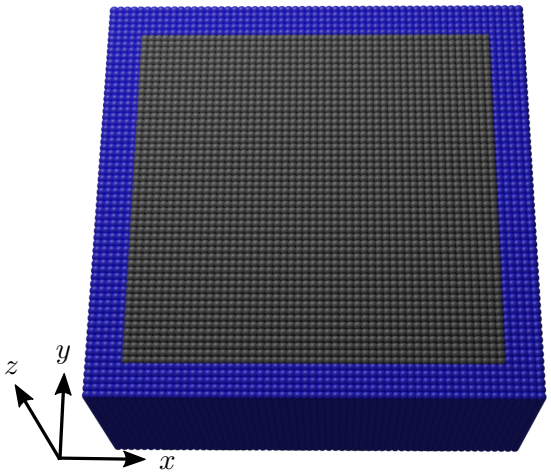

Figure 5.9: Cuboid represented by SPH particles. Black particles denote solid particles on which the heat equation is solved. Blue particles denote SPH wall particles which are kept at constant temperature.

chosen lattice spacing results in a total number of 520251 SPH particles plus Dirichlet wall particles placed around the cuboid except at $z/L = 0$ in this setup. The smoothing length is set to $h = 1.5\Delta x$ and the ray density is given by $n_{\mathrm{ray}} = 2000$. To apply the Neumann boundary condition, no particles are placed at $z/L = 0$, which results in adiabatic behavior.

Figure 5.11 shows the peak temperature at $x/L = y/L = z/L = 0$ versus time obtained by Eq. (5.20) as a solid black line. The corresponding

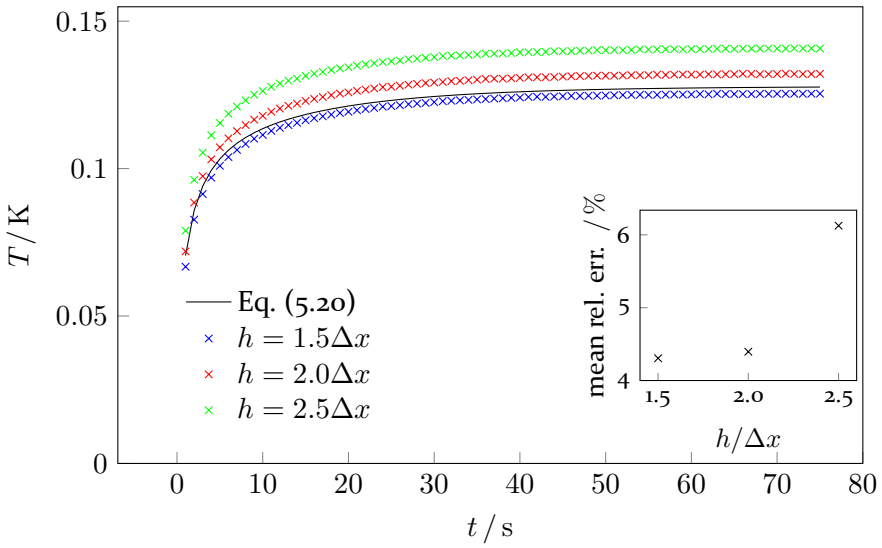

Figure 5.10: Simulated peak temperature as a function of the smoothing length and computed mean relative errors. The mean relative error is computed from the simulated temperatures and the corresponding analytical prediction in Eq. (5.20) in the range $0\,\mathrm{s} \leq t \leq 75\,\mathrm{s}$ for varying smoothing length.

SPH particle temperature is given for varying smoothing length, $h/\Delta x \in \{1.5,\ 2.0\ 2.5\}$, as blue, red, and green crosses, respectively. The temperature of the analytical solution converges towards an equilibrium temperature of approximately $0.128\,\mathrm{K}$ that is twice the equilibrium temperature predicted by Eq. (5.17). The obtained peak temperature of the SPH particle located in the center of the beam at $x/L = y/L = z/L = 0$ overestimates the analytical prediction in Eq. (5.20) with increasing smoothing length ($h = 2.0\Delta x$, $h = 2.5\Delta x$) and underestimates it with $h = 1.5\Delta x$. A reason for this could be the Neumann boundary condition, which is applied by disregarding the truncation of the kernel function at free boundaries. For instance, more precise boundary conditions could alleviate this problem, as demonstrated in [185]. The corresponding time-averaged relative error of the temperature of particles located in the center of the Gaussian intensity distribution decreases with decreasing smoothing length from 6.13 % for $h = 2.5\Delta x$ to 4.30 % for $h = 1.5\Delta x$.

Figure 5.11 shows the radial temperature field obtained from SPH simulations at $y/L = 0$ and $z/L = 0$. Here, the mean relative error between the simulated

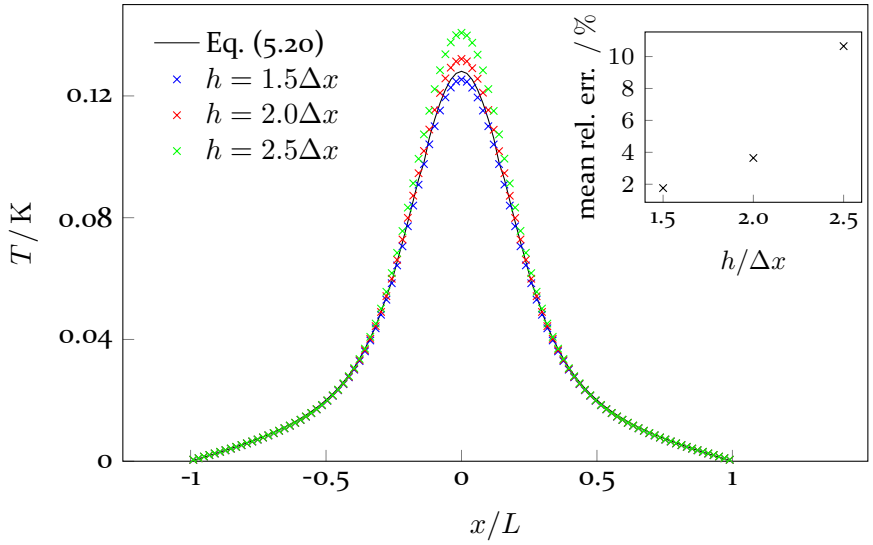

Figure 5.11: Radial temperature field at $z/L = y/L = 0$ obtained by Eq. (5.20) and SPH simulations as a function of the smoothing length at $t = 75\,\mathrm{s}$. In addition, the corresponding mean relative errors are shown as a function of the smoothing length.

temperature field of the irradiated layer of SPH particles and theory decreases with decreasing smoothing length from 10.65 % for $h = 2.5\Delta x$ to 1.76 % $h = 1.5\Delta x$.

5.3 Application example: absorbtance of titanium powder

In this section, the absorbtance of laser irradiation by a monodisperse and a polydisperse titanium powder bed (Ti grade2 AP&C) at temperatures below the melting point is measured. The particle size distribution of the polydisperse powder is shown in Fig. 5.12 and is measured by optical evaluation of several samples using microscopy [S166]. In contrast, the monodisperse powder is set up by spheres with a diameter of $44.65\,\mu\mathrm{m}$, which represents the mean value of the mass fraction with the largest sphere diameter in the polydisperse powder.

The software LIGGGHTS [100] is used to deposit titanium particles into a box with a base area of $(500 \times 500)\,\mu\mathrm{m}^2$ and up to a height of approximately $250\,\mu\mathrm{m}$. The final arrangement of the deposited powder particles is used to construct an STL file. Therefore, each particle is substituted with a spherical triangulated surface mesh with the same center of mass and radius. In a subsequent step,

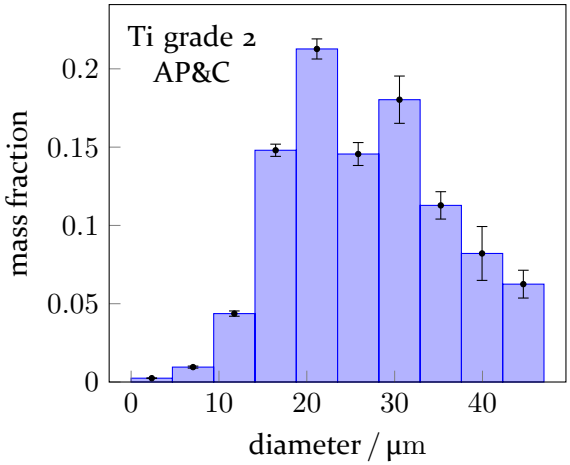

Figure 5.12: Measured particle size distribution of Ti grade2 AP&C according to [S166].

the obtained STL file is read by the used SPH software. Each surface mesh of a sphere is filled by SPH particles placed on a rectangular lattice using a ray casting algorithm. Moreover, each set of SPH particles representing a distinct titanium particle is identified using a unique identification number. This number is used to identify SPH particles representing a single titanium particle and for which a surface mesh is computed using the CGAL-library [197]. A wall with a thickness of $10\Delta x$ is placed below the deposited titanium powder. In the following simulation cases, an initial particle spacing of $\Delta x = 2.5\,\mu\mathrm{m}$, and a smoothing length of $h = 2.0\Delta x$ is employed. This leads to $2.7{\cdot}10^6$ and $2.8{\cdot}10^6$ SPH particles used to discretize the monodisperse and polydisperse powder, which consist of 773 or 5718 titanium particles, respectively. The material properties of titanium presented in Section 3 are applied to the SPH particles. The porosity of the monodisperse and polydisperse powder is computed from the material that is located in a box with dimensions $(400 \times 400 \times 200)\,\mu\mathrm{m}^3$. To avoid boundary effects, SPH particles that are located in the vicinity of the domain boundaries are excluded from the porosity computation. The estimated porosity of the monodisperse and polydisperse powder is 0.402 and 0.366, respectively. The resultant powders, discretized by SPH particles, are shown in Fig. 5.13. The computed surface meshes using the CGAL-library are used to visualize the powder using Blender [42].

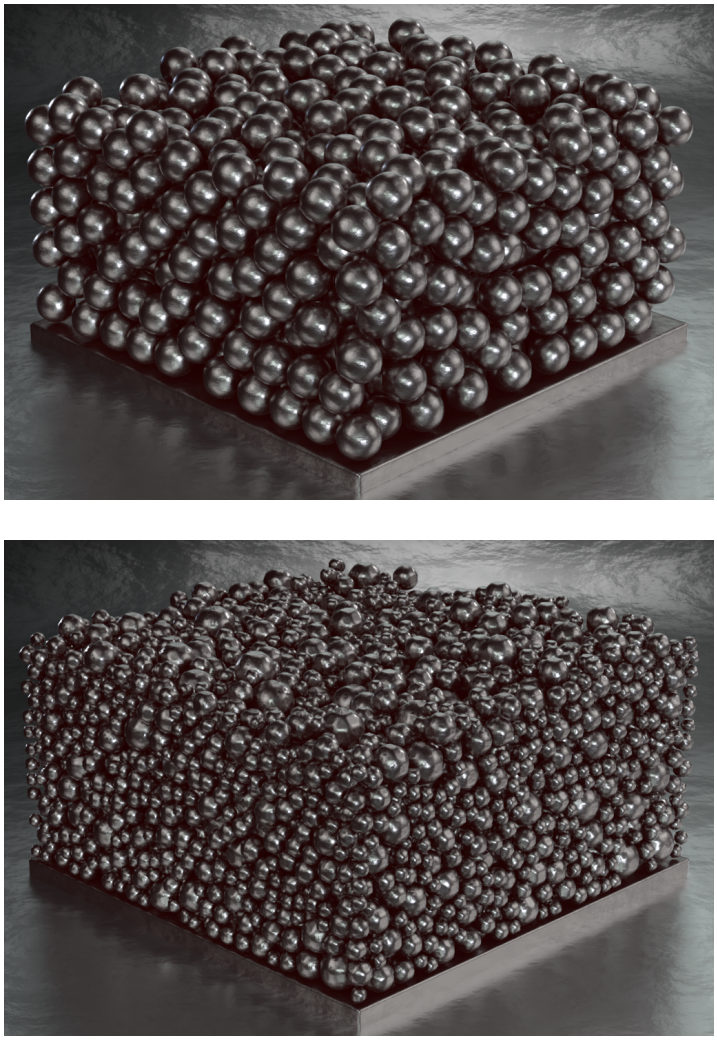

Figure 5.13: Deposited monodisperse (top) and polydisperse titanium powder bed (bottom).

To model the reflectance of the powders, Eqs. (3.22) to (3.25) are used to describe the real and imaginary parts of the refractive index of a clean titanium surface. Moreover, assuming an aged titanium surface, Eqs. (3.28) to (3.31) are used. The absorbed power of the laser by the powder is measured within a single time step of the numerical simulation. Since the computational cost does not represent a numerical limitation in this scenario, $n_{\mathrm{ray}} = 1000$ to achieve the highest accuracy.

Figure 5.14 shows the measured absorbtance, computed as the ratio of absorbed laser power to total laser power by the SPH particles representing the monodisperse and polydisperse powder, assuming a clean or aged material surface. The measured absorbtance of solid titanium is shown as a function of the powder temperature adjusted between $300\,\mathrm{K}$ and $1800\,\mathrm{K}$ in steps of $300\,\mathrm{K}$. It can be seen that aged titanium powder has a

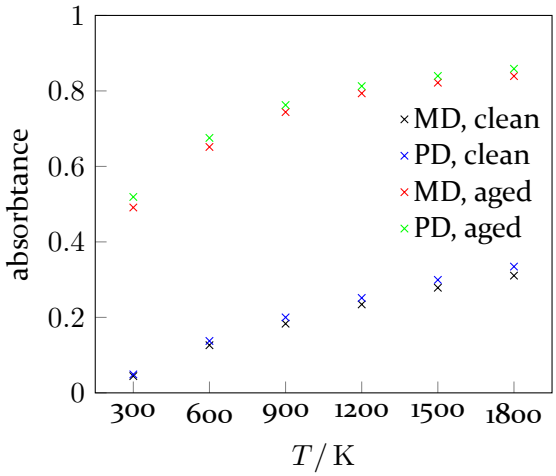

Figure 5.14: Measured effective absorbtance of monodisperse (MD) and polydisperse (PD) titanium powder at different temperatures that are irradiated by a laser beam with a wavelength of $1.08\,\mu\mathrm{m}$

significantly higher absorbtance than titanium powder with clean surfaces. The absorptance of the clean monodisperse powder increases from 0.04 (300 K) to 0.31 (1800 K) whereas the absorptance of the aged monodisperse powder increases from 0.49 (300 K) to 0.84 (1800 K). At all investigated temperatures, the absorptance of the polydisperse powder is slightly higher than that of the monodisperse powder. This effect increases with higher temperatures. For example, the absorptance of monodisperse powder (aged surface) is 0.84, whereas the absorptance of polydisperse powder (aged surface) is 0.86 at 1800 K. Maybe this behavior can be explained by the angle of incidence between the rays and the surface normals of the powder particles. A more plane surface morphology could increase the absorbed laser energy more strongly than the influence of the porosity of the powder bed.

Figure 5.15 shows the absorbed power by the titanium powder as a function of the height scaled with the maximum particle diameter, $D_{\max} = 42.3\,\mu\mathrm{m}$. The absorbed laser power by the titanium powder is measured from $z/D_{\max} = 0$ to the material surface in steps of the spatial discretization,

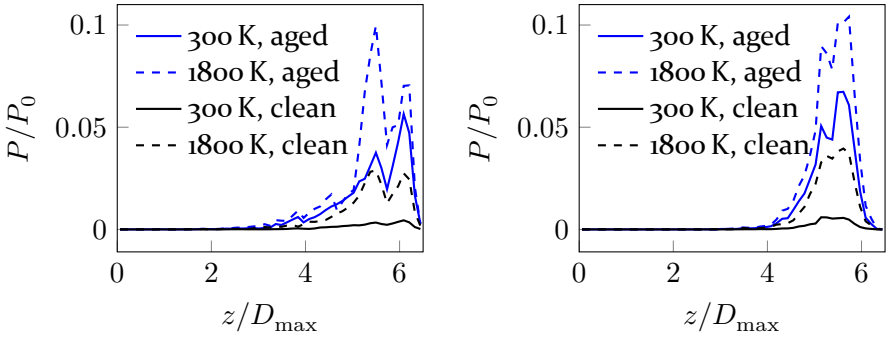

(a) Measured absorbed laser power by monodisperse titanium powder.

(b) Measured absorbed laser power by polydisperse titanium powder.

Figure 5.15: Absorbed laser power by a monodisperse and a polydisperse titanium powder for a wavelength of 1.08 µm as a function of the powder height.

Δx. Figure 5.15a shows the measured absorbed power by the monodisperse powder, and Fig. 5.15b shows the measured power by polydisperse powder. In the case of monodisperse powder, the rays propagate deeper into the powder bed when compared to the propagation depth into the polydisperse powder. This can be seen by the higher amount of absorbed power within the region $2 \leq z/D_{\max} \leq 4$. Moreover, close to the surface, the absorbed power exhibits several peaks at $z/D_{\max} \in \{3.45,\ 3.81,\ 5.46,\ 6.06\}$, which can be attributed to the particle layers within the powder bed that are directly exposed to the irradiation. In contrast, the absorbed power measured for the polydisperse powder shows two peaks at $z/D_{\max} = 5.59$ and $z/D_{\max} = 5.0$.

5.4 Concluding remarks

This chapter presented the developed ray tracing algorithm, which discretizes a laser with a Gaussian intensity distribution into many energy portions. The method can be applied to laser-metal interaction problems with arbitrary surface morphologies under the assumption of geometrical optics in particle-based simulation methods.

To validate the presented ray tracing algorithm, two analytical expressions for the forced heat equation in a bounded domain are derived using the concept of Green's functions and the method of images. In the first set of boundary conditions, all sides of a cube are kept at a constant temperature. The upper half of the cube is transparent to laser irradiation. In contrast, the lower half completely absorbs the incident irradiation within a thin material layer with a thickness equal to the SPH discretization length, Δx. The influence

of the ray density, the smoothing length, and spatial discretization on the obtained temperature fields in the SPH simulations is investigated for this setup. A ray density of $n_{\mathrm{ray}} \geq 100$ was found to have no significant effect on the mean relative error between the simulated and analytical temperatures of the absorbing surface layer. As a result, $n_{\mathrm{ray}} \approx 100$ is a good compromise between numerical cost and accuracy. Moreover, the estimated mean relative error to the analytical prediction decreases with increasing spatial resolution and decreasing smoothing length. With $7.9\,\%$, the lowest measured relative error is obtained for $h = 1.5\Delta x$, $x/L = 101$, and $n_{\mathrm{ray}} = 2000$.

In the second set of boundary conditions, the side of a cuboid that is facing the laser beam is assumed to be thermally insulating. All the other sides of the cuboid are kept at a constant temperature. The lowest measured relative error in this scenario is $4.13\,\%$ for $h = 1.5\Delta x$, $x/L = 101$, and $n_{\mathrm{ray}} = 2000$.

In conclusion, the ray density in the ray tracing algorithm should be adjusted to $n_{\mathrm{ray}} \approx 100$ to balance numerical cost and accuracy, the smoothing length should be as small as possible, and the spatial resolution should be chosen as high as possible to achieve the best accuracy.

The developed ray tracing algorithm was subsequently used to investigate the absorption of the laser irradiation by a monodisperse and a polydisperse titanium powder surrounded by an argon atmosphere. The monodisperse and polydisperse powders have a porosity of 0.402 and 0.366, respectively. The titanium particles, which compose the powders, are assumed to have either a clean or an aged surface. Moreover, the absorptance of the titanium powders was investigated in a temperature range from $300\,\mathrm{K}$ to $1800\,\mathrm{K}$. It was found that the powder beds that exposed an aged titanium surface exhibited a significantly higher absorptance than the titanium powder with a clean surface at all investigated temperatures. Moreover, the polydisperse powder absorbs more incident laser irradiation than the monodisperse powder at all investigated temperatures. It seems that the more homogeneous surface in the case of the polydisperse powder absorbs more laser radiation than the more porous monodisperse powder bed. The lowest absorbtance of 0.04 was measured for monodisperse clean powder at $300\,\mathrm{K}$ and the highest absorbtance of 0.84 was estimated for polydisperse powder with an aged surface at $1800\,\mathrm{K}$.

By investigating the absorbed laser power as a function of the propagation depth into the powder, it was found that most irradiation is absorbed within the first layers of the powder bed. Furthermore, the laser irradiation propagates deeper into the monodisperse powder bed than the polydisperse powder bed due to the higher void fraction between the titanium particles. In addi-

tion, a more significant amount of laser energy is absorbed at higher powder temperatures.

6 Modeling interfacial tension at free boundaries

When simulating fluid flows with free surfaces using SPH [68, 119], surface tension is modeled either by introducing pairwise forces between the particles [139, 143, 194, 195] or by the phenomenological CSF [26, 133].

Pairwise forces are motivated by the molecular origin of surface tension [167] and are readily applicable to the simulation of free surfaces. It is widely used for solving problems in droplet dynamics, drop interaction with textured surfaces [179], and contact angle hysteresis [16]. When used in simulations, however, such models reveal an artificial virial pressure [195] and require a much greater computational effort than CSF to obtain similar results since a larger smoothing length is needed [139]. If one used the same smoothing length, simulations appear too dissipative [139] and noisy.

The CSF model does not suffer from this problem. For instance, it can reliably predict the dynamics due to surface tension gradients at phase boundaries, known as the Marangoni effect. However, its application to free surfaces is problematic since the truncation of the kernel integral near the free surface leads to unacceptable errors of the local curvature [133].f The need for reliable simulations of LASER-assisted additive manufacturing processes [95] is a vital motivation to develop stable and efficient numerical methods for fluid flows involving dynamic capillary-driven flows at gas-liquid interfaces.

Several methods have been proposed to correct the kernel truncation error at the free surface in CSF. Ordoubadi et al. [151] used mirror particles to provide the contribution of the omitted ambient phase to achieve stable two-dimensional flows in Weakly Compressible SPH. Hirschler et al. [77] simulated two-dimensional droplet collisions using CSF with kernel correction factors at the free surface. Unfortunately, these methods apply only to two-dimensional problems. Recently, Fürstenau et al. [66] improved the curvature estimate at the free surface by employing the curvature tensor computation and using a kernel renormalization technique. This approach also includes the application of extra capillary pressure at the free boundary in addition to the standard CSF formulation to stabilize the free surface boundary.

The current chapter presents an alternative surface tension model for use in SPH simulations. This model is based solely on the Young-Laplace (YL) pressure jump across an interface applied as a boundary condition to free surface particles. In addition, a CSF approach for free surfaces, capable of

modeling wetting phenomena, is presented. Therefore, the contact angle model proposed by [31] is modified for the application to free surface problems. Lastly, the modeling approach for Marangoni forces is presented.

The accuracy and robustness of the proposed approaches are demonstrated by utilizing examples that are known to be notoriously difficult for SPH. These include droplet oscillations and coalescence, the fragmentation of a fluid filament following the Plateau-Rayleigh instability, droplet spreading on a solid substrate with and without gravity, and the retardation of an accelerated drop that attempts to pass over the edge between two inclined planes. Lastly, the velocity field in a cavity, caused by Marangoni flow at the liquid-gas interface due to an applied temperature gradient, is validated.

This chapter introduces the following notation for different subsets of SPH particles located within the domain Ω. The subset of solid particles is denoted by $\Omega^s \subseteq \Omega$ and the subset of liquid particles is denoted by $\Omega^l \subseteq \Omega$. Moreover, a subset of solid particles represents the wall ($\Omega^w \subseteq \Omega^s$). Surface particles are identified by the vertices of the computed surface mesh introduced in Chapter 5 and are denoted by $\Omega^v \subseteq \Omega$.

6.1 Boundary pressure method[1]

In this section, surface tension is modeled by applying the YL pressure difference as a boundary condition at the liquid-gas interface. The YL pressure boundary condition can be applied to weakly compressible SPH and ISPH. Here, the YL pressure boundary condition is applied to ISPH, particularly to the PPE in Eq. (4.49) and the pressure gradient in Eq. (4.36). In contrast to [66] and the standard CSF approach [26], no forces are directly applied to free surface particles. This is achieved by supplementing the missing contribution of neighboring particles semi-analytically to the Laplacian of pressure in the PPE [138] instead of a scaling approach [66, 144]. Such an approach, in which the contribution of the particle neighborhood is estimated additively from the initial configuration of particles with full kernel support, has been successfully applied to both free surface [138] and wall boundary conditions [108]. Figure 6.1 shows a schematic representation of this model.

[1] The content of this section has been published in P22.

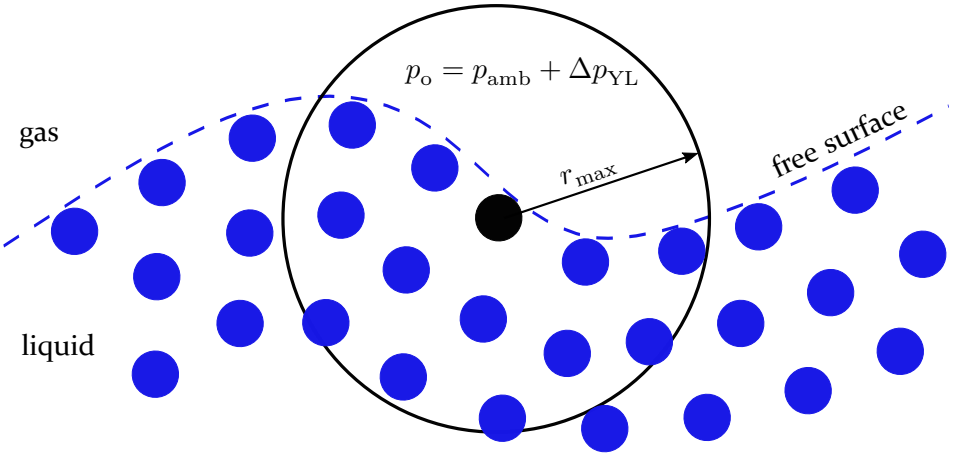

Figure 6.1: Sketch of a free boundary where the truncation of the kernel integral of a particle is used to impose the YL pressure. The kernel of the black particle includes an insufficient number of neighboring (blue) particles. This leads to errors when computing physical quantities via kernel integration. The Dirichlet boundary condition for pressure is applied analytically through the volume beyond the free surface.

6.1.1 Curvature computation and external pressure

The free surface formulation of the pressure gradient in Eq. (4.36) and the corresponding free surface formulation of the PPE in Eq. (4.49) allow imposing an external pressure field p_o to free surface particles given by

$$p_{o,a} = p_{amb,a} + \Delta p_{YL,a} \,. \tag{6.1}$$

Here, $p_{amb,a}$ is the ambient background pressure and $\Delta p_{YL,a}$ is the YL pressure difference across a curved surface at position of particle a. The pressure difference across the interface depends on the surface tension coefficient σ and the local mean curvature, $\bar{\kappa}_a$, given by [167]

$$\Delta p_{YL,a} = 2\sigma_a \bar{\kappa}_a \,, \tag{6.2}$$

in three spatial dimensions. The mean curvature is given by

$$\bar{\kappa}_a = \frac{\kappa_{1,a} + \kappa_{2,a}}{2} \,, \tag{6.3}$$

where $\kappa_{a,1}$ and $\kappa_{a,2}$ are the principal curvatures.

In the following, the procedure presented by [66] to compute the mean curvature for each SPH particle is employed. Starting with the normal vector

$\mathbf{n}_a^{\mathrm{lg,l}}$ that points from liquid to gaseous phase and is computed using liquid SPH particles by

$$\mathbf{n}_a^{\mathrm{lg,l}} = -\sum_{b\in\Omega^{\mathrm{l}}} \frac{m_b}{\rho_b}\nabla W_{ab}\,. \tag{6.4}$$

According to [134], the normal vectors should be smoothed to diminish erroneous normal vectors and to increase the stability of the surface tension model by

$$\tilde{\mathbf{n}}_a^{\mathrm{lg,l}} = \frac{1}{S_a^{\mathrm{l}}}\sum_b \frac{m_b}{\rho_b}\mathbf{n}_b^{\mathrm{lg,l}} W_{ab}. \tag{6.5}$$

Here, the Shepard filter computed from liquid particles, S_a^{l}, given by Eq. (4.69) is used to account for the kernel truncation of particles near the free surface. Moreover, normal vectors whose magnitude is smaller than a given threshold, ϵ_{n}, typically adjusted in the range $\epsilon_{\mathrm{n}} = [\frac{0.1}{h}, \dots, \frac{0.2}{h}]$, are discarded to increase the accuracy of the computed mean curvature. Subsequently, the smoothed and filtered normal vectors from Eq. (6.5) are normalized by

$$\hat{\tilde{\mathbf{n}}}_a^{\mathrm{lg,l}} = \frac{\tilde{\mathbf{n}}_a^{\mathrm{lg,l}}}{\left|\tilde{\mathbf{n}}_a^{\mathrm{lg,l}}\right|}\,. \tag{6.6}$$

Now, the curvature tensor at the location of a liquid particle is computed by [66]

$$\mathbf{K}_a^{\mathrm{l}} = \sum_{b\in\Omega^{\mathrm{l}}} \frac{m_b}{\rho_b}\hat{\tilde{\mathbf{n}}}_{ab}^{\mathrm{lg,l}} \otimes \hat{\nabla}^{\mathrm{l}} W_{ab}, \qquad \hat{\tilde{\mathbf{n}}}_{ab}^{\mathrm{lg,l}} = \hat{\tilde{\mathbf{n}}}_a^{\mathrm{lg,l}} - \hat{\tilde{\mathbf{n}}}_b^{\mathrm{lg,l}}\,, \tag{6.7}$$

where $\otimes$ represents the dyadic or outer product, and $\hat{\nabla}^{\mathrm{l}} W_{ab}$ is the normalized kernel gradient [25, 144],

$$\hat{\nabla}^{\mathrm{l}} W_{ab} = \mathbf{L}_a^{\mathrm{l}} \nabla W_{ab}\,, \tag{6.8}$$

computed by using the correction matrix $\mathbf{L}_a^{\mathrm{l}}$,

$$\mathbf{L}_a^{\mathrm{l}} = \left(\sum_{b\in\Omega^{\mathrm{l}}} \frac{m_b}{\rho_b}\mathbf{r}_{ab} \otimes \nabla W_{ab}\right)^{-1}\,. \tag{6.9}$$

The curvature tensor $\mathbf{K}_a^{\mathrm{l}}$ must be projected into tangent space to compute the principal curvatures. For the coordinate transformation, the following basis vectors are employed

$$\mathbf{t}_a^{(1)} = \begin{cases} \hat{\tilde{\mathbf{n}}}_a^{\mathrm{lg,l}} \times (0,1,0) & \text{if} \quad \left| \hat{\tilde{\mathbf{n}}}_a^{\mathrm{lg,l}} \times (0,1,0) \right| > 0.01 \\ \hat{\tilde{\mathbf{n}}}_a^{\mathrm{lg,l}} \times (1,0,0) & \text{else} \end{cases} , \tag{6.10}$$

$$\hat{\mathbf{t}}_a^{(1)} = \frac{\mathbf{t}_a^{(1)}}{\left| \mathbf{t}_a^{(1)} \right|} , \tag{6.11}$$

and

$$\mathbf{t}_a^{(2)} = \hat{\tilde{\mathbf{n}}}_a^{\mathrm{lg,l}} \times \hat{\mathbf{t}}_a^{(1)} , \qquad \hat{\mathbf{t}}_a^{(2)} = \frac{\mathbf{t}_a^{(2)}}{\left| \mathbf{t}_a^{(2)} \right|} . \tag{6.12}$$

Here, $\mathbf{t}_a^{(1)}$, $\mathbf{t}_a^{(2)}$ are tangential vectors to the surface and $\hat{\mathbf{t}}^{(1)}$, $\hat{\mathbf{t}}_a^{(2)}$ their normalized vectors. The symbol $\times$ denotes the cross product of vectors. Now, the basis can be changed using the metric tensor, $\mathbf{T}$, and its corresponding transposed tensor, $\mathbf{T}^{\mathrm{T}}$, leading to

$$\mathbf{K}'_a = \mathbf{T}_a^{\mathrm{T}} \mathbf{K}_a \mathbf{T}_a . \tag{6.13}$$

The metric $\mathbf{T}_a$ is given by

$$\mathbf{T}_a = (\mathbf{L}_{\mathrm{B},a}^{\mathrm{T}})^{-1} \cdot \mathbf{G}_a = \mathbf{L}_{\mathrm{B},a} \cdot \mathbf{G}_a = \mathbf{L}_{\mathrm{B},a} , \tag{6.14}$$

where $\mathbf{G}_a$ is a matrix whose columns are represented by the Cartesian basis vectors, and $\mathbf{L}_{\mathrm{B},a} = (\hat{\tilde{\mathbf{n}}}_a^{\mathrm{lg,l}}, \hat{\mathbf{t}}_a^{(1)}, \hat{\mathbf{t}}_a^{(2)})$ is the orthonormal matrix build from the local basis vectors.

The curvature tensor defined in tangential space can be obtained by removing the normal component corresponding to the first row and first column of $\mathbf{K}'_a$. Thus, the principal curvatures are given by the eigenvalues of $\mathbf{K}'_a$.

By modifying the Laplace pressure jump in Eq. (6.2) using the Shepard filter, the free surface becomes more stable,

$$\Delta p'_{\mathrm{YL},a} = \sigma_a \bar{\kappa}_a \left(1 + \frac{1}{S_a^{\mathrm{l}}} \right) . \tag{6.15}$$

Accordingly, the external pressure in Eq. (6.1) is modified to

$$p_{\mathrm{o},a} = p_{\mathrm{amb},a} + \Delta p'_{\mathrm{YL},a} . \tag{6.16}$$

Eq. (6.16) can now be applied to Eq. (4.36) and Eq. (4.49) for liquid SPH particles. The introduced approximation to the Laplace pressure in Eq. (6.15) is consistent with respect to spatial resolution as shown in Section 6.1.2.

6.1.2 Validation

The proposed simulation method for surface tension at free boundaries is validated by means of various three-dimensional problems. The momentum equation of each liquid SPH particle is solved according to

$$\frac{\mathrm{D}\mathbf{u}_a}{\mathrm{D}t} = \begin{cases} \mathbf{f}^{\mathrm{c}}_{\mathrm{p},a} + \mathbf{f}^{\mathrm{c}}_{\eta,a} & \text{if } S_a \leq 0.95 \\ \mathbf{f}^{\mathrm{b}}_{\mathrm{p},a} + \mathbf{f}_{\eta,a} & \text{else} \end{cases}, \tag{6.17}$$

where the pressure, $\mathbf{f}^{\mathrm{c}}_{\mathrm{p},a}$, and viscous acceleration, $\mathbf{f}^{\mathrm{c}}_{\eta,a}$, are given by Eqs. (4.37) and (4.41) and are solved for SPH particles located in the vicinity of a free boundary. In contrast, the pressure, $\mathbf{f}^{\mathrm{b}}_{\mathrm{p},a}$, and viscous acceleration, $\mathbf{f}_{\eta,a}$, of SPH particles with sufficient neighboring particle support are given by Eqs. (4.35) and (4.38). Moreover, the PPE is solved by Eq. (4.49) for particles near the free surface and by Eq. (4.48) for SPH particles located in the bulk of the fluid.

For all test cases, the following parameters, if not otherwise stated, are employed: $\sigma = 0.01\,\mathrm{N\,m^{-1}}$, $\eta = 0.01\,\mathrm{Pa\,s}$, $\rho = 1000\,\mathrm{kg\,m^{-3}}$, $p_{\mathrm{amb}} = 0\,\mathrm{Pa}$ and $\epsilon_{\mathrm{n}} = 0.1/h$. The SPH particles are initially arranged on a rectangular lattice with spacing Δx. The smoothing length is $h = 2.5\Delta x$, and the numerical timestep size is adjusted according to the CFL conditions for the maximum acceleration, velocity, viscous diffusion, and surface tension given in Eq. (4.66). The contribution of the viscous forces to the conservation of momentum in Eq. (4.34) is computed by Eq. (4.41) instead of Eq. (4.38). Explicit imposition of surface tension force is not required in Eq. (6.17) since the YL pressure is applied as a boundary condition in the PPE.

6.1.2.1 Laplace pressure jump

At equilibrium, the pressure inside a drop is larger than outside due to the surface tension, σ. This effect is termed Laplace pressure jump. In the performed simulations initially $\{4\,224, 9\,915, 14\,321, 113\,104, 268\,096\}$ SPH particles are placed on a rectangular lattice with spacing $\Delta x \in \left\{\frac{r_0}{10}, \frac{r_0}{13.3}, \frac{r_0}{15}, \frac{r_0}{30}, \frac{r_0}{40}\right\}$ inside a sphere of radius $r_0 = 10^{-3}\,\mathrm{m}$. The threshold for the smoothed normal vectors in Eq. (6.5) is $\epsilon_{\mathrm{n}} = \frac{0.1}{h}$ for $\Delta x = \frac{r_0}{40}$, $\Delta x = \frac{r_0}{30}$ and $\Delta x = \frac{r_0}{20}$, and $\epsilon_{\mathrm{n}} = \frac{0.15}{h}$ for both $\Delta x = \frac{r_0}{10}$ and $\Delta x = \frac{r_0}{13.3}$. This agrees with [66], who reports stable results for $\epsilon_{\mathrm{n}} = 0.1/h$ to $\epsilon_{\mathrm{n}} = 0.2/h$. For small droplets, the physical value of

the Laplace pressure jump can be substantial; for the parameters given above, the pressure inside the drop exceeds the ambient pressure by $20\,\mathrm{Pa}$ according to Eq. (6.2).

Figure 6.2a shows the pressure along a cut through the symmetry axis of the drop at $(t = 1\,\mathrm{s})$ when equilibrium was assumed. The pressure inside the droplet converges towards the analytical prediction for an increasing number of SPH particles (increasing resolution). In the case of the asymmetric initial particle configuration shown by the blue dots, the sphere translates in space, as expected. The deviation of the numerical results from the theory is shown in Fig. 6.2b. It decreases from 13.6 % (4 224 SPH particles) to 2.5 % (268 096 SPH particles). It can be concluded that YL predicts not only the correct analytical value but also leads to a constant pressure inside the drop, independently of the amount of SPH particles used. This is different from results known from the literature, e.g. [133, 222], where the simulated pressure decreases in the vicinity of the droplet boundary.

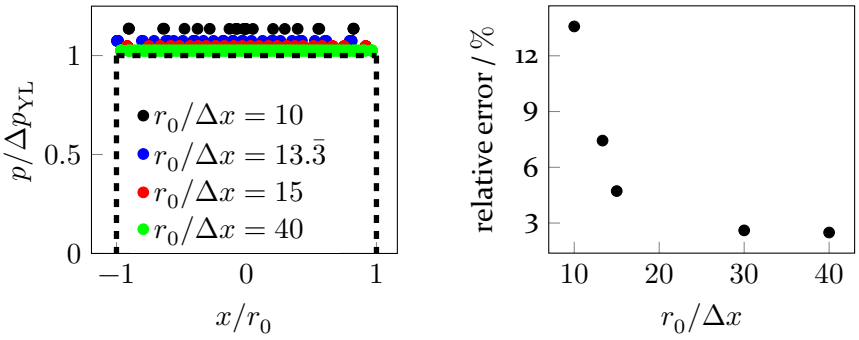

(a) Simulated pressure in a drop centered at $y/r_0 = z/r_0 = 0$ at $t = 1$ s for different spatial resolution. Note that the initially asymmetric positions of SPH particles for $\Delta x = \frac{r_0}{13.3}$ leads to a translation of the droplet in the negative x-direction.

(b) Deviation of the simulated steady state pressure inside the droplet from the analytical value, Eq. (6.2). The plot shows the relative error of the computed Laplace pressure as a function of the spatial resolution.

Figure 6.2: Comparison of the computed steady state pressure inside a droplet with the analytical prediction of the YL equation, Eq. (6.2).

6.1.2.2 Droplet oscillations

As a further validation test, the oscillation of a droplet with initial ellipsoidal shape

$$\frac{x^2}{(0.159\,r_0)^2} + \frac{y^2}{(0.794\,r_0)^2} + \frac{z^2}{(0.794\,r_0)^2} = 1, \tag{6.18}$$

as shown in Fig. 6.3, is investigated. The radius of the droplet at equilibrium

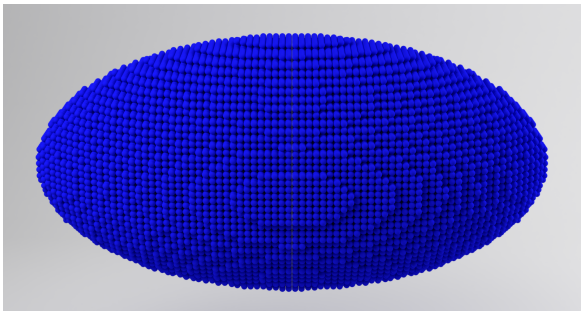

Figure 6.3: Initial arrangement of SPH particles representing an ellipsoid.

is $r_0 = 1.26 \cdot 10^{-3}\,\mathrm{m}$. For the SPH simulation, 66 928 particles are used. The period of the oscillation of an incompressible and inviscid drop was given by Rayleigh [163]

$$T_{\mathrm{osc}} = \pi \sqrt{\frac{r_0^3 \rho}{2\sigma}}\,. \tag{6.19}$$

For the chosen parameters, $T_{\mathrm{osc}} \approx 0.0314\,\mathrm{s}$. In the experiment, the initial deviation from the spherical shape leads to an oscillation with a decreasing amplitude due to the fluid's viscosity. In this simulation, the dynamic viscosity is $\eta = 6.5 \cdot 10^{-3}\,\mathrm{Pa\,s}$. Figure 6.4 shows the oscillation of the minor and major axes. The dimensionless capillary number characterizes the decay of the amplitude,

$$\mathrm{Ca} \equiv \frac{\eta U}{\sigma}, \tag{6.20}$$

which relates the viscous drag forces to surface tension. The characteristic velocity, U, is computed from the relaxation during the first oscillation, and the time needed for one oscillation, $T_{\mathrm{osc}} = 0.0358$, is calculated using Fourier analysis.

Here, $\mathrm{Ca} \approx 4.8 \cdot 10^{-2}$, and the relative error of the measured to the predicted time (given by Eq. (6.19)) for one oscillation period is 14.1 %

6.1.2.3 Cube droplet relaxation

In this test case, the relaxation of an initially cubic droplet under the action of surface tension is considered. The initial fluid cube of edge length $L = 10^{-3}\,\mathrm{m}$ consists of 64 000 SPH particles with $\Delta x = \frac{L}{20}$. Figure 6.5 shows the temporal evolution of the drop. The surface tension, combined with viscous forces, leads to an oscillatory relaxation of the drop, which eventually assumes the shape of a sphere.

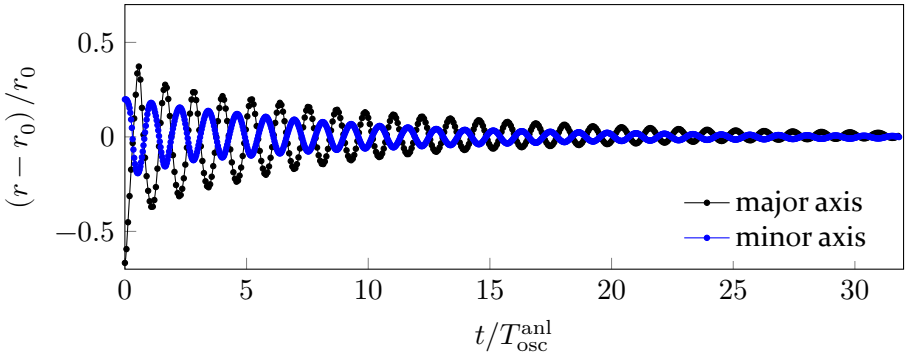

Figure 6.4: Damped oscillation of a viscous droplet using the YL pressure boundary condition. The curves show the extension of the drop along the major and minor axes as functions of time.

This example demonstrates the high precision of the novel method: even though there are regions of high curvature near the corners of the initial cube, with sparse particle support of the kernel function, the curvature is computed with sufficient accuracy to provide a stable fluid phase. The preserved symmetric configuration of the SPH particles during the simulation is another indicator for the simulation's stability.

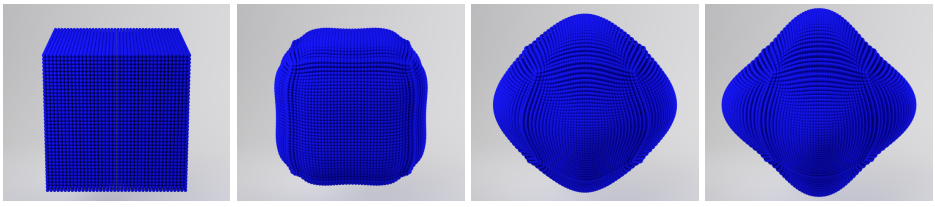

(a) t = 0 ms (b) t = 2 ms (c) t = 4 ms (d) t = 6 ms

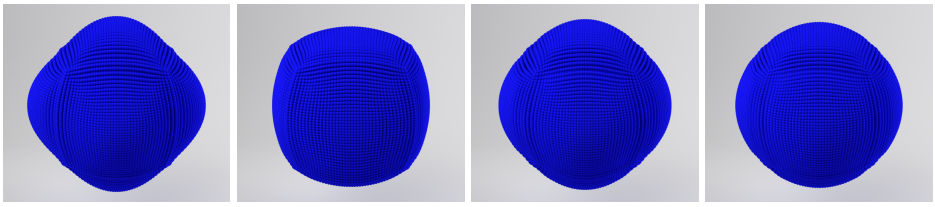

(e) t = 8 ms (f) t = 10 ms (g) t = 18 ms (h) t = 30 ms

Figure 6.5: Relaxation of an initially cubic droplet. The figures show snapshots of the droplet at increasing time.

6.1.2.4 Coalescence of spherical droplets

The stability of the novel simulation method with respect to concave surfaces is demonstrated by means of a simulation of two spherical droplets of radii $r_0 = 10^{-3}\,\mathrm{m}$. The initial particle spacing is $\Delta x = \frac{r_0}{20}$ resulting in a total of 67 104 SPH particles. Fig. 6.6 shows a snapshot of the coalescence process for an increasing time, evolving asymptotically to a larger droplet.

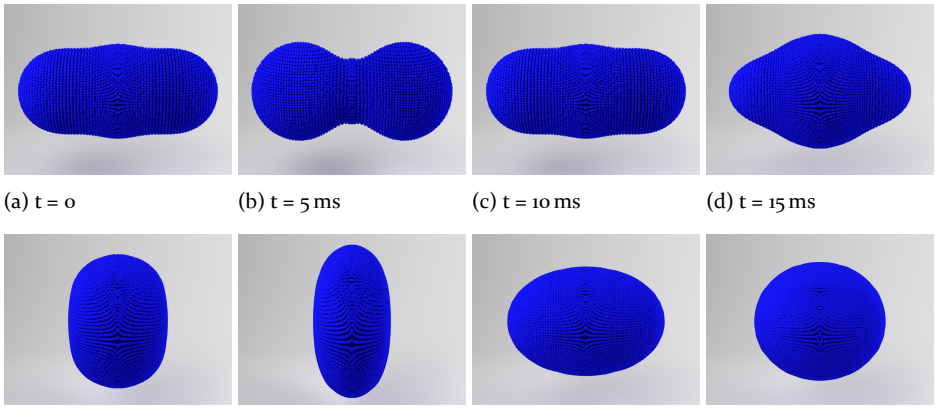

(a) t = 0 (b) t = 5 ms (c) t = 10 ms (d) t = 15 ms

(e) t = 20 ms (f) t = 25 ms (g) t = 37.5 ms (h) t = 150 ms

Figure 6.6: Coalescence of two spheres. The images show snapshots of the process with increasing time.

6.1.2.5 Plateau-Rayleigh instability

The final example verifies the novel simulation method by means of a simulation of the breakup of a cylindrical liquid jet known as Plateau-Rayleigh instability. The first SPH simulation of the Plateau-Rayleigh instability was performed by Olejnik and Szewc [147]. In their simulation, the liquid and gas phases were simulated and represented by SPH particles.

In this section, the break-up of the liquid cylindrical jet in a domain that is periodically repeated along the axis of the cylinder is investigated. The system's dimensions are given by the length $L = 0.0105\,\mathrm{m}$ and the radius $r_0 = 0.1\,L$ of the cylinder, periodically repeated at $x/L = 0$ and $x/L = 1$. The fluid is specified by its viscosity, $\eta = 0.01\,\mathrm{Pa\,s}$, density, $\rho = 1000\,\mathrm{kg\,m^{-3}}$, and surface tension, $\sigma = 0.022\,\mathrm{N\,m^{-1}}$. With the initial particle spacing, $\frac{L}{\Delta x} = 210$ and $\frac{r_0}{\Delta x} = 21$, 293 160 SPH particles are simulated. In contrast to the previous examples, a smaller smoothing length is applied, $h = 1.75\Delta x$, to increase the sensitivity of the surface curvature to local deformations. The instability,

according to linear stability analysis [55], is triggered by imposing an initial velocity field where the component in the x-direction is given by

$$u_x\left(t = 0\,\mathrm{s}\right) = u_0 \sin\left(\frac{2\pi x}{L}\right) . \tag{6.21}$$

Here, $u_0 = 0.171\,\mathrm{m\,s^{-1}}$ is the initial velocity amplitude and $x \in [0, L]$ in a periodic domain. This enforces divergent and convergent liquid regions within the initial liquid cylinder. As a result, the cylinder breaks into two drops with different radii centered at $x/L = 0.5$ and $x/L = 0$, $x/L = 1$ due to the applied periodic boundary conditions. To compare the shape and breakup time of the evolving drop at $x/L = 0.5$ with the literature, the dimensionless numbers given in [47] are considered to describe this problem. These are the Reynolds number, Re, the Weber number, We, and the capillary number, Ca,

$$\mathrm{Re} \equiv \frac{\rho U r_0}{\eta}\,; \quad \mathrm{We} \equiv \frac{\rho r_0 U^2}{\sigma}\,; \quad \mathrm{Ca} \equiv \frac{\mathrm{We}}{\mathrm{Re}}\,. \tag{6.22}$$

The properties employed in this test lead to $\mathrm{Re} \approx 18$, $\mathrm{We} \approx 1.4$, and $\mathrm{Ca} \approx 0.078$. The temporal evolution of the drop at $x/L = 0.5$ is given in dimensionless time t/t_c, where

$$t_c \equiv \sqrt{\frac{\rho r_0^3}{\sigma}} \approx 7.25 \cdot 10^{-3}\,\mathrm{s}\,. \tag{6.23}$$

Figure 6.7 shows a series of simulation snapshots at different times. The initial velocity field leads to the swelling of a droplet in the center of the simulation domain. Due to the surface tension, the filament tightens further and further until it eventually tears off at $\frac{t}{t_c} \approx 3.42$.

Figure 6.8 shows details of the simulation results compared to data from the literature. The initial growth process, quantified by the maximum radius of the filament, is in quantitative agreement with the data by Dai and Schmidt [47].

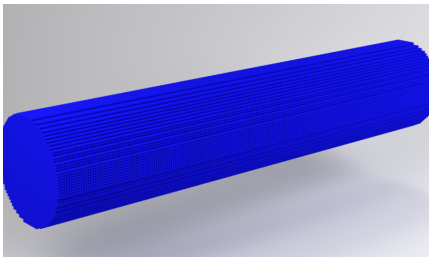

(a) $t/t_c = 0$

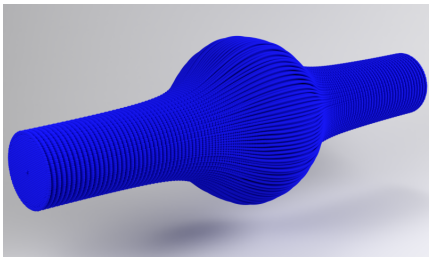

(b) $t/t_c = 1.38 \quad t = 10\,\text{ms}$.

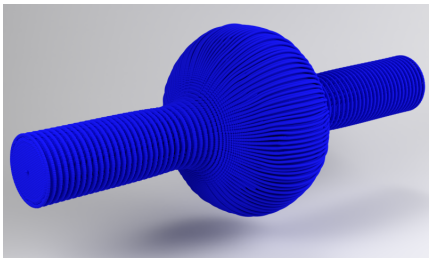

(c) $t/t_c = 2.07 \quad t = 15\,\text{ms}$.

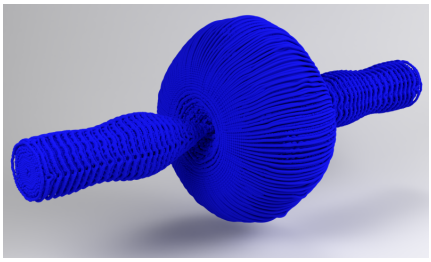

(d) $t/t_c = 3.45 \quad t = 25\,\text{ms}$.

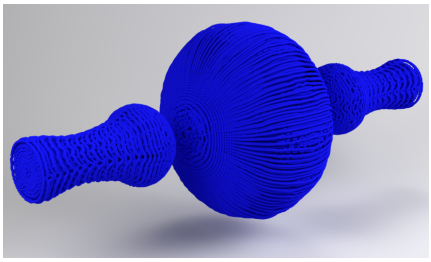

(e) $t/t_c = 4.14 \quad t = 30\,\text{ms}$.

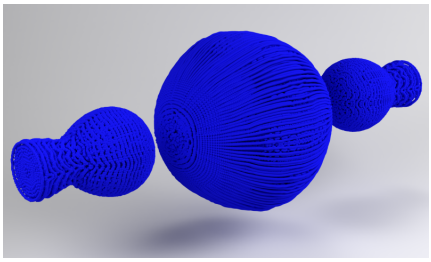

(f) $t/t_c = 4.83 \quad t = 35\,\text{ms}$.

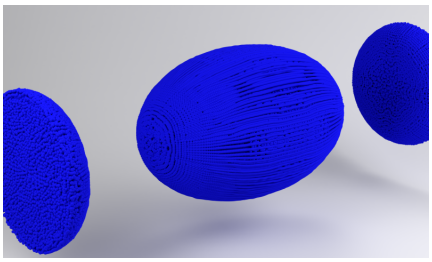

(g) $t/t_c = 6.90 \quad t = 50\,\text{ms}$.

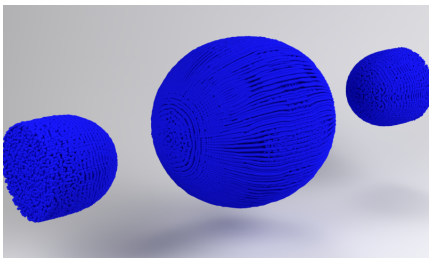

(h) $t/t_c = 8.28 \quad t = 60\,\text{ms}$.

Figure 6.7: Plateau-Rayleigh instability triggered by the initial velocity field. The tear-off takes place at $\frac{t}{t_c} \approx 3.42$, see also Fig. 6.8.

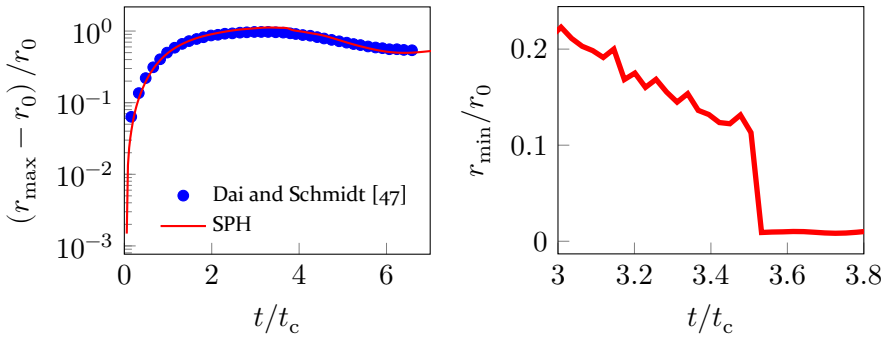

(a) Largest radius of the filament as a function of time. The data are in quantitative agreement with the results by Dai and Schmidt [47] who simulated the process using a lattice-based method.

(b) Smallest radius of the filament as a function of time, close to the time of tear-off. From this image, the moment of tear-off is determined at $\frac{t}{t_c} \approx 3.42$.

Figure 6.8: Quantitative measures describing the simulation of the Plateau-Rayleigh instability.

They used a lattice-based method to simulate the Plateau-Rayleigh instability using the same parameters as the simulation presented here. The exact time of the tear-off can be determined from the evolution of the smallest radius of the filament shown in Fig. 6.8b. From the data shown there, the tear-off time $\frac{t}{t_c} \approx 3.42$ is estimated. This value is slightly smaller than the times predicted in the literature, ($\frac{t}{t_c} \approx 6.49$ [47]; $\frac{t}{t_c} \approx 4.49$ [147]). Reasons for this difference in the tear-off time may be a different criterion for determining the tearing off, different regularization techniques, or the larger smoothing length used in this simulation compared to [147].

6.2 Continuum surface force method[1]

The CSF model introduced by [26] converts the surface stress boundary condition given in Eq. (2.64) into a volume force that is distributed across the two-phase interface. In this section, the CSF model is applied to free-boundaries. Moreover, the wetting force model by [31] which can be used in conjunction with CSF, is modified for the application to free-surface problems. For this reason, two approaches for modeling wetting and non-wetting contact angles are presented. In the absence of a solid substrate, both methods can be applied to model a liquid. Moreover, the Marangoni force model is introduced.

[1] Selected parts of the content of this section are submitted and intended for publication in Proceedings of CASICAM 2022 by Springer Nature. Reproduced with permission from Springer Nature.

For an in-viscid, incompressible fluid, the surface stress condition in Eq. (2.64) can be reduced to [26]

$$\mathbf{f}_{\sigma,a} = \frac{1}{\rho_a}\left(2\sigma_a\bar{\kappa}_a\hat{\tilde{\mathbf{n}}}_a + \nabla_{\mathrm{s}}\sigma_a\right)\delta_{\mathrm{s}}\,. \tag{6.24}$$

Here, δ_{s} is the interfacial delta function that peaks at the interface, and ∇_{s} is the surface gradient. Moreover, $\hat{\tilde{\mathbf{n}}}_a$ is the smoothed normalized normal vector at the position of a particle a. The first term on the right-hand side of Eq. (6.24) acts in the normal direction toward the two-phase interface, whereas the second term on the right-hand side acts tangentially to the phase boundary. The resultant surface tension force, which acts on interfacial SPH particles, given by its normal, $\mathbf{f}^{\perp}_{\sigma,a}$, and tangential component, $\mathbf{f}^{\parallel}_{\sigma,a}$, can be written as

$$\mathbf{f}_{\sigma,a} = \mathbf{f}^{\perp}_{\sigma,a} + \mathbf{f}^{\parallel}_{\sigma,a}\,, \tag{6.25}$$

which is added to the right-hand side of the momentum equation in Eq. (4.34).

For numerical reasons, the surface delta function must be replaced with an appropriate function whose integral is normalized to one. Moreover, the function must take a value of zero for all fluid elements that are not located within the two-phase transition region. Therefore, using

$$\delta_{\mathrm{s}} = |\mathbf{n}_a|\,, \tag{6.26}$$

where $\mathbf{n}_a$ is the normal vector of a particle before normalization, the normal component of surface tension, $\mathbf{f}^{\perp}_{\sigma,a}$, can be written as

$$\mathbf{f}^{\perp}_{\sigma,a} = 2\frac{\sigma_a}{\rho_a}\bar{\kappa}_a\hat{\tilde{\mathbf{n}}}_a\,|\mathbf{n}_a|\,. \tag{6.27}$$

The tangential component of surface tension will be introduced in Section 6.2.2. Similar to Eq. (6.15), the Shepard filter is applied to Eq. (6.27) to increase the stability of the approach according to

$$\mathbf{f}^{\perp}_{\sigma,a} = \left(1 + \frac{1}{S^{\mathrm{n}}_a}\right)\frac{\sigma_a}{\rho_a}\bar{\kappa}_a\hat{\tilde{\mathbf{n}}}_a\,|\mathbf{n}_a|\,, \tag{6.28}$$

where S^{n}_a is the Shepard filter computed from SPH particles ($\Omega^{\mathrm{n}} \subset \Omega$) whose normal vectors are not discarded by the threshold ϵ_{n} by

$$S^{\mathrm{n}}_a = \sum_{b\in\Omega}\frac{m_b}{\rho_b}W_{ab} \quad \text{if } |\mathbf{n}_b| > \epsilon_{\mathrm{n}}\,. \tag{6.29}$$

6.2.1 Wetting forces

To model the spreading of a fluid on a solid substrate, according to Breinlinger et al. [31], the spreading force per unit length which applies at the three-phase contact line can be described as a function of the transient, Θ, and the equilibrium contact angle, Θ_∞, by

$$\mathbf{F}_{\mathrm{w}}^{\mathrm{slg}} = \sigma \left(\cos\Theta - \cos\Theta_\infty\right) . \tag{6.30}$$

The subset of liquid SPH particles in the vicinity of the three-phase contact angle is affected by Eq. (6.30).

In the following, two approaches are presented, which attempt to model wetting contact angles $\Theta_\infty < 90^\circ$ or non-wetting contact angles $\Theta_\infty > 90^\circ$ in problems where the gas phase is not represented by SPH particles.

6.2.1.1 Wetting contact angles ($\Theta_\infty < 90^\circ$)

To model wetting contact angles, the normal vectors of liquid SPH particles and selected solid SPH particles in the vicinity of the three-phase contact line are modified. The normal vectors at the positions of the SPH particles are computed by

$$\mathbf{n}_a^{\mathrm{lg}} = -\sum_b \frac{m_b}{\rho_b} \nabla W_{ab} , \qquad \hat{\tilde{\mathbf{n}}}_a^{\mathrm{lg}} = \frac{\tilde{\mathbf{n}}_a^{\mathrm{lg}}}{\left|\tilde{\mathbf{n}}_a^{\mathrm{lg}}\right|} \tag{6.31}$$

and the smoothed normal vectors and normalized smoothed normal vectors are given by

$$\tilde{\mathbf{n}}_a^{\mathrm{lg}} = \frac{1}{S_a} \sum_b \frac{m_b}{\rho_b} \mathbf{n}_b^{\mathrm{lg}} W_{ab} , \qquad \hat{\tilde{\mathbf{n}}}_a^{\mathrm{lg}} = \frac{\tilde{\mathbf{n}}_a^{\mathrm{lg}}}{\left|\tilde{\mathbf{n}}_a^{\mathrm{lg}}\right|} . \tag{6.32}$$

The normal vectors $\mathbf{n}_a^{\mathrm{lg}}$ and $\hat{\tilde{\mathbf{n}}}_a^{\mathrm{lg}}$ are used to substitute $\mathbf{n}_a$ and $\hat{\mathbf{n}}_a$ in Eq. (6.28) to model wetting contact angles.

Similarly, the normal vectors pointing outwards of the solid phase at the position of an SPH particle a are given by

$$\mathbf{n}_a^{\mathrm{sf}} = -\sum_{b\in\Omega^{\mathrm{s}}} \frac{m_b}{\rho_b} \nabla W_{ab} , \qquad \hat{\mathbf{n}}_a^{\mathrm{sf}} = \frac{\mathbf{n}_a^{\mathrm{sf}}}{\left|\mathbf{n}_a^{\mathrm{sf}}\right|} . \tag{6.33}$$

The corresponding smoothed and normalized smoothed normal vectors are defined by

$$\tilde{\mathbf{n}}_a^{\mathrm{sf}} = \frac{1}{S_a^{\mathrm{s}}} \sum_{b\in\Omega^{\mathrm{s}}} \frac{m_b}{\rho_b} \mathbf{n}_a^{\mathrm{sf}} W_{ab} , \qquad \hat{\tilde{\mathbf{n}}}_a^{\mathrm{sf}} = \frac{\tilde{\mathbf{n}}_a^{\mathrm{sf}}}{\left|\tilde{\mathbf{n}}_a^{\mathrm{sf}}\right|} . \tag{6.34}$$

Here, S_a^{s} is the Shepard filter that is computed using only solid particles by

$$S_a^{\mathrm{s}} = \sum_{b \in \Omega^{\mathrm{s}}} \frac{m_b}{\rho_b} W_{ab} \,. \tag{6.35}$$

To include the wetting forces, the smoothed normal correction proposed by [31] is applied to liquid particles in the vicinity of the three-phase contact line (Ω^{slg}). These particles are identified by the normal vectors, which are not discarded by the applied threshold ($\left|\mathbf{n}_a^{\mathrm{lg}}\right| \geq \epsilon_{\mathrm{n}}$) in combination with the condition $S_a^{\mathrm{s}} > 0$ to identify liquid SPH particles which have solid particles in their neighborhood.

To apply the normal correction to the normal vectors at the position of the SPH particles that are located in the vicinity of the three-phase contact line, the tangent and normalized tangent vectors of particles near the solid-fluid interface must be computed by

$$\mathbf{t}_a^{\mathrm{sf}} = \hat{\tilde{\mathbf{n}}}_a^{\mathrm{lg}} - \left(\hat{\tilde{\mathbf{n}}}_a^{\mathrm{lg}} \cdot \hat{\tilde{\mathbf{n}}}_a^{\mathrm{sf}}\right) \hat{\tilde{\mathbf{n}}}_a^{\mathrm{sf}} \,, \qquad \hat{\mathbf{t}}_a^{\mathrm{sf}} = \frac{\mathbf{t}_a^{\mathrm{sf}}}{|\mathbf{t}_a^{\mathrm{sf}}|} \,. \tag{6.36}$$

Now, the corrected normal vectors of liquid SPH particles (Ω^{l}) are obtained from the desired equilibrium contact angle

$$\hat{\mathbf{n}}_{\infty,a}^{\mathrm{lg}} = \hat{\mathbf{t}}_a^{\mathrm{sf}} \sin\Theta_\infty - \hat{\tilde{\mathbf{n}}}_a^{\mathrm{sf}} \cos\Theta_\infty \,. \tag{6.37}$$

To avoid an instantaneous change of the modified normal vectors, a transition from the computed normal vectors, $\hat{\tilde{\mathbf{n}}}_a^{\mathrm{lg}}$, to the desired normal vectors, $\hat{\tilde{\mathbf{n}}}_{\infty,a}^{\mathrm{lg}}$, is applied depending on distance of the particle to the solid phase by

$$\hat{\tilde{\mathbf{n}}}_a^{\mathrm{slg}} = \frac{f_a \hat{\tilde{\mathbf{n}}}_a^{\mathrm{lg}} + (1 - f_a)\, \hat{\mathbf{n}}_{\infty,a}^{\mathrm{lg}}}{\left| f_a \hat{\tilde{\mathbf{n}}}_a^{\mathrm{lg}} + (1 - f_a)\, \hat{\mathbf{n}}_{\infty,a}^{\mathrm{lg}} \right|} \,. \tag{6.38}$$

Here, f_a is the normal distance between a liquid SPH particle and the closest solid SPH particle in the direction of $\hat{\tilde{\mathbf{n}}}_a^{\mathrm{s}}$ scaled with the kernel radius and is given by

$$f_a\left(d_a^{\mathrm{s}}\right) = \begin{cases} 0 & \forall \quad d_a^{\mathrm{s}} < 0, \\ d_a^{\mathrm{s}} / r_{\max} & \forall \quad 0 \leq d_a^{\mathrm{s}} \leq r_{\max} \\ 1 & \forall \quad d_a^{\mathrm{s}} > r_{\max} \end{cases} . \tag{6.39}$$

The distance d_a^{s} is defined by

$$d_a^{\mathrm{s}} = \min\left((\mathbf{r}_a - \mathbf{r}_b) \cdot \hat{\tilde{\mathbf{n}}}_a^{\mathrm{sf}}\right) - \Delta x\,. \tag{6.40}$$

The normal vectors computed in Eq. (6.38) replace the normal vectors obtained by Eq. (6.31) if a liquid SPH particle $a \in \Omega^{\mathrm{l}}$ is located in the vicinity of the three-phase contact line ($a \in \Omega^{\mathrm{slg}}$) which is verified by

$$a \in \Omega^{\mathrm{slg}} \text{ if } S_a^{\mathrm{s}} > 0 \wedge |\mathbf{n}_a| > \epsilon_{\mathrm{n}} \tag{6.41}$$

in this work. Thus, the normal vectors of the liquid SPH particles are given by

$$\hat{\tilde{\mathbf{n}}}_a^{\mathrm{lg}} = \begin{cases} \hat{\tilde{\mathbf{n}}}_a^{\mathrm{slg}} & \text{if } a \in \Omega^{\mathrm{slg}} \\ \hat{\tilde{\mathbf{n}}}_a^{\mathrm{lg}} & \text{else} \end{cases}. \tag{6.42}$$

In the course of this work, it was found that including the modified normal vectors of liquid SPH particles into the curvature computation is not sufficient to obtain stable droplet shapes for adjusted equilibrium contact angles ($\Theta_{\infty} < 90^{\circ}$) when a free boundary is present. For this reason, the normal vectors of selected solid SPH particles in the vicinity of the three-phase contact line are modified and included in the curvature computation of liquid SPH particles to increase the support of neighboring SPH particles. The proposed approach applies a fixed normal correction to selected solid particles in the neighborhood of a fluid SPH particle, intending to correct the otherwise underestimated curvatures, which have led to the continuous spreading of the liquid droplet on a solid substrate.

Therefore, the normal vectors of solid particles b in the neighborhood of a liquid, central SPH particle a, are modified by

$$\hat{\mathbf{n}}_{\infty,b}^{\mathrm{lg,s}} = \begin{cases} \hat{\mathbf{t}}_a^{\mathrm{sf}} \sin\Theta_{\infty}^{\mathrm{s}} - \hat{\tilde{\mathbf{n}}}_a^{\mathrm{sf}} \cos\Theta_{\infty}^{\mathrm{s}} & \text{if } a \in \Omega^{\mathrm{slg}} \wedge \mathbf{r}_{ab} \cdot \hat{\tilde{\mathbf{n}}}_a^{\mathrm{lg}} > 0 \\ 0 & \text{else} \end{cases}. \tag{6.43}$$

Here, $\Theta_{\infty}^{\mathrm{s}}$ is the desired contact angle to adjust the solid normal vectors. Furthermore, the condition $\hat{\tilde{\mathbf{n}}}_a^{\mathrm{lg}} > 0$ identifies all neighboring solid SPH particles which are located on the liquid side of the tangent plane at the position of the liquid particle a defined by the normal vector of the liquid particle a. Solid SPH particles that are located on the gas side of the tangent plane are not considered in the curvature computation of the liquid SPH particle. Moreover,

$\Theta^{\mathrm{s}}_{\infty}$ is a free parameter to calibrate the wetting forces. By setting $\Theta^{\mathrm{s}}_{\infty} > \Theta_{\infty}$, the underestimated curvatures are corrected to larger values, which prevents the continuous spreading of the liquid on the solid substrate. Figure 6.9 shows cuts through the axis of symmetry of two drops resting on a solid substrate. For a desired equilibrium contact angle of $\Theta_{\infty} = 30^{\circ}$ or $\Theta_{\infty} = 60^{\circ}$, the presented approach modifies the normal vectors of the red-colored solid SPH particles during the curvature computation. Note that each liquid SPH particle has its own set of identified solid particles whose normal vectors are used temporarily according to Eq. (6.43) during the curvature computation. The identification

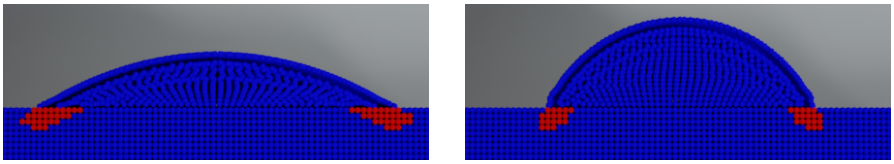

(a) $\Theta_{\infty} = 30^{\circ}$ (b) $\Theta_{\infty} = 60^{\circ}$

Figure 6.9: Identified solid SPH particles (red) representing an extension of the liquid-gas interface.

of the solid SPH particles, the correction of the normal vectors of the solid SPH particles, and the computation of the curvature at the position of a liquid SPH particle a are carried out simultaneously according to

$$\begin{aligned} \bar{\kappa}_a = &- 0.5 \sum_{b \in \Omega^{\mathrm{l}}} \frac{m_b}{\rho_b} \left(\hat{\tilde{\mathbf{n}}}^{\mathrm{lg}}_a - \hat{\tilde{\mathbf{n}}}^{\mathrm{lg}}_b \right) \hat{\nabla} W_{ab} \\ &- 0.5 \sum_{b \in \Omega^{\mathrm{s}}} \frac{m_b}{\rho_b} \left(\hat{\tilde{\mathbf{n}}}^{\mathrm{lg}}_a - \hat{\mathbf{n}}^{\mathrm{lg,s}}_{\infty,b} \right) \hat{\nabla} W_{ab} \,, \end{aligned} \tag{6.44}$$

using the divergence approximation in Eq. (4.13). Here, the normalized kernel gradient [25, 144] is given by

$$\hat{\nabla} W_{ab} = \mathbf{L}_a \nabla W_{ab} \,, \tag{6.45}$$

where the correction matrix, $\mathbf{L}_a$, is computed by including all neighboring particles

$$\mathbf{L}_a = \left(\sum_b \frac{m_b}{\rho_b} \mathbf{r}_{ab} \otimes \nabla W_{ab} \right)^{-1} . \tag{6.46}$$

Note that the normal vectors of the included solid SPH particles are not considered in the computation of S^{n}_a in Eq. (6.29) since they only exist temporarily during the curvature computation.

Due to the avoided discretization of the gas phase using SPH particles, the application of arbitrary contact angles to the free-surface CSF model is still challenging in terms of stability and robustness. Therefore, additional conditions to achieve higher stability in the simulations are employed. The applied normalized kernel gradient in Eq. (6.45) is replaced with the normalized kernel gradient computed exclusively from liquid SPH particles in Eq. (6.8) if the number of neighboring SPH particles leads to an empirical threshold of $S_a < 0.6$.

For very low wetting contact angles, $\Theta_\infty \leq 30^\circ$, the maximum height of the liquid film might be in the same length scale as the kernel radius, $r_{\max}$. In this case, the smoothed normal correction leads to an incorrect computed surface curvature due to erroneous normal corrections for SPH particles if $\hat{\tilde{\mathbf{n}}}_a^{\mathrm{lg}} \approx \hat{\tilde{\mathbf{n}}}_a^{\mathrm{sf}}$. For this reason, the normal correction of liquid SPH particles is only applied if $\hat{\tilde{\mathbf{n}}}_a^{\mathrm{lg}} \cdot \hat{\tilde{\mathbf{n}}}_a^{\mathrm{sf}} \leq 0.995$.

6.2.1.2 Non-wetting contact angles ($\Theta_\infty > 90^\circ$)

Instead of computing the curvature using liquid and selected solid particles, as done in the previous section for wetting contact angles, only liquid SPH particle neighbors are now considered for modeling non-wetting contact angles. Analogous to the normal correction scheme shown in Section 6.2.1.1, the tangent vector, $\mathbf{t}_a^{\mathrm{sf,l}}$, at the position of a liquid SPH particle must be computed by

$$\mathbf{t}_a^{\mathrm{sf,l}} = \hat{\tilde{\mathbf{n}}}_a^{\mathrm{lg,l}} - \left(\hat{\tilde{\mathbf{n}}}_a^{\mathrm{lg,l}} \cdot \hat{\tilde{\mathbf{n}}}_a^{\mathrm{sf}}\right) \hat{\tilde{\mathbf{n}}}_a^{\mathrm{sf}}, \qquad \hat{\mathbf{t}}_a^{\mathrm{sf,l}} = \frac{\mathbf{t}_a^{\mathrm{sf,l}}}{\left|\mathbf{t}_a^{\mathrm{sf,l}}\right|}, \tag{6.47}$$

where $\hat{\tilde{\mathbf{n}}}_a^{\mathrm{lg,l}}$ is given in Eq. (6.6). Furthermore, the corrected normal vectors of liquid SPH particles ($a \in \Omega^{\mathrm{l}}$) for a desired equilibrium contact angle are obtained through a smooth transition from the computed normal vectors, $\hat{\tilde{\mathbf{n}}}_a^{\mathrm{lg}}$, to the desired normal vectors, $\hat{\tilde{\mathbf{n}}}_a^{\mathrm{lg},\infty}$, according to

$$\hat{\tilde{\mathbf{n}}}_a^{\mathrm{slg,l}} = \frac{f_a \hat{\tilde{\mathbf{n}}}_a^{\mathrm{lg,l}} + (1 - f_a)\, \hat{\mathbf{n}}_{\infty,a}^{\mathrm{lg}}}{\left| f_a \hat{\tilde{\mathbf{n}}}_a^{\mathrm{lg,l}} + (1 - f_a)\, \hat{\mathbf{n}}_{\infty,a}^{\mathrm{lg}} \right|}, \tag{6.48}$$

where

$$\hat{\mathbf{n}}_{\infty,a}^{\mathrm{lg}} = \hat{\mathbf{t}}_a^{\mathrm{sf,l}} \sin\Theta_\infty - \hat{\tilde{\mathbf{n}}}_a^{\mathrm{sf}} \cos\Theta_\infty . \tag{6.49}$$

The distance to the solid substrate, f_a, can be computed by Eq. (6.39). The modified normal vectors, $\tilde{\hat{\mathbf{n}}}_a^{\mathrm{slg,l}}$, replace the computed normal vectors if the liquid SPH particle is located in vicinity of the three-phase contact line (identified by Eq. (6.41)) by

$$\tilde{\hat{\mathbf{n}}}_a^{\mathrm{lg}} = \begin{cases} \tilde{\hat{\mathbf{n}}}_a^{\mathrm{slg,l}} & \text{if } a \in (\Omega^{\mathrm{slg}} \wedge \Omega^{\mathrm{l}}) \\ \hat{\tilde{\mathbf{n}}}_a^{\mathrm{lg,l}} & \text{else} \end{cases} . \tag{6.50}$$

Thus, the mean curvature of a liquid SPH particle is given by

$$\bar{\kappa}_a = -0.5 \sum_{b \in \Omega^{\mathrm{l}}} \frac{m_b}{\rho_b} \left(\tilde{\hat{\mathbf{n}}}_a^{\mathrm{lg,l}} - \tilde{\hat{\mathbf{n}}}_b^{\mathrm{lg,l}} \right) \hat{\nabla}^{\mathrm{l}} W_{ab} \,, \tag{6.51}$$

where the renormalized kernel gradient, $\hat{\nabla}^{\mathrm{l}} W_{ab}$, is obtained by Eq. (6.8). The normal vectors $\mathbf{n}_a$ and $\tilde{\hat{\mathbf{n}}}_a$ in Eq. (6.28) are substituted with $\mathbf{n}_a^{\mathrm{lg}}$ and $\tilde{\hat{\mathbf{n}}}_a^{\mathrm{lg}}$ provided by Eqs. (6.31) and (6.50) to model non-wetting contact angles.

6.2.2 Marangoni forces

If the liquid-gas interface is exposed to large temperature gradients, as is the case in laser processing of metals, thermocapillary flow arises. This motion occurs in this work at the liquid-gas interface in a tangential direction and transports mass from hot to cooler regions due to surface tension gradients. According to the CSF formulation in Eq. (6.24), the volumetric Marangoni force, denoted by the superscript $\parallel$ is given by

$$\mathbf{f}_{\sigma,a}^{\parallel} = \nabla_{\mathrm{s}} \sigma_a \delta_{\mathrm{s}} / \rho_a \,. \tag{6.52}$$

As introduced in Eq. (3.15) in Section 3.5, the surface tension is assumed to depend linearly on the temperature. Thus, the surface tension coefficient of a particle a is given by

$$\sigma_a = \sigma_0 + \sigma_T (T_a - T_0) \,, \tag{6.53}$$

where T_a is the temperature of a particle a. Using the linear dependence in Eq. (6.53), the surface gradient of the temperature is obtained by removing the normal component by [202]

$$\nabla_{\mathrm{s}} T_a = \nabla T_a - \left(\nabla T_a \cdot \tilde{\hat{\mathbf{n}}}_a^{\mathrm{lg}} \right) \tilde{\hat{\mathbf{n}}}_a^{\mathrm{lg}} \,, \tag{6.54}$$

where ∇T_a is obtained by

$$\nabla T_a = -\sum_b \frac{m_b}{\rho_b} \left(T_a - T_b\right) \hat{\nabla} W_{ab} \tag{6.55}$$

using Eq. (4.13) and the renormalized kernel gradient given in Eq. (4.26). Finally, Eq. (6.56) is applied to a single layer of interfacial SPH particles at the liquid-gas interface. Thus, the surface delta function in Eq. (6.52) is substituted with $\delta_\mathrm{s} = 1/\Delta x$ if $a \in \Omega^\mathrm{v}$, which leads to

$$\mathbf{f}^{\parallel}_{\sigma,a} = \frac{1}{\rho_a \Delta x} \sigma_{T,a} \left(\nabla T_a - \left(\nabla T_a \cdot \hat{\tilde{\mathbf{n}}}^{\mathrm{lg}}_a \right) \hat{\tilde{\mathbf{n}}}^{\mathrm{lg}}_a \right) . \tag{6.56}$$

To avoid the penetration of liquid SPH particles into solid walls, which could lead to unstable simulations, Eq. (6.56) is only applied to liquid SPH particles if $S^\mathrm{s}_a \leq 0.5$.

6.2.3 Validation

To validate the presented modified CSF and wetting models, which are applicable to free surface problems, the momentum equation for the liquid phase is modeled by

$$\frac{\mathrm{D}\mathbf{u}_a}{\mathrm{D}t} = \mathbf{f}_{\mathrm{p},a} + \mathbf{f}_{\eta,a} + \mathbf{f}^{\perp}_{\sigma,a} + \mathbf{f}_{g,a} \tag{6.57}$$

in the following validation cases (except of Section 6.2.3.6 where the Marangoni forces are validated). To ensure incompressibility, the PPE in Eq. (4.49) is solved for liquid SPH particles near the free boundary and using Eq. (4.48) otherwise. The PPE is solved for solid wall particles according to Eq. (4.68) if $S^\mathrm{l}_a > 10^{-3}$ and using Eq. (4.48) for the remaining solid SPH particles. Furthermore, the no-slip boundary condition at walls, introduced in Section 4.4, is applied. The numerical time step is adjusted according to the CFL condition in Eq. (4.66).

6.2.3.1 Laplace pressure jump

As already shown in Section 6.1.2.1, the equilibrium pressure inside a sphere depends on its radius. Therefore, the pressure inside a drop with a radius of $r_0 = 10^{-3}\,\mathrm{m}$ is compared with the analytical prediction of Eq. (6.2). With $\sigma = 0.01\,\mathrm{N\,m^{-1}}$ the pressure inside the drop exceeds the ambient pressure by $\Delta p_\mathrm{YL} = 20\,\mathrm{Pa}$. Moreover, $\eta = 0.05\,\mathrm{Pa\,s}$, $\rho = 1000\,\mathrm{kg\,m^{-3}}$, $p_\mathrm{amb} = 0\,\mathrm{Pa}$ and no body forces due to gravity are applied.

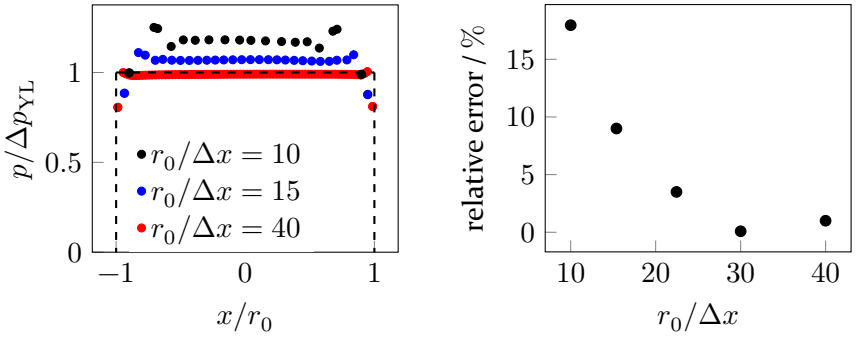

(a) Pressure field in a drop centered in the origin of Euclidean space along the x-axis ($y/r_0 = z/r_0 = 0$) for different spatial resolutions. The pressure is averaged in time in the range of $0.8 \leq t \leq 1\,\mathrm{s}$.

(b) Relative error of the simulated steady state pressure inside the droplet from the analytical value, Eq. (6.2).

Figure 6.10: Comparison of the computed steady state pressure inside a droplet with the analytical prediction of the YL equation, Eq. (6.2).

All smoothed normal vectors with a magnitude smaller than $\epsilon_{\mathrm{n}} = \frac{0.3}{h}$ are discarded from the curvature computation. The smoothing length of the kernel function is set to $h = 2\Delta x$. Furthermore, $\{4\,224,\ 9\,915, 44\,720,\ 113\,104,\ 268\,096\}$ SPH particles are placed on a rectangular lattice with spacing $\Delta x \in \{\frac{r_0}{10}, \frac{r_0}{15}, \frac{r_0}{22}, \frac{r_0}{30}, \frac{r_0}{40}\}$. The pressure inside the drop along a cut through the symmetry axis is averaged from $t = 0.8\,\mathrm{s}$ to $t = 1.0\,\mathrm{s}$. The reason for taking the average of the pressure field lies in observed temporal fluctuations. The computed equilibrium pressure is shown in Fig. 6.10a. When comparing the averaged equilibrium pressure with the pressure field in Fig. 6.2 obtained by the YL pressure boundary condition, the pressure inside the drop is not constant along the measured symmetry axis of the drop. Instead, the pressure decreases in the vicinity of the liquid-gas interface compared to the pressure in the center of the drop. This result agrees with results known from the literature, e.g. [133, 222], where the simulated pressure decays in the vicinity of the liquid-gas droplet boundary. For an increasing number of SPH particles (increasing spatial resolution), the pressure in the center of the droplet converges towards the analytical prediction. The deviation of the numerical results from the analytical prediction is shown in Fig. 6.10b. The relative error decreases from $18.0\,\%$ using 4 224 SPH particles to $0.8\,\%$ for 113 104 SPH particles and takes a value $1.0\,\%$ when 268 096 SPH particles discretize the drop. The increase of the relative error using 268 096 SPH particles compared to fewer SPH particles could lie in using the Shepard filter to scale the YL-pressure in Eq. (6.29).

The applied normal threshold in this validation case could be a reason for underestimating the analytical YL pressure inside the drop for high spatial resolution since it truncates the applied forces at the liquid-gas interface.

6.2.3.2 Droplet oscillations

In contrast to Section 6.1.2.2, where the frequency of oscillation is compared to the analytical prediction for an inviscid fluid, here, the simulated frequency of oscillation and the damping coefficient is compared to the corresponding analytical values for a viscous drop. The spatial-temporal change of the liquid-gas interface of an axis-symmetric drop is given by [1]

$$r\left(\theta, t\right) = r_0 \left(1 + \epsilon_2(t) P_2\left(\cos\left(\theta\right)\right) - \frac{1}{5}\epsilon_2^2(t)\right) , \tag{6.58}$$

where P_2 is the second degree Legendre polynomial, r_0 is the droplet radius in equilibrium shape and $\epsilon_2(t)$ is given by

$$\epsilon_2(t) \approx 0.08 \mathrm{e}^{-\lambda_2 t} \cos\left(\omega_{2,0} t\right) . \tag{6.59}$$

Here, the frequency of oscillation $\omega_{2,0}$ and damping constant λ_2 are given by

$$\omega_{2,0} = \sqrt{\frac{8\sigma}{\rho r_0^3}} , \qquad \lambda_2 = \frac{5\eta}{\rho r_0^2} . \tag{6.60}$$

In contrast to Section 6.1.2.2, where the frequency of oscillation is compared to the analytical prediction for an inviscid fluid, here, the simulated frequency of oscillation and the damping coefficient is compared to the corresponding analytical values for a viscous drop.

The initial radius at $t = 0\,\mathrm{s}$ is given as a function of the angle θ by

$$r\left(\theta, t = 0\right) = r_0 \left(1 + 0.08 P_2\left(\cos\left(\theta\right)\right) - \frac{1}{5} 0.08^2\right) . \tag{6.61}$$

Using $\Delta x = 5{\cdot}10^{-5}\,\mathrm{m}$, 33 240 SPH particles are initially placed on a rectangular lattice representing an ellipsoid with a near spherical shape as shown in Fig. 6.11. In this simulation test case $\sigma = 0.01\,\mathrm{N\,m^{-1}}$, $\rho = 1000\,\mathrm{kg\,m^{-3}}$, $\eta = 5{\cdot}10^{-3}\,\mathrm{Pa\,s}$ and $h = 2\Delta x$. According to Eq. (6.19) the time period for one oscillation is given by $T_{\mathrm{osc}} = 2.22{\cdot}10^{-2}\,\mathrm{s}$, which agrees with Eq. (6.60) since $T_{\mathrm{osc}} = 2\pi/\omega_{2,0}$. Moreover, the damping constant is $\lambda_2 = 25\,\mathrm{s^{-1}}$. Figure 6.12 shows the major and minor axes of the drop which oscillates over time due to initial ellipsoidal shape. The capillary number is computed according to Eq. (6.20) from the

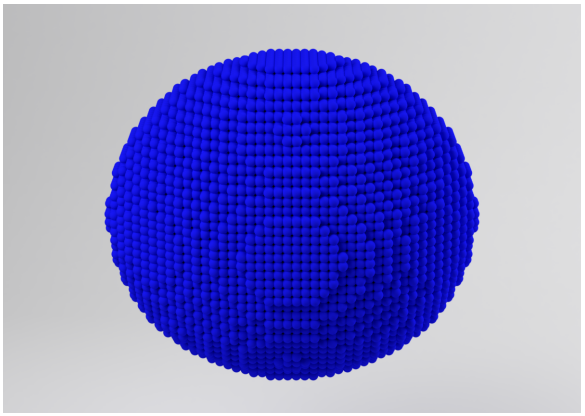

Figure 6.11: Ellipsoid close to spherical shape represented by SPH particles.

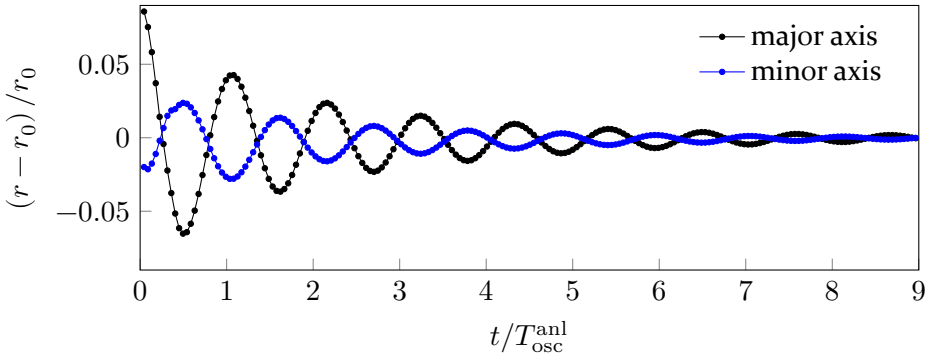

Figure 6.12: Damped oscillation of a viscous droplet. The curves show the extension of the drop along the major and minor axes as functions of time.

first oscillation of the major axis and is given by $\mathrm{Ca} = 9.9 \cdot 10^{-3}$.

Fitting the formula of a damped harmonic oscillator with amplitude A_{osc},

$$\omega = A_{\text{osc}} \exp\left(-\lambda_{\text{osc}}\right) \cos\left(\omega_{\text{osc}} t\right) , \tag{6.62}$$

to the simulated interface position of the major axis over time, allows to measure the damping constant and the angular frequency given by $\lambda_{\text{osc}} = 22.44\,\mathrm{s}^{-1}$ and $\omega_{\text{osc}} = 261.5\,\mathrm{s}^{-1}$, respectively. The relative error between the simulated and theoretical angular frequency and damping constant is 7.5 % and 5.1 %. It was found that adjusting the normal threshold, ϵ_{n}, to an appropriate value is crucial for obtaining stable simulations. The problem lies in distributing the surface tension forces across the liquid-gas interface to the liquid SPH particles. Any asymmetry in the applied forces with respect to

Table 6.1: Equilibrium contact angles used to correct the normal vectors of liquid and solid SPH particles in the vicinity of the three-phase contact line .

Θ_∞ / °	15	30	45	60	75	90	105	120	135	150
$\Theta^{\mathrm{s}}_\infty$ / °	15	32	50	65	85	105	-	-	-	-

the axes of symmetry leads to destabilization of the oscillating drop. If the normal threshold is too low, the curvature computation becomes erroneous. In contrast, if the normal threshold is too high, surface tension may be applied only to an interfacial layer of SPH particles.

6.2.3.3 Equilibrium shape of drops resting on a plane substrate

Depending on the adjusted equilibrium contact angle in Eq. (6.30), the liquid phase shows a wetting or non-wetting behavior on a solid substrate. In this section $\eta = 5 \cdot 10^{-2}\,\mathrm{Pa\,s}$, $\rho = 1000\,\mathrm{kg\,m^{-3}}$ and $p_\mathrm{o} = 0\,\mathrm{Pa}$. Initially, a hemisphere with radius $r_0 = 10^{-3}\,\mathrm{m}$ is represented by SPH particles placed on a rectangular lattice with $r_0/\Delta x = 20$. The smoothing length and kernel radius are given by $h = 2.5\Delta x$ and $r_{\max} = 5\Delta x$, respectively. Therefore, the thickness of the underlying solid substrate is $5\Delta x$. Moreover, the threshold for the normal vectors is $0.1/h$. For the desired contact angle, Θ_∞, the normal vectors of the liquid particles are modified. Similarly, the approach presented in Section 6.2.1.1 necessitates modifying the normal vectors (corresponding to a contact angle $\Theta^{\mathrm{s}}_\infty$) of selected solid SPH particles, which can be seen as an extension of the liquid geometry. The applied contact angles of solid and liquid particles are shown in Tab. 6.1. Figure 6.13 shows the drop shapes for different adjusted contact angles, $\Theta_\infty \in \{15^\circ,\ 60^\circ,\ 120^\circ,\ 150^\circ\}$, at $t = 1\,\mathrm{s}$ where equilibrium is assumed. The corresponding total kinetic energy of all liquid SPH particles is shown in Fig. 6.14 over time. It can be seen that the kinetic energy of the SPH particles for wetting contact angles decreases by several orders of magnitude. For $\Theta_\infty = 15^\circ$ and $\Theta_\infty = 60^\circ$, the kinetic energy at $t = 1\,\mathrm{s}$ is given by $1.16 \cdot 10^{-14}\,\mathrm{J}$ and $6.94 \cdot 10^{-15}\,\mathrm{J}$, respectively. Compared to the wetting contact angles, the non-wetting contact angles lead to larger kinetic energies of the liquid SPH particles. At $t = 1\,\mathrm{s}$ the kinetic energies are given by $7.43 \cdot 10^{-12}\,\mathrm{J}$ and $1.38 \cdot 10^{-12}\,\mathrm{J}$ for $\Theta_\infty = 120^\circ$ and $\Theta_\infty = 150^\circ$. Moreover, the kinetic energies fluctuate more strongly compared to the wetting contact angles. The reason lies in the application of the wetting forces to the triple line region. For non-wetting contact angles, problems in identifying these particles arise. This leads to a vortex flow of particles in this

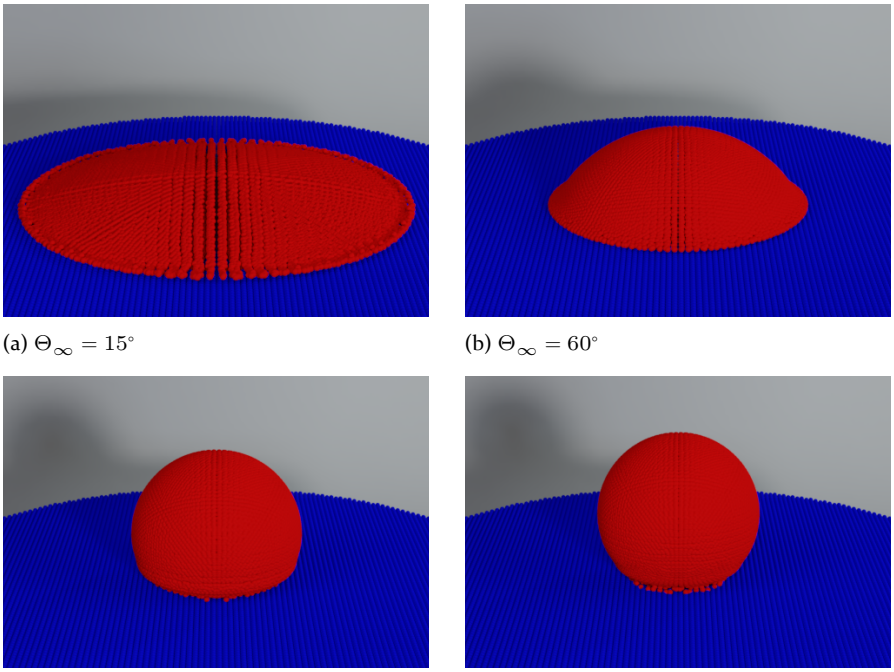

(a) $\Theta_\infty = 15°$ (b) $\Theta_\infty = 60°$

(c) $\Theta_\infty = 120°$ (d) $\Theta_\infty = 150°$

Figure 6.13: Droplet shapes at $t = 1\,\mathrm{s}$ as a function of the adjusted wetting forces. Red SPH particles denote the liquid phase and blue colored SPH particles represent the solid substrate.

region, which also results in translational movement of the drop across the solid substrate and prevents a decrease in the total kinetic energy.

Figures 6.15 and 6.16 show the interface particle positions at $y/r_0 = 0$ at $t = 1\,\mathrm{s}$ for wetting and non-wetting contact angles. In the legend, the measured and the adjusted equilibrium contact angles (in brackets) are given. The contact angles are measured using the following relation:

$$\begin{cases} \Theta = \frac{\pi}{2} + \arctan\left(\frac{H-r}{B}\right) & \text{if } H < r \\ \Theta = \frac{\pi}{2} - \arctan\left(\frac{r-H}{B}\right) & \text{else} \end{cases}, \tag{6.63}$$

where r, H, B are the radius, height and base radius of the drop. The radius is given by

$$r = \frac{H^2 + B^2}{2H}. \tag{6.64}$$

With decreasing contact angles, the drop spreads increasingly on the solid substrate. In contrast, for non-wetting contact angles, as shown in Fig. 6.16, the

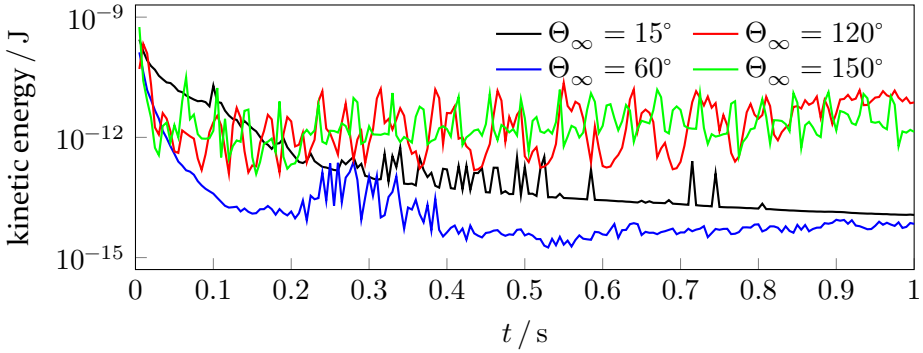

Figure 6.14: Total kinetic energy of spreading droplets as a function of time. Wetting contact angles lead to a decrease in kinetic energy with time, whereas non-wetting contact angles lead to an increase over time.

contact area of drop and the solid substrate becomes smaller with increasing equilibrium contact angles.

Using the following set of equations:

$$r = \left(\frac{2r_0^3}{2 - 3\cos(\Theta_\infty) + \cos^3(\Theta_\infty)} \right)^{1/3}, \tag{6.65}$$

$$H = r\left(1 - \cos\left(\Theta_\infty\right)\right), \tag{6.66}$$

$$B = \sqrt{2rH - H^2}, \tag{6.67}$$

where r_0 is the radius of the hemisphere, the base radius and drop height as a function of the equilibrium contact angle can be computed assuming a hemisphere with an initial base radius of r_0 and constant volume.

Figure 6.17a shows the analytical base radius and drop height computed by Eqs. (6.66) and (6.67) as a function of Θ_∞. In addition, the drop height and drop base radius measured in the simulations are shown. Furthermore, Fig. 6.17b shows the deviation of the measured contact angle from the desired equilibrium contact angle. The deviation of simulated and desired equilibrium contact angle in the range $15° \leq \Theta_\infty \leq 135°$ is between $0.8\,\%$ and $4.4\,\%$. For higher contact angles, the relative error increases to a value of $14.3\,\%$ at $\Theta_\infty \leq 150°$ due to the mentioned issues in applying the forces to particles in the triple line region for non-wetting contact angles.

Smaller relative errors could be achieved by reducing the normal threshold for SPH particles in the vicinity of the solid substrate in order to improve the

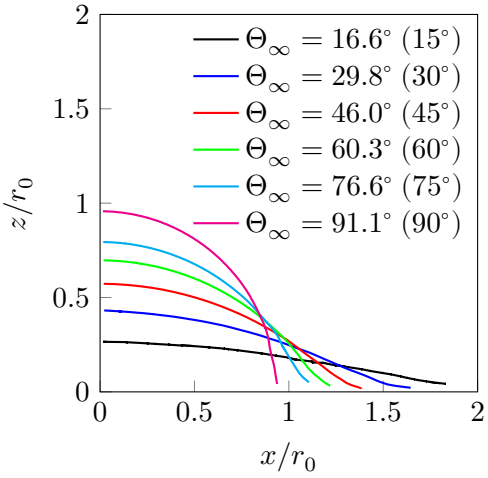

Figure 6.15: Liquid-gas interface position of the droplet for different wetting contact angles at $t = 1$ s, where steady state is assumed.

sensitivity of the detection of particles to which surface tension forces are applied.

6.2.3.4 Droplet deformation due to gravity

The height of a drop resting on a solid substrate decreases with increasing gravitational forces directed normally toward the solid wall. A measure for the ratio of gravitational to surface tension forces is the Bond number, defined as

$$\mathrm{Bo} = \rho g_z r_0^2 / \sigma \,. \tag{6.68}$$

Here, g_z is the body acceleration directed in the z-direction, $\mathbf{f}_g = [0,\ 0,\ g_z]$. In the following, the droplet height is measured as a function of the Bond number, ranging from 10^{-3} (capillary-dominated regime) to 10^2 (gravity-dominated regime). For this reason, 16 776 liquid SPH particles are placed on a rectangular lattice, forming a hemispherical shape. The equilibrium contact angle is adjusted to $\Theta_\infty = 50°$ ($\Theta_\infty^\mathrm{s} = 55°$), which leads to an initial radius according to Eq. (6.65) of $r_0 = 7.93 \cdot 10^{-4}$ m. For the gravity-dominated regime, the height of the droplet converges to the height that depends on the capillary length (the length where Laplace pressure and pressure caused by gravity are equal to each other) given by [56]

$$H_\infty = 2\sqrt{\frac{\sigma}{\rho g_z}} \sin\left(\frac{\Theta_\infty}{2}\right). \tag{6.69}$$

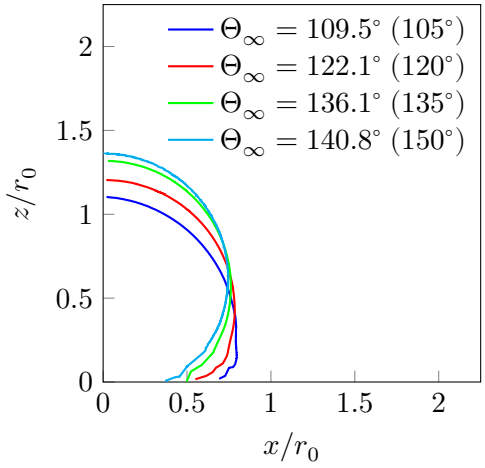

Figure 6.16: Liquid-gas interface position of the droplet for different non-wetting contact angles at $t = 1\,\mathrm{s}$, where steady state is assumed.

Figure 6.18 shows the ratio of the simulated droplet height to the initial height H/H_0 as a function of the Bond number for $\Theta_\infty = 50^\circ$ by black circles. With an increasing Bond number, the droplet becomes increasingly flat. Up to $\mathrm{Bo} = 10^{-2}$ the height of the droplet and the overall droplet shape are unaffected by gravity. For $\mathrm{Bo} > 10^{-2}$, the droplet height is affected by gravity, and the droplet increasingly spreads on the solid substrate with higher values of Bo. It can be seen that the drop height converges towards the capillary length. Nevertheless, for $5 \leq \mathrm{Bo} \leq 100$ the simulated drop height is greater than the capillary length. Figure 6.19 shows the corresponding interfacial particle positions at $y/H_0 = 0$ for various Bo numbers.

6.2.3.5 Pinning of drops at surface edges

The contact line between two inclined planes represents a barrier to liquid droplets that attempt to pass over this surface discontinuity. To move from the first to the second plane, the droplet's contact angle must exceed an upper limit defined by $\Theta = \Theta_\infty + \Psi$, where Ψ is the inclination angle of the planes to each other. To reach the upper limit, a force must be applied to the droplet so that it can pass over the edge. If the accelerating force is too small, the droplet remains pinned at the contact line of the two planes. In this problem, a hemisphere with an initial radius $r_0 = 10^{-3}\,\mathrm{m}$ is placed on a solid substrate. The contact angle is adjusted to $\Theta_\infty = 75^\circ$ ($\Theta^\mathrm{s}_\infty = 80^\circ$). The SPH particles are initially placed on a rectangular lattice with a spacing $\Delta x = 5 \cdot 10^{-5}\,\mathrm{m}$. Moreover, $\eta = 5\,\mathrm{mPa\,s}$, $\rho = 1000\,\mathrm{kg\,m^{-3}}$. As soon as the droplet has reached

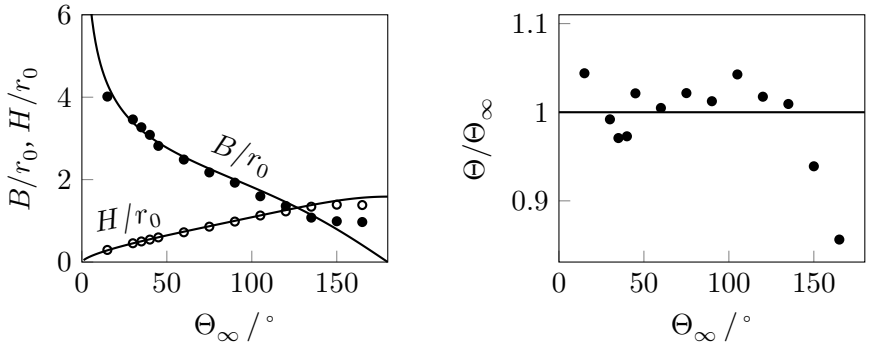

(a) Measured drop base diameter (B) and height (H) for varying adjusted equilibrium contact angles. Solid lines represent the analytically predicted drop width and height, whereas circles denote the results obtained from SPH simulations.

(b) Deviation of the simulated contact angle from the desired equilibrium contact angle (solid line).

Figure 6.17: Comparison of the drop geometry for varying desired equilibrium contact angles with theory.

its equilibrium shape, a body acceleration of $\mathbf{f}_g = [7.5,\ 0.0,\ -7.5]$ that is directed towards the edge of the two planes is applied to all liquid SPH particles for $t > 0.05\,\mathrm{s}$. Simulation snapshots at $t = 50\,\mathrm{ms}$ can be seen in column (a) of Fig. 6.21. In column (b) at $t = 100\,\mathrm{s}$ the drops are decelerated due to the contact discontinuity until the contact angle exceeds $\Theta_\infty + \Psi$. Due to the smoothing nature of the SPH method, pinning starts to occur if the contact line of the two planes lies within the smoothing length of an SPH particle. Instead of a sharp force, the particles experience a smooth counteracting force so that some SPH particles are able to pass the contact line. An asymmetrical shape of the pinned droplets can be observed. The last column shows that droplets have been able to pass the contact line of the inclined planes with $\Psi \in \{22.5^\circ,\ 45.0^\circ,\ 67.5^\circ\}$. In contrast, the contact line of the planes that are inclined by $\Psi = 90.0$ to each other represents a barrier to the drop, which can not be passed since $\Theta_\infty + \Psi = 165^\circ$ is not reached.

Figure 6.22 shows the sum of the kinetic energies of all liquid SPH particles for the different test cases as a function of time. From $t = 0\,\mathrm{ms}$ to $t = 50\,\mathrm{ms}$ the body force is disabled in the simulations and the droplets take its equilibrium shapes for the adjusted wetting forces. Then the drop is continuously accelerated for $t > 50\,\mathrm{ms}$, leading to a sharp increase in kinetic energy. The drop approaches the contact line between the two planes around $t = 55\,\mathrm{ms}$, leading to a deceleration of the drop as a function of Ψ. The drop, which approaches the edge of the two planes inclined by $\Psi = 90^\circ$, experiences

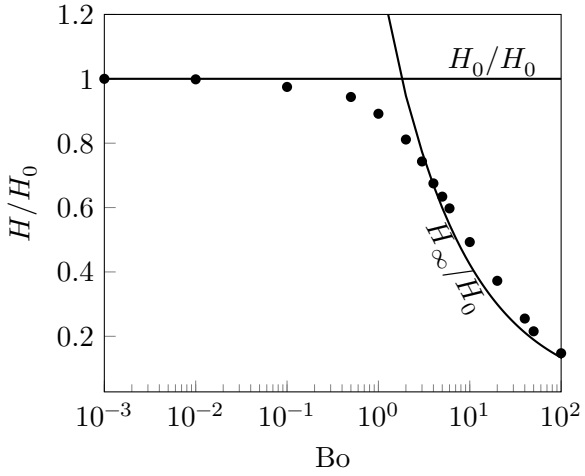

Figure 6.18: Drop height as a function of the Bond number. Increasing gravitational forces leads to a transition from a surface tension-dominated regime to a gravity-dominated regime. Blue circles show the drop height obtained from SPH simulations, whereas the solid lines denote the analytical prediction.

the highest deceleration, which results in the arrest of the drop. For smaller ψ values, the acceleration by g is large enough to move the drop across the surface discontinuity, which can be seen by the increase in kinetic energy for $t > 80\,\mathrm{ms}$. In addition, sharp spikes of kinetic energy can be seen in all simulated cases. Due to the no-slip boundary condition, several liquid SPH particles detach from the liquid droplet and wet the solid substrate. Due to the low number of liquid SPH particles attached to the solid phase behind the moving drop, the computed curvatures for these particles can approach large, inaccurate values due to the low number of liquid particle neighbors. Thus, these particles experience either high accelerations towards the solid substrate or into the ambiance. The wall boundary condition prevents the penetration of liquid SPH particles into the solid due to extensive pressure values. However, this may also cause the repulsion of liquid particles into the ambiance. This issue could be solved by computing the mean curvature of liquid SPH particles only if there is a sufficient number of liquid SPH particle neighbors and otherwise leaving the particles unaffected by surface tension.

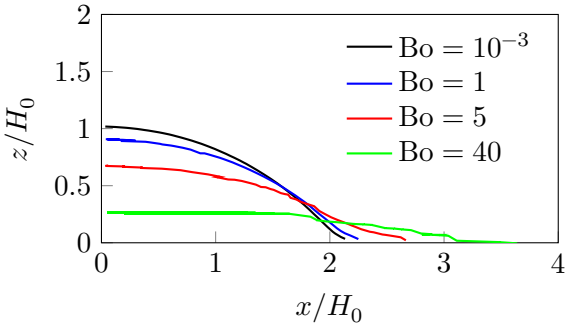

Figure 6.19: Liquid-gas interface position as a function of the Bond number obtained at y/H_0 for $\Theta_\infty = 50°$.

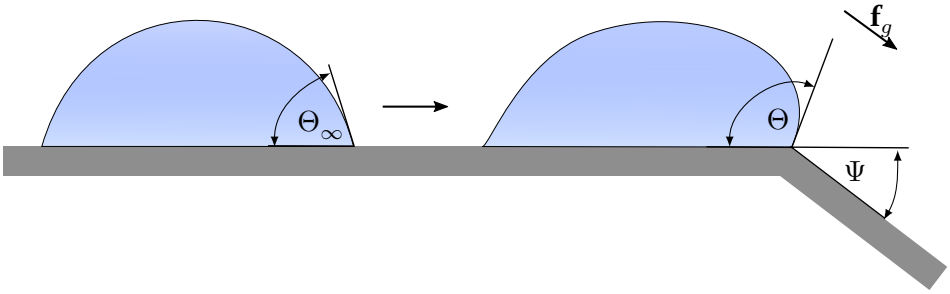

Figure 6.20: Schematic of the pinning process of a drop at the contact line between two inclined planes. The applied body acceleration $\mathbf{f}_g = [7.5,\ 0.0,\ -7.5]$ moves the droplet towards the contact line of the inclined planes and which can only be passed by the drop if $\Theta = \Theta_\infty + \Psi$.

6.2.3.6 Marangoni flow in a heated cavity

To validate the tangential term in Eq. (6.56), the normal contribution of surface tension and the forces due to wetting with the solid walls are disregarded and disabled. Thus, the momentum balance for liquid SPH particles yields:

$$\frac{\mathrm{D}\mathbf{u}_a}{\mathrm{D}t} = \begin{cases} \mathbf{f}^{\mathrm{c}}_{\mathrm{p},a} + \mathbf{f}_{\eta,a} + \mathbf{f}^{\parallel}_{\sigma,a} + \mathbf{f}_{g,a} & \text{if } S_a \leq 0.95 \\ \mathbf{f}_{\mathrm{p},a} + \mathbf{f}_{\eta,a} + \mathbf{f}^{\parallel}_{\sigma,a} + \mathbf{f}_{g,a} & \text{else} \end{cases} . \tag{6.70}$$

The energy equation is solved by applying a temperature gradient within the domain. In this test case, no phase transitions occur, and the heat conduction equation is solved by

$$\rho_a \mathrm{c}_{p,a} \frac{\mathrm{D}T_a}{\mathrm{D}t} = \sum_b \frac{m_b}{\rho_b} \frac{4k_a k_b}{k_a + k_b} (T_a - T_b) F_{ab} \,. \tag{6.71}$$

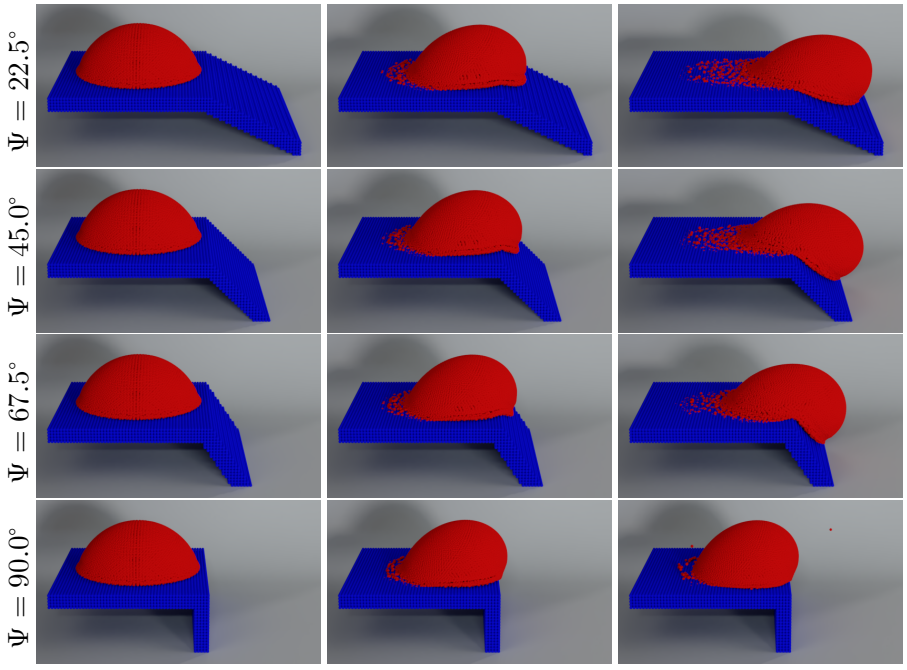

(a) $t = 50\,\mathrm{ms}$ (b) $t = 100\,\mathrm{ms}$ (c) $t = 150\,\mathrm{ms}$

Figure 6.21: Simulation snapshots of droplets that are accelerated towards the contact line of two inclined planes. Column (a) shows droplets in absence of gravitational forces resting on a solid plane with $\Theta_\infty = 50°$. Column (b) shows the droplets approaching the contact discontinuity. In column (c), some droplets could pass over the surface discontinuity where the drop that attempts to pass the contact line between two planes that are inclined by $\Psi = 90°$ remains pinned.

Equation (6.71) is integrated in time using the implicit Euler scheme in Eq. (4.65) but excluding the source terms which account for laser irradiation, heat radiation, evaporation, and the effective heat capacity, by

$$T_a^{n+1} - \Delta t \sum_b \frac{m_b}{\rho_b} \frac{4 k_a k_b}{k_a + k_b} (T_a^{n+1} - T_b^{n+1}) F_{ab} = T_a^n \,. \tag{6.72}$$

The Dirichlet wall boundary conditions for the temperature are applied in the linear system of equations by setting in Eq. (6.72) $T_a^{n+1} = T_b^{n+1}$ which leads to

$$T_a^{n+1} = T_a^{n+1} \,, \tag{6.73}$$

where the off-diagonal elements on the left-hand side of Eq. (6.73) are zero, and no source terms occur on the right-hand side of Eq. (6.73).

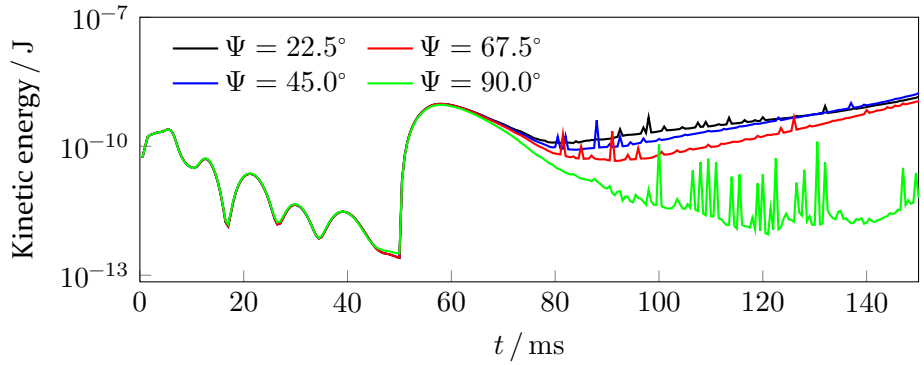

Figure 6.22: Measured kinetic energies of drops that are accelerated towards the surface discontinuity between two planes that are inclined to each other by Ψ.

In this validation case a two-dimensional cavity that is enclosed by walls at $x/L = 0$, $x/L = 1$ and $z/H = 0$ in Cartesian coordinates is considered. Between the walls, a liquid is filled to a height of $z/H = 1$. The length and height of the cavity are given by $L = 800 \cdot 10^{-6}\,\mathrm{m}$ and $H = L/8$. The walls at $x/L = 0$ and $x/L = 1$ are kept at constant temperatures so that the difference in temperature is $\Delta T = 400\,\mathrm{K}$ and $T(x/L = 0) < T(x/L = 1)$. Due to the arising accelerations along with the liquid-gas interface, the liquid is transported along with the interface towards the cold wall. Due to gravity, a circular flow evolves. The liquid is heating up due to the hot wall at $x/L = 1$. This leads to a tangential flow at the liquid-gas interface due to the temperature gradient from the hot to the cold wall. Due to gravity, a circular flow evolves, and the velocity at the bottom wall ($z/H = 0$) vanishes due to the applied no-slip boundary condition.

The analytical prediction of the velocity at $x/L = 0.5$ along the z-coordinates is given by [109]

$$u_x(z) = \frac{\sigma_T \Delta T z}{4\eta H L}\left(3z - 2H\left[1 + \frac{3x\sigma_T \Delta T}{2\rho g_z H^2 L}\right]\right). \tag{6.74}$$

Here, g_z is applied in the z-direction and $\mathbf{f}_g = [0,\ 0,\ g_z]$. The corresponding SPH simulations are carried out with periodic boundary conditions applied in the y-direction. Moreover, viscosity, density and temperature dependent surface tension coefficient of the liquid are given by $\eta = 3.3 \cdot 10^{-3}\,\mathrm{Pa\,s}$, $\rho = 4318\,\mathrm{kg\,m^{-3}}$ and $\sigma_T = -5 \cdot 10^{-5}\,\mathrm{N\,m^{-1}\,K^{-1}}$, respectively. The maximum velocity in this system is then given by $u_{\max}\,(L/2, H) = 0.1894\,\mathrm{m\,s^{-1}}$ according to Eq. (6.74). Moreover, thermal conductivity and heat capacity are given

by $k = 100\,\mathrm{W\,m^{-1}\,K^{-1}}$ and $c_p = 100\,\mathrm{J\,kg^{-1}\,K^{-1}}$, respectively. The thermodynamic properties are chosen so that the thermal transport is much faster than the material transport by convection, which is defined by the Péclet number

$$\mathrm{Pe} = \frac{L u_{\max}}{D_{\mathrm{th}}} = 6.54 \cdot 10^{-3}\,, \tag{6.75}$$

where D_{th} is the thermal diffusivity given by

$$D_{\mathrm{th}} = \frac{k}{\rho c_p}\,. \tag{6.76}$$

Furthermore, the applied gravitational forces are large compared to inertial forces to avoid wave formation of the liquid phase, which is characterized by the Froude number

$$\mathrm{Fr} = \frac{u_{\max}}{\sqrt{g_z L}} = 6.76 \cdot 10^{-2}\,. \tag{6.77}$$

The smoothing length and the kernel radius in this simulation are set to $h = 2\Delta x$ and $r_{\max} = 4\Delta x$. Therefore, the walls are represented by four layers of SPH particles ($4\Delta x$). Initially, SPH particles are placed on a rectangular lattice with $L/\Delta x \in \{80, 160, 320, 640\}$ ($H/\Delta x \in \{10, 20, 40, 80\}$) and the depth in the y-direction is discretized with 14 layers of SPH particles which yields {11 200, 44 800, 179 200, 716 800} liquid SPH particles.

Figure 6.23 shows the obtained velocities at $x = L/2$ in the y-direction obtained by theory (solid line) in Eq. (6.74), and SPH simulations. The velocity field of the SPH simulation is averaged in the y-direction, in which the domain is periodic. For an increasing number of SPH particles, the mean relative error between the velocities at $x/L = 0.5$ of the analytical solution and the simulation decreases from 1.5 % ($L/\Delta x = 80$) to 0.15 % ($L/\Delta x = 640$).

6.3 Concluding remarks

This chapter presented a surface tension model for ISPH that is entirely handled by a pressure boundary condition. Therefore, the PPE and pressure gradient are modified, so that particles in the vicinity of the free surface experience an external pressure. To compute the Laplace pressure, the mean curvature of the SPH particles is calculated from the eigenvalues of the curvature tensor following the approach presented by [66]. To increase the stability of the YL pressure boundary condition, the Laplace pressure is scaled with the Shepard filter. Using the proposed YL pressure boundary condition to model the equilibrium pressure inside a drop with a radius of 1 mm has led

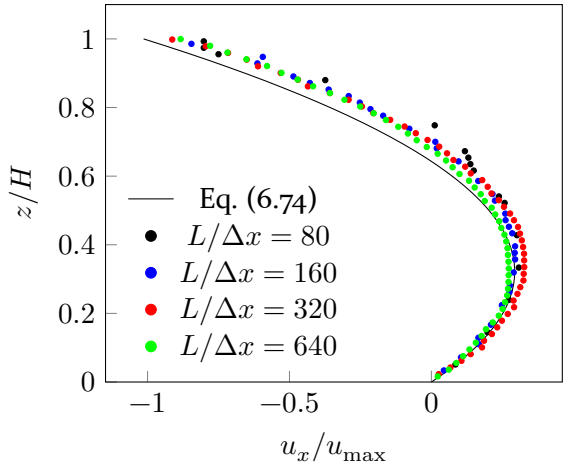

Figure 6.23: Equilibrium velocity field in a liquid-filled cavity with constant temperature gradient measured at $x/L = 0.5$. The temperature gradient leads to Marangoni forces at the liquid-gas interface which causes a circular flow in the cavity.

to a relative error of 13.6 % using 4 224 SPH particles and 2.5 % using 268 096 SPH particles when compared to the analytical Laplace pressure.

Moreover, oscillations of an initially ellipsoidal drop have been simulated. The relative error of the frequency of oscillation computed from the first oscillation is estimated to be 11.4 % when compared to the analytical prediction. In addition, more problems such as cube droplet relaxation or the coalescence of spherical drops are simulated successfully using the YL pressure boundary condition. In the final simulation case, the YL pressure boundary condition was used to simulate the Plateau-Rayleigh instability, representing the disintegration of a liquid cylinder into individual drops. Compared to other works, the tear-off occurs slightly faster than the times predicted in the literature. The developed approach of applying a pressure boundary condition to SPH particles near a liquid-gas interface is not limited to model surface tension but can be used for any ambient pressure field, such as the recoil pressure which occurs in the laser metal processing.

Since wetting phenomena and Marangoni forces play an essential role in the laser melting of metals, the CSF model has been adopted to apply to SPH particles located near a free boundary. In CSF, the curvature is computed by the divergence of unit normal vectors using a renormalized kernel gradient instead of computing the eigenvalues of the curvature tensor in this work. The proposed free surface CSF approach is validated by comparing the equilibrium pressure inside a drop with a radius of 1 mm with the analytically predicted

Laplace pressure. In this scenario, the relative error decreases from $18.0\,\%$, using 4 224 SPH particles, to $1.0\,\%$, using 268096 SPH particles. In addition, the oscillation of a viscous drop was simulated. The corresponding frequency of oscillation and the damping rate of the amplitude deviates by 7.5 %, and 5.1 % from the analytical solution for this problem and the adjusted material and simulation parameters, respectively.

To include wetting forces into the developed numerical software, the wetting force model proposed by Breinlinger et al. [31] is modified to apply to free surface problems. Therefore, two approaches were presented to model wetting ($\Theta < 90^\circ$) or non-wetting ($\Theta > 90^\circ$) equilibrium contact angles, respectively.

In the first approach, the mean curvature of a liquid SPH particle is estimated by including both liquid SPH particles and selected solid SPH particles located in the vicinity of the three-phase line in the computation. Neighboring solid SPH particles of a liquid SPH particle near the three-phase contact line are identified by their distance from the tangent plane constructed from the corrected normal vector corresponding to Θ_∞ at the position of a liquid SPH particle. Solid SPH particles lying on the gas side of the tangent plane are excluded from the computation of the curvature of a liquid SPH particle. Solid particles that are identified to be located on the liquid side of the tangent plane can be viewed as a geometric extension of the liquid-gas interface into the solid substrate. The normal vectors of the identified solid SPH particles within the neighborhood of a liquid SPH particle that are needed for the computation of the curvature are obtained by projecting the liquid SPH particle's normal vector to the positions of the solid SPH particles, and subsequently, modifying these normal vectors depending on another equilibrium contact angle, $\Theta^{\mathrm{s}}_\infty$. By taking $\Theta^{\mathrm{s}}_\infty > \Theta_\infty$, the computed curvature is affected so that a presumably underestimated curvature, which might result in non-terminating spreading on a solid substrate, is prevented. The ratio of $\Theta^{\mathrm{s}}_\infty$ to Θ_∞ must be calibrated.

The second approach attempts to model non-wetting contact angles ($\Theta > 90^\circ$). For this reason, the mean curvature of a liquid SPH particle is computed by only including the normal vectors of neighboring liquid SPH particles and discarding solid SPH particles. In contrast to the first approach for wetting contact angles, the correction matrix used to renormalize the SPH kernel gradient is only computed from liquid SPH particles. Furthermore, the normal vectors of liquid SPH particles in the vicinity of the three-phase contact line are modified analogously to the first approach.

A range of validation cases was performed to verify the proposed wetting model, ranging from the simulation of drops resting on a plane surface with

and without gravity to the pinning of accelerated drops towards the contact line between two inclined planes. The relative errors of the simulated equilibrium contact angles in the absence of gravity are estimated between $0.8\,\%$ and $4.4\,\%$ for $15^\circ \leq \Theta_\infty \leq 135^\circ$. For greater desired equilibrium contact angles, the estimated relative error increased to $14.3\,\%$ $\Theta_\infty = 150^\circ$. Furthermore, the height of a drop resting on a plane substrate with $\Theta_\infty = 50^\circ$ is measured as a function of the Bond number. The simulated height of the drop in the range $3 \leq \mathrm{Bo} \leq 40$ is larger than the corresponding capillary length, which may be attributed to errors in the curvature computation. Moreover, it was shown that the proposed approach to model wetting contact angles minimizes the liquid drops' total kinetic energy. In contrast, the kinetic energy of SPH particles in the case of non-wetting contact angles does not converge to a minimum. The reason for this could be difficulties in identifying SPH near the three-phase contact line and erroneously computed forces applied to that region's particles. In addition, the behavior of drops that are accelerated towards the edge between two inclined planes was investigated in this chapter. Therefore, the kinetic energy of drops is measured for different inclination angles between the two planes ($\Psi \in \{22.5^\circ,\ 45.0^\circ,\ 67.5^\circ,\ 90.0^\circ\}$). It was shown that the total kinetic energy of the drop decreases when approaching the edge of the two planes. For small inclination angles, the drop can pass this contact line, whereas, for $\Psi = 90.0^\circ$, the drop is pinned to the edge. Lastly, to model the interfacial flow due to temperature gradients, Marangoni forces are applied exclusively to a single layer of SPH particles at the liquid-gas boundary, identified by the meshing algorithm introduced in Chapter 5. The equilibrium velocity field in a cavity enforced by an applied temperature gradient was compared to the corresponding analytical prediction. Here, the mean relative error between the analytical solution and the simulation decreases from 1.5 % using 11 200 SPH particles to 0.15 % using 716 800 SPH particles.

7 Application: laser welding[1]

This chapter investigates the influence of the laser processing parameters on the melt and welding seam geometry. In particular, the influence of wetting forces and the material surface quality are explored. Therefore, the Institute of Photonic Technologies (LPT) at the Friedrich-Alexander-Universität Erlangen-Nürnberg (FAU) measured the welding seam geometries obtained by single-line laser tracks on titanium grade 2 metal sheets. The experimentally produced welding seams are compared to the seam geometry prediction obtained with the developed simulation tool for identical sets of parameters. Some of these parameter sets lead to evaporation of the liquid phase in the simulations. Therefore, this chapter introduces the pressure boundary condition used to apply the recoil pressure at the evaporating titanium surface. The emerging vapor due to evaporation may absorb a significant amount of the laser energy. For this reason, an absorption model for laser irradiation in the emerging vapor phase is presented. In this work, the optical properties of titanium are modeled by differentiating between clean and aged surfaces. Nevertheless, these optical properties at the surface can change due to melting and subsequent melt flow. For that reason, a modeling approach to capture the effective real and imaginary parts of the refractive index at the material surface is introduced in this chapter. The developed model is used to study the influence of the titanium surface properties on the obtained melt geometry, and a correlation between laser process parameters and weld seam geometry is established.

7.1 Experiments

The LPT of the FAU provides the experimental data in this section. A laser beam with a Gaussian intensity distribution is used to produce welding seams on titanium grade 2 metal sheets. Each laser track is produced with a different set of laser processing parameters. In the performed experiments, an Aconity mini from Aconity GmbH is employed. In addition, a redPower Qube fiber laser from SPI Lasers Ltd. with a wavelength of $1.08\,\mu\mathrm{m}$ is used. The laser is operated in continuous wave mode and uses the Axialscan 30 from Raylase. The spot radius of the laser beam, which includes 86.5 % of the total energy of the Gaussian intensity distribution at the material surface, is adjusted

[1] Selected parts of the content of this section are submitted and intended for publication in Proceedings of CASICAM 2022 by Springer Nature. Reproduced with permission from Springer Nature.

to $120\,\mu\mathrm{m}$ or $75\,\mu\mathrm{m}$. The beam quality factor is $M^2 = 1.2$. In preparation for the experiments, the metal sheets were sandblasted to remove surface contaminants. The experiments were carried out at room temperature without preheating the titanium samples. Moreover, the processing chamber is filled with argon at atmospheric pressure. Subsequently, two cuts through the solidified welding seam, where the equilibrium shape of the welding seam is assumed, are applied using an angle grinder. The obtained cross-sections through the welding seam are polished with OP-S and H_2O_2 and subsequently etched according to Kroll (H_2o, HNO_3, HF). Images of the welding seam were taken using a Zeiss microscope with a polarization filter.

Table D.1 shows the melt depth and width measured by the LPT as a function of laser power, P_0, laser scanning velocity, u_1, and beam waist radius, w_0. In addition, the energy density for the corresponding parameter set is computed by [136]

$$E_A = \frac{P_0}{2w_0u_1}\,. \tag{7.1}$$

Depending on the processing parameters, a continuous or discontinuous welding seam is observed in the experiments. This is mentioned in Tab. D.1 in the last column, "quality", where "1" corresponds to a continuous welding seam and "0" to a discontinuous welding seam. The measured melt width, depth, and the surface geometry of the welding will be compared to the simulation results in Sections 7.3 and 7.4.

7.2 Numerical model

This section finalizes the developed numerical model. In Section 5.3, the influence of the surface quality and morphology of clean or aged titanium powder has been investigated below melting temperature. Due to the complex melt flow, the optical properties of the material surface could change between clean and aged titanium. Therefore, a model for the effective real and imaginary parts of the refractive index is proposed. Moreover, the high intensity of the laser irradiation that is absorbed by the material may lead to evaporation. This can lead, on the one hand, to recoil pressure acting on the evaporating surface and, on the other hand, to a significant reduction of the laser power arriving at the hot titanium surface due to absorption in the emerging vapor phase. A simple model is presented to consider the laser absorption in the vapor phase. Lastly, the introduced effective heat capacity accounts for the release or the absorption of the latent heat during phase transitions (crystallization, melting, solidification) in a narrow temperature range (mushy region) around the phase transition temperature. As a result,

the temperature change per numerical time step of each SPH particle must be smaller than the width of the mushy region to model these phase transitions correctly. For this reason, an adaptive time-stepping scheme for the solution of the energy equation is introduced in this section.

7.2.1 Effective optical surface properties

As mentioned in Section 2.3.4, the absorption of laser irradiation by any metal depends significantly on its surface properties. Pollution, an oxide layer, or surface roughness decreases the material's optical reflectivity. It is assumed that Eqs. (3.22) to (3.25) describe the optical properties of a clean titanium surface, whereas Eqs. (3.28)–(3.31) represent an aged titanium surface with lower reflectivity when compared to an atomically clean titanium surface.

The ray tracing algorithm introduced in Section 5.1, evaluates the optical properties of the material surface at the moment a ray intersects a triangle of the triangulated surface mesh. A triangle is composed of three vertices represented by SPH particles (Ω^{v}). Upon melting and subsequent mixing of SPH particles, a triangle can be composed of SPH particles that represent clean and aged titanium. Therefore, the effective real, $n^{\mathrm{s}}_{1,\mathrm{eff}}$, and imaginary part, $n^{\mathrm{s}}_{2,\mathrm{eff}}$, of the refractive index is modeled by

$$\begin{aligned} n^{\mathrm{s}}_{1,\mathrm{eff}} &= \varkappa n^{\mathrm{s}}_{1,\mathrm{aged}} + (1-\varkappa)\, n^{\mathrm{s}}_{1,\mathrm{clean}} \\ n^{\mathrm{s}}_{2,\mathrm{eff}} &= \varkappa n^{\mathrm{s}}_{2,\mathrm{aged}} + (1-\varkappa)\, n^{\mathrm{s}}_{2,\mathrm{clean}} \end{aligned} \tag{7.2}$$

assuming that the mean temperature of the three vertices (SPH particles) is below the melting temperature. Here, $\varkappa = \{1/3,\ 2/3,\ 1\}$ if 1, 2, or 3 SPH particles are modeled with the optical properties of the aged titanium surface. Accordingly, the effective real, $n^{\mathrm{l}}_{1,\mathrm{eff}}$, and imaginary part, $n^{\mathrm{l}}_{2,\mathrm{eff}}$, of the refractive index of a triangle whose temperature exceeds melting temperature (liquid) is given by

$$\begin{aligned} n^{\mathrm{l}}_{1,\mathrm{eff}} &= \varkappa n^{\mathrm{l}}_{1,\mathrm{aged}} + (1-\varkappa)\, n^{\mathrm{l}}_{1,\mathrm{clean}} \\ n^{\mathrm{l}}_{2,\mathrm{eff}} &= \varkappa n^{\mathrm{l}}_{2,\mathrm{aged}} + (1-\varkappa)\, n^{\mathrm{l}}_{2,\mathrm{clean}}\,. \end{aligned} \tag{7.3}$$

Figure 7.1 shows a cut through the initial configuration of SPH particles arranged on a rectangular lattice representing a polydisperse titanium powder deposited on a solid substrate. All interfacial particles (red) are modeled with the optical properties of aged titanium, whereas all blue particles, which are initially not located at the interface, are modeled with the optical properties of clean titanium. The surface particles are identified by the employed meshing

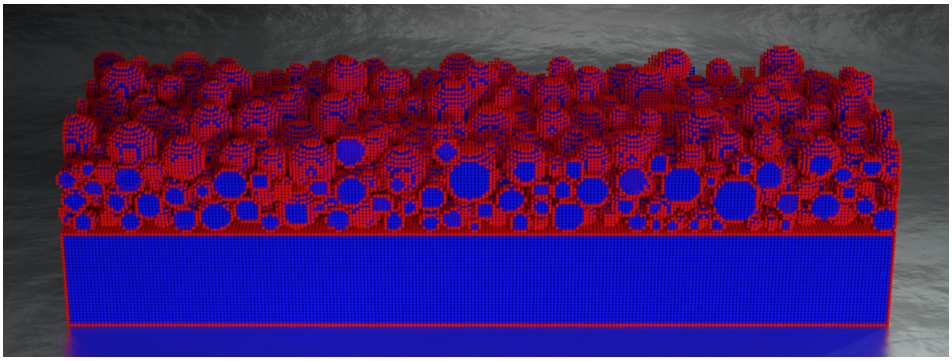

Figure 7.1: Cut through the initial SPH particle configuration of a deposited polydisperse titanium powder bed. Surface particles (red) and bulk particles (blue) are modeled with distinct optical properties.

algorithm.

7.2.2 Recoil pressure and optical absorption of metal vapor

SPH particles whose temperature exceeds the boiling temperature evaporate. This results in a recoil pressure that acts on evaporating SPH particles at the liquid gas interface. The recoil pressure, $p_{\mathrm{recoil},a}$, that acts on an evaporating SPH particle, a, is greater than the ambient pressure by a certain pressure difference given by

$$\Delta p_{\mathrm{recoil},a} = p_{\mathrm{recoil},a} - p_{\mathrm{amb}} \,. \tag{7.4}$$

Here, $\Delta p_{\mathrm{recoil},a}$ is the pressure difference between the recoil pressure, given by Eq. (2.48), and the ambient pressure, $p_{\mathrm{amb}} = 1\,\mathrm{atm}$.

Thus, the external pressure which is applied to the PPE and the pressure gradient in Eqs. (4.49) and (4.36) is given by

$$p_{\mathrm{o},a} = \Delta p_{\mathrm{recoil},a} \,. \tag{7.5}$$

Nevertheless, applying (7.5) to the PPE and the pressure gradient in Eq. (4.49) and Eq. (4.36) has led to unstable free surfaces with the onset of evaporation. For this reason, $\Delta p_{\mathrm{recoil},a}$ is additionally smoothed by

$$\Delta \tilde{p}_{\mathrm{recoil},a} = \frac{1}{S_a^{\mathrm{v}}} \sum_{b \in \Omega^{\mathrm{v}}} \frac{m_b}{\rho_b} \Delta p_{\mathrm{recoil},b} W_{ab} \,, \tag{7.6}$$

where S_a^{v} is the Shepard filter computed from surface SPH particles (Ω^{v}) that are identified by the surface meshing algorithm by

$$S_a^{\mathrm{v}} = \sum_{b \in \Omega^{\mathrm{v}}} \frac{m_b}{\rho_b} W_{ab} \,. \tag{7.7}$$

Thus, $\Delta p_{\mathrm{recoil},a}$ in Eq. (7.5) is substituted with the corresponding smoothed pressure difference which yields:

$$p_{\mathrm{o},a} = p_{\mathrm{amb},a} + \Delta \tilde{p}_{\mathrm{recoil},a} \,. \tag{7.8}$$

Due to evaporation, metal vapor propagates towards the laser source and may absorb a significant amount of the laser energy. The absorbance of the metal vapor is assumed to be linearly proportional to the evaporation coefficient, ϕ, introduced in Section 2.2.2. Therefore, the power carried by a ray in the ray tracing algorithm is reduced according to

$$P_{\mathrm{ray,i}} = (1 - \phi)\, P_{\mathrm{ray,i}} \tag{7.9}$$

if it intersects a triangle with a temperature of $T > T_{\mathrm{boil}}$. In Eq. (7.9) a proportionality constant of unity is assumed. However, a non-unity proportionality constant could be used to calibrate the vapor absorption model with experiments.

To model the evaporated mass, SPH particles are removed from the simulation once they are evaporated. Therefore, the mass fraction w, defined as the ratio of the evaporated to the initial mass of an SPH particle, is introduced. At the beginning of the simulation, $w = 0$. If the SPH particle exceeds the boiling temperature, the evaporated mass per time can be computed by the evaporation rate in Eq. (2.29). Upon temporal integration, the absolute amount of evaporated mass at time $n + 1$ is obtained by

$$w_a^{n+1} = w_a^n + \frac{\dot{m}_{\mathrm{vap},a} \Delta x^2 \Delta t}{m_a} \,, \tag{7.10}$$

where w_a^n is the evaporation mass fraction of particle a at time n.

7.2.3 Adaptive thermal time stepping

To resolve the temperature-dependent material properties, notably the mushy region of the employed latent heat model (see Eq. (4.52)), the numerical

time step must be chosen small enough that these properties are sufficiently approximated.

This represents a non-linear problem due to the variety of physical phenomena that affect the heating rate of the material. Therefore, the temporal integration of the energy equation is carried out using a thermal numerical time step, Δt_{th}, which is executed in an internal loop under the assumption $\Delta t_{\mathrm{th}} < \Delta t$. This is generally true as long as the laser is switched on in the following simulations. A linear controller is used to adjust Δt_{th} as a function of the maximum temperature change of an SPH particle between two consecutive time steps by

$$\Delta t_{\mathrm{th}}^{n+1} = \exp\left(0.1 \cdot \frac{\Delta T_{\mathrm{max}} - \Delta T_{\mathrm{control}}}{\Delta T_{\mathrm{control}}}\right) \cdot 0.1 \sum_{i=1}^{10} \Delta t_{\mathrm{th}}^{n-i} \,. \tag{7.11}$$

Here, $\Delta T_{\mathrm{control}}$ is the desired temperature change between two consecutive time steps, and ΔT_{max} is the highest temperature change of an SPH in the simulated system between two consecutive thermal numerical time steps, Δt_{th}. The maximum temperature change of the SPH particles is given by

$$\Delta T_{\mathrm{max}} = \max\left(|T_a^n - T_a^{n-1}|\right) \,. \tag{7.12}$$

The presented adaptive thermal time step to solve the energy equation is employed for all simulations in this chapter and Chapter 8. The implementation of Δt_{th} into the software is shown by Algorithm 1 assuming $\Delta t_{\mathrm{th}} < \Delta t$. To reduce the computational costs of the meshing algorithm, the triangulated surface mesh is computed only every $n_{\mathrm{tr}} = 5$ time steps in all subsequent simulations. Within each numerical time step Δt, the energy equation is solved multiple times using the thermal numerical time step Δt_{th} until the simulated thermal time, t_{th}, is equal to the global numerical time step that is used to advance the SPH particles in space.

7.3 Influence of laser parameters and material aging

The developed simulation model is verified in this section by comparing the obtained welding seam geometries with the corresponding experimentally measured melt widths and depths for the same set of laser parameters shown in Tab. D.1. The material is characterized by the material properties of titanium given in Chapter 3.1. The titanium melt is modeled using the momentum balance

$$\frac{\mathrm{D}\mathbf{u}_a}{\mathrm{D}t} = \mathbf{f}_{\mathrm{p},a} + \mathbf{f}_{\eta,a} + \mathbf{f}_{\sigma,a}^{\perp} + \mathbf{f}_{\sigma,a}^{\parallel} + \mathbf{f}_{g,a} \,. \tag{7.13}$$

Data : Particle position $\mathbf{r}_a^n$, velocity $\mathbf{u}_a^n$, temperature T_a^n at time n
Result : Updated $\mathbf{r}_a^{n+1}$, $\mathbf{u}_a^{n+1}$, T_a^{n+1} at time $n+1$

while *t < end time* **do**
  $\mathbf{r}_a^* = \mathbf{r}_a^n + \Delta t \mathbf{u}_a^n$
  if $n \,\%\, n_{\mathrm{tr}} = 0$ **then** compute triangulated surface mesh
  $t_{\mathrm{th}} \leftarrow 0\,\mathrm{s}$
  while $t_{\mathrm{th}} < \Delta t$ **do**
    $\Delta t_{\mathrm{th}} \leftarrow$ solution of Eq. (7.11)
    if $t_{\mathrm{th}} + 2\Delta t_{\mathrm{th}} > \Delta t$ **then** $\Delta t_{\mathrm{th}} \leftarrow \Delta t - t_{\mathrm{th}}$
    update $\tilde{c}_{p,a}$, k_a, σ_a by Eqs. (4.52), (3.14), (3.13), (3.15)
    $\dot{q}_{\mathrm{l,ray},a} \leftarrow$ solution of Eq. (5.13) if $a \in \Omega^{\mathrm{v}}$
    $\dot{q}_{\mathrm{r},a} \leftarrow$ solution of Eq. (2.54) if $a \in \Omega^{\mathrm{v}}$
    $\dot{q}_{\mathrm{vap},a} \leftarrow$ solution of Eq. (2.55)
    $\tilde{c}_{p,a}\rho_a \frac{\mathrm{D}T_a}{\mathrm{D}t} \leftarrow$ solution of Eq. (4.51)
    $T_a^{n+1} \leftarrow T_a^n + \frac{1}{\tilde{c}_{p,a}\rho_a}\frac{\mathrm{D}T_a}{\mathrm{D}t}\Delta t_{\mathrm{th}}$
    $t_{\mathrm{th}} \leftarrow t_{\mathrm{th}} + \Delta t_{\mathrm{th}}$
  end
  $\mathbf{f}_{\eta,a} \leftarrow$ solution of Eq. (4.38)
  $\mathbf{f}_{\sigma,a} \leftarrow$ solution of Eq. (6.24)
  $\mathbf{u}_a^* = \mathbf{u}_a^n + \left(\mathbf{f}_{\eta,a} + \mathbf{f}_{\sigma,a} + \mathbf{f}_{g,a}\right)\Delta t \mathbf{u}_a^n$
  $p_a \leftarrow$ solution of Eq. (4.48), Eq. (4.49) and (4.68)
  $\mathbf{f}_{p,a} \leftarrow$ solution of Eq. (4.37)
  $w_a^{n+1} = w_a^n + \frac{\dot{m}_{\mathrm{vap},a}\Delta x^2 \Delta t}{m_a}$
  if $w_a^{n+1} > 1$ **then**
    remove SPH particle
  else
    $\mathbf{u}_a^{n+1} = \mathbf{u}_a^n + \mathbf{f}_{p,a}\Delta t$
    $\mathbf{r}_a^{n+1} = \mathbf{r}_a^n + \left(\frac{\mathbf{u}_a^n + \mathbf{u}_a^{n+1}}{2}\right)\Delta t$
  end
  $t \leftarrow t + \Delta t$
  $n \leftarrow n + 1$
end

Algorithm 1: Algorithm to determine position, velocity, and temperature of the SPH particles. Adaptive thermal time steps are used to solve the energy equation.

Furthermore, the energy balance for solid and liquid titanium,

$$\rho_a \tilde{c}_{p,a} \frac{\mathrm{D}T_a}{\mathrm{D}t} = \sum_b \frac{m_b}{\rho_b} \frac{4k_a k_b}{k_a + k_b} (T_a - T_b) F_{ab} + \frac{\dot{q}_{\mathrm{l,ray},a} + \dot{q}_{\mathrm{r},a} + \dot{q}_{\mathrm{vap},a}}{\Delta x} , \tag{7.14}$$

is solved using the explicit Euler scheme with the introduced thermal numerical time step. The thermal time step follows the CFL condition for thermal diffusion given in Eq. (4.66).

Moreover, the mass balance of liquid SPH particles is solved using Eqs. (4.48) or (4.49) as a function of S_a. The PPE of solid wall particles is solved according to Eq. (4.68) whereas the pressure of the remaining solid particles is obtained by Eq. (4.48). In addition, the no-slip boundary condition as introduced in Section 4.4 is ensured by SPH wall particles. The external pressure, which includes the effect of recoil pressure caused by evaporation, is considered by applying Eq. (7.8) to the PPE in Eq. (4.49) as well as to the pressure gradient in Eq. (4.49) for liquid SPH particles. The momentum equation and mass balance are solved using the numerical time step estimated based on the CFL condition given in Eq. (4.66).

The simulated solid block of titanium with length, L, height H, and depth, D, is aligned with the x-, y-, and z-axes of Euclidean space. The laser beam with a total power of $P_0 \in \{100\,, 200\}\,\mathrm{W}$ is moving in the x-direction from $x/L = 0.12$ to $x/L = 0.88$. Furthermore, when using $P_0 \in \{350\,, 500\}\,\mathrm{W}$ the laser is moving from $x/L = 0.14$ to $x/L = 0.96$. In all simulation cases, the laser tracks have a length of $1000\,\mu\mathrm{m}$. The melt width and depth are measured at $x/L \approx 0.75$ in the simulations, where an equilibrium cross-section of the melt is assumed. Moreover, the spot radius of the laser beam is $w_0 = 120\,\mu\mathrm{m}$.

The dimensions of the simulated domain, initial particle spacing, and the corresponding number of SPH particles are given in Tab. D.2 as a function of the process parameters. The dimensions of the simulated material are chosen to be as small as possible to minimize the computational cost but large enough that the applied adiabatic boundary conditions do not affect the melt geometry in the range of $0.1 \leq x/L \leq 0.9$ due to heat accumulation in the material when compared to a semi-infinite body. The kernel radius and smoothing length are given by $r_{\mathrm{max}} = 4\Delta x$ and $h = 2\Delta x$. The equilibrium contact angle, which serves as an input parameter in the employed wetting model in these simulations, is adjusted to $\Theta_\infty = 45^\circ$ ($\Theta^{\mathrm{s}}_\infty = 50^\circ$) and which is considered a

good approximation for a wide range of laser processing parameters. Moreover, the threshold used to discard erroneous normal vectors is $\epsilon_{\mathrm{n}} = 0.1/h$.

The surface mesh is computed every five time steps, Δt. Moreover, half the width of the mushy region is $\Delta T = 2\,\mathrm{K}$ and the adaptive time step is adjusted by the linear controller to $\Delta T_{\mathrm{control}} = 2\mathrm{K}$. The chosen $\Delta T_{\mathrm{control}}$ has been estimated in preceding tests and does not influence the melt geometry when compared to smaller values, $\Delta T_{\mathrm{control}} < 2\mathrm{K}$. In addition, the ray density is $n_{\mathrm{ray}} = 75$, the ambient temperature required by Eq. (2.54) is $T_0 = 300\,\mathrm{K}$ and the ambient pressure which is required for Eq. (2.33) is $p_{\mathrm{a}} = 1\,\mathrm{atm}$. Moreover, the initial temperature of the simulated material is $300\,\mathrm{K}$. For the solution of the PPE at free boundaries, $p_{\mathrm{amb}} = 0\,\mathrm{Pa}$. The rays of the ray-tracing algorithm are initialized uniformly within a circle with radius $r_{\mathrm{ray},0} = 2w_0$. Moreover, gravity acts in the z-direction with $g_z = -9.81\,\mathrm{m\,s^{-2}}$, $\mathbf{f}_{g,a} = [0,\ 0,\ g_z]$.

To estimate the melt width and depth, the number of melted layers of SPH particles is counted. One layer corresponds to the chosen discretization length, Δx. In Fig. 7.2 and Fig. 7.6, simulation and experimental results for the melt depth (upper image) and melt width (lower image) are compared. The experimental results are shown as crosses connected by solid black lines, whereas the simulation results are connected by dashed lines. For each experimental data point of the melt width and depth, three simulations were performed. In the first simulation (sim. 1) the optical properties of all SPH particles are described by Eqs. (3.22) to (3.23) assuming clean titanium. The second simulation (sim. 2) utilizes the model introduced in Section 7.2.1 in Eqs. (7.2) and (7.3), where effective surface properties are assumed. The last simulation (sim. 3) models the absorption of laser irradiation in the evaporating vapor in conjunction with the effective optical properties (Eqs. (7.2) and (7.3)) at the surface.

Figure 7.2 shows the measured melt depth and width obtained from experiments and simulations for $P_0 = 100\,\mathrm{W}$. In sim. 1 no melting occurs for energy densities below $0.69\,\mathrm{J\,mm^{-2}}$. The high reflectivity at the titanium surface prevents melting since the major fraction of the incident laser irradiation is reflected and therefore lost to the ambiance. For energy densities of $1.04\,\mathrm{J\,mm^{-2}}$ and higher, melting occurs. The melt depth and width obtained by sim. 1. show a large deviation from the measured experimental values. Nevertheless, melt width and depth converge with increasing laser energy density towards experimental values. It can be seen that the optical properties of the material surface have a significant influence on the melt geometry at lower energy densities but a decreasing influence on the melt geometry with increasing laser energy densities. The results that are obtained by sim. 2, and

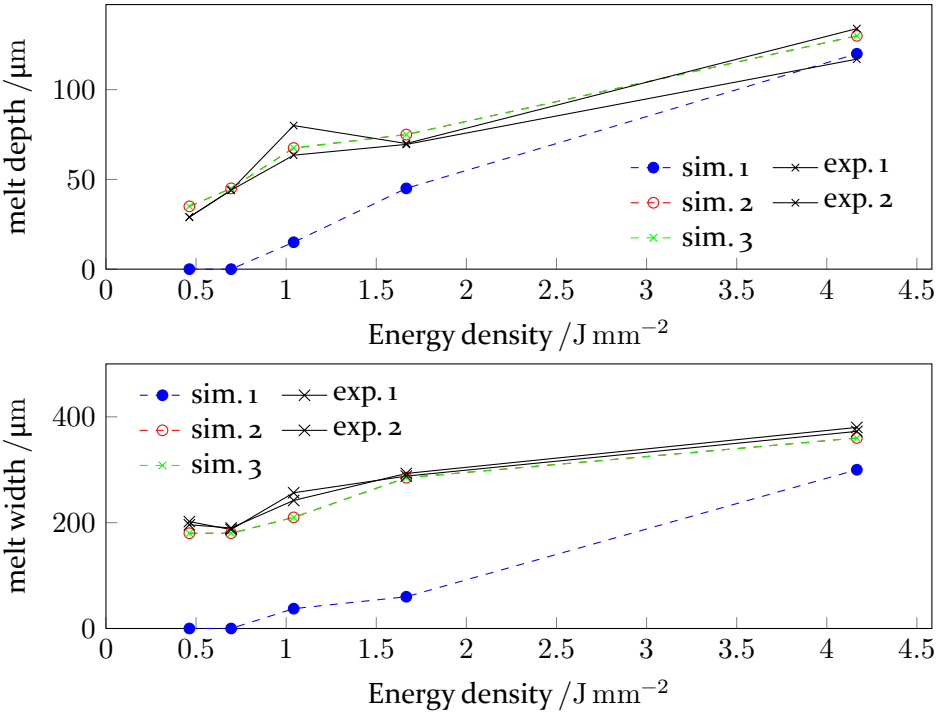

Figure 7.2: Comparison of simulated melt depth (top) and melt width (bottom) with experiments for $P_0 = 100\,\mathrm{W}$ and $w_0 = 120\,\mu\mathrm{m}$. Experimental data provided by Florian Huber, LPT, FAU.

sim. 3. coincide for all investigated energy densities. This implies that the surface temperature remains below the boiling temperature; hence, no laser energy is absorbed by emerging metal vapor. Moreover, sim. 2 and sim. 3 show quantitative agreement with experiments for all investigated energy densities.

Figure 7.3 shows the melt depth and width obtained from experiments and simulations for $P_0 = 200\,\mathrm{W}$. In comparison to $P_0 = 100\,\mathrm{W}$, the experimentally measured melt depth fluctuates for energy densities between $E_A = 0.93\,\mathrm{J\,mm^{-2}}$ and $E_A = 3.33\,\mathrm{J\,mm^{-2}}$. Moreover, the average melt depth decreases from 134 µm to 64 µm for $E_A = 3.33\,\mathrm{J\,mm^{-2}}$ to $E_A = 8.33\,\mathrm{J\,mm^{-2}}$ which may be attributed to laser absorption by the evaporating titanium vapor.

The reason for these fluctuations in the experiments is not clear, but it may be related to complex melt flow or the evaporation process. The resultant vapor plume could lead to non-equilibrium melt geometries since it could distract the laser beam from its original focal plane. In addition, according to Tab. D.1 a non-stable welding seam geometry was observed in the experiments

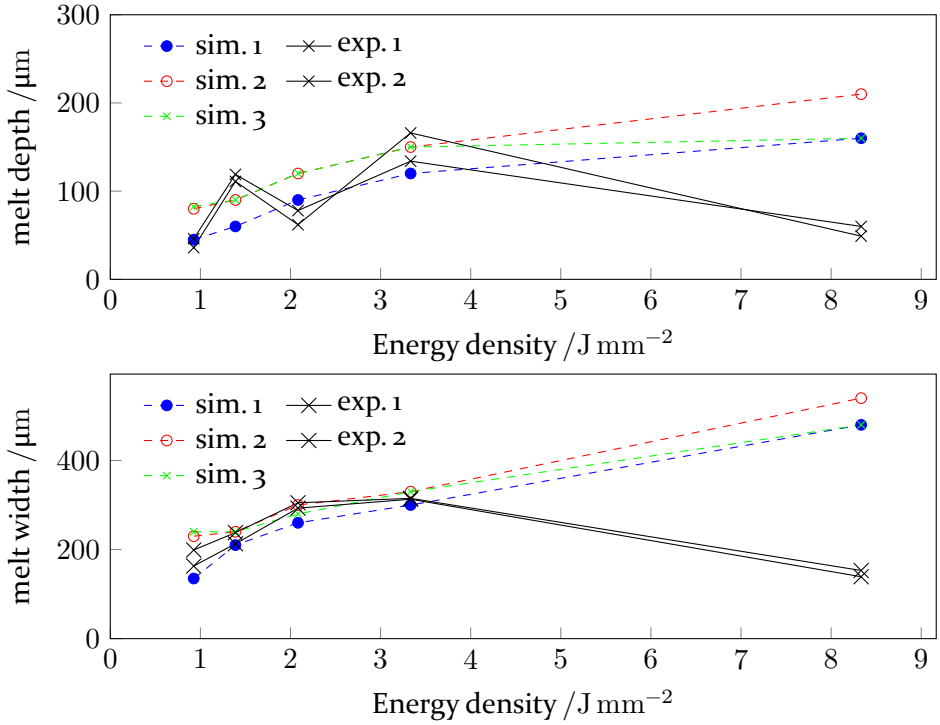

Figure 7.3: Comparison of simulated melt depth (top) and melt width (bottom) with experiments for $P_0 = 200\,\mathrm{W}$ and $w_0 = 120\,\mu\mathrm{m}$. Experimental data provided by Florian Huber, LPT, FAU.

for $E_A = 1.34\,\mathrm{J\,mm^{-2}}$ ($P_0 = 100\,\mathrm{W}$, $u_1 = 600\,\mathrm{mm\,s^{-1}}$). The performed simulations can not reproduce these fluctuations in melt depth observed in the experiments. Instead, the simulations follow the trend of the increasing melt depth towards higher energy densities of the laser up to $E_A = 3.33\,\mathrm{J\,mm^{-2}}$. At greater laser energy density ($E_A = 8.33\,\mathrm{J\,mm^{-2}}$), the absorption of laser energy in the vapor plume due to evaporation affects the melt geometry, as can be seen by the deviation of the measured melt depth in sim. 2 and sim. 3. Moreover, at $E_A = 8.33\,\mathrm{J\,mm^{-2}}$ the measured melt depth of sim. 1 is identical to the melt depth of sim. 2, which implies that the effect of the surface quality on the melt geometry decreases for high laser energy densities. Furthermore, it can be seen that the melt depth measured in sim. 1 is smaller than the corresponding melt depth obtained from sim. 2 for all energy densities, except for $E_A = 8.33\,\mathrm{J\,mm^{-2}}$, caused by distinct optical surface properties.

The mean melt width obtained by the experiments increases with increasing energy density up to $E_A = 3.33\,\mathrm{J\,mm^{-2}}$. For higher energy density,

the melt width decreases from 315 µm ($E_A = 3.33\,\mathrm{J\,mm^{-2}}$) to 153 µm ($E_A = 8.33\,\mathrm{J\,mm^{-2}}$) and hence shows a similar trend as the melt depth. In the simulations, the measured melt width increases from 360 µm ($E_A = 3.33\,\mathrm{J\,mm^{-2}}$) to 560 µm($E_A = 8.33\,\mathrm{J\,mm^{-2}}$). Hence, the simulation is not capable of capturing the behavior obtained in the experiments, which might be caused by the evaporation of metal. Nevertheless, the measured melt width is in quantitative agreement with the experiments up to $E_A = 3.33\,\mathrm{J\,mm^{-2}}$, where evaporation has a minor influence on the melt geometry. A more profound investigation of the evaporating vapor and its interaction with the laser beam is necessary to understand the experimentally observed decrease in melt width and depth at higher energy densities.

In Fig. 7.4, the experimentally measured melt depth and melt width obtained by a laser with a power of $P_0 = 350\,\mathrm{W}$ are shown along with the simulation results. It can be seen that the experimentally measured mean melt depth

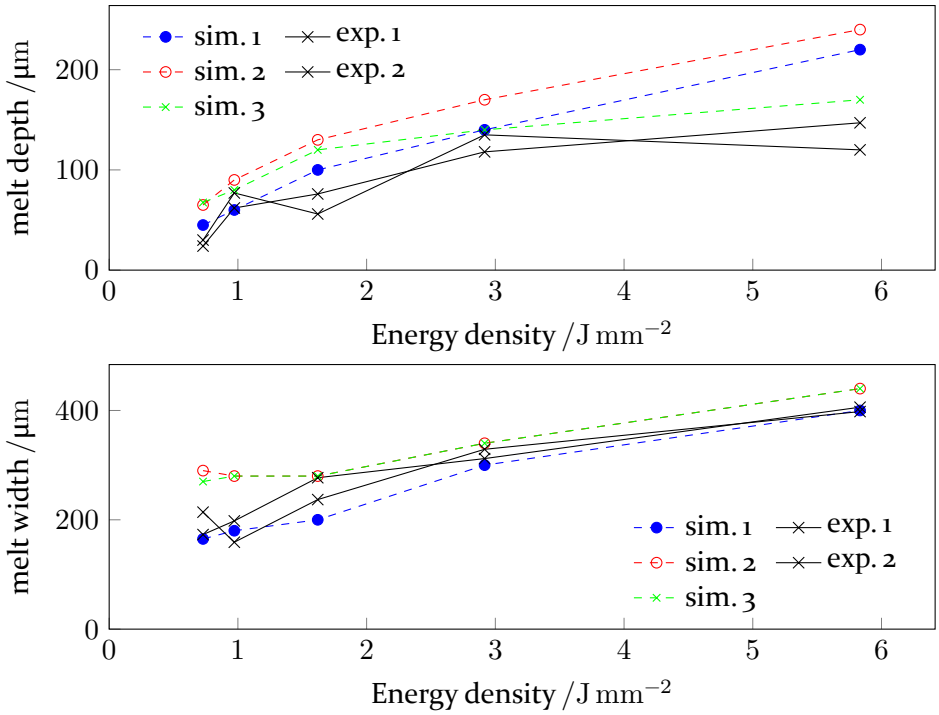

Figure 7.4: Comparison of simulated melt depth (top) and melt width (bottom) with experiments for $P_0 = 350\,\mathrm{W}$ and $w_0 = 120\,\mu\mathrm{m}$. Experimental data provided by Florian Huber, LPT, FAU.

and mean melt width increase with an increasing energy density of the laser beam. Moreover, the melt geometry does not fluctuate noticeably as it did for

$P_0 = 200\,\mu\mathrm{m}$ in Fig. 7.3. In contrast to the simulations for $P_0 = 100\,\mathrm{W}$ and $P_0 = 200\,\mathrm{W}$, where the best agreement between simulation and experiment was achieved by sim. 3, here sim. 1 shows the best correspondence with the experiments for energy densities below $E_A = 2.92\,\mathrm{J\,mm^{-2}}$.

Nevertheless, the melt width and depth obtained by sim. 3 show the best qualitative agreement with the experiments considering all measured energy densities due to the employed vapor absorption model. By comparing the measured results of sim. 2 and sim. 3, it can be seen that the melt depth is significantly affected by the laser absorption in the vapor phase for $E_A = 5.83\,\mathrm{J\,mm^{-2}}$.

Assuming a clean titanium surface in combination with the laser absorption in the evaporating vapor phase could lead to better agreement with the experiments in the range from $E_A = 0.73\,\mathrm{J\,mm^{-2}}$ to $E_A = 5.83\,\mathrm{J\,mm^{-2}}$. This should be verified in future work. The melt width obtained in sim. 2 and sim. 3 is overestimated compared to the experimental results up to $E_A = 0.97\,\mathrm{J\,mm^{-2}}$ whereas for higher energy densities, a good agreement across all performed simulations can be observed. However, the best agreement for high energy densities is obtained by sim. 1.

An even better agreement with the experiments could be achieved by using a higher spatial resolution of the simulation domain. The reason for this lies in using interfacial particles to represent the aged titanium surface. Using more particles reduces the volume fraction of surface particles, which could shift the measured melt width and depth to the results of sim. 1 since these particles are melted faster and subsequently leave the hot regions in the center of the laser spot due to Marangoni forces earlier. The displacement of surface SPH particles due to Marangoni forces is shown in Fig. 7.5 for $P_0 = 600\,\mathrm{W}$, $w_0 = 120\,\mu\mathrm{m}$ and $u_1 = 3000\,\mathrm{mm\,s^{-1}}$. The dimension of the domain and the discretization length is given in Tab. D.3 together with Tab. 7.1. It can be seen that surface SPH particles (red, aged titanium) are moving tangentially along the surface due to the surface temperature gradient from hot to cooler regions. The surface particles accumulate at the solid-liquid-gas interface, as can be seen at $t = 30\,\mu\mathrm{s}$ and $t = 40\,\mu\mathrm{s}$. At a later time, the surface particles mix with bulk particles (blue, clean titanium). However, the highest concentration of surface particles can be found along the solid-liquid-gas interface in front of the laser beam. Finally, Fig. 7.6 shows the experimental and simulation results for the melt depth and melt width for a laser power of $P_0 = 500\,\mathrm{W}$. Here, the influence of the laser absorption in the metal vapor is more pronounced in the measured melt depth than in the measured melt width, as can be seen for $E_A = 8.33\,\mathrm{J\,mm^{-2}}$. Furthermore, it can be seen that the melt depth obtained

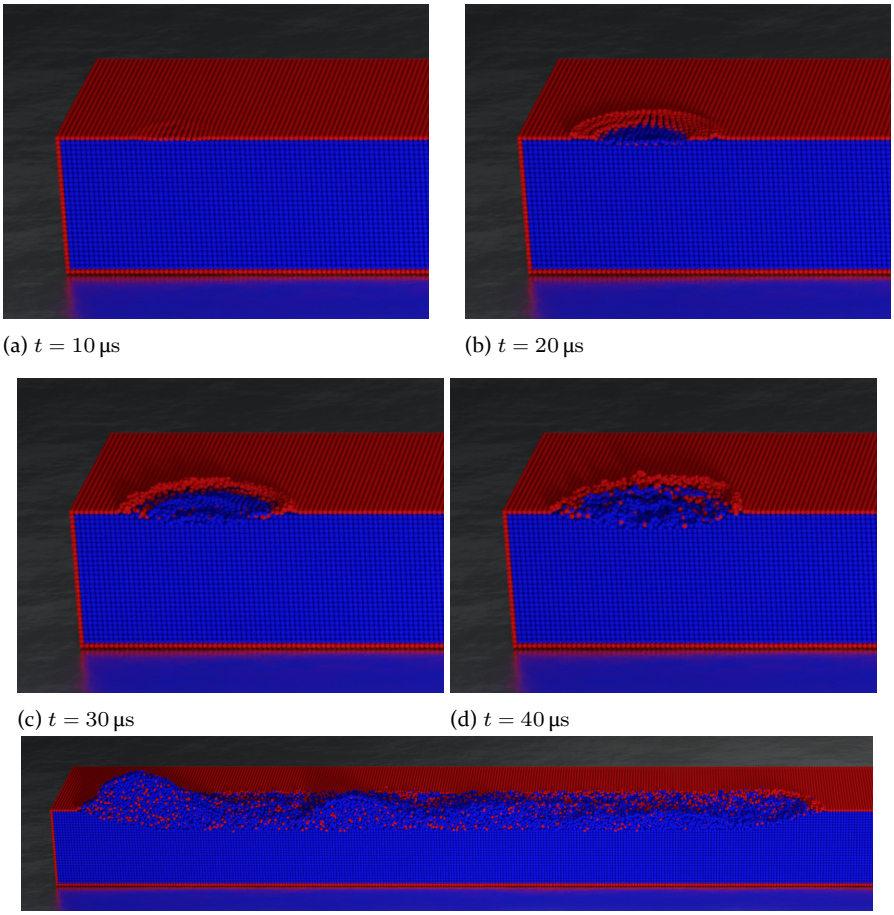

(a) $t = 10\,\mu s$ (b) $t = 20\,\mu s$

(c) $t = 30\,\mu s$ (d) $t = 40\,\mu s$

(e) $t = 620\,\mu s$

Figure 7.5: Simulation snapshots of a single-line laser track at different times for $P_0 = 600\,\mathrm{W}$, $u_1 = 3000\,\mathrm{mm\,s^{-1}}$, $w_0 = 120\,\mu\mathrm{m}$, $\Theta_\infty = 55^\circ$ and $\Theta_\infty^\mathrm{s} = 60^\circ$. Red particles are modeled with the optical properties of aged titanium and blue particles are modeled with the optical properties of clean titanium.

by sim. 3 is smaller compared to sim. 1 and sim. 2. The reason for this is the amount of energy absorbed by the vapor phase in sim. 3. In contrast, the melt width obtained by sim. 3 at $E_A = 4.17\,\mathrm{J\,mm^{-2}}$ is larger than in the results obtained by sim. 1 and sim. 2. An explanation for this behavior could be the formation of a keyhole which allows more laser energy to be transmitted deeper into the material and which is why less energy is absorbed near the material surface. Therefore, the melt width decreases while the melt depth increases. In addition, Fig. 7.7 shows simulation snapshots for $P_0 = 500\,\mathrm{W}$. Here, liquid particles are colored red and solid particles are colored blue.

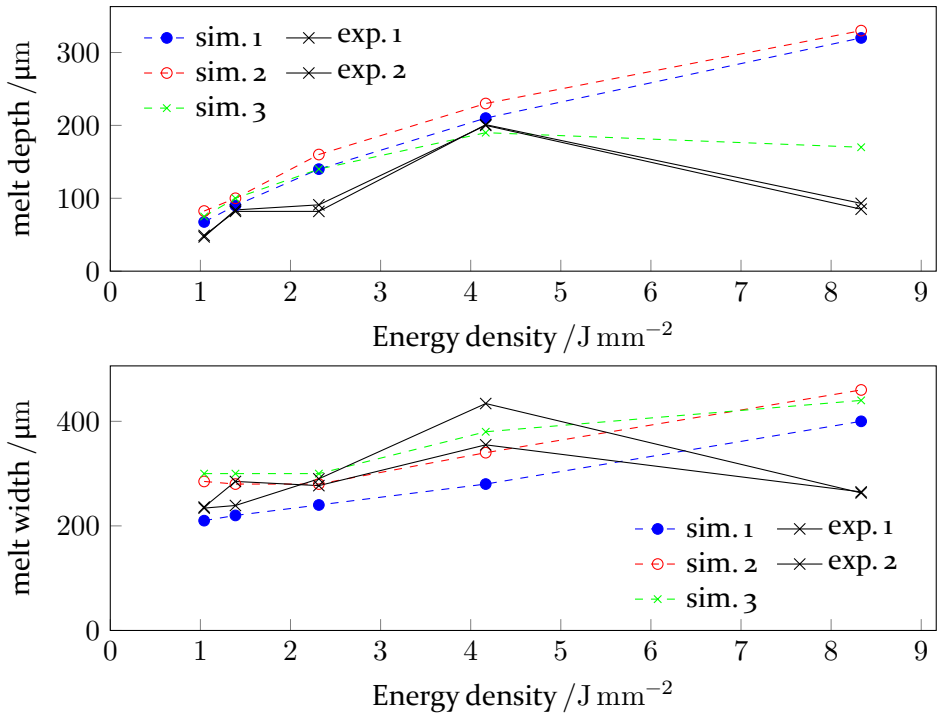

Figure 7.6: Comparison of simulated melt depth (top) and melt width (bottom) with experiments for $P_0 = 500\,\mathrm{W}$ and $w_0 = 120\,\mu\mathrm{m}$. Experimental data provided by Florian Huber, LPT, FAU.

It can be seen that a keyhole does indeed form due to the resultant recoil pressure at the evaporating surface. The keyhole is increasingly pronounced with decreasing scanning velocities of the laser beam.

7.4 Influence of laser parameters and wetting forces

In this section, the influence of the wetting forces on the surface geometry of the solidified welding seam is investigated for the material properties of titanium given in Chapter 3.1. As mentioned in Section 2.2.4, the equilibrium contact angle in homologous wetting problems is not known a priori but can be estimated by experiments as shown by [170, 171, 172]. Therefore, single-line tracks of the laser beam on a solid titanium block are simulated for the laser parameters given in Tab. 7.1. The parameter sets are distinguished by assigning numbers from 1 to 7, as shown by the first column in Tab. 7.1. The parameter set number is used to refer to the investigated laser parameters more easily. The corresponding dimensions of the simulated domain and the

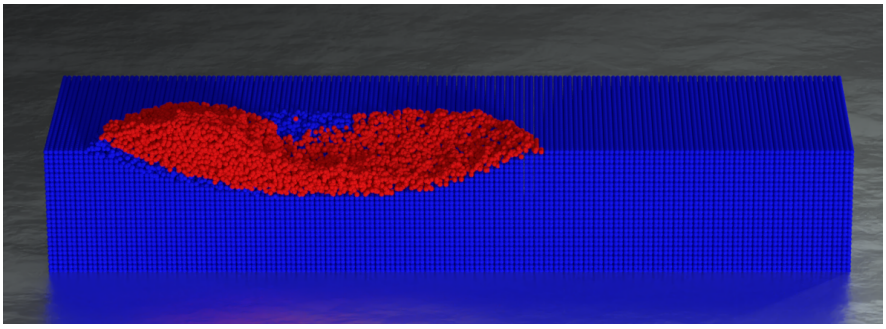

(a) Simulation snapshot at $t = 1.25\text{ms}$ for$u_1 = 2000\,\text{mm}\,\text{s}^{-1}$.

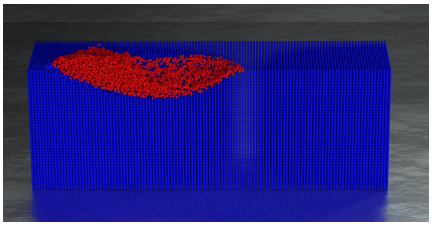

(b) Simulation snapshot at $t = 1.5\text{ms}$ for $u_1 = 1500\,\text{mm}\,\text{s}^{-1}$.

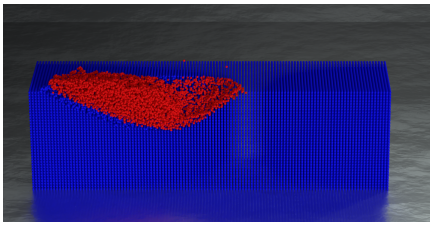

(c) Simulation snapshot at $t = 2.5\text{ms}$ for $u_1 = 900\,\text{mm}\,\text{s}^{-1}$.

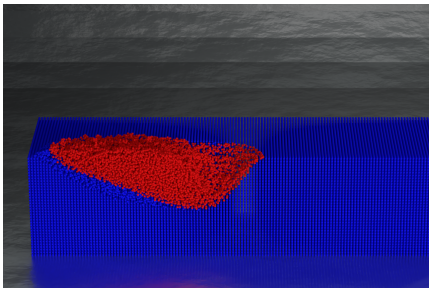

(d) Simulation snapshot at $t = 5.0\text{ms}$ for $u_1 = 500\,\text{mm}\,\text{s}^{-1}$.

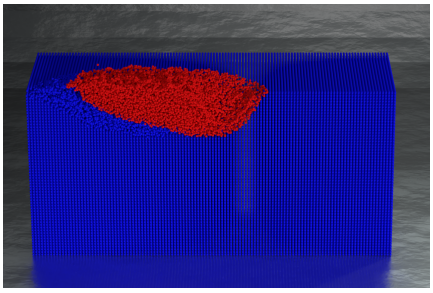

(e) Simulation snapshot at $t = 10.0\text{ms}$ for $u_1 = 250\,\text{mm}\,\text{s}^{-1}$

Figure 7.7: Simulation snapshots at different times for $P_0 = 500\,\text{W}$, $w_0 = 120\,\mu\text{m}$ and varying laser scanning velocity.

spatial discretization by SPH particles for each parameter set are given in the appendix in Tab. D.3. To relate the data of Tab. 7.1 to Tab. D.3, the parameter set number is used. The corresponding experimental images of the weld are provided for each parameter set by the LPT and shown in the appendix in Fig. D.1. For parameter set 7, no experimental data are provided.

In this section the same numerical model as employed in the previous Section 7.3 is used. The simulated domain is aligned with the axes of Euclidean space. The laser moves in the x-direction and starts at a distance of $165\,\mu\text{m}$

Table 7.1: Processing parameter sets that are investigated regarding their influence on the obtained surface geometry of the welding seam.

set	P_0 / W	u_1 / mm s^{-1}	w_0 / µm	E_A / J mm^{-2}
1	100	600	120	0.69
2	350	500	120	2.92
3	350	1500	120	0.97
4	500	1500	120	3.47
5	600	3000	120	0.83
6	350	2000	75	1.17
7	200	600	75	2.22

from the domain boundary. The kernel radius and the smoothing length are given by $r_{\max} = 4\Delta x$ and $h = 2\Delta x$, respectively. The mushy region of the employed latent heat model is defined by $\Delta T = 2\,\mathrm{K}$ and the adaptive thermal time step is adjusted to $\Delta T_{\text{control}} = 2\mathrm{K}$ by the linear controller. In addition, rays which discretize the laser beam energy are initialized within a circle with a radius of $r_{\text{ray},0} = 2w_0$ and with a density of $n_{\text{ray}} = 75$. The surface mesh required for the ray tracing algorithm is computed every five time steps to reduce the computational cost of the simulations. Moreover, gravity acts in the z-direction with $\mathbf{f}_{g,a} = [0,\ 0,\ -9.81\,\mathrm{m\,s^{-2}}]$, the ambient temperature is $T_0 = 300\,\mathrm{K}$ (necessary for Eq. (2.54)), the ambient pressure is $p_a = 1\,\mathrm{atm}$ (necessary for Eq. (2.33)) and the background pressure in the simulation is $p_{\text{amb}} = 0\,\mathrm{Pa}$ (required by Eqs. (7.8) and (4.49)). The initial temperature of the simulated material is $T_0 = 300\,\mathrm{K}$. The threshold for the normal vectors is adjusted in all subsequent simulations to $\epsilon_{\text{n}} = 0.1/h$. In the first set of simulations (using parameter set 1) the wetting forces are adjusted by the desired equilibrium contact angle, Θ_∞. Therefore, Θ_∞ is increased from $\Theta_\infty = 20^\circ$ to $\Theta_\infty = 40^\circ$ in steps of 5°. The corresponding values of Θ^{s}_∞ for each Θ_∞ are given in Tab. 7.2. Figure 7.8 shows the obtained welding

Table 7.2: Adjusted wetting forces in the simulations with parameter set 1 ($w_0 = 120\,\mu\mathrm{m}$, $P_0 = 100\,/\mathrm{W}$ and $u_1 = 600\,\mathrm{mm\,s^{-1}}$).

Θ_∞ / $^\circ$	20	25	30	35	40
Θ^{s}_∞ / $^\circ$	22	27	32	38	45

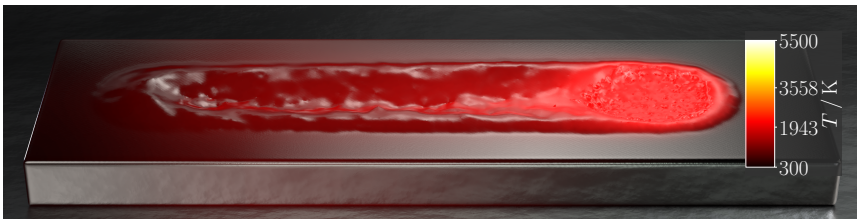

(a) $\Theta_\infty = 20°$, $\Theta^s_\infty = 22°$

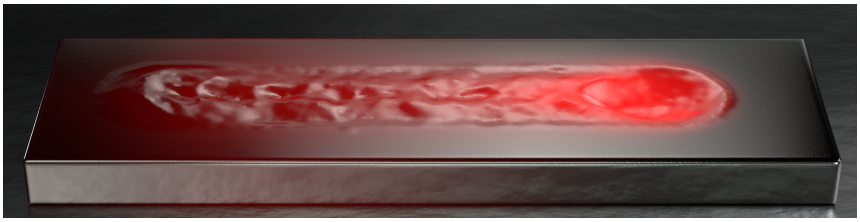

(b) $\Theta_\infty = 25°$, $\Theta^s_\infty = 27°$

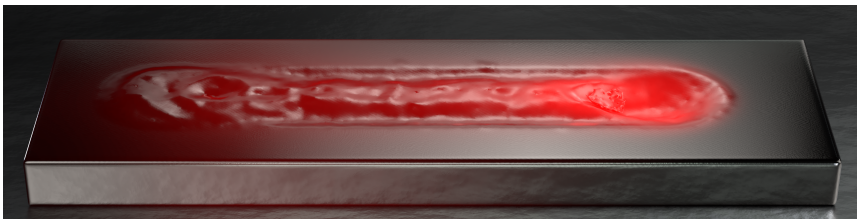

(c) $\Theta_\infty = 30°$, $\Theta^s_\infty = 32°$

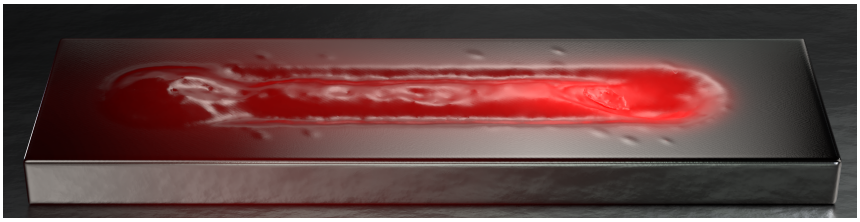

(d) $\Theta_\infty = 35°$, $\Theta^s_\infty = 38°$

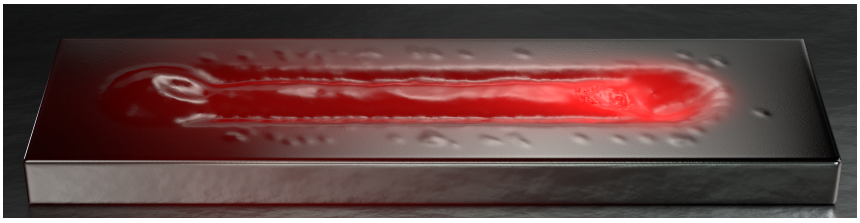

(e) $\Theta_\infty = 40°$, $\Theta^s_\infty = 45°$

Figure 7.8: Simulation snapshots of single-line laser tracks at $t = 1.7\,\mathrm{ms}$ using parameter set 1 ($w_0 = 120\,\mu\mathrm{m}$, $P_0 = 100\,\mathrm{W}$, $u_1 = 600\,\mathrm{mm\,s^{-1}}$) and varying wetting forces.

seam geometries as a function of the applied wetting forces as well as the corresponding temperature fields at $t = 1.7\,\mathrm{ms}$. The wetting forces which result from adjusting Θ_∞ and Θ_∞^s in the simulations, and which act at the three-phase contact line, affect the shape of the welding seam. It can be seen that high wetting forces ($\Theta_\infty = 20^\circ$), as shown in Fig. 7.8a, lead to a depression along the scanning path of the laser beam. This is caused by the liquid, which attempts to wet the solid titanium with a certain spreading velocity. As a result, a heap forms at the melt boundaries due to the combined effects of solidification and liquid spreading on the solid substrate. For increasing equilibrium contact angles, the applied wetting forces at the three-phase triple line decrease. As a result, the depression obtained for $\Theta_\infty = 20^\circ$ vanishes, which can be seen in Figs. 7.8b and 7.8c, where $\Theta_\infty = 25^\circ$ and $\Theta_\infty = 30^\circ$, respectively.

If the wetting forces are further decreased, the liquid melt starts to coalesce along the scanning path of the laser beam, which can be observed for $\Theta_\infty \geq 35^\circ$ and $\Theta_\infty = 40^\circ$ in Fig. 7.8d and Fig. 7.8e. As a result of the lower wetting forces, the molten titanium accumulates in the vicinity of the starting position of the laser beam. In contrast, a depression arises at the end of the laser track, as can be seen in Fig. 7.8d and Fig. 7.8e. The behavior of the melt at the beginning and end of the laser track is least pronounced for $\Theta_\infty = 25^\circ$ in Fig. 7.8b.

Moreover, small elevations on top of the solid material on both sides of the welding seam in Fig. 7.8d and Fig. 7.8e arise. This can be attributed to SPH particles that have emerged from the melt pool and solidified on the material block. Possibly, lower wetting forces lead to a less stable melt. To compare the welding seams obtained by simulations with the experiments, two-dimensional histograms of the y- and z-coordinates of those SPH particles located within $0.33 \leq x/L \leq 0.54$ at $t = 1\,\mathrm{ms}$, are computed. The investigated section of the domain is chosen so that non-equilibrium effects of the melt, in particular the formed heap at the beginning and the depression at the end of the weld, are excluded from the computation of the histogram.

As a result, five histograms for the varying wetting forces and parameter set 1 are obtained as shown in Fig. D.2 in the appendix. The computed histograms allow for identifying regions with high and low particle numbers and thus extracting the welding seam contours. Due to problems encountered when using numerical methods to estimate the exact welding seam contours, the contours must be determined with the bare eye.

Figure 7.9 shows the estimated welding seam contours extracted from Fig. D.2 for parameter set 1 depending on the applied wetting forces. Moreover, the corresponding experimental images of the weld cross-sections are shown to allow for a comparison with the simulations. The best agreement with the experimental welding seam geometry is obtained for $\Theta_\infty = 25^\circ$ or $\Theta_\infty = 30^\circ$. Higher values of Θ_∞ (too low wetting forces) result in convex surface contours. In contrast, smaller values of Θ_∞ (too high wetting forces) lead to the formation of a depression that does not comply with the experimental observation.

Figure 7.10 shows the temporal evolution of the welding seam using $\Theta_\infty = 25^\circ$ as well as the corresponding temperature fields. It can be seen that the temperature remains below the boiling temperature throughout the simulation. In addition, the start and end of the laser track show the already mentioned heap and depression, respectively.

To relate the adjusted wetting forces to the laser processing parameters, the temperature difference between the liquid phase located near the solid-liquid interface and the melting temperature is computed for every simulation snapshot. Therefore, the normal distance of all liquid SPH particle positions to the closest solid SPH particle position is computed by

$$d_a^{\mathrm{s}} = \min\left(\left|(\mathbf{r}_a - \mathbf{r}_b)\cdot\tilde{\hat{\mathbf{n}}}_a^{\mathrm{sf}}\right|\right), \tag{7.15}$$

where particle $a \in \Omega^{\mathrm{l}}$ and particle $b \in \Omega^{\mathrm{s}}$. Subsequently, all liquid SPH particles that are located in a distance of $10\,\mu\mathrm{m} < d_a^{\mathrm{s}} < 12\,\mu\mathrm{m}$ are used to compute the Stefan number given by

$$\mathrm{St} = \frac{c_p^{\mathrm{sl}}\,(T^{\mathrm{l}} - T_{\mathrm{m}})}{h_{\mathrm{m}}}\,. \tag{7.16}$$

Here, $c_p^{\mathrm{sl}} = 881.72\,\mathrm{J\,kg^{-1}\,K}$ is the mean value of the heat capacities of the solid and liquid phase at melting temperature, $T_{\mathrm{m}} = 1943\,\mathrm{K}$, and T^{l} is given by

$$T^{\mathrm{l}} = \frac{1}{N_{\mathrm{SPH}}^{\mathrm{l}}}\sum_{b\in\Omega^{\mathrm{l}}} T_b\,, \tag{7.17}$$

where $N_{\mathrm{SPH}}^{\mathrm{l}}$ is the number of liquid SPH particles located in a distance of $10\,\mu\mathrm{m} < d_a^{\mathrm{sl}} < 12\,\mu\mathrm{m}$ to the solid phase, respectively.

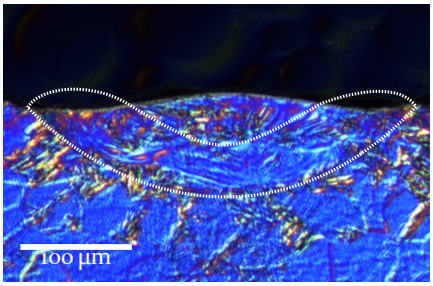

(a) $\Theta_\infty = 20^\circ$

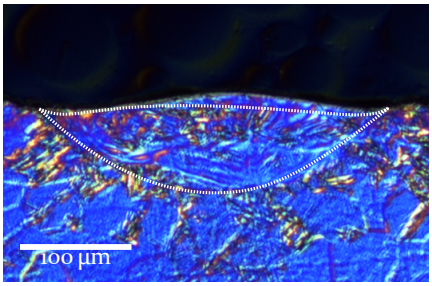

(b) $\Theta_\infty = 25^\circ$

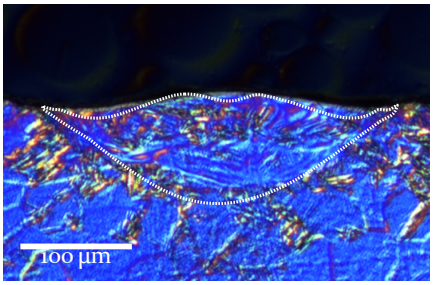

(c) $\Theta_\infty = 30^\circ$

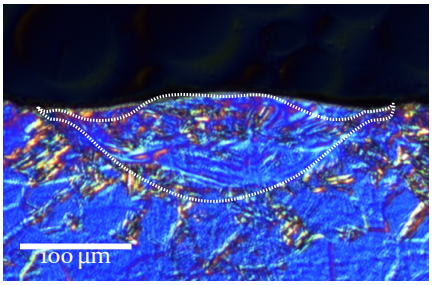

(d) $\Theta_\infty = 35^\circ$

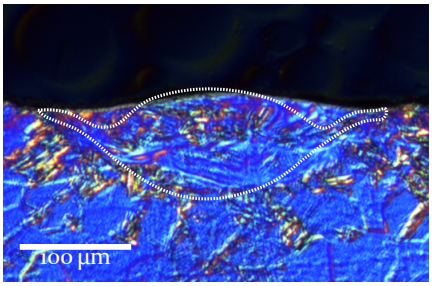

(e) $\Theta_\infty = 40^\circ$

Figure 7.9: Comparison of the weld geometries obtained by experiments and simulations with varying wetting forces for parameter set 1 ($w_0 = 120\,\mu\text{m}$, $P_0 = 100\,\text{W}$, $u_1 = 600\text{mm}\,\text{s}^{-1}$). Experimental images provided by Florian Huber, LPT, FAU.

(a) $t = 10^{-3}$ ms

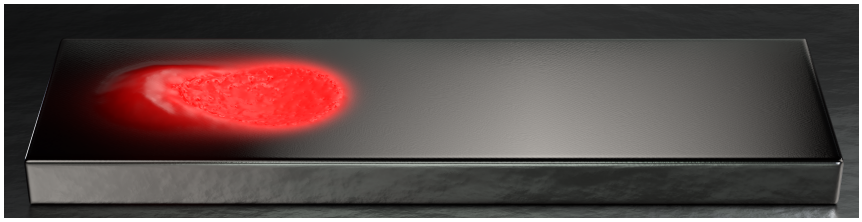

(b) $t = 0.5$ ms

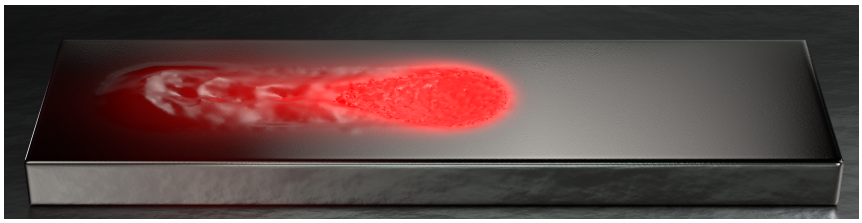

(c) $t = 1.0$ ms

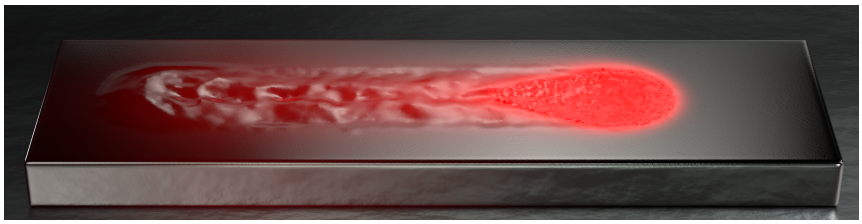

(d) $t = 1.5$ ms

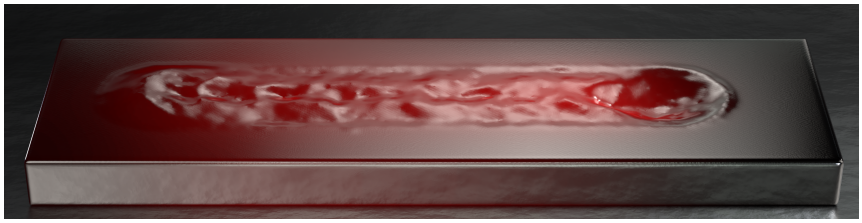

(e) $t = 2.0$ ms

Figure 7.10: Simulation snapshots of single-line laser tracks at different times using parameter set 1 ($w_0 = 120\,\mu\text{m}$, $P_0 = 100\,\text{W}$, $u_1 = 600\,\text{mm}\,\text{s}^{-1}$) and $\Theta_\infty = 25^\circ$.

Figure 7.11 shows the computed Stefan numbers as a function of ξ, which represents laser position scaled with $L_0 = 1\,\mathrm{mm}$ given by

$$\xi = (u_1 t)/L_0\,. \tag{7.18}$$

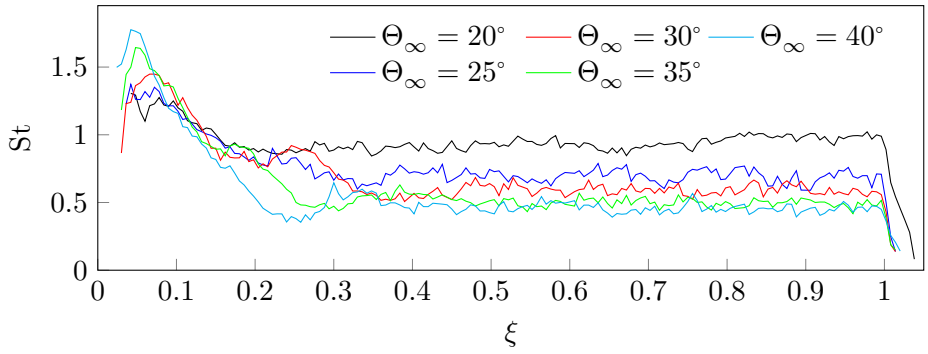

Figure 7.11: Stefan numbers as a function of the laser position obtained by simulations with parameter set 1 ($w_0 = 120\,\mu\mathrm{m}$, $P_0 = 100\,\mathrm{W}$, $u_1 = 600\,\mathrm{mm\,s^{-1}}$) and varying wetting forces.

The temperature difference between the liquid phase with $10\,\mu\mathrm{m} < d_a^{\mathrm{sl}} < 12\,\mu\mathrm{m}$ and melting temperature takes a maximum value after the laser has melted the first layers of SPH particles, approximately at $\xi = 0.05$, for all investigated wetting forces, adjusted via Θ_∞.

As the laser advances along its predefined path, the melt geometry approaches an equilibrium shape, and the Stefan number converges towards a minimum for all investigated wetting forces. Fluctuations in St can be seen in the range $0.2 \leq \xi < 1$. This may be attributed to the liquid flow and SPH particles entering and leaving the region where the liquid's temperature is measured. Moreover, it can be seen that the Stefan number increases with increasing wetting forces (decreasing Θ_∞). A reason for this could be the film thickness of the melt on the solid substrate. For higher wetting forces, the liquid spreads faster on the solid substrate, which is why the measured temperature difference between the advancing front of the liquid and the solid substrate is greater, which results in higher Stefan numbers. Another reason could be the shape of the melt. For high wetting forces (small values of Θ_∞), the surface of the weld remains flat or becomes depressed. Therefore, according to the Fresnel equations, the laser irradiates more surface area elements close to normal incidence, which results in a higher fraction of absorbed laser energy. In contrast, a higher fraction of the incident irradiation of the laser beam is

reflected due to the elevated weld shape obtained by lower wetting forces. When the laser beam is turned off at $\xi = 1$, the Stefan number decreases rapidly and approaches zero when all SPH particles are solidified.

Figure 7.12 shows the weld shapes obtained by experiments and simulations for parameter set 6. The wetting forces in the simulations are adjusted as given

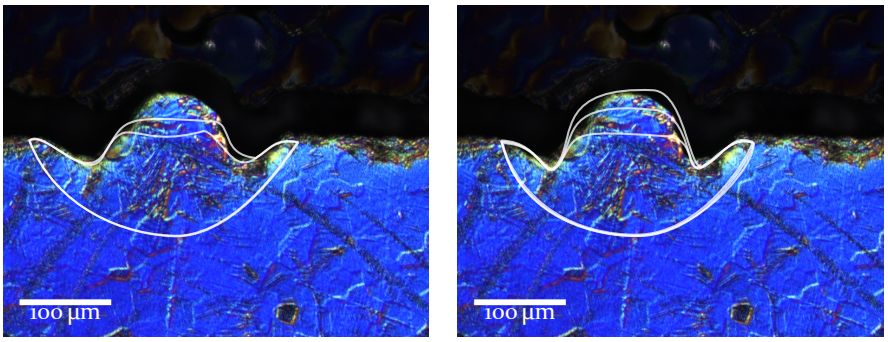

(a) $\Theta_\infty = 50°$ (b) $\Theta_\infty = 60°$

(c) $\Theta_\infty = 70°$ (d) $\Theta_\infty = 80°$

Figure 7.12: Comparison of the weld geometries obtained by experiments and simulations with varying wetting forces for parameter set 6 ($w_0 = 75\,\mu\text{m}$, $P_0 = 350\,\text{W}$, $u_1 = 2000$). Experimental images provided by Florian Huber, LPT, FAU.

in Tab. 7.3. The weld contours of the simulation are obtained in the same way

Table 7.3: Adjusted wetting forces in the simulations with parameter set 6 ($w_0 = 75\,\mu\text{m}$, $P_0 = 350\,/\text{W}$ and $u_1 = 2000\,\text{mm}\,\text{s}^{-1}$).

$\Theta_\infty\,/\,°$	50	60	70	80
$\Theta_\infty^{\text{s}}\,/\,°$	55	65	75	85

as for parameter set 1. The two-dimensional histograms are computed from

all SPH particles that are located within $0.28 \leq x/L \leq 0.58$ and are shown in Fig. D.3 in the appendix. The extracted contours from the simulations are compared to the experimental weld geometry in Fig. 7.12. Each image shows two or three contours extracted from the simulation data and the histograms in Fig. D.3. The occurrence of multiple contours of the weld cross-section can be addressed to discontinuous welding seams caused by weak wetting forces between the liquid and solid phase. The occurrence of heaps and depressions in the welding seam is also called humping. It can be seen that the height of the humps increases with increasing Θ_∞ and thus, decreasing wetting forces. The best agreement with the experimental weld is obtained for $\Theta_\infty = 60°$.

The comparisons of the weld geometries obtained by experiments and simulations for parameter sets 3 and 4 are shown in the appendix D. Since the simulations that use parameter sets 3 and 4 overestimate the dimensions of the weld geometry compared to the experiments, comparing the weld contours obtained by simulations with the experimental image of the weld is aggravated. It is assumed that $\Theta_\infty = 60°$ leads to the best agreement with the experiments since the experimental welding seam shapes are similar to those shown in Fig. 7.12.

To investigate the influence of low wetting forces on the Stefan number, simulations with parameter set 5 are carried out for the equilibrium contact angles given in Tab. 7.4. Subsequently, the Stefan numbers are computed by

Table 7.4: Adjusted wetting forces in the simulations with parameter set 5 ($w_0 = 120\,\mu\text{m}$, $P_0 = 600\,/\text{W}$ and $u_1 = 3000\,\text{mm}\,\text{s}^{-1}$).

$\Theta_\infty\,/\,°$	35	45	55	65	70
$\Theta_\infty^s\,/\,°$	40	50	60	70	75

Eq. (7.16) as a function of the dimensionless laser position. The results are shown in Fig. 7.13. Here, the measured Stefan number shows only a weak dependence on the wetting forces. This is in agreement with the results plotted in Fig. 7.11, where the computed Stefan number shows no significant change from $\Theta_\infty = 35°$ to $\Theta_\infty = 40°$. In addition, Fig. 7.14 shows simulation snapshots using parameter set 5 ($w_0 = 120\,\mu\text{m}$, $P_0 = 600\,\text{W}$, $u_1 = 3000\,\text{mm}\,\text{s}^{-1}$) and $\Theta_\infty = 55°$.

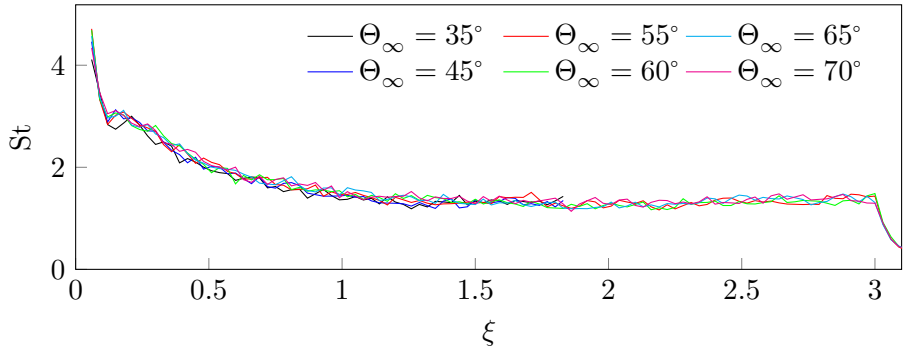

Figure 7.13: Stefan numbers as a function of the laser position obtained by simulations with parameter set 5 ($w_0 = 120\,\mu\mathrm{m}$, $P_0 = 600\,\mathrm{W}$, $u_1 = 3000\,\mathrm{mm\,s^{-1}}$) and varying wetting forces.

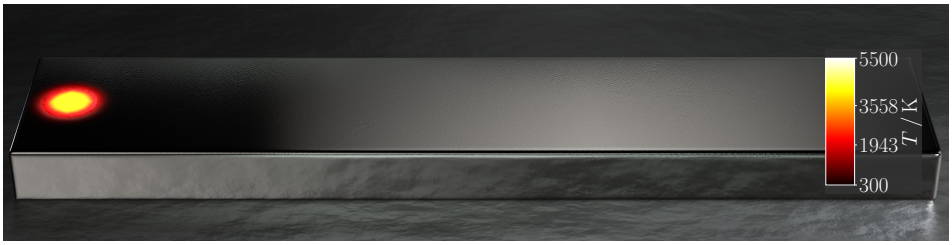

(a) $t = 10^{-3}$ ms

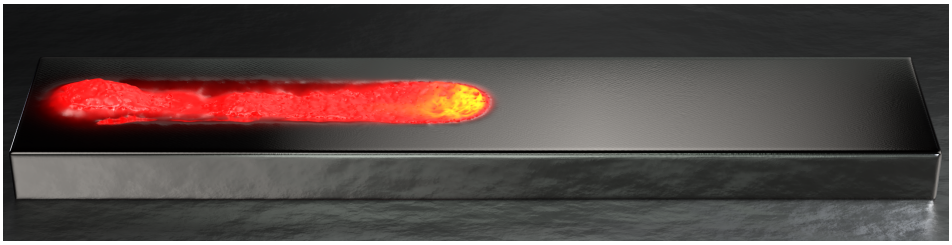

(b) $t = 0.5$ ms

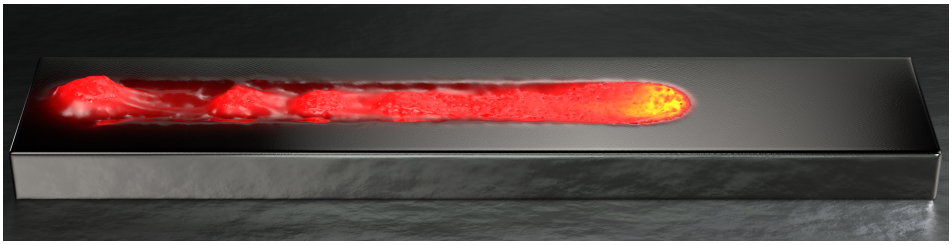

(c) $t = 0.75$ ms

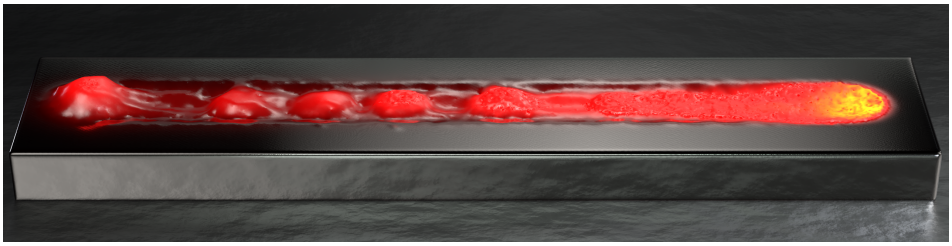

(d) $t = 1.0$ ms

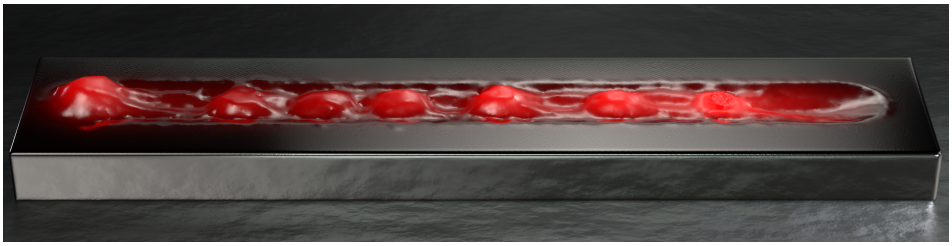

(e) $t = 1.25$ ms

Figure 7.14: Simulation snapshots of single-line laser tracks at different times using parameter set 5 ($w_0 = 120\,\mu\text{m}$, $P_0 = 600\,\text{W}$, $u_1 = 3000\,\text{mm}\,\text{s}^{-1}$) and $\Theta_\infty = 55^\circ$.

Compared to the simulation which employs parameter set 1 ($w_0 = 120\,\mu\mathrm{m}$, $P_0 = 100\,\mathrm{W}$, $u_1 = 600\,\mathrm{mm\,s^{-1}}$), the melt pool is more elongated. Due to the adjusted wetting forces, humping can also be observed. Furthermore, it can be seen that liquid melt coalesces at the tail of the melt. This could indicate that the occurrence of humping depends on the available time before the liquid phase is re-solidified. The longer a volume element of the titanium remains liquid, the longer the wetting forces act at the three-phase contact line of that liquid volume element. Moreover, the experimentally obtained welding seams using the parameter set 2, 5, and 7 are similar to those of the already investigated weld geometries where the parameter sets 1, 3, 4, and 6 are applied. For this reason, no further simulations are carried out to find the optimal wetting forces.

Table 7.5 shows the applied equilibrium contact angles used to adjust the wetting forces for parameter sets 1 to 7. Since no significant influence of the

Table 7.5: Laser processing parameters and corresponding calibrated equilibrium contact angles in the simulations.

set	$P\,/\,\mathrm{W}$	$u_1\,/\,\mathrm{mm\,s^{-1}}$	$w_0\,/\,\mathrm{m}$	$E_A\,/\,\mathrm{J\,mm^{-2}}$	$\Theta_\infty\,/^\circ$	$\Theta_\infty^\mathrm{s}\,/^\circ$
1	100	600	120	0.69	25	27
2	350	500	120	2.92	60	65
3	350	1500	120	0.97	60	65
4	500	1500	120	3.47	60	65
5	600	3000	120	0.83	60	65
6	350	2000	75	1.17	60	65
7	200	600	75	2.22	60	65

Stefan number on the wetting forces is observed in Fig. 7.13 for $\Theta_\infty^\mathrm{s} > 35^\circ$, it is assumed that the Stefan numbers, which are obtained by the simulations with the parameter sets given in Tab. 7.5, are comparable to each other. The estimated Stefan numbers for parameter sets 1, 2, 4, 5, and 6 are shown as a function of the laser position in Fig. 7.15. It can be seen that the computed Stefan number is affected by the adjusted laser processing parameters. When the obtained Stefan number is compared to the corresponding experimental images of the weld shape in Fig. 7.16, it can be seen that higher Stefan numbers are associated with more elevated welding seams. Higher Stefan numbers are related to higher temperature differences between liquid SPH particles near the solid-liquid interface particles and the melting temperature. This implies

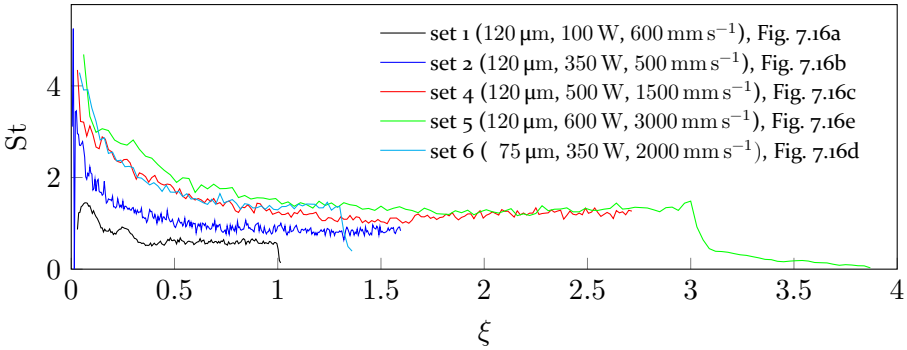

Figure 7.15: Stefan numbers as a function of the laser position obtained by the simulations with parameter set 1, 2, 4, 5, 6, and the corresponding adjusted wetting forces given in Tab. 7.5.

a greater temperature gradient across the solid-liquid interface, which may influence the resultant wetting forces.

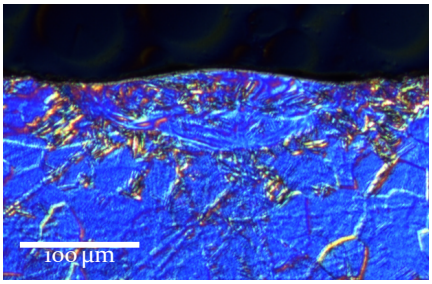

(a) Image of the weld cross section obtained by parameter set 1 in the experiments ($w_0 = 120\,\mu\text{m}$, $P_0 = 100\,\text{W}$, $u_1 = 600\,\text{mm}\,\text{s}^{-1}$).

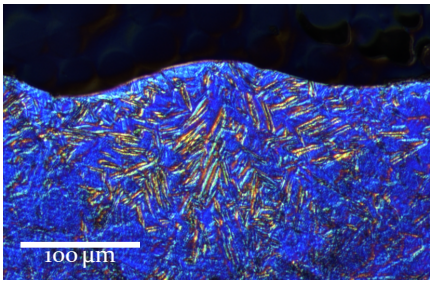

(b) Image of the weld cross section obtained by parameter set 2 in the experiments ($w_0 = 120\,\mu\text{m}$, $P_0 = 350\,\text{W}$, $u_1 = 500\,\text{mm}\,\text{s}^{-1}$).

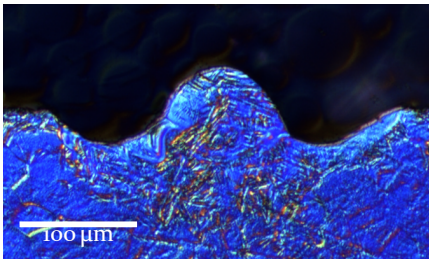

(c) Image of the weld cross section obtained by parameter set 4 in the experiments ($w_0 = 120\,\mu\text{m}$, $P_0 = 500\,\text{W}$, $u_1 = 1500\,\text{mm}\,\text{s}^{-1}$).

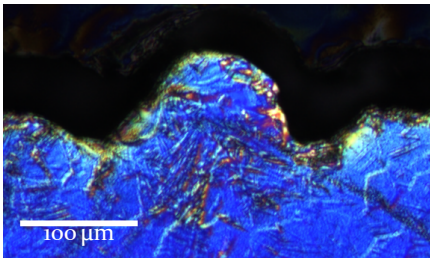

(d) Image of the weld cross section obtained by parameter set 6 in the experiments ($w_0 = 120\,\mu\text{m}$, $P_0 = 350\,\text{W}$, $u_1 = 2000\,\text{mm}\,\text{s}^{-1}$).

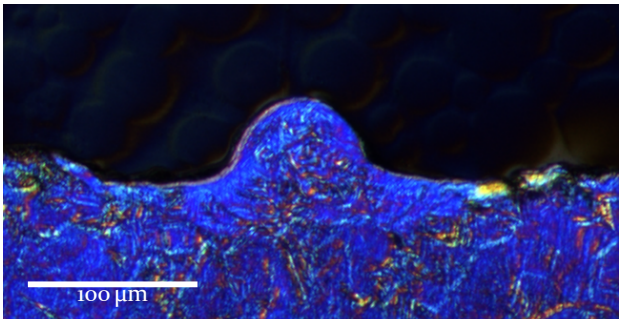

(e) Image of the weld cross section obtained by parameter set 5 in the experiments ($w_0 = 120\,\mu\text{m}$, $P_0 = 600\,\text{W}$, $u_1 = 3000\,\text{mm}\,\text{s}^{-1}$).

Figure 7.16: Microscopy images of the welding seam cross-sections obtained by experiments for various laser process parameters. Images provided by Florian Huber, LPT, FAU.

To represent each parameter set with a single number that describes the temperature field in the vicinity of the solid-liquid interface, the mean value of the Stefan numbers obtained in the range of $0.25 \leq \xi \leq 0.5$ is computed for each simulation. The computed mean Stefan numbers, denoted as $\overline{\mathrm{St}}$, are given in Tab. 7.6 as a function of the process parameters.

Table 7.6: Laser processing parameters and estimated mean Stefan number of the liquid phase in the vicinity of the solid-liquid interface.

set	P_0 / W	u_l / mm s^{-1}	w_0 / m	E_A / J mm^{-2}	Θ_∞ / °	Θ_∞^s / °	$\overline{\mathrm{St}}$
1	100	600	120	0.69	25	27	1.33
2	350	500	120	2.92	60	65	1.48
3	350	1500	120	0.97	60	65	2.76
4	500	1500	120	3.47	60	65	2.87
5	600	3000	120	0.83	60	65	3.56
6	350	2000	75	1.17	60	65	2.95
7	200	600	75	2.22	60	65	2.02

Consequently, $\overline{\mathrm{St}} = 1.33$ (parameter set 1, $\Theta_\infty = 25°$) and $\overline{\mathrm{St}} = 1.48$ (parameter set 2, $\Theta_\infty = 60°$) can be associated with the slightly elevated welding seams in Fig. 7.16a and Fig. 7.16b. The shape of the simulated weld cross-section with parameter set 2 has not been compared to the experimental image of the weld, which is why Θ_∞ is questionable. It is assumed that the correct value for the equilibrium contact angle for parameter set 2 should lie in the range $30° < \Theta_\infty < 60°$. However, since no significant deviation of the measured Stefan numbers could be seen for $\Theta_\infty > 35°$ in Figs. 7.11 and 7.13, it is assumed that $\overline{\mathrm{St}} = 1.48$ represents the difference of the liquid phase to the melting temperature in the vicinity of the solid-liquid interface correctly.

In addition, $\overline{\mathrm{St}} = 2.87$ (parameter set 4), $\overline{\mathrm{St}} = 2.95$ (parameter set 6) and $\overline{\mathrm{St}} = 3.56$ (parameter set 5) correspond to the highly elevated welding seams shown in Figs. 7.16c, 7.16d and 7.16e, respectively. Since good agreement of the weld shapes, obtained from simulations and experiments, can be observed for parameter set 1 (see Fig. 7.8 with $\Theta_\infty = 25°$) and parameter set 6 (see Fig. 7.12 with $\Theta_\infty = 60°$), it is assumed that the wetting forces decrease with increasing $\overline{\mathrm{St}}$.

To relate $\overline{\mathrm{St}}$ to the processing parameters, the laser intensity is plotted over the laser scanning velocity in Fig. 7.17. Furthermore, the data points in Fig. 7.17

are colored according to the corresponding values of $\overline{\mathrm{St}}$. Here, the filled

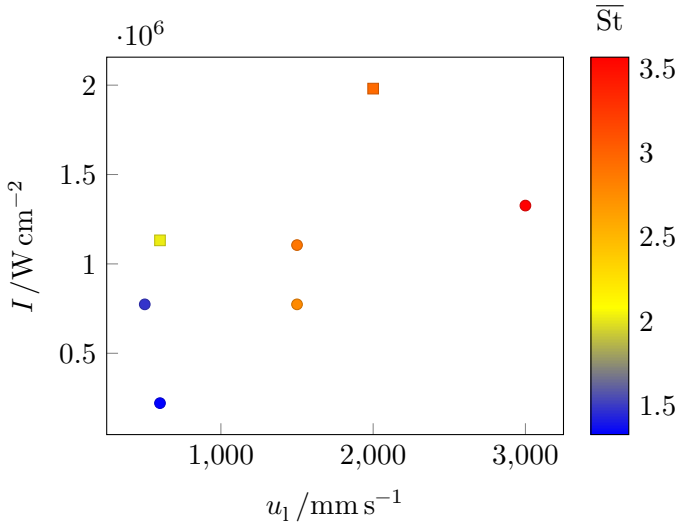

Figure 7.17: Computed mean Stefan number as a function of the laser intensity and laser scanning velocity. The filled circles denote the simulation results with $w_0 = 120\,\mu\mathrm{m}$ and the filled squares denote the simulation results with $w_0 = 75\,\mu\mathrm{m}$.

circles show the measured $\overline{\mathrm{St}}$ values in the simulations for parameter sets 1 to 5 with $w_0 = 120\,\mu\mathrm{m}$. In contrast, the filled squares show the values $\overline{\mathrm{St}}$ obtained from simulations with parameter sets 6 and 7, where the beam waist radius is $w_0 = 75\,\mu\mathrm{m}$. The estimated mean Stefan numbers increase with increasing laser scanning velocity and intensity due to the greater temperature difference to the melting temperature measured in the vicinity of the solid-liquid interface.

This means that stable and flat welding seams are obtained by choosing laser processing parameters which lead to small Stefan numbers. In contrast, harsh laser parameters (high intensity, high laser scanning velocity) result in elevated welding seams or even lead to bead formation of the melt, which is known as the humping phenomenon shown in Fig. 7.14. Thus, to avoid the humping phenomenon, the evolving temperature difference across the solid-liquid interface must be minimized by reducing the laser intensity or scanning velocity. Preheating the solid material may also reduce the occurrence of humping.

7.5 Concluding remarks

This chapter finalized the numerical method used for laser melting of metals by applying the smoothed pressure difference between recoil pressure and ambient pressure as a boundary condition to the PPE in Eq. (4.49) and the free surface formulation of the pressure gradient in Eq. (4.36). Moreover, a model that describes the effective optical properties of titanium has been presented. The energy equation is solved using adaptive numerical time steps to overcome the imposed restrictions on the numerical time step due to the latent heat model. Due to the non-linearity of the material's heating rate, a linear controller is used to adjust the thermal adaptive time step size to the desired value.

The LPT of the FAU provided experimental measurements of the weld geometry for several laser processing parameters. The weld geometries obtained by simulations using the SPH software are compared to the corresponding experimentally measured melt depth and width.

Therefore, three sets of simulations have been performed for each parameter set to investigate the surface properties of titanium and the resultant weld depth and width. It was found that the simulated weld geometry obtained by welding processes in the heat conduction regime, without evaporation, agrees quantitatively with the experiments when an aged titanium surface for the optical properties is assumed. Nevertheless, when considering a clean titanium surface, melt width and depth are drastically underestimated. This effect becomes less pronounced with decreasing laser scanning velocities and higher energy densities.

If the laser power is increased, the experimentally measured cross-sectional area of the weld does not increase linearly with decreasing laser scanning velocity but fluctuates. This may be attributed to complex melt flow, evaporation, or defocusation due to the evaporating vapor. The performed simulations can not reproduce these fluctuations. Still, the tendency of increasing melt depth and width with decreasing laser scanning velocity can be reproduced qualitatively. Here, the best simulation results, when compared to the experiments, are obtained using the numerical model that employs effective optical properties and, in addition, correlates the absorbed laser energy by the emerging vapor with the evaporation coefficient.

Subsequently, the influence of the wetting forces that act on the three-phase contact line of the melt has been investigated. For this reason, the applied wetting forces in the SPH simulations were adjusted iteratively until a qualitative agreement with the experimental weld shapes was achieved. Moreover,

the Stefan numbers, which characterize the temperature difference of selected SPH particles located in the vicinity of the solid-liquid interface to the melting temperature, are computed in all simulations. It is found that large Stefan numbers are related to more elevated welding seams, whereas small Stefan numbers are related to flat welding seams. Moreover, the Stefan number can be related to laser intensity and scanning velocity. An increase in laser power, a decrease in laser spot size, or an increase in the scanning velocity leads to greater Stefan numbers.

Finally, the Stefan numbers are related to the wetting forces. Higher Stefan numbers require to reduce the wetting forces in the simulations to obtain comparable welding seam geometries with the experiments. It can be seen that low wetting forces can result in the humping phenomenon prevalent in welding processes. In contrast, small Stefan numbers demand high wetting forces to obtain welding seam geometries comparable to experiments. Nevertheless, if the wetting forces are adjusted too high, the weld forms a depression along the moving direction of the laser beam.

To avoid the occurrence of the humping phenomenon, the laser intensity or the laser scanning velocity must be reduced.

8 Application: additive manufacturing

In this chapter, the developed simulation software, finalized in Chapter 7, is used to simulate LMD-w as well as SLM. Therefore, the kernel radius and the smoothing length are given by $r_{\max} = 4\Delta x$ and $h = 2\Delta x$. The width of the mushy region of the latent heat model is $\Delta T = 2\,\mathrm{K}$ and the adaptive time step is adjusted by the linear controller to $\Delta T_{\mathrm{control}} = 2\mathrm{K}$. The rays used to discretize the laser beam are initialized within a circle with radius $r_{\mathrm{ray},0} = 2w_0$ and with a ray density of $n_{\mathrm{ray}} = 75$. The normal threshold is $\epsilon_{\mathrm{n}} = 0.1/h$. Moreover, the ambient temperature is $T_0 = 300\,\mathrm{K}$ (necessary for Eq. (2.54)), the ambient pressure is $p_a = 1\,\mathrm{atm}$ (necessary for Eq. (2.33)) and the background pressure in the simulation is $p_{\mathrm{amb}} = 0\,\mathrm{Pa}$ (required by Eqs. (7.8) and (4.49)). Furthermore, the initial temperature of the simulated material is $T_0 = 300\,\mathrm{K}$.

8.1 Wire-based laser metal deposition

The application of 3D printing in space is increasingly attracting the interest of the scientific community. However, handling powder in space is difficult, which is why wire-based laser metal deposition is a potential candidate for application in space. To estimate the influence of gravity on the LMD-w process, the developed software is used to simulate the LMD-w process with and without gravity.

To represent the LMD-w process under conditions of zero-gravity, the body acceleration is given by $g_z = 0\,\mathrm{m\,s^{-1}}$, whereas the corresponding process under earth conditions is simulated using $g_z = -9.81\,\mathrm{m\,s^{-2}}$. Moreover, the conservation laws are solved as given in Section 7.3. The dimension of the solid substrate onto which the metal is deposited by melting a wire with a diameter of $1\,\mathrm{mm}$ has the dimension of $(9.8 \times 5.0 \times 1.0)\,\mathrm{mm}^3$. The simulated domain aligns with the axes of Euclidean space. Furthermore, the wire is oriented at 45° with respect to the solid substrate in the direction $[-0.707,\ 0,\ -0.707]$. The wire is irradiated by a laser beam with $P_0 = 1750\,\mathrm{W}$ and $w_0 = 0.56\,\mathrm{mm}$. Thus, the spot size of the laser is slightly larger than the diameter of the wire.

Wire and laser are moved in the x-direction with the same velocity, $u_1 = 100\,\mathrm{mm\,s^{-1}}$. Furthermore, the feed velocity of the wire in the direction $\hat{\mathbf{u}}_{\mathrm{wire}} = [-0.707, 0.0, -0.707]$ is adjusted depending on the distance between the wire tip (which is connected by a liquid bridge to the solid substrate in the

course of the simulations) and the solid substrate using a linear controller. The intermediate feed velocity at time n is given by

$$u_{\mathrm{feed}}^{n} = \begin{cases} a_{\mathrm{wire}} \Delta z_{\mathrm{wire}} & \text{if } a_{\mathrm{wire}} \left(\Delta z_{\mathrm{wire}}\right) < u_{\mathrm{feed,max}} \\ u_{\mathrm{feed,max}} & \text{else} \end{cases} , \tag{8.1}$$

where

$$\Delta z_{\mathrm{wire}} = z_{\mathrm{control}} - z_{\mathrm{wire,min}} = 0.4\,\mathrm{mm}\,, \tag{8.2}$$

is the desired distance in the z-direction of the wire tip to the solid substrate, $z_{\mathrm{wire,min}}$ represents the lowest z-position of a solid SPH particle that belongs to the subset of SPH particles representing wire, $u_{\mathrm{feed}}^{\mathrm{max}} = 200\,\mathrm{mm\,s^{-1}}$ is the maximum allowed feed velocity, and a_{wire} is a scaling parameter defined as

$$a_{\mathrm{wire}} = \frac{u_{\mathrm{feed,max}}}{\Delta x}\,. \tag{8.3}$$

The intermediate feed velocity in Eq. (8.1) is damped by taking the average of the intermediate feed velocities from the previous ten time steps,

$$\bar{u}_{\mathrm{feed}} = 0.1 \sum_{i=0}^{9} u_{\mathrm{feed}}^{n-i}\,. \tag{8.4}$$

The final velocity of the wire is composed of the laser scanning velocity vector, $\mathbf{u}_{\mathrm{l}} = [u_{\mathrm{l}},\, 0,\, 0]$, and the feed velocity, $\bar{u}_{\mathrm{feed}}$, by

$$\mathbf{u}_{\mathrm{wire}} = \mathbf{u}_{\mathrm{l}} + \hat{\mathbf{u}}_{\mathrm{wire}} \bar{u}_{\mathrm{feed}}\,. \tag{8.5}$$

The equilibrium contact angle for the wetting model is adjusted to $\Theta_{\infty} = 45^{\circ}$ with $\Theta_{\infty}^{\mathrm{s}} = 50^{\circ}$. The feed velocity of the wire depends on its distance to the desired z-position, guided by the linear controller, shown in Fig. 8.1 for the simulation with applied gravity. It can be seen that the linear controller is capable of steering the feed velocity (solid blue line) depending on the wire tip position (solid black line) to maintain the position of the wire tip at a desired height above the solid substrate. Figure 8.2 shows simulation snapshots of LMD-w with (left column) and without applied gravity (right column). At $t = 1\,\mathrm{ms}$, the laser irradiation starts to melt the wire. Moreover, a narrow region on the solid substrate is heated and melted since the laser spot diameter is slightly larger than the wire diameter. The continuous heating of the wire leads to the evolution of a liquid drop attached to the tip of the wire. When comparing the drop attached to the wire at $t = 19\,\mathrm{ms}$ obtained by the simulation with and without gravity, it can be seen that the center

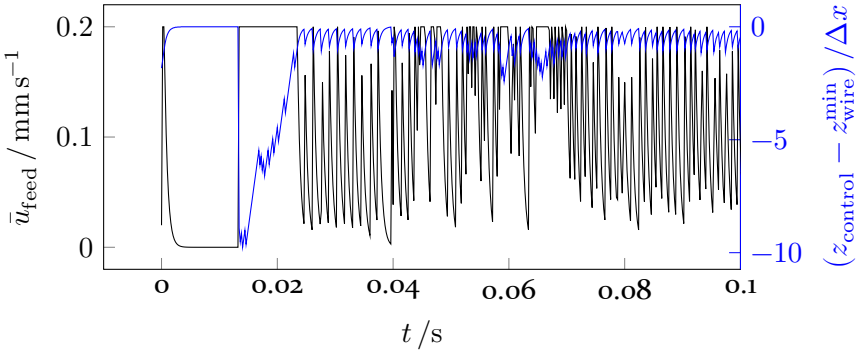

Figure 8.1: Adjusted wire feed velocity by the linear controller as a function of the wire distance to the desired height above the solid substrate for a LMD-w process under gravitational forces.

of gravity of the drop that experiences gravity is already closer to the solid substrate compared to the drop in the simulation without gravity. Due to the adjusted feed velocity of the wire and the inertia of the liquid drop, a liquid bridge forms between the solid substrate and the wire, as can be seen at $t = 36\,\text{ms}$. It can be seen that the axial velocity in the x-direction, u_1, is chosen too large, which is why the liquid bridge breaks approximately at $t = 50\,\text{ms}$. Nevertheless, the liquid bridges can be restored in both cases at $t = 75\,\text{ms}$ but with different effects on the deposited material. The simulation with gravity leads to the fragmentation of the deposited titanium. In contrast, titanium can be deposited without forming a fragmented bead in the absence of gravity. This can be explained by the amount of deposited material, which changes due to the effect of gravity compared to the simulation without gravity. In the absence of gravity, the liquid bridge can be maintained for a longer time. From these simulations, it can be seen that the LMD-w process is more stable in the absence of gravity for the simulated processing parameters compared to the LMD-w process carried out on earth.

8.2 Selective Laser Melting

To simulate the SLM process, titanium powder with the size distribution shown in Fig. 5.12 is deposited into a box. The particle size fractions for the two smallest particle diameters are ignored to reduce the computational costs of the subsequent SPH simulations. The box has the base dimensions of $(1500 \times 640)\,\mu\text{m}^2$ and is filled approximately up to a height of $85\,\mu\text{m}$ using LIGGGHTS [100].

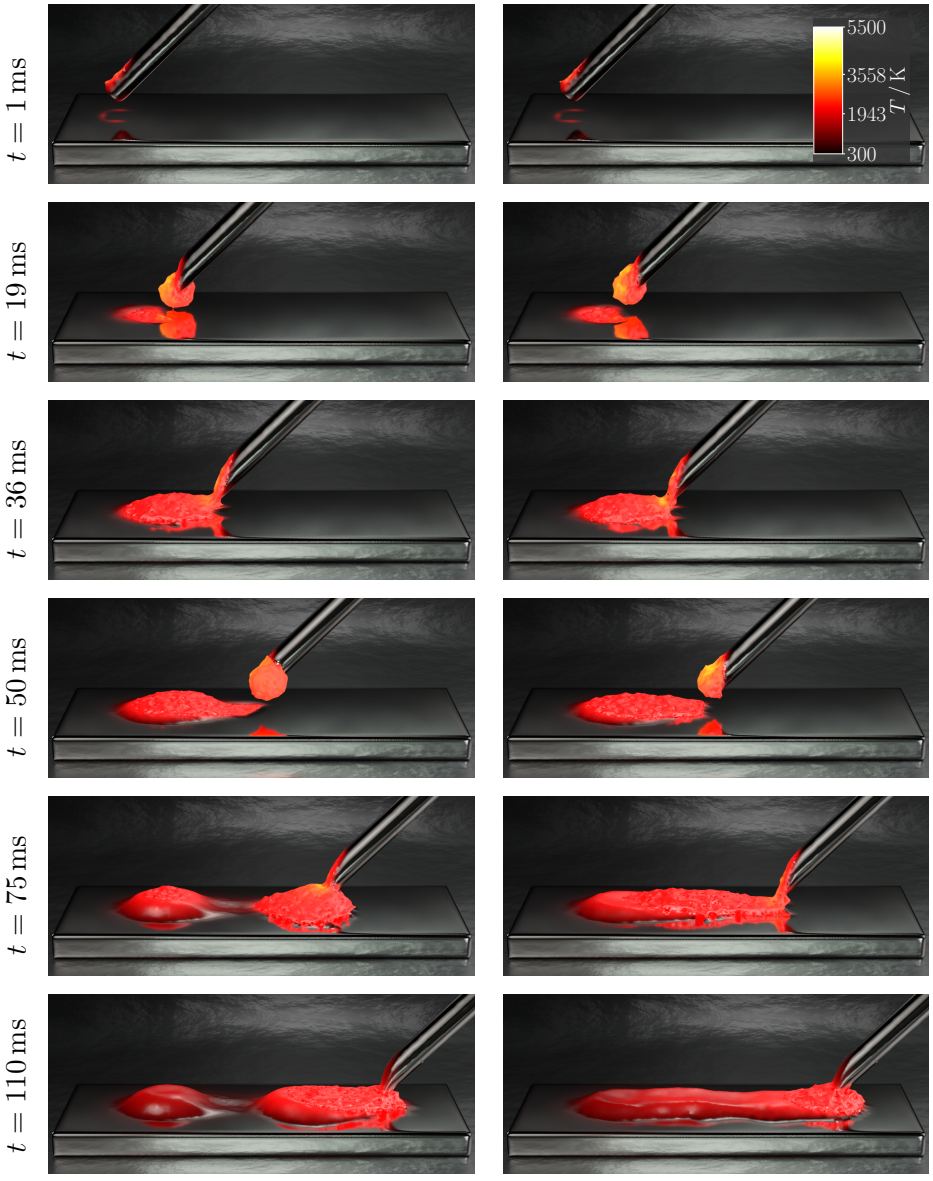

(a) $g_z = 9.81\,\mathrm{m\,s^{-2}}$ (b) $g_z = 0\,\mathrm{m\,s^{-2}}$

Figure 8.2: Comparison of the LMD-w simulations with (left column) and without gravitational forces (right column) and $u_1 = 100\,\mathrm{mm\,s^{-1}}$.

Only a spatial fraction of the deposited titanium powder with the dimension (600×340) µm² is selected to simulate the SLM process. Moreover, a solid substrate is put underneath the powder with a height of $50\,\mu\mathrm{m}$. The powder

bed is represented by SPH particles which are placed on a rectangular lattice with a spacing $\Delta x = 2.5 \cdot 10^{-6}\,\mathrm{m}$. This results in 1 049 660 SPH particles used to discretize the domain. As shown in [P20], the spherical shape of the powder leads to higher peak temperatures when compared to the laser welding simulations in Chapter 7. Therefore, to exclude evaporation effects, the laser parameters are adjusted to $P_0 = 100\,\mathrm{W}$, $w_0 = 120\,\mu\mathrm{m}$, $u_\mathrm{l} = 900\,\mathrm{mm\,s^{-1}}$.

The laser is moving in x-direction along the x-axis of the simulated domain, which is aligned with the axes of Euclidean space. The single-line track has a length of 400 µm. The start and end of the scanning path have a distance of $100\,\mu\mathrm{m}$ to the domain boundaries.

In this simulation, the CSF and the wetting model derived in Section 6.2 are replaced with the pairwise force model shown in [139]. This is necessary due to the complexity of the surface geometry, which has led to erroneous curvature estimates and unstable simulations when using CSF. Increasing the number of SPH particles used to simulate the SLM process could tackle this problem. However, that would lead to long simulation times. Accordingly, the terms of the CSF model in the momentum balance are replaced with the pairwise force term, $\mathbf{f}_{\sigma,a}^{\mathrm{pf}}$, according to

$$\frac{\mathrm{D}\mathbf{u}_a}{\mathrm{D}t} = \mathbf{f}_{\mathrm{p},a} + \mathbf{f}_{\eta,a} + \mathbf{f}_{\sigma,a}^{\mathrm{pf}} + \mathbf{f}_{g,a}\,. \tag{8.6}$$

Note that the employed pairwise force model cannot model Marangoni forces due to temperature gradients. The contact angle in the pairwise force model is adjusted by the ratio of attractive forces between SPH particles of the same kind and attractive forces between different types of SPH particles (solid and liquid phase) to $\Theta_\infty = 45^\circ$. Moreover, the solid titanium particles are immobile in space.

Figure 8.3 shows simulation snapshots at different times. Upon irradiation by the laser, liquid bridges are formed among titanium particles, as can be seen at $t = 0.01\,\mathrm{ms}$ and $t = 0.03\,\mathrm{ms}$.

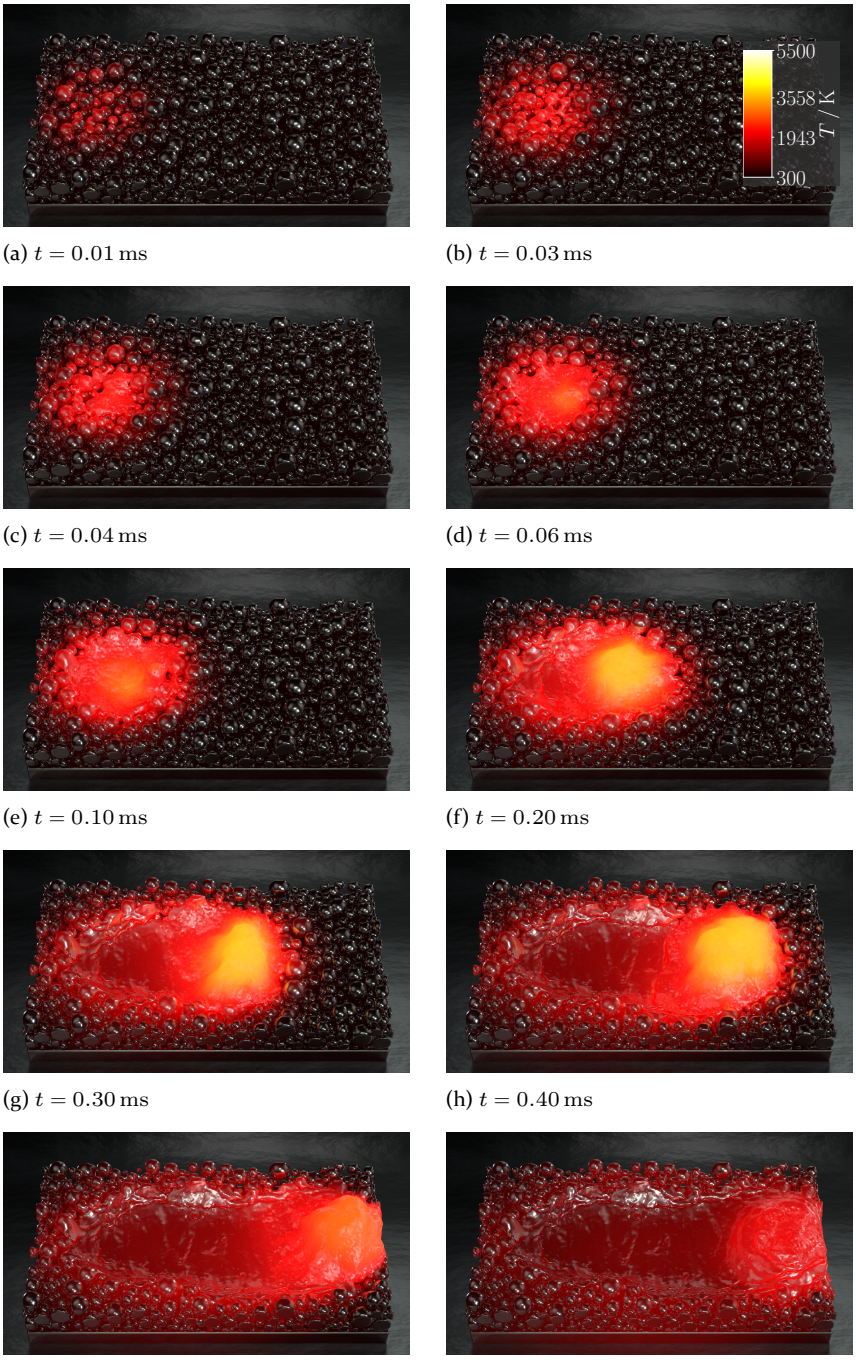

(a) $t = 0.01\,\mathrm{ms}$ (b) $t = 0.03\,\mathrm{ms}$

(c) $t = 0.04\,\mathrm{ms}$ (d) $t = 0.06\,\mathrm{ms}$

(e) $t = 0.10\,\mathrm{ms}$ (f) $t = 0.20\,\mathrm{ms}$

(g) $t = 0.30\,\mathrm{ms}$ (h) $t = 0.40\,\mathrm{ms}$

(i) $t = 0.50\,\mathrm{ms}$ (j) $t = 0.80\,\mathrm{ms}$

Figure 8.3: Simulation snapshots of the SLM process at different times using $w_0 = 120\,\mu\mathrm{m}$, $P_0 = 100\,\mathrm{W}$ and $u_1 = 900\,\mathrm{mm\,s^{-1}}$.

The evolving melt is accumulating due to the attractive forces between SPH particles and moves along with the laser beam in the x-direction. This behavior is different from the laser welding simulations carried out in this work and may be contributed to the balling phenomenon. Whether this behavior is caused by the employed pairwise force model and the absence of Marangoni forces or by the complex morphology of the powder bed has to be evaluated in more detail in the future. If the motion of the melt is caused by the employed pairwise forces and the incorporated contact angle model, it could indicate that pairwise forces are inappropriate to model laser melting processes. The employed CSF model, applied at free surfaces, should be further refined to allow the simulation of laser melting of complex geometries such as metal powder beds. A comparison of both approaches in more simple scenarios of laser melting could also clarify the observed behavior in this simulation.

8.3 Concluding remarks

This chapter shows two other application cases for the developed software. The LMD-w process with and without gravity has been simulated in the first scenario. It is found that the liquid bridge remains stable for a longer time in the absence of gravity. In contrast, the simulation with gravity leads to discontinuously deposited beads on the solid substrate.

In the second scenario, SLM has been simulated. Therefore, a polydisperse titanium powder bed is generated, and subsequently, each deposited particle is represented by many SPH particles. Due to the complex geometry of the powder bed, using CSF is not straightforward because of inaccurate curvature estimates, which leads to unstable simulations. This is why CSF is replaced with the pairwise force model shown in [139]. As a result, Marangoni forces are not modeled. It could be seen that the melt is accumulating due to attractive forces between SPH particles and is collectively moving in the same direction as the laser beam, leaving a sink along the path of the laser. Since this behavior could not be observed in the laser welding simulations of the previous chapter, it might be attributed to the balling phenomenon. To eliminate the possibility that the missing Marangoni forces trigger this behavior in the pairwise force model, the CSF model, which can be applied to free surfaces, should be refined for the application to complex geometries.

9 Summary and conclusion

In this work, the laser melting process of titanium is investigated by employing the ISPH method. In the ambiance of titanium, argon as an inert gas at atmospheric pressure is assumed. To minimize the computational cost of the developed numerical method, the ambient gas phase is not represented by SPH particles; instead, appropriate boundary conditions are applied at the liquid-gas interface.

The heat capacity, thermal conductivity, surface tension, and optical properties of titanium are considered temperature-dependent. At room temperature, the reported optical properties of titanium for a wavelength of $1.08\,\mu\mathrm{m}$ in the literature imply a reflectivity for normal incidence between $49\,\%$ [155] and $97.0\,\%$ [215] when using Fresnel laws. The variance of the experimentally estimated optical properties may be attributed to the sensibility of these measurements on the quality of the material surface. The formation of an oxidation layer, contamination with other chemicals, or a rough surface may affect the measured optical properties of titanium significantly. For this reason, this work distinguishes between a clean and an aged titanium surface.

To prevent the penetration of liquid SPH particles into solid walls, the impermeability condition of the wall is met by solving the PPE for solid SPH wall particles exclusively using liquid neighboring SPH particles. Moreover, the no-slip boundary condition is ensured by mirroring the fluid velocity of the liquid SPH particles to the solid SPH wall particles as proposed by [4]. The accuracy and robustness of the wall boundary conditions are verified by comparing the simulated transient velocity fields in a Poiseuille flow problem with to an analytical solution. In this test case, the deviation between simulation and theory is $1.6\,\%$ for the highest investigated spatial discretization.

Moreover, a ray-tracing algorithm is implemented into the employed SPH software to model the energy transfer of the Gaussian laser beam into the material. In this method, the laser beam is discretized into a finite number of rays, whereas each ray carries a fraction of the total laser power. The rays are homogeneously distributed in a circular area located above the irradiated surface. The energy carried by a ray depends on its radial distance to the center axis of the laser beam. To model the transfer of the rays to the SPH particles, a surface mesh is computed from the SPH particle positions. Any triangle of the surface mesh is made up of three SPH particles. Upon intersection of a ray with a triangle, the energy carried by the ray is transferred to the SPH particles as a function of their optical properties according to Fresnel laws.

To estimate the accuracy of the ray-tracing approach, analytical predictions of the forced heat equation with a Gaussian laser source term in a bounded domain are derived for two sets of boundary conditions. By imposing the first set of boundary conditions, the time-dependent temperature field in a cube where all sides are kept at constant temperature and whose upper half is transparent to laser irradiation is investigated. The effect of the statistical number of rays intersecting a triangle (ray density), smoothing length, and spatial discretization is analyzed. As a result, $n_{\mathrm{ray}} \approx 100$ is found as the optimal ray density in terms of numerical cost and accuracy. It can be shown that the time-averaged relative error between the temperature of the SPH particle located in the center of the laser beam and the analytical prediction decreases with decreasing smoothing length, increasing spatial resolution, and an increasing number of rays. For a smoothing length of $h = 1.5\Delta x$ and the highest investigated spatial resolution and ray density, the time-averaged relative error of the simulated temperature in the center of the laser beam to the corresponding analytical prediction is $1.8\,\%$. Furthermore, the lowest mean relative error between the temperature field of the irradiated layer of SPH particles and the theoretical temperature field, at a time where equilibrium is assumed, is $7.9\,\%$. In the second test case, the time-dependent temperature field in a cuboid where all sides, except for the plane facing the laser beam, are kept at a constant temperature is investigated. In this case, the plane irradiated by the laser beam represents a thermally insulated surface. The lowest computed time-averaged relative error between the simulated peak temperatures in the center of the laser beam and the corresponding analytical predictions is $4.3\,\%$. Moreover, the lowest mean relative error between the equilibrium temperature field of the irradiated layer of SPH particles and the theoretical predicted temperature field is $1.8\,\%$.

The presented ray-tracing approach was subsequently used to investigate effective laser absorption by a monodisperse and a polydisperse titanium powder bed at different temperatures below melting temperature and as a function of the surface quality. The powder is surrounded by argon gas at atmospheric pressure. It was found that the powder beds with the assumed aged surfaces exhibited a significantly higher absorptance than the corresponding titanium powder with clean surfaces. Moreover, the fraction of the absorbed laser energy increases with increasing temperature according to the temperature dependence of the material's surface reflectivity. The lowest absorptance of 0.04 is measured for the monodisperse clean powder at $300\,\mathrm{K}$ and the highest absorptance of 0.84 is measured for the aged polydisperse powder at $1800\,\mathrm{K}$. Furthermore, the laser irradiation propagates more deeply into the monodisperse powder bed than into the polydisperse powder bed due to the higher

void fraction between the titanium particles. Moreover, it was found that most irradiation is absorbed within the first layers of the titanium powder beds. Due to the higher void fraction of the monodisperse powder compared to the polydisperse titanium powder, the laser irradiation propagates more deeply into the monodisperse powder.

In this work, the truncation of the kernel integral of SPH particles in the vicinity of a free boundary is computed analytically. It is used to impose the time-varying pressure field of the ambient gas phase to the PPE and the pressure gradient approximation. Subsequently, surface tension is modeled by applying the Young-Laplace pressure to SPH particles in the vicinity of the liquid-gas interface as a boundary condition. The mean curvature at the position of liquid SPH particles near the liquid-gas interface is computed as the eigenvalues of the curvature tensor as proposed by [66]. To achieve sufficient accuracy in the curvature computation, the kernel gradient is renormalized using a correction matrix [25, 144]. The accuracy and robustness of the presented approach have been shown in a range of notoriously difficult test cases, including the measurement of the equilibrium pressure inside a spherical drop, whose relative error to the analytical estimated Young-Laplace pressure difference is 2.5 % using 268 096 SPH particles to represent the sphere. Furthermore, droplet oscillation, coalescence of drops, and the separation of a liquid cylinder into several drops following the Plateau-Rayleigh instability have been investigated.

Furthermore, the CSF model [26] is modified for the application to free surface problems. The mean curvature at the position of SPH particles near the liquid-gas interface is estimated by the SPH approximation of the divergence of normal vectors and using the renormalized kernel gradient [25, 144]. Using the modified CSF approach, the time-averaged relative error of the measured equilibrium pressure inside a spherical drop with varying spatial resolution has led to temporal pressure fluctuations. For this reason, the relative error between simulation and theory is computed from the simulated time-averaged pressure inside the drop and is estimated to be $1\,\%$ for a sphere represented by $268\,096$ particles. In another test case, the relative error of the oscillation frequency and the damping constant of an oscillating drop in zero-gravity between simulation and theory is estimated to be 7.5 %, and 5.1 %, respectively.

To include wetting forces, the smoothed normal correction scheme by Breinlinger et al. [31] is adopted. Here, the normal vectors of SPH particles located in the vicinity of the three-phase contact line are modified so that the resulting curvature encourages the wetting or non-wetting behavior of the liquid on a solid substrate. The normal vectors' orientation is determined by the desired

equilibrium contact angle, Θ_∞, that a liquid drop should have on a plane solid substrate. Thus, the equilibrium contact angle is an input parameter to the simulation. Applying this approach to model wetting forces with no other modification results in insufficient accuracy of the applied wetting forces due to the missing contribution of SPH particles representing the gas phase. For this reason, two modifications to the smoothed normal correction scheme are presented to model wetting phenomena at free boundaries.

In the first approach, wetting contact angles ($\Theta < 90^\circ$) are modeled. Here, the mean curvature of a liquid SPH particle is computed by including liquid SPH particles and selected solid SPH particles located in the vicinity of the three-phase contact line in the kernel approximation. The solid SPH particle neighbors of a liquid SPH particle near the three-phase contact line are identified according to their distance to the tangent plane, which is constructed from the corrected normal vector corresponding to Θ_∞ at the position of a liquid SPH particle. Solid SPH particles, located on the tangent plane's gaseous side, are excluded from the curvature computation of a liquid SPH particle. Thus, the solid SPH particles identified on the tangent plane's liquid side can be seen as a geometric extension of the liquid-gas interface into the solid substrate. The normal vectors of the identified solid SPH particles in the neighborhood of a liquid SPH particle, which are required for the computation of the curvature, are obtained by projecting the liquid SPH particle's normal vector to the positions of the solid SPH particles and subsequently, modifying these normal vectors as a function of another contact angle, Θ^s_∞. By taking $\Theta^s_\infty > \Theta_\infty$, the computed curvature is affected so that a possibly underestimated curvature, which would lead to non-terminating spreading on a solid substrate, is prevented. The ratio of Θ^s_∞ and Θ_∞ must be calibrated.

The second approach attempts to model non-wetting contact angles ($\Theta > 90^\circ$). For this reason, the mean curvature of a liquid SPH particle is computed by including only the normal vectors of neighboring liquid SPH particles and disregarding solid SPH particles. In contrast to the first approach, the correction matrix used to renormalize the SPH kernel gradient is also computed using liquid SPH particles alone. Moreover, the normal vectors of liquid SPH particles in the vicinity of the three-phase contact line are modified analogously to the first approach.

To verify the presented modifications to the smoothed normal correction scheme by Breinlinger et al. [31], a range of validation cases were performed, ranging from the simulation of drops resting on a plane surface with and without gravity to the pinning of drops that are accelerated towards the contact line of two planes that are inclined to each other. The simulated equilibrium

contact angles of drops in the absence of gravity deviate by $0.8\,\%$ and $4.4\,\%$ for $15^\circ \leq \Theta_\infty \leq 135^\circ$ to the desired equilibrium contact angle. For higher desired equilibrium contact angles, the relative error between measured and desired equilibrium contact angle increases to $14.3\,\%$ for $\Theta_\infty = 150^\circ$. The reason for these errors in the regime of non-wetting contact angles lies in the challenging detection of SPH particles located in the vicinity of the three-phase contact line and in inaccurately computed wetting forces caused by considering only liquid SPH particles in the corresponding computations for the curvature.

Furthermore, the height of the drop is measured as a function of the applied gravitational forces, adjusted by the Bond number. The simulated height of the drop in the range $3 \leq \mathrm{Bo} \leq 40$ is larger than the corresponding capillary length, which may be caused by overestimated curvatures of SPH particles in the vicinity of the three-phase contact line. Lastly, the pinning of drops accelerated towards the contact line of two planes as a function of their inclination angle is investigated. It can be seen that higher inclination angles lead to a stronger deceleration of the moving drop. Moreover, for an inclination angle of 90°, the liquid drop cannot pass the surface discontinuity of the two planes.

Marangoni forces, which arise due to surface tension gradients and are caused by temperature gradients in this work, are modeled at the liquid-gas interface by computing the surface gradient of temperature using the renormalized kernel gradient. The Marangoni forces are applied to a single layer of liquid SPH surface particles. The accuracy of this approach is verified by comparing the simulated velocity field in a cavity that is heated from one side and cooled from the other side with theory. A relative error of $0.15\,\%$ between the simulated and theoretical velocity field is obtained for the highest investigated spatial resolution.

To simulate laser-metal interaction problems, the employed numerical model is extended with a model that accounts for the absorption of laser radiation in the emerging vapor plume due to the rapid evaporation of the metal. In the presented model, the absorption of the laser energy by the emerging vapor is assumed to be linearly proportional to the temperature-dependent evaporation coefficient, which the employed evaporation model provides. Moreover, the recoil pressure caused by the metal's rapid evaporation is computed on a single layer of interfacial SPH particles at the liquid-gas interface. After that, the computed recoil pressure is projected to the position of SPH particle neighbors of the evaporating SPH particle. Thus, the smoothed recoil pressure is obtained for SPH particles located in the vicinity of the liquid-gas interface and can be imposed as a pressure boundary condition to the

PPE and the pressure gradient approximation, analogous to the presented pressure-based surface tension model. The reason for using the smoothed recoil pressure lies in more stable and robust simulations. In addition, due to the melting of titanium, SPH particles that are located initially at the material surface and which may represent aged titanium are possibly located in the bulk when the material is resolidified. Since any triangle of the computed surface mesh consists of three vertices, the effective optical properties of a triangle are computed as a linear combination of the optical properties of the SPH particles that constitute the triangle. Furthermore, an adaptive time-stepping scheme for the solution of the energy equation is introduced to overcome the imposed time step restriction of the employed latent heat model. Within each numerical time step, the energy equation is solved multiple times using a thermal numerical time step that is smaller than the numerical time step used to advance the SPH particles in space according to the momentum balance. Therefore, a linear controller is used to adjust the thermal numerical time step as a function of the material's heating rate and cooling rate.

The developed numerical model is subsequently used to investigate the laser melting of titanium at atmospheric pressure using argon as an inert gas. Therefore, the weld geometries obtained in simulations of single-line laser tracks on titanium are compared to the weld geometries obtained by experiments for the same set of laser parameters. The experimental data are provided by the LPT of the Friedrich-Alexander-Universität Erlangen-Nürnberg. For each parameter set, three simulations were performed. In these simulations, a clean titanium surface, an aged titanium surface, or a clean titanium surface in conjunction with the presented vapor absorption model are investigated. The aged titanium surface is modeled by initially assigning the optical properties of aged titanium to a boundary layer of SPH particles, whereas the remaining SPH particles are modeled with the optical properties of clean titanium. It was found that the simulated weld geometries obtained for laser parameters that do not lead to evaporation effects agree quantitatively with the experiments when an aged titanium surface is assumed. In contrast, when assuming a clean titanium surface, melt width and depth are underestimated compared to experiments. Nevertheless, the melt width and depth converge to the experimentally measured values for decreasing laser scanning velocities, indicating that the material's surface quality is essential, especially when the laser is operated at relatively low power. At higher laser powers, the experimentally measured cross-sectional area of the weld shows fluctuations. This behavior may be attributed to complex melt flow or the defocusation of the laser as a result of the evaporating vapor. In the simulations, these fluctuations in the melt geometry cannot be observed, and the simulated melt depth and width

follow the experimental prediction qualitatively. The best agreement with the experiments is obtained when laser absorption in the evaporating metal vapor is considered, and an aged titanium surface is assumed.

Subsequently, the surface geometry of the welding seam has been investigated as a function of laser processing parameters. The processing parameters could be shown to affect the temperature difference between the melt in the vicinity of the solid-liquid phase interface and the material's melting temperature. The temperature difference is used to compute the Stefan number, which is related to the welding seam's shape. The wetting forces applied to specific process parameters in these simulations are found iteratively by comparing the simulated welding seam cross-section with the experimentally obtained images of the weld cross-section. As a result, the computed Stefan numbers are related to the wetting forces, which depend on the process parameters of the laser.

The higher the Stefan number, the more elevated the welding seam becomes; hence, the lower the wetting forces in the simulations must be adjusted to match the experimental results. Sufficiently low wetting forces lead to the fragmentation of the liquid melt. The origin of this humping phenomenon, which may occur in welding processes, is assumed to lie in the dependence of wetting forces and the Stefan number. This is in contrast to previous theories which ascribe the origin of the humping phenomenon to Raleigh's capillary instability [28, 71], Kelvin-Helmholtz instability [105, 203], hydraulic jump [180], or to Marangoni forces [125]. Finally, it could be shown that the measured mean Stefan number increases with increasing laser intensity and scanning velocity.

In the last chapter, simulations of LMD-w and SLM are carried out. The LMD-w process is investigated regarding its applicability to zero-gravity environments. By comparing the LMD-w process with and without gravity, it has been found that the liquid bridge connecting wire and substrate remains more stable in the absence of gravity. A single laser track on polydisperse titanium powder is simulated in the SLM process. Due to the complex geometry of the powder bed, using CSF to model surface tension in this test case is not straightforward due to the orientation of the surface normal vectors on each titanium particle. This is why CSF is replaced with the pairwise force model shown in [139] which does not model Marangoni forces. It could be seen that the melt is accumulating due to attractive forces between SPH particles and moves collectively with the laser beam spot. Since this behavior could not be observed in the laser welding simulation shown in this work, the origin

could lie in absent Marangoni forces. Nevertheless, this observation must be investigated in future work to clarify this phenomenon.

Bibliography

[1] Aalilija, A.; Gandin, C.-A.; Hachem, E.: On the analytical and numerical simulation of an oscillating drop in zero-gravity. In: *Comput. Fluids* 197 (2020), 104362.

[2] Abioye, T. E.; Folkes, J.; Clare, A. T.: A parametric study of Inconel 625 wire laser deposition. In: *J. Mater. Process. Technol.* 213.12 (2013), 2145–2151.

[3] Aboulkhair, N. T.; Everitt, N. M.; Ashcroft, I.; Tuck, C.: Reducing porosity in AlSi10Mg parts processed by selective laser melting. In: *Addit. Manuf.* 1-4 (2014), 77–86.

[4] Adami, S.; Hu, X. Y.; Adams, N. A.: A generalized wall boundary condition for smoothed particle hydrodynamics. In: *J. Comput. Phys.* 231.21 (2012), 7057–7075.

[5] Agarwala, M.; Bourell, D.; Beaman, J.; Marcus, H.; Barlow, J.: Direct selective laser sintering of metals. In: *Rapid Prototyp. J.* 1.1 (1995), 26–36.

[6] Alexeev, I.; Leitz, K.-H.; Otto, A.; Schmidt, M.: Application of Bessel beams for ultrafast laser volume structuring of non transparent media. In: *Phys. Procedia* 5 (2010), 533–540.

[7] Alexiades, V.: *Mathematical modeling of melting and freezing processes*. CRC Press, 1992.

[8] Amanatides, J.; Woo, A.: *A fast voxel traversal algorithm for ray tracing.* In: *Eurographics*. Vol. 87. 3. 1987, 3–10.

[9] Anisimov, S. I.; Rakhmatulina, A. K.: The dynamics of the expansion of a vapor when evaporated into a vacuum. In: *Sov. Phys. JETP* 37 (1973), 441.

[10] Anisimov, S.: Evaporation of metal on absorbing laser radiation. In: *ZH EKSP TEOR FIZ* 54.1 (1968), 339–342.

[11] Arcella, F. G.; Froes, F. H.: Producing titanium aerospace components from powder using laser forming. In: *JOM* 52.5 (2000), 28–30.

[12] Atkins, P. W.; de Paula, J.: Physikalische Chemie, 4. vollständig überarbeitete Auflage. 2006.

[13] Babadagli, T.: Dynamics of capillary imbibition when surfactant, polymer, and hot water are used as aqueous phase for oil recovery. In: *J. Colloid Interface Sci.* 246.1 (2002), 203–213.

[14] Babadagli, T.; Boluk, Y.: Oil recovery performances of surfactant solutions by capillary imbibition. In: *J. Colloid Interface Sci.* 282.1 (2005), 162–175.

[15] Bandyopadhyay, A.; Heer, B.: Additive manufacturing of multi-material structures. In: *Mater. Sci. Eng. R Rep.* 129 (2018), 1–16.

[16] Bao, Y.; Li, L.; Shen, L.; Lei, C.; Gan, Y.: Modified smoothed particle hydrodynamics approach for modelling dynamic contact angle hysteresis. In: *Acta Mech Sin* 35.3 (2019), 472–485.

[17] Barcarolo, D.; Cadelier, J.; Guibert, D.; Leffe, M. de: Hydrodynamic performancesimulations using sph for automotive applications. In: *9th international SPHERIC workshop* (2014), 321–326.

[18] Bird, R. B.; Stewart, W. E.; Lightfood, E. N. L.: *Transport Phenomena, Revised 2nd Edition by R. Byron Bird Warren E. Stewart Edwin N. Lightfoot (2006-12-11)*. John Wiley & Sons, Inc., 2006.

[19] Blackburn, J.: 3 - Laser welding of metals for aerospace and other applications. In: ed. by Chaturvedi, M. C. Woodhead Publishing Series in Welding and Other Joining Technologies. Woodhead Publishing, 2012, 75–108.

[23] Boes, J.; Röttger, A.; Mutke, C.; Escher, C.; Theisen, W.: Microstructure and mechanical properties of X65MoCrWV3-2 cold-work tool steel produced by selective laser melting. In: *Addit. Manuf.* 23 (2018), 170–180.

[24] Bonet, J.; Kulasegaram, S.: Correction and stabilization of smooth particle hydrodynamics methods with applications in metal forming simulations. In: *Int. J. Numer. Methods Eng.* 47.6 (2000), 1189–1214.

[25] Bonet, J.; Lok, T.-S. L.: Variational and momentum preservation aspects of Smooth Particle Hydrodynamic formulations. In: *Comput. Methods Appl. Mech. Eng.* 180.1 (1999), 97–115.

[26] Brackbill, J.; Kothe, D. B.; Zemach, C.: A continuum method for modeling surface tension. In: *J. Comput. Phys.* 100.2 (1992), 335–354.

[27] Bradshaw, F. J.: The optical emissivity of titanium and zirconium. In: *Proc. Phys. Soc. London Sect. A* 63.8 (1950), 573–577.

[28] Bradstreet, B. J.: Effect of surface tension and metal flow on weld bead formation. In: *Weld J.* (1968), 47.

[29] Brandão, A. D.; Gerard, R.; Gumpinger, J.; Beretta, S.; Makaya, A.; Pambaguian, L.; Ghidini, T.: Challenges in additive manufacturing of space parts: Powder feedstock cross-contamination and tts impact on end products. In: *Materials* 10.5 (2017), 522.

[30] Brandes, E.; Brook, G.: *Smithells Metals Reference Book (Seventh Edition*. Oxford: Butterworth-Heinemann, 1992.

[31] Breinlinger, T.; Polfer, P.; Hashibon, A.; Kraft, T.: Surface tension and wetting effects with smoothed particle hydrodynamics. In: *J. Comput. Phys.* 243 (2013), 14–27.

[32] Brookshaw, L.: A method of calculating radiative heat diffusion in particle simulations. In: *Publ. Astron. Soc. Aust.* 6.02 (1985), 207–210.

[33] Calvert, P.: Inkjet printing for materials and devices. In: *Chem. Mater.* 13.10 (2001), 3299–3305.

[34] Chen, C. M.; Kovacevic, R.: Finite element modeling of friction stir welding—thermal and thermomechanical analysis. In: *Int. J. Mach. Tools Manuf.* 43.13 (2003), 1319–1326.

[35] Chen, Y.; Zhang, K.; Huang, J.; Hosseini, S. R. E.; Li, Z.: Characterization of heat affected zone liquation cracking in laser additive manufacturing of Inconel 718. In: *Mater. Des.* 90 (2016), 586–594.

[36] Cho, J.-H.; Na, S.-J.: Implementation of real-time multiple reflection and Fresnel absorption of laser beam in keyhole. In: *J. Phys. D: Appl. Phys.* 39.24 (2006), 5372–5378.

[37] Choo, D.-K.; Moon, H.-K.; Kang, T.; Lee, S.: Analysis and prevention of cracking during strip casting of AISI 304 stainless steel. In: *Metall. Mater. Trans. A* 32.9 (2001), 2249.

[38] Choudhury, B.; Chandrasekaran, M.: Investigation on welding characteristics of aerospace materials – A review. In: *Mater. Today: Proceedings* 4.8 (2017), 7519–7526.

[39] Chu, F.; Zhang, K.; Shen, H.; Liu, M.; Huang, W.; Zhang, X.; Liang, E.; Zhou, Z.; Lei, L.; Hou, J.; Huang, A.: Influence of satellite and agglomeration of powder on the processability of AlSi10Mg powder in laser powder bed fusion. In: *J. Mater. Res. Technol.* 11 (2021), 2059–2073.

[40] Cleary, P. W.; Monaghan, J. J.: Conduction modelling using smoothed particle hydrodynamics. In: *J. Comput. Phys.* 148.1 (1999), 227–264.

[41] Cleary, P. W.; Prakash, M.; Das, R.; Ha, J.: Modelling of metal forging using SPH. In: *Appl. Math. Model.* 36.8 (2012), 3836–3855.

[42] Community, B. O.: Blender - a 3D modelling and rendering package. Blender Foundation. Stichting Blender Foundation, Amsterdam, 2018.

[43] Courtois, M.; Carin, M.; Masson, P. L.; Gaied, S.; Balabane, M.: A new approach to compute multi-reflections of laser beam in a keyhole for heat transfer and fluid flow modelling in laser welding. In: *J. Phys. D: Appl. Phys.* 46.50 (2013), 505305.

[44] Crespo, A. J.; Gómez-Gesteira, M.; Dalrymple, R. A.: Boundary conditions generated by dynamic particles in SPH methods. In: *Comput. Mater. Contin.* 5.3 (2007), 173–184.

[45] Cummins, S. J.; Rudman, M.: An SPH projection method. In: *J. Comput. Phys.* 152.2 (1999), 584–607.

[46] Dai, D.; Gu, D.: Thermal behavior and densification mechanism during selective laser melting of copper matrix composites: Simulation and experiments. In: *Mater. Des.* 55 (2014), 482–491.

[47] Dai, M.; Schmidt, D. P.: Adaptive tetrahedral meshing in free-surface flow. In: *J. Comput. Phys.* 208.1 (2005), 228–252.

[48] Dal, M.; Fabbro, R.: An overview of the state of art in laser welding simulation. In: *Opt. Laser Techn.* 78 (2016), 2–14.

[49] Das, S.: Physical Aspects of Process Control in Selective Laser Sintering of Metals. In: *Adv. Eng. Mater.* 5.10 (2003), 701–711.

[50] DebRoy, T.; Wei, H. L.; Zuback, J. S.; Mukherjee, T.; Elmer, J. W.; Milewski, J. O.; Beese, A. M.; Wilson-Heid, A.; De, A.; Zhang, W.: Additive manufacturing of metallic components – Process, structure and properties. In: *Prog. Mater. Sci.* 92 (2018), 112–224.

[51] Dehnen, W.; Aly, H.: Improving convergence in smoothed particle hydrodynamics simulations without pairing instability. In: *Mon. Not. R. Astron. Soc.* 425.2 (2012), 1068–1082.

[52] Deng, D.; Murakawa, H.: Numerical simulation of temperature field and residual stress in multi-pass welds in stainless steel pipe and comparison with experimental measurements. In: *Comput. Mater. Sci* 37.3 (2006), 269–277.

[53] Desai, P.: Thermodynamic properties of titanium. In: *Int. J. Thermophys.* 8.6 (1987), 781–794.

[54] Diebold, U.: The surface science of titanium dioxide. In: *Surf. Sci. Rep.* 48.5 (2003), 53–229.

[55] Drazin, P. G.; Reid, W. H.: *Hydrodynamic Stability*. 2nd ed. Cambridge Mathematical Library. Cambridge: Cambridge University Press, 2004.

[56] Dupont, J.-B.; Legendre, D.: Numerical simulation of static and sliding drop with contact angle hysteresis. In: *J. Comput. Phys.* 229.7 (2010), 2453–2478.

[57] Ebadian, M. A.; Lin, C. X.: A review of high-heat-flux heat removal technologies. In: *J. Heat Transf.* 133.11 (2011).

[58] Ehrenfest, P.: Continuous quantum phase transitions. In: *Proc. Kon. Akad. Wetenschap, Amsterdam* 36 (1933), 153.

[59] Eskin, D. G.; Suyitno; Katgerman, L.: Mechanical properties in the semi-solid state and hot tearing of aluminium alloys. In: *Prog. Mater. Sci.* 49.5 (2004), 629–711.

[60] Farrokhpanah, A.; Bussmann, M.; Mostaghimi, J.: New smoothed particle hydrodynamics (SPH) formulation for modeling heat conduction with solidification and melting. In: *Numer. Heat Transf. B: Fundam.* 71.4 (2017), 299–312.

[61] Farrokhpanah, A.; Mostaghimi, J.; Bussmann, M.: Free-surface enthalpy method for transient convection/diffusion phase change. In: *arXiv preprint arXiv:1701.00463* (2017).

[62] Fischer, J.: Distribution of pure vapor between two parallel plates under the influence of strong evaporation and condensation. In: *Phys. Fluids* 19.9 (1976), 1305–1311.

[63] Fleissner, F.; Eberhard, P.: A co-simulation approach for the 3D dynamic simulation of vehicles considering sloshing in cargo and fuel tanks. In: *PAMM* 9.1 (2009), 133–134.

[64] Fleissner, F.; Lehnart, A.; Eberhard, P.: Dynamic simulation of sloshing fluid and granular cargo in transport vehicles. In: *Veh. Syst. Dyn.* 48.1 (2010), 3–15.

[65] Fortov, V. E.; Dremin, A. N.; Leont'ev, A. A.: Evaluation of the parameters of the critical point. In: *Teplofiz Vys Temp* 13.5 (1975), 1072–1080.

[66] Fürstenau, J.-P.; Weißenfels, C.; Wriggers, P.: Free surface tension in incompressible smoothed particle hydrodynamcis (ISPH). In: *Comput. Mech.* 65.2 (2020), 487–502.

[67] Geenen, K.; Röttger, A.; Feld, F.; Theisen, W.: Microstructure, mechanical, and tribological properties of M3:2 high-speed steel processed by selective laser melting, hot-isostatic pressing, and casting. In: *Addit. Manuf.* 28 (2019), 585–599.

[68] Gingold, R. A.; Monaghan, J. J.: Smoothed particle hydrodynamics: theory and application to non-spherical stars. In: *MNRAS* 181.3 (1977), 375–389.

[69] Glowacki, M. H.: The effects of the use of different shielding gas mixtures in laser welding of metals. In: *J. Phys. D: Appl. Phys.* 28.10 (1995), 2051–2059.

[70] Gong, H.; Rafi, K.; Gu, H.; Starr, T.; Stucker, B.: Analysis of defect generation in Ti–6Al–4V parts made using powder bed fusion additive manufacturing processes. In: *Addit. Manuf.* 1-4 (2014), 87–98.

[71] Gratzke, U.; Kapadia, P.; Dowden, J.; Kroos, J.; Simon, G.: Theoretical approach to the humping phenomenon in welding processes. In: *J. Phys. D: Appl. Phys.* 25 (2000), 1640.

[72] Gu, D.; Meiners, W.; Wissenbach, K.; Poprawe, R.: Laser additive manufacturing of metallic components: materials, processes and mechanisms. In: *Int. Mater. Rev.* 57.3 (2012), 133–164.

[73] Gu, D.; Hagedorn, Y.-C.; Meiners, W.; Meng, G.; Batista, R. J. S.; Wissenbach, K.; Poprawe, R.: Densification behavior, microstructure evolution, and wear performance of selective laser melting processed commercially pure titanium. In: *Acta Mater.* 60.9 (2012), 3849–3860.

[74] Gu, D.; Shen, Y.: Balling phenomena in direct laser sintering of stainless steel powder: Metallurgical mechanisms and control methods. In: *Mater. Des.* 30.8 (2009), 2903–2910.

[75] Gunenthiram, V.; Peyre, P.; Schneider, M.; Dal, M.; Coste, F.; Fabbro, R.: Analysis of laser–melt pool–powder bed interaction during the selective laser melting of a stainless steel. In: *J. Laser Appl.* 29.2 (2017), 022303.

[76] Hertz, H.: Ueber die Verdunstung der Flüssigkeiten, insbesondere des Quecksilbers, im luftleeren Raume. In: *Ann. Phys.* 253.10 (1882), 177–193.

[77] Hirschler, M.; Oger, G.; Nieken, U.; Touzé, D. L.: Modeling of droplet collisions using Smoothed Particle Hydrodynamics. In: *Int. J. Multiph. Flow* 95 (2017), 175–187.

[78] Hoch, M.: *High temperature specific heat of body-centered-cubic refractory metals*. Tech. rep. General Electric Co., Cincinnati, Ohio. Missile and Space Div., 1969.

[79] Hong, K.-M.; Shin, Y. C.: Prospects of laser welding technology in the automotive industry: A review. In: *J. Mater. Process. Technol.* 245 (2017), 46–69.

[80] Hsiao, J.; Chung, B. T.: An efficient algorithm for finite element solution to two-dimensional heat transfer with melting and freezing. In: *J. Heat Transf.* 108.2 (1986), 462–464.

[81] Hu, H.; Fetzer, F.; Berger, P.; Eberhard, P.: Simulation of laser welding using advanced particle methods. In: *GAMM-Mitteilungen* 39.2 (2016), 149–169.

[82] Hu, H.; Fetzer, F.; Berger, P.; Eberhard, P.: *Process simulation of deep penetration laser welding by coupling a smoothed particle hydrodynamics model with a ray-tracing scheme*. In: CIMNE, 2017, 450–460.

[83] Huang, C.; Kou, S.: Liquation cracking in full-penetration Al-Cu welds. In: *Weld. J.* 83.2 (2004), 50–S.

[84] Hurt, C.; Brandt, M.; Priya, S. S.; Bhatelia, T.; Patel, J.; Selvakannan, P.; Bhargava, S.: Combining additive manufacturing and catalysis: a review. In: *Catal. Sci. Technol* 7.16 (2017), 3421–3439.

[85] Hussein, A.; Hao, L.; Yan, C.; Everson, R.: Finite element simulation of the temperature and stress fields in single layers built without-support in selective laser melting. In: *Mater. Des. (1980-2015)* 52 (2013), 638–647.

[86] Iida, T.; Guthrie, R. I. L.: *The physical properties of liquid metals*. Oxford; New York: Clarendon Press ; Oxford University Press, 1988.

[87] Ishikawa, T.; Paradis, P.-F.; Okada, J. T.; Watanabe, Y.: Viscosity measurements of molten refractory metals using an electrostatic levitator. In: *Meas. Sci. Technol.* 23.2 (2012), 025305.

[88] Jacobson, M. I.: *An investigation of the lattice parameters, electrical resistivity, and magnetic susceptibility of some titanium alloys: proposal of an electronic band structure*. The Ohio State University, 1958.

[89] Jalar, A.; Che Lah, N. A.; Othman, N. K.; Shamsudin, R.; Daud, A. R.; Sayd Bakar, S. R.: Characterization of Oxide Growth on Surface of Al-Mg-Si Welded Joint. In: *Adv. Mater. Sci. Eng.* 2014 (2014), e272804.

[90] Jia, Q.; Gu, D.: Selective laser melting additive manufacturing of Inconel 718 superalloy parts: Densification, microstructure and properties. In: *J. Alloys Compd.* 585 (2014), 713–721.

[91] Johnson, P. B.; Christy, R. W.: Optical constants of transition metals: Ti, V, Cr, Mn, Fe, Co, Ni, and Pd. In: *Phys. Rev. B* 9.12 (1974), 5056–5070.

[92] Keicher, D. M.; Smugeresky, J. E.: The laser forming of metallic components using particulate materials. In: *JOM* 49.5 (1997), 51–54.

[93] Kempen, K.; Vrancken, B.; Buls, S.; Thijs, L.; Van Humbeeck, J.; Kruth, J.-P.: Selective Laser Melting of Crack-Free High Density M2 High Speed Steel Parts by Baseplate Preheating. In: *J. Manuf. Sci. Eng.* 136.6 (2014).

[94] Ketterson, J. B.: *The Physics of Solids*. Oxford, New York: Oxford University Press, 2016.

[95] Khairallah, S. A.; Anderson, A. T.; Rubenchik, A.; King, W. E.: Laser powder-bed fusion additive manufacturing: Physics of complex melt flow and formation mechanisms of pores, spatter, and denudation zones. In: *Acta Mater.* 108 (2016), 36–45.

[96] Kim, D.-K.; Hwang, J.-H.; Kim, E.-Y.; Heo, Y.-U.; Woo, W.; Choi, S.-H.: Evaluation of the stress-strain relationship of constituent phases in AlSi10Mg alloy produced by selective laser melting using crystal plasticity FEM. In: *J. Alloys Compd.* 714 (2017), 687–697.

[97] King, W. E.; Barth, H. D.; Castillo, V. M.; Gallegos, G. F.; Gibbs, J. W.; Hahn, D. E.; Kamath, C.; Rubenchik, A. M.: Observation of keyhole-mode laser melting in laser powder-bed fusion additive manufacturing. In: *J. Mater. Process. Technol.* 214.12 (2014), 2915–2925.

[98] Klassen, A.: Simulation of evaporation phenomena in selective electron beam melting. doctoralthesis. FAU University Press, 2018, xxiii, 238 S.

[99] Klassen, A.; Scharowsky, T.; Körner, C.: Evaporation model for beam based additive manufacturing using free surface lattice Boltzmann methods. In: *J. Phys. D: Appl. Phys.* 47.27 (2014), 275303.

[100] Kloss, C.; Goniva, C.; König, A.; Amberger, S.; Pirker, S.: Models, algorithms and validation for opensource DEM and CFD-DEM. In: *Prog. Comput. Fluid Dyn.* 12 (2012), 140–152.

[101] Knight, C. J.: Theoretical modeling of rapid surface vaporization with back pressure. In: *AIAA journal* 17.5 (1979), 519–523.

[102] Knudsen, M.: Die Molekularströmung der Gase durch Öffnungen und die Effusion. In: *Ann. Phys.* 333.5 (1909), 999–1016.

[103] Kobryn, P. A.; Ontko, N. R.; Perkins, L. P.; Tiley, J. S.: *Additive Manufacturing of Aerospace Alloys for Aircraft Structures.* Tech. rep. ADA521726. 2006.

[104] Kruth, J. P.; Froyen, L.; Van Vaerenbergh, J.; Mercelis, P.; Rombouts, M.; Lauwers, B.: Selective laser melting of iron-based powder. In: *J. Mater. Process. Technol.* 14th Interntaional Symposium on Electromachining (ISEM XIV) 149.1 (2004), 616–622.

[105] Kumar, A.; Debroy, T.: Toward a unified model to prevent humping defects in gas tungsten arc welding. In: *Weld J.* 85 (2006), 292–s.

[106] Leal, R.; Barreiros, F. M.; Alves, L.; Romeiro, F.; Vasco, J. C.; Santos, M.; Marto, C.: Additive manufacturing tooling for the automotive industry. In: *Int. J. Adv. Manuf. Technol.* 92.5 (2017), 1671–1676.

[107] Lee, J. Y.; Ko, S. H.; Farson, D. F.; Yoo, C. D.: Mechanism of keyhole formation and stability in stationary laser welding. In: *J. Phys. D: Appl. Phys.* 35.13 (2002), 1570–1576.

[108] Leroy, A.; Violeau, D.; Ferrand, M.; Kassiotis, C.: Unified semi-analytical wall boundary conditions applied to 2-D incompressible SPH. In: *J. Comput. Phys.* 261 (2014), 106–129.

[109] Levich, V.; Krylov, V.: Surface-tension-driven phenomena. In: *Annu. Rev. Fluid Mech.* 1.1 (1969), 293–316.

[110] Lewy, H.; Friedrichs, K.; Courant, R.: Über die partiellen Differenzengleichungen der mathematischen Physik. In: *Mathematische annalen* 100 (1928), 32–74.

[111] Leyens, C.; Beyer, E.: 8 - Innovations in laser cladding and direct laser metal deposition. In: ed. by Lawrence, J.; Waugh, D. G. Woodhead Publishing Series in Electronic and Optical Materials. Woodhead Publishing, 2015, 181–192.

[112] Li, C.; Fu, C. H.; Guo, Y. B.; Fang, F. Z.: A multiscale modeling approach for fast prediction of part distortion in selective laser melting. In: *J. Mater. Process. Technol.* 229 (2016), 703–712.

[113] Li, R.; Liu, J.; Shi, Y.; Wang, L.; Jiang, W.: Balling behavior of stainless steel and nickel powder during selective laser melting process. In: *Int. J. Adv. Manuf. Technol.* 59.9 (2012), 1025–1035.

[114] Li, R.; Shi, Y.; Wang, Z.; Wang, L.; Liu, J.; Jiang, W.: Densification behavior of gas and water atomized 316L stainless steel powder during selective laser melting. In: *Appl. Surf. Sci.* 256.13 (2010), 4350–4356.

[115] Lindgren, L.-E.: Numerical modelling of welding. In: *Comput. Methods Appl. Mech. Eng.* 195.48 (2006), 6710–6736.

[116] Liu, M.; Liu, G.; Lam, K.: Constructing smoothing functions in smoothed particle hydrodynamics with applications. In: *J. Comput. Appl. Math.* 155.2 (2003), 263–284.

[117] Liu, Y.; Yang, Y.; Mai, S.; Wang, D.; Song, C.: Investigation into spatter behavior during selective laser melting of AISI 316L stainless steel powder. In: *Mater. Des.* 87 (2015), 797–806.

[118] Louvis, E.; Fox, P.; Sutcliffe, C. J.: Selective laser melting of aluminium components. In: *J. Mater. Process. Technol.* 211.2 (2011), 275–284.

[119] Lucy, L. B.: A numerical approach to the testing of the fission hypothesis. In: *Astron. J.* 82 (1977), 1013.

[120] Marsaglia, G.: Xorshift RNGs. In: *J. Stat. Softw.* 8 (2003), 1–6.

[121] Mash, I.; Motulevich, G.: Optical constants and electronic characteristics of titanium. In: *Sov. Phys. JETP* 36 (1973), 516–519.

[122] Melchels, F. P. W.; Domingos, M. A. N.; Klein, T. J.; Malda, J.; Bartolo, P. J.; Hutmacher, D. W.: Additive manufacturing of tissues and organs. In: *Prog. Polym. Sci* 37.8 (2012), 1079–1104.

[123] Mercelis, P.; Kruth, J.-P.: Residual stresses in selective laser sintering and selective laser melting. In: *Rapid Prototyp. J.* 12.5 (2006), 254–265.

[124] Mertens, R.; Vrancken, B.; Holmstock, N.; Kinds, Y.; Kruth, J.-P.; Van Humbeeck, J.: Influence of powder bed preheating on microstructure and mechanical properties of H13 tool steel SLM parts. In: *Phys. Procedia* 83 (2016), 882–890.

[125] Mills, K. C.; Keene, B. J.: Factors affecting variable weld penetration. In: *Int. Mater. Rev.* 35.1 (1990), 185–216.

[126] Mills, K. C.; Monaghan, B. J.; Keene, B. J.: Thermal conductivities of molten metals: Part 1 Pure metals. In: *Int. Mater. Rev.* 41.6 (1996), 209–242.

[127] Möller, T.; Trumbore, B.: Fast, Minimum Storage Ray-Triangle Intersection. In: *J. Graph. Tools* 2.1 (1997), 21–28.

[128] Monaghan, J. J.: Smoothed particle hydrodynamics. In: *Annu. Rev. Astron. Astrophys.* 30.1 (1992), 543–574.

[129] Monaghan, J. J.: Smoothed particle hydrodynamics. In: *Rep. Prog. Phys.* 68.8 (2005), 1703.

[130] Monaghan, J. J.: Simulating free surface flows with SPH. In: *J. Comput. Phys.* 110.2 (1994), 399–406.

[131] Monaghan, J. J.; Huppert, H. E.; Worster, M. G.: Solidification using smoothed particle hydrodynamics. In: *J. Comput. Phys.* 206.2 (2005), 684–705.

[132] Moosbrugger, C.: *ASM ready reference: electrical and magnetic properties of metals*. Asm. International, 2000.

[133] Morris, J. P.: Simulating surface tension with smoothed particle hydrodynamics. In: *Int. J. Numer. Methods Fluids* 33.3 (2000), 333–353.

[134] Morris, J. P.; Fox, P. J.; Zhu, Y.: Modeling low Reynolds number incompressible flows using SPH. In: *J. Comput. Phys.* 136.1 (1997), 214–226.

[135] Müller, M.; Schirm, S.; Teschner, M.: Interactive blood simulation for virtual surgery based on smoothed particle hydrodynamics. In: *Technol. Health Care* 12.1 (2004), 25–31.

[136] Munir, K. S.; Li, Y.; Wen, C.: 1 - Metallic scaffolds manufactured by selective laser melting for biomedical applications. In: ed. by Wen, C. Woodhead Publishing, 2017, 1–23.

[137] Murr, L.; Martinez, E.; Pan, X.; Gaytan, S.; Castro, J.; Terrazas, C.; Medina, F.; Wicker, R.; Abbott, D.: Microstructures of Rene 142 nickel-based superalloy fabricated by electron beam melting. In: *Acta Mater.* 61.11 (2013), 4289–4296.

[138] Nair, P.: Modeling Free Surface Flows and Fluid Structure Interactions using Smoothed Particle Hydrodynamics. PhD thesis. Bangalore: Department of Mechanical Engineering, Indian Institute of Science, 2015.

[139] Nair, P.; Pöschel, T.: Dynamic capillary phenomena using Incompressible SPH. In: *Chem. Eng. Sci.* 176 (2018), 192–204.

[140] Naito, S.; Arai, T.; Yokoyama, I.; Waseda, Y.: The Long-Wavelength Limit of the Structure Factor of Liquid 3d Transition Metals Using One-Component Plasma Model. In: *High Temp. Mater. Process.* 8.2 (1989), 125–134.

[141] Najmon, J. C.; Raeisi, S.; Tovar, A.: 2 - Review of additive manufacturing technologies and applications in the aerospace industry. In: ed. by Froes, F.; Boyer, R. Elsevier, 2019, 7–31.

[142] Nasar, A.; Rogers, B. D.; Revell, A.; Stansby, P.: Flexible slender body fluid interaction: vector-based discrete element method with Eulerian smoothed particle hydrodynamics. In: *Comput. Fluids* 179 (2019), 563–578.

[143] Nugent, S.; Posch, H.: Liquid drops and surface tension with smoothed particle applied mechanics. In: *Phys. Rev. E* 62.4 (2000), 4968.

[144] Oger, G.; Doring, M.; Alessandrini, B.; Ferrant, P.: An improved SPH method: Towards higher order convergence. In: *J. Comput. Phys.* 225.2 (2007), 1472–1492.

[145] Olakanmi, E. O.; Cochrane, R. F.; Dalgarno, K. W.: Densification mechanism and microstructural evolution in selective laser sintering of Al–12Si powders. In: *J. Mater. Process. Technol.* 211.1 (2011), 113–121.

[146] Olakanmi, E. O.; Cochrane, R. F.; Dalgarno, K. W.: A review on selective laser sintering/melting (SLS/SLM) of aluminium alloy powders: Processing, microstructure, and properties. In: *Prog. Mater. Sci.* 74 (2015), 401–477.

[147] Olejnik, M.; Szewc, K.: Smoothed particle hydrodynamics modelling of the Rayleigh-Plateau instability. In: (2018), 675.

[148] Oliari, S. H.; D'Oliveira, A. S. C. M.; Schulz, M.: Additive Manufacturing of H11 with Wire-Based Laser Metal Deposition. In: *Soldag. e Inspecao* 22 (2017), 466–479.

[149] Omini, M.: Melting point and structure factor of liquid metals. In: *Philos. Mag.* 26.2 (1972), 287–295.

[150] Ordal, M. A.; Bell, R. J.; Alexander, R. W.; Newquist, L. A.; Querry, M. R.: Optical properties of Al, Fe, Ti, Ta, W, and Mo at submillimeter wavelengths. In: *Appl. Opt.* 27.6 (1988), 1203–1209.

[151] Ordoubadi, M.; Yaghoubi, M.; Yeganehdoust, F.: Surface tension simulation of free surface flows using smoothed particle hydrodynamics. In: *Scientia Iranica* 24.4 (2017), 2019–2033.

[152] Ouchi, C.; Iizumi, H.; Mitao, S.: Effects of ultra-high purification and addition of interstitial elements on properties of pure titanium and titanium alloy. In: *Mater. Sci. Eng. A* 243.1 (1998), 186–195.

[153] Ouyang, D.; Li, N.; Xing, W.; Zhang, J.; Liu, L.: 3D printing of crack-free high strength Zr-based bulk metallic glass composite by selective laser melting. In: *Intermetallics* 90 (2017), 128–134.

[154] Oyar, P.: Laser sintering technology and balling phenomenon. In: *Photomed. Laser Surg.* 36.2 (2018), 72–77.

[155] Palm, K. J.; Murray, J. B.; Narayan, T. C.; Munday, J. N.: Dynamic Optical Properties of Metal Hydrides. In: *ACS Photonics* 5.11 (2018), 4677–4686.

[156] Park, K. B.; Choi, J.; Na, T.-W.; Kang, J.-W.; Park, K.; Park, H.-K.: Oxygen Reduction Behavior of HDH TiH2 Powder during Dehydrogenation Reaction. In: *Metals* 9.11 (2019), 1154.

[157] Pasandideh-Fard, M.; Mostaghimi, J.: Droplet impact and solidification in a thermal spray process: droplet-substrate interaction. In: *Thermal spray: Practical Solutions for Engineering Problems, CC Berndt (Ed.), Pub. ASM. International, Material Park, Ohio-USA* (1996), 637–646.

[158] Peck, E. R.; Fisher, D. J.: Dispersion of Argon. In: *J. Opt. Soc. Am.* 54.11 (1964), 1362–1364.

[159] Percus, J. K.; Yevick, G. J.: Analysis of Classical Statistical Mechanics by Means of Collective Coordinates. In: *Phys. Rev.* 110 (1 1958), 1–13.

[160] Powell, R. W.; Ho, C. Y.; Liley, P. E.: *Thermal conductivity of selected materials, part 2*. U.S. Dept. of Commerce, National Bureau of Standards, 1968.

[161] Qin, J.; Pang, W.-M.; Nguyen, B. P.; Ni, D.; Chui, C.-K.: *Particle-based simulation of blood flow and vessel wall interactions in virtual surgery*. In: *Proceedings of the 2010 Symposium on Information and Communication Technology*. ACM. 2010, 128–133.

[162] Radovanovic, M.; Madic, M.: Experimental investigations of CO2 laser cut quality: a review. In: *Nonconv. Technol. Rev.* 4.4 (2011), 35.

[163] Rayleigh, L.: *On the capillary phenomena of jets*. In: *Proc. R. Soc. London*. Vol. 29. 196-199. 1879, 71–97.

[164] Ren, J.; Ouyang, J.; Jiang, T.; Li, Q.: Simulation of complex filling process based on the generalized Newtonian fluid model using a corrected SPH scheme. In: *Comput. Mech.* 49.5 (2012), 643–665.

[165] Renk, K. F.: *Basics of Laser Physics: For Students of Science and Engineering*. Springer Science & Business Media, 2012.

[167] Rowlinson, J. S.; Widom, B.: *Molecular theory of capillarity*. Courier Corporation, 2013.

[168] Ruschak, K. J.: Coating Flows. In: *Annu. Rev. Fluid Mech.* 17.1 (1985), 65–89.

[169] Russo, R. E.; Mao, X.; Liu, H.; Gonzalez, J.; Mao, S. S.: Laser ablation in analytical chemistry–a review. In: *Talanta* 57.3 (2002), 425–451.

[170] Schiaffino, S.; Sonin, A. A.: Molten droplet deposition and solidification at low Weber numbers. In: *Phys. Fluids* 9.11 (1997), 3172–3187.

[171] Schiaffino, S.; Sonin, A. A.: Motion and arrest of a molten contact line on a cold surface: An experimental study. In: *Phys. Fluids* 9.8 (1997), 2217–2226.

[172] Schiaffino, S.; Sonin, A. A.: On the theory for the arrest of an advancing molten contact line on a cold solid of the same material. In: *Phys. Fluids* 9.8 (1997), 2227–2233.

[173] Schuocker, D.: *Handbook of the EuroLaser Academy: Volume 2*. Softcover reprint of the original 1st ed. 1998 Edition. London: Springer, 1999.

[174] Seemann, R.; Brinkmann, M.; Pfohl, T.; Herminghaus, S.: Droplet based microfluidics. In: *Rep. Prog. Phys* 75.1 (2011), 016601.

[175] Sennaroglu, A.: *Photonics and Laser Engineering: Principles, Devices, and Applications*. English. Illustrated edition. New York: McGraw-Hill Education Ltd, 2010.

[176] Seydel, U.; Fucke, W.: Electrical resistivity of liquid Ti, V, Mo and W. In: *J. Phys. F: Met. Phys* 10.8 (1980), L203–L206.

[177] Shah, D.; Volkov, A. N.: Simulations of deep drilling of metals by continuous wave lasers using combined smoothed particle hydrodynamics and ray-tracing methods. In: *Appl. Phys. A* 126.2 (2020), 82.

[178] Shepard, D.: *A two-dimensional interpolation function for irregularly-spaced data*. In: *Proceedings of the 1968 23rd ACM national conference*. 1968, 517–524.

[179] Shigorina, E.; Kordilla, J.; Tartakovsky, A. M.: Smoothed particle hydrodynamics study of the roughness effect on contact angle and droplet flow. In: *Phys. Rev. E* 96.3 (2017), 033115.

[180] Shimada, W.; Hoshinouchi, S.: A Study on Bead Formation by Low Pressure TIG Arc and Prevention of Under-Cut Bead. In: *Trans. Jpn. Weld Soc.* 14.1 (1983), 60–61.

[181] Sibold, D.; Urbassek, H. M.: Monte Carlo study of Knudsen layers in evaporation from elemental and binary media. In: *Phys. Fluids A.* 5.1 (1993), 243–256.

[182] Sidambe, A. T.: Biocompatibility of Advanced Manufactured Titanium Implants—A Review. In: *Materials* 7.12 (2014), 8168–8188.

[183] Siegel, E.: Optical reflectivity of liquid metals at their melting temperatures. In: *Phys. Chem. Liquids* 5.1 (1976), 9–27.

[184] Siegman, A.: *Defining, measuring, and optimizing laser beam quality*. In: *Photonics West - Lasers and Applications in Science and Engineering*. 1993.

[185] Sikarudi, M. A. E.; Nikseresht, A. H.: Neumann and Robin boundary conditions for heat conduction modeling using smoothed particle hydrodynamics. In: *Comput. Phys. Commun.* 198 (2016), 1–11.

[186] Simchi, A.; Petzoldt, F.; Pohl, H.: Direct metal laser sintering: Material considerations and mechanisms of particle bonding. In: *Int. J. Powder Metall.* 37.Nr.2 (2001), 49–62.

[187] Sing, S. L.; An, J.; Yeong, W. Y.; Wiria, F. E.: Laser and electron-beam powder-bed additive manufacturing of metallic implants: A review on processes, materials and designs. In: *J. Orthop. Res.* 34.3 (2016), 369–385.

[188] Singh, M.; Haverinen, H. M.; Dhagat, P.; Jabbour, G. E.: Inkjet Printing—Process and Its Applications. In: *Adv. Mater* 22.6 (2010), 673–685.

[189] Sleijpen, G. L.; Van der Vorst, H. A.; Fokkema, D. R.: BiCGstab (l) and other hybrid Bi-CG methods. In: *Numer. Algorithms* 7.1 (1994), 75–109.

[190] Sun, S.; Brandt, M.; Dargusch, M. S.: Machining Ti–6Al–4V alloy with cryogenic compressed air cooling. In: *Int. J. Mach. Tools Manuf.* 50.11 (2010), 933–942.

[191] Sun, Z.; Ion, J. C.: Laser welding of dissimilar metal combinations. In: *J. Mater. Sci.* 30.17 (1995), 4205–4214.

[192] Tang, H. P.; Yang, G. Y.; Jia, W. P.; He, W. W.; Lu, S. L.; Qian, M.: Additive manufacturing of a high niobium-containing titanium aluminide alloy by selective electron beam melting. In: *Mater. Sci. Eng. A* 636 (2015), 103–107.

[193] Tao, W.; Yang, Z.; Chen, Y.; Li, L.; Jiang, Z.; Zhang, Y.: Double-sided fiber laser beam welding process of T-joints for aluminum aircraft fuselage panels: Filler wire melting behavior, process stability, and their effects on porosity defects. In: *Opt. Laser Technol.* 52 (2013), 1–9.

[194] Tartakovsky, A.; Meakin, P.: Modeling of surface tension and contact angles with smoothed particle hydrodynamics. In: *Phys. Rev. E* 72.2 (2005), 026301.

[195] Tartakovsky, A. M.; Panchenko, A.: Pairwise force smoothed particle hydrodynamics model for multiphase flow: surface tension and contact line dynamics. In: *J. Comput. Phys.* 305 (2016), 1119–1146.

[196] Teng, C.; Pal, D.; Gong, H.; Zeng, K.; Briggs, K.; Patil, N.; Stucker, B.: A review of defect modeling in laser material processing. In: *Addit. Manuf.* 14 (2017), 137–147.

[197] The CGAL Project: *CGAL User and Reference Manual*. 5.4. CGAL Editorial Board, 2022.

[198] Theberge, A. B.; Courtois, F.; Schaerli, Y.; Fischlechner, M.; Abell, C.; Hollfelder, F.; Huck, W. T. S.: Microdroplets in microfluidics: An evolving platform for discoveries in chemistry and biology. In: *Angewandte Chemie International Edition* 49.34 (2010), 5846–5868.

[199] Thomas, B.; Samarasekera, I.; Brimacombe, J.: Comparison of numerical modeling techniques for complex, two-dimensional, transient heat-conduction problems. In: *Metall. Mater. Trans. B* 15.2 (1984), 307–318.

[200] Thurnay, K.: *Thermal properties of transition metals*. Tech. rep. 0947-8620. Germany, 1998, 136.

[201] Tolochko, N. K.; Mozzharov, S. E.; Yadroitsev, I. A.; Laoui, T.; Froyen, L.; Titov, V. I.; Ignatiev, M. B.: Balling processes during selective laser treatment of powders. In: *Rapid Prototyp. J.* 10.2 (2004), 78–87.

[202] Tong, M.; Browne, D. J.: An incompressible multi-phase smoothed particle hydrodynamics (SPH) method for modelling thermocapillary flow. In: *Int. J. Heat Mass Transf.* 73 (2014), 284–292.

[203] Tytkin, Y. M.: The Mechanism of Formation of a Coarse Flaky Surface of Weld Metal in Welding Under High-Power Conditions.(Translation). In: *Weld. Prod.* 28.2 (1981), 3–5.

[204] Ucar, Y.; Akova, T.; Akyil, M. S.; Brantley, W. A.: Internal fit evaluation of crowns prepared using a new dental crown fabrication technique: laser-sintered Co-Cr crowns. In: *J. Prosthet. Dent.* 102.4 (2009), 253–259.

[205] Ujihara, K.: Reflectivity of metals at high temperatures. In: *J. Appl. Phys.* 43.5 (1972), 2376–2383.

[206] Valiev, R. Z.; Sabirov, I.; Zemtsova, E. G.; Parfenov, E. V.; Dluhoš, L.; Lowe, T. C.: 4.3 - Nanostructured commercially pure titanium for development of miniaturized biomedical implants. In: ed. by Froes, F. H.; Qian, M. Woodhead Publishing Series in Biomaterials. Woodhead Publishing, 2018, 393–417.

[207] Vigna, S.: Further scramblings of Marsaglia's xorshift generators. In: *J. Comput. Appl. Math.* 315 (2017), 175–181.

[208] Violeau, D.: *Fluid Mechanics and the SPH Method*. Oxford University Press, 2015.

[209] Voller, V. R.; Prakash, C.: A fixed grid numerical modelling methodology for convection-diffusion mushy region phase-change problems. In: *Int. J. Heat Mass Transf.* 30.8 (1987), 1709–1719.

[210] Wall, W. E.; Ribarsky, M. W.; Stevenson, J. R.: Optical properties of titanium and titanium oxide surfaces. In: *J. Appl. Phys.* 51.1 (1980), 661–667.

[211] Wei, P.: Thermal Science of Weld Bead Defects: A Review. In: *J. Heat Transf.* 133 (2011), 031005.

[212] Weinstein, S. J.; Ruschak, K. J.: COATING FLOWS. In: *Annu. Rev. Fluid Mech.* 36.1 (2004), 29–53.

[213] Weller, C.; Kleer, R.; Piller, F. T.: Economic implications of 3D printing: Market structure models in light of additive manufacturing revisited. In: *Int. J. Prod. Econ.* 164 (2015), 43–56.

[214] Wendland, H.: Piecewise polynomial, positive definite and compactly supported radial functions of minimal degree. In: *Adv. Comput. Math.* 4.1 (1995), 389–396.

[215] Werner, W. S. M.; Glantschnig, K.; Ambrosch-Draxl, C.: Optical Constants and Inelastic Electron-Scattering Data for 17 Elemental Metals. In: *J. Phys. Chem. Ref. Data* 38.4 (2009), 1013–1092.

[216] Williams, F.: On vaporization of mist by radiation. In: *Int. J. Heat Mass Transf.* (1965), 575–587.

[217] Xia, M.; Gu, D.; Yu, G.; Dai, D.; Chen, H.; Shi, Q.: Porosity evolution and its thermodynamic mechanism of randomly packed powder-bed during selective laser melting of Inconel 718 alloy. In: *Int. J. Mach. Tools Manuf.* 116 (2017), 96–106.

[218] Xiao, R.; Zhang, X.: Problems and issues in laser beam welding of aluminum–lithium alloys. In: *J. Manuf. Process.* 16.2 (2014), 166–175.

[219] Yadroitsev, I.; Krakhmalev, P.; Yadroitsava, I.; Johansson, S.; Smurov, I.: Energy input effect on morphology and microstructure of selective laser melting single track from metallic powder. In: *J. Mater. Process. Technol.* 213.4 (2013), 606–613.

[220] Yaggee, F. L.; Gilbert, E. R.; Styles, J. W.: Thermal expansivities, thermal conductivities, and densities of vanadium, titanium, chromium and some vanadium-base alloys: A comparison with austenitic stainless steel. In: *JLCM* 19.1 (1969), 39–51.

[221] Yang, J.; Han, J.; Yu, H.; Yin, J.; Gao, M.; Wang, Z.; Zeng, X.: Role of molten pool mode on formability, microstructure and mechanical properties of selective laser melted Ti-6Al-4V alloy. In: *Mater. Des.* 110 (2016), 558–570.

[222] Comparison of Surface Tension Models in Smoothed Particles Hydrodynamics Method. Vol. Volume 6: 15th International Conference on Multibody Systems, Nonlinear Dynamics, and Control. International Design Engineering Technical Conferences and Computers and Information in Engineering Conference. 2019.

[223] Yang, Y. S.; Lee, S. H.: A study on the joining strength of laser spot welding for automotive applications. In: *J. Mater. Process. Technol.* 94.2 (1999), 151–156.

[224] Yang, Y.; Lu, J.-b.; Luo, Z.-Y.; Wang, D.: Accuracy and density optimization in directly fabricating customized orthodontic production by selective laser melting. In: *Rapid Prototyp. J.* 18.6 (2012), 482–489.

[225] Yap, C. Y.; Chua, C. K.; Dong, Z. L.; Liu, Z. H.; Zhang, D. Q.; Loh, L. E.; Sing, S. L.: Review of selective laser melting: Materials and applications. In: *Appl. Phys. Rev.* 2.4 (2015), 041101.

[226] Ye, J.; Khairallah, S. A.; Rubenchik, A. M.; Crumb, M. F.; Guss, G.; Belak, J.; Matthews, M. J.: Energy Coupling Mechanisms and Scaling Behavior Associated with Laser Powder Bed Fusion Additive Manufacturing. In: *Adv. Eng. Mater.* 21.7 (2019), 1900185.

[227] Yilbas, B. S.: Laser heating process and experimental validation. In: *Int. J. Heat Mass Transf.* 40.5 (1997), 1131–1143.

[228] Young, T.: III. An essay on the cohesion of fluids. In: *Philos. Trans. R. Soc. London* 95 (1805), 65–87.

[229] Ytrehus, T.: Kinetic Theory description and experimental results for vapor motion in arbitrary strong evaporation. In: *VKI Training Center for Experimental Aerodynamics Technical Note 112* (1975).

[230] Ytrehus, T.; Østmo, S.: Kinetic theory approach to interphase processes. In: *Int. J. Multiph. Flow* 22.1 (1996), 133–155.

[231] YU, P.; Cardona, M.: *Fundamentals of Semiconductors: Physics and Materials Properties*. Springer Science & Business Media, 2010.

[232] Zeng, H.; Du, X.-W.; Singh, S. C.; Kulinich, S. A.; Yang, S.; He, J.; Cai, W.: Nanomaterials via laser ablation/irradiation in liquid: a review. In: *Adv. Funct. Mater.* 22.7 (2012), 1333–1353.

[233] Zhang, B.; Li, Y.; Bai, Q.: Defect Formation Mechanisms in Selective Laser Melting: A Review. In: *Chin. J. Mech. Eng.* 30.3 (2017), 515–527.

[234] Zhang, J.; Song, B.; Wei, Q.; Bourell, D.; Shi, Y.: A review of selective laser melting of aluminum alloys: Processing, microstructure, property and developing trends. In: *J. Mater. Sci. Technol.* 35.2 (2019), 270–284.

[235] Zhou, K.; Wang, H. P.; Chang, J.; Wei, B.: Experimental study of surface tension, specific heat and thermal diffusivity of liquid and solid titanium. In: *Chem. Phys. Lett.* 639 (2015), 105–108.

[236] Zhu, H. H.; Lu, L.; Fuh, J. Y. H.: Study on Shrinkage Behaviour of Direct Laser Sintering Metallic Powder. In: *Proc. Inst. Mech. Eng. B: J. Eng. Manuf.* 220.2 (2006), 183–190.

[237] Zohdi, T. I.: Rapid Simulation of Laser Processing of Discrete Particulate Materials. In: *Arch. Comput. Methods Eng.* 20.4 (2013), 309–325.

Own publications referring to this work

[P20] Blank, M.; Nair, P.; Pöschel, T.: *Heat conduction due to laser beam heating: effect of surface geometry*. In: *SPHERIC 2018 Proceeding of the 13th SPHERIC International Workshop*. 2018, 364–370.

[P21] Blank, M.; Nair, P.; Pöschel, T.: Capillary viscous flow and melting dynamics: Coupled simulations for additive manufacturing applications. In: *Int. J. Heat Mass Transf.* 131 (2019), 1232–1246.

[P22] Blank, M.; Nair, P.; Pöschel, T.: Modeling surface tension in Smoothed Particle Hydrodynamics using Young–Laplace pressure boundary condition. In: *Comput. Methods in Appl. Mech. Eng.* 406 (2023), 115907.

Student thesis referring to this work*

[S166] Rogge, T.; Blank, M.; Pöschel, T.: Simulation des Ablagerungsprozesses von Metallpulver für SLM Prozesse. MA thesis. Friedrich-Alexander-Universität Erlangen-Nürnberg, 2021.

* The 2nd (3rd) author names the supervisor; the last author is head of the institute.

Appendix

A Derivation of the Fresnel power reflectance

This section presents the derivation of the reflectivity of electromagnetic radiation at an interface between two optical media whose imaginary parts of the refractive index are unequal zero. In contrast to Eqs. (2.22) and (2.23), this leads to a more general formulation of the reflectivity for s- and p-polarization with respect to the plane of incidence. Moreover, both phases are assumed to have the same magnetic permeability. Therefore, in the following, the superscripts (1), e.g. the gas phase, and (2), e.g. the metal irradiated by the laser beam, denote the phases on both sides of the interface. The Fresnel coefficient for s-polarization (perpendicular orientation of the electric field with respect to the plane of incidence) is given by the amplitude ratio of the incident, and reflected electric field, by [231]

$$\left|\left(\frac{\mathbf{E}_\mathrm{r}}{\mathbf{E}_\mathrm{i}}\right)^{\perp}\right| = \frac{\cos\theta_\mathrm{i} - \sqrt{\underline{n}^2 - \sin^2\theta_\mathrm{i}}}{\cos\theta_\mathrm{i} + \sqrt{\underline{n}^2 - \sin^2\theta_\mathrm{i}}}\,. \tag{A.1}$$

Here, $\underline{n}$ is the ratio of the complex refractive indices of phases (1) and (2), and is given by

$$\begin{aligned}\underline{n} =& \frac{\bar{n}_1^{(2)}}{\bar{n}_1^{(1)}} = \frac{n_1^{(2)} + i n_2^{(2)}}{n_1^{(1)} + i n_2^{(1)}} \\ =& \underbrace{\frac{n_1^{(1)} n_1^{(2)} + n_2^{(1)} n_2^{(2)}}{\left(n_1^{(1)}\right)^2 + \left(n_2^{(1)}\right)^2}}_{\bar{n}} + i \cdot \underbrace{\frac{n_1^{(1)} n_2^{(2)} - n_1^{(2)} n_2^{(1)}}{\left(n_1^{(1)}\right)^2 + \left(n_2^{(1)}\right)^2}}_{\bar{k}} \\ =& \bar{n} + i\bar{k}\,.\end{aligned} \tag{A.2}$$

Substitution of $\underline{n} = \bar{n} + i\bar{k}$, given in Eq. (A.2), into Eq. (A.1) leads to

$$\left|\left(\frac{\mathbf{E}_\mathrm{r}}{\mathbf{E}_\mathrm{i}}\right)^{\perp}\right| = \frac{\cos\theta_i - \sqrt{\bar{n}^2 - \bar{k}^2 - \sin^2\theta_i + 2i\bar{n}\bar{k}}}{\cos\theta_i + \sqrt{\bar{n}^2 - \bar{k}^2 - \sin^2\theta_i + 2i\bar{n}\bar{k}}}\,. \tag{A.3}$$

By substituting the radicand in Eq. (A.3) using

$$\bar{N} = \bar{n}^2 - \bar{k}^2 - \sin^2\theta_\mathrm{i}\,, \quad \bar{K} = 2\bar{n}\bar{k}\,, \tag{A.4}$$

this leads to

$$\left|\left(\frac{\mathbf{E}_\mathrm{r}}{\mathbf{E}_\mathrm{i}}\right)^{\perp}\right| = \frac{\cos\theta_\mathrm{i} - \sqrt{\bar{N} + i\bar{K}}}{\cos\theta_\mathrm{i} + \sqrt{\bar{N} + i\bar{K}}}\,. \tag{A.5}$$

Taking the square of Eq. A.5 gives the reflectivity for s-polarized light by

$$R^{\perp} = \frac{\cos^2\theta_\mathrm{i} - 2\cos\theta_\mathrm{i}\sqrt{\bar{r}}\cos\left(\frac{1}{2}\bar{\phi}\right) + \bar{r}}{\cos^2\theta_\mathrm{i} + 2\cos\theta_\mathrm{i}\sqrt{\bar{r}}\cos\left(\frac{1}{2}\bar{\phi}\right) + \bar{r}}\,, \tag{A.6}$$

where $\bar{r}$ and $\bar{\phi}$ are given by

$$\bar{r} = \sqrt{\bar{N}^2 + \bar{K}^2}\,, \qquad \bar{\phi} = \arccos\frac{\bar{N}}{\bar{r}}\,. \tag{A.7}$$

Analogously, the reflectivity for p-polarization (parallel orientation of the electric field with respect to the plane of incidence) can be derived. Starting with the Fresnel coefficient for p-polarization given by [231]

$$\left|\left(\frac{\mathbf{E}_\mathrm{r}}{\mathbf{E}_\mathrm{i}}\right)^{\parallel}\right| = \frac{\underline{n}^2\cos\theta_\mathrm{i} - \sqrt{\underline{n}^2 - \sin^2\theta_\mathrm{i}}}{\underline{n}^2\cos\theta_\mathrm{i} + \sqrt{\underline{n}^2 - \sin^2\theta_\mathrm{i}}}, \tag{A.8}$$

the reflectivity, $R^{\perp}$, is given by

$$R^{\parallel} = \frac{\cos^2\theta_i r'^2 - 2\cos\theta_i r'\sqrt{r}\cos\left(\phi' - \frac{1}{2}\phi\right) + r}{\cos^2\theta_i r'^2 + 2\cos\theta_i r'\sqrt{r}\cos\left(\phi' - \frac{1}{2}\phi\right) + r}\,, \tag{A.9}$$

using the substitutions given in Eq. (A.10)

$$\bar{N}' = n^2 - k^2\,, \quad r' = \sqrt{\bar{N}'^2 + K^2}\,, \quad \bar{\phi}' = \arccos\frac{\bar{N}'}{\bar{r}'}\,. \tag{A.10}$$

B Evaporation model

The mass and heat-loss to the ambiance, and the resultant surface pressure on the surface of the condensed phase, are estimated using the evaporation model by [101].

The net mass flux of evaporating particles at the ambient side of the Knudsen layer is given as a function of the flow velocity, u_Kn, and gas density, ρ_Kn, by

$$j^\mathrm{net} = u_\mathrm{Kn}\rho_\mathrm{Kn}\,. \tag{B.11}$$

Moreover, the pressure, p_{Kn}, at the outer edge of the Knudsen layer can be formulated using the ideal gas law by

$$p_{\mathrm{Kn}} = \rho_{\mathrm{Kn}} R_{\mathrm{g,sp}} T_{\mathrm{Kn}} = \rho_{\mathrm{Kn}} \frac{k_{\mathrm{B}}}{m_{\mathrm{A,v}}} T_{\mathrm{Kn}} \,. \tag{B.12}$$

In addition, according to [101] the pressure ratio and temperature ratio of the gas, relating the properties at the outer edge of the Knudsen layer to the properties directly at the evaporating surface, are given by

$$p_{\mathrm{Kn}} = p_{\mathrm{s}} \cdot \frac{\rho_{\mathrm{Kn}}}{\rho_{\mathrm{s}}} \frac{T_{\mathrm{Kn}}}{T_{\mathrm{s}}} \,, \qquad T_{\mathrm{Kn}} = T_{\mathrm{s}} \cdot \frac{T_{\mathrm{Kn}}}{T_{\mathrm{s}}} \,. \tag{B.13}$$

C Analytical expressions for the forced heat equation in a bounded domain

The forced heat equation with a Gaussian laser source term represents an inhomogeneous boundary value problem according to

$$\mathcal{L}T = f. \tag{C.14}$$

Here, $\mathcal{L}$ represents a linear differential operator acting on the temperature T and f is the Gaussian laser source term. In order to solve Eq. (C.14) one needs to find an inverse operator that solves this problem according to

$$T = \mathcal{L}^{-1} f. \tag{C.15}$$

Since $\mathcal{L}$ is expected to be an integral operator, a function or kernel, G, must be found that fulfills

$$\mathcal{L}^{-1} f(x) = \int_a^b G(x, x') f(x') \mathrm{d}x' \,. \tag{C.16}$$

Here x' marks the spatial position of the source term. If such a functions exists it is called Green's function to $\mathcal{L}$ and hence

$$T(x) = \int_a^b G(x, x') f(x') \mathrm{d}x'. \tag{C.17}$$

This implies that

$$\mathcal{L} G(x, x') = \delta(x - x') \,, \tag{C.18}$$

where $\delta(x - x')$ is the Dirac delta distribution. Green's functions can be constructed using direct integration, eigenvector expansion, or the Fourier transform. Here, the Fourier transform is used to derive the analytical expressions which are utilized to validate the employed ray tracing approach presented in Chapter 5.

In the first problem, the solution to the three-dimensional forced heat equation,

$$\nabla^2 T - k\frac{\partial T}{\partial t} = f(x, y) \ , \tag{C.19}$$

is required. Therefore, the Green's function to the inhomogeneous heat equation in Eq. (C.33), is given by

$$\frac{\partial}{\partial t} G(\mathbf{x}, t; \mathbf{x}', t') - D_{\mathrm{th}} \nabla^2 G(\mathbf{x}, t; \mathbf{x}', t') = \delta^d(\mathbf{x} - \mathbf{x}')\, \delta(t - t') \ , \tag{C.20}$$

where $\mathbf{x}'$ represents the spatial position at a certain time t' and $\delta^d(\mathbf{x} - \mathbf{x}')$ denotes the product of d Dirac delta distributions depending on the number of spatial dimensions.

To solve Eq. (C.20), Fourier transformations are applied to the terms that include spatial coordinates according to

$$\begin{aligned} \mathcal{F}\left[G(\mathbf{x}, t; \mathbf{x}', t')\right] &= \tilde{G}(\mathbf{k}, t; \mathbf{x}', t') \ , \\ \mathcal{F}\left[\delta^d(\mathbf{x} - \mathbf{x}')\right] &= \mathrm{e}^{-i\mathbf{k}\cdot\mathbf{x}'} \ , \\ \mathcal{F}\left[D_{\mathrm{th}} \nabla^2 G(\mathbf{x}, t; \mathbf{x}', t')\right] &= -D_{\mathrm{th}} |\mathbf{k}|^2 \tilde{G}(\mathbf{k}, t; \mathbf{x}', t') \ , \end{aligned} \tag{C.21}$$

where $\tilde{G}(\mathbf{k}, t; \mathbf{x}', t')$ is the Fourier transform of $G(\mathbf{x}, t; \mathbf{x}', t')$ with respect to the spatial coordinates, $\mathbf{k}$ is the spatial frequency vector which represents the spatial coordinates in frequency domain, and ∇^2 is the Laplace operator.

Using the Fourier transforms provided by Eq. (C.21), Eq. (C.20) is given by

$$\frac{\mathrm{d}}{\mathrm{d}t} \tilde{G}(\mathbf{k}, t; \mathbf{x}', t') + D_{\mathrm{th}} |\mathbf{k}|^2 \tilde{G}(\mathbf{k}, t; \mathbf{x}', t') = \mathrm{e}^{-i\mathbf{k}\cdot\mathbf{x}'} \delta(t - t') \ , \tag{C.22}$$

which represents a first order, linear, inhomogenous differential equation of the form

$$\frac{\mathrm{d}y}{\mathrm{d}t} + p(t)\, y = q(t) \, . \tag{C.23}$$

Here, y, $p\,(t)$ and $q(t)$ are given by

$$\begin{aligned} \tilde{G}\,(\mathbf{k},t;\mathbf{x}',t')\ , \\ p\,(t) = D_{\mathrm{th}}\,|\mathbf{k}|^2\ , \\ q(t) = \mathrm{e}^{-i\mathbf{k}\cdot\mathbf{x}'}\,\delta\,(t-t')\ . \end{aligned} \tag{C.24}$$

The general solution to Eq. (C.23) is given by

$$y = \mathrm{e}^{-P(t)} \int \mathrm{e}^{P(t)} q(t)\mathrm{d}t\,, \qquad P(t) = \int_0^t p(t)\mathrm{d}t\,. \tag{C.25}$$

Applying Eq. (C.25), as well as the initial condition $\tilde{G}\,(\mathbf{k},0;\mathbf{x}',t') = 0$ to equation (C.22), leads to

$$\tilde{G}\,(\mathbf{k},t;\mathbf{x}',t') = \mathrm{e}^{-i\mathbf{k}\cdot\mathbf{x}'-D|\mathbf{k}|^2 t} \int_0^t \mathrm{e}^{D|\mathbf{k}|^2 t}\delta\,(t-t')\,\mathrm{d}t\,, \tag{C.26}$$

which can be solved according to

$$\tilde{G}\,(\mathbf{k},t;\mathbf{x}',t') = \begin{cases} 0 & t < t' \\ \mathrm{e}^{-i\mathbf{k}\cdot\mathbf{x}'+D|\mathbf{k}|^2(t-t')} & t > t' \end{cases}\ . \tag{C.27}$$

Equation (C.27) can be written as

$$\tilde{G}\,(\mathbf{k},t;\mathbf{x}',t') = \Theta\,(t-t')\,\mathrm{e}^{-i\mathbf{k}\cdot\mathbf{x}'+D|\mathbf{k}|^2(t-t')} \tag{C.28}$$

using the Heaviside step function Θ_{H}. By transforming Eq. (C.28) back to spatial coordinates, Green's function is given by

$$G\,(\mathbf{x},t;\mathbf{x}',t') = \frac{\Theta_{\mathrm{H}}\,(t-t')}{(2\pi)^d} \int_{\mathbb{R}} \mathrm{e}^{i\mathbf{k}\cdot(\mathbf{x}-\mathbf{x}')}\mathrm{e}^{D|\mathbf{k}|^2(t-t')}\mathrm{d}^d k\,, \tag{C.29}$$

which leads to

$$G\,(\mathbf{x},t;\mathbf{x}',t') = \Theta_{\mathrm{H}}\,(t-t')\,S_d\,(\mathbf{x}-\mathbf{x}',t-t')\ , \tag{C.30}$$

where S_d is the fundamental solution, or heat kernel, of the heat equation given by

$$S_d\,(\mathbf{x}-\mathbf{x}',t-t') = \frac{1}{(4\pi D\,(t-t'))^{d/2}} \exp\left(\frac{|\mathbf{x}-\mathbf{x}'|^2}{4D_{\mathrm{th}}\,(t-t')}\right)\ . \tag{C.31}$$

Thus, the temperature within an infinite domain is given by

$$T(\mathbf{x},t)=\int_0^\infty\int_{\mathbb{R}} G\left(\mathbf{x},t;\mathbf{x}',t'\right)f\left(\mathbf{x}',t'\right)\mathrm{d}^d\mathbf{x}'\mathrm{d}t'. \tag{C.32}$$

In the first problem, the boundary conditions given by

$$T|_{R^d\times\{0\}}=0\,\mathrm{K}\qquad\lim_{|\mathbf{x}|\to\infty}T=0\,\mathrm{K} \tag{C.33}$$

shall be imposed. This represents a cube centered in the origin of Euclidean space, whose sides are kept at a constant temperature. The laser source term is applied in the x-y-plane at $z/L=0$ which means that the domain $z/L>0$ is transparent for laser irradiation.

The method of images is employed to apply the boundary condition to this problem in a bounded domain. Thus, the solution to the forced heat equation can be described by a linear combination of heat sources, f, that are added to Eq. (C.32). To obtain Dirichlet boundary conditions at $|\mathbf{x}|\to L$ an odd periodic extension, where heat sources are placed alternating $2L$ periodically in each dimension, is applied to Eq. (C.30). This leads to

$$\begin{aligned}G\left(\mathbf{x},t;\mathbf{x}',t'\right)=&\frac{\Theta_{\mathrm{H}}\left(t-t'\right)}{\left(4\pi D_{\mathrm{th}}\left(t-t'\right)\right)^{3/2}}\sum_{m=-\infty}^{\infty}\sum_{n=-\infty}^{\infty}\sum_{o=-\infty}^{\infty}(-1)^{m+n+o}\\&\cdot\exp\left(\frac{\left(x-x'+2mL\right)^2+\left(y-y'+2nL\right)^2+\left(z-z'+2oL\right)^2}{4D_{\mathrm{th}}\left(t-t'\right)}\right),\end{aligned} \tag{C.34}$$

considering an arbitrary source term f in three dimensions. Finally, the temperature field in the bounded domain is given by

$$\begin{aligned}T(\mathbf{x},t)=&\int_{t'=0}^{t_1}\int_{z'=-L}^{L}\int_{y'=-L}^{L}\int_{x'=-L}^{L}\frac{f\left(\mathbf{x}',t'\right)}{\left(4\pi D_{\mathrm{th}}\left(t-t'\right)\right)^{3/2}}\\&\sum_{m=-\infty}^{\infty}\sum_{n=-\infty}^{\infty}\sum_{o=-\infty}^{\infty}(-1)^{m+n+o}\\&\cdot\exp\left(\frac{\left(x-x'+2mL\right)^2+\left(y-y'+2nL\right)^2+\left(z-z'+2oL\right)^2}{4D_{\mathrm{th}}\left(t-t'\right)}\right)\\&\mathrm{d}x'\mathrm{d}y'\mathrm{d}z'\mathrm{d}t',\end{aligned} \tag{C.35}$$

where the integral limits are the spatial domain boundaries and t_1 represents the pulse duration of the laser beam. Now, f can be substituted with the Gaussian source term in Eq. (2.49). Moreover, assuming a non-divergent laser

beam with $w(z) = w_0$ whose energy is absorbed by a thin surface layer of material, the integral in z' vanishes and Eq. (C.35) can be written as

$$\begin{aligned} T(\mathbf{x},t) = &\frac{2P_0}{\pi w_0^2}\int_{t'=0}^{t_1}\int_{y'=-L}^{L}\int_{x'=-L}^{L}\frac{1}{\left(4\pi D_{\mathrm{th}}\left(t-t'\right)\right)^{3/2}} \\ &\cdot\exp\left(-\frac{2\left(x'^2+y'^2\right)}{w_0^2}\right)\sum_{m=-\infty}^{\infty}\sum_{n=-\infty}^{\infty}\sum_{o=-\infty}^{\infty}(-1)^{m+n+o} \\ &\cdot\exp\left(\frac{\left(x-x'+2mL\right)^2+\left(y-y'+2nL\right)^2+\left(z+2oL\right)^2}{4D_{\mathrm{th}}\left(t-t'\right)}\right) \\ &\mathrm{d}x'\mathrm{d}y'\mathrm{d}t\,. \end{aligned} \tag{C.36}$$

The second problem is represented by the following set of initial and boundary conditions

$$\begin{aligned} T|_{R^d\times\{0\}} = 0\,\mathrm{K}\,,\quad \lim_{z\to 0}\frac{\mathrm{d}T}{\mathrm{d}t} = 0\,\mathrm{K\,s^{-1}}\ \forall t \\ \lim_{|x|\to L}T = 0\,\mathrm{K}\,,\ \lim_{|y|\to L}T = 0\,\mathrm{K}\,,\ \lim_{z\to -L}T = 0\,\mathrm{K}\,. \end{aligned} \tag{C.37}$$

This represents a cuboid kept at a constant temperature on all sides except for the plane at $z/L = 0$, which is irradiated by the laser beam. Here, adiabatic conditions shall be applied. Following the same procedure which has led to Eq. (C.36), and applying an odd periodic extension to achieve Dirichlet boundary conditions and an even periodic extension to obtain the Neumann boundary condition at $z/L = 0$, the solution of the forced heat equation and the given boundary conditions in Eq. (C.37) can be expressed as

$$\begin{aligned} T(\mathbf{x},t) = &\frac{4P_0}{\pi w_0^2}\int_{t'=0}^{t_1}\int_{y'=-L}^{L}\int_{x'=-L}^{L}\frac{1}{\left(4\pi D_{\mathrm{th}}\left(t-t'\right)\right)^{3/2}} \\ &\cdot\exp\left(-\frac{2\left(x'^2+y'^2\right)}{w_0^2}\right)\sum_{m=-\infty}^{\infty}\sum_{n=-\infty}^{\infty}\sum_{o=-\infty}^{\infty}(-1)^{m+n+o} \\ &\cdot\exp\left(\frac{\left(x-x'+2mL\right)^2+\left(y-y'+2nL\right)^2+\left(z+2oL\right)^2}{4D_{\mathrm{th}}\left(t-t'\right)}\right) \\ &\mathrm{d}x'\mathrm{d}y'\mathrm{d}t\,. \end{aligned} \tag{C.38}$$

D Supplementary material regarding laser welding of titanium

The LPT of the FAU provided the measurement data on the weld width and weld depth shown in Tab. D.1 for various laser processing parameters. The first three columns denote the laser parameters: total power (P_0), laser scanning velocity (u_1) and energy density (E_A) given by Eq. (7.1). Two measurements of the melt width and depth have been provided for each parameter set, denoted as 1 and 2. The last column shows the quality of the obtained welding seam. One represents a continuous and zero a discontinuous welding seam.

Table D.2 shows the domain sizes, discretization lengths, and resulting number of SPH particles simulated to measure melt width and melt depth as a function of the processing parameters.

To investigate the surface geometry of as a function of the adjusted wetting forces, the laser processing parameters given in Tab. D.3 are investigated. Figure D.1 shows microscopy images of cross sections through the welding seam for various laser process parameters. In dependence on the process parameters, the welding seam is flat (see Fig. D.1a), or becomes more elevated, as can be seen, for instance, in Fig. D.1f.

Figure D.2 shows the histograms that are computed from the SPH particle positions obtained by parameter set 1 and varying wetting forces. All SPH particles that are laying within $0.33 \leq x/L \leq 0.54$ are binned as a function of their y- and z-coordinates at $t = 1\,\mathrm{ms}$. The largest number of SPH particles are positioned in the vicinity of the solid-liquid interface. In contrast, the lowest number of SPH particles is located near the solid-gas interface. With decreasing wetting forces (larger Θ_∞), the welding seam becomes more elevated.

Figure D.3 shows the histograms computed from the SPH particle positions obtained by parameter set 6 and varying wetting forces. All SPH particles that are laying within $0.28 \leq x/L \leq 0.58$ are binned as a function of their y- and z-coordinates at $t = 1\,\mathrm{ms}$.

In addition, the comparison of the weld geometries from experiments and simulations using parameter set 3 and 4 is shown in the appendix. Table D.4 shows the adjusted wetting forces in these simulations. Moreover, Figs. D.4, D.5, D.6, D.7 show the corresponding histograms and extracted contour lines which are compared to the experimental weld geometry.

Table D.1: Experimental measurements of weld width and weld depth as a function of the laser parameters and $w_0 = 120\,\mu\mathrm{m}$. The last column denotes the quality of the obtained welding seam. A "1" represents a continuous welding seam, whereas a "0" represents a discontinuous welding seam. Experimental data provided by Florian Huber, LPT, FAU.

laser parameter			melt width		melt depth		quality
P_0	u_l	E_A	1	2	1	2	
W	mm s^{-1}	J mm^{-2}	µm	µm	µm	µm	
100.0	900.0	0.46	29.0	29.0	202.0	196.0	1
100.0	600.0	0.69	44.0	44.0	187.0	190.0	1
100.0	400.0	1.04	63.5	80.0	256.5	242.0	1
100.0	250.0	1.67	69.5	70.0	288.0	293.0	1
100.0	100.0	4.17	117.0	134.0	372.5	380.0	1
200.0	900.0	0.93	41.0	36.0	181.0	163.0	1
200.0	600.0	1.39	115.0	111.0	225.0	213.0	0
200.0	400.0	2.08	70.0	62.0	299.0	293.0	1
200.0	250.0	3.33	150.0	166.0	315.0	313.0	1
200.0	100.0	8.33	54.0	49.0	146.0	139.0	1
350.0	2000.0	0.73	27.0	24.0	193.5	173.0	0
350.0	1500.0	0.97	69.5	62.0	178.5	198.0	0
350.0	900.0	1.62	66.0	76.0	256.0	277.0	1
350.0	500.0	2.92	126.0	118.0	320.0	312.0	1
350.0	250.0	5.83	133.0	147.0	402.0	406.0	1
500.0	2000.0	1.04	48.0	47.0	235.0	236.0	0
500.0	1500.0	1.39	83.0	84.0	262.0	285.0	0
500.0	900.0	2.31	86.5	91.0	283.5	277.0	0
500.0	500.0	4.17	200.0	200.0	394.5	355.0	1
500.0	250.0	8.33	264.0	85.0	264.0	265.0	1

Table D.2: Domain dimensions, applied spatial discretization as well as total amount of simulated SPH particles as a function of the laser properties and $w_0 = 120\,\mu\mathrm{m}$.

P/W	$v_\mathrm{l}\,/\mathrm{m\,s^{-1}}$	$\Delta x\,/\,\mu\mathrm{m}$	$L\,/\,\mu\mathrm{m}$	$H\,/\,\mu\mathrm{m}$	$D\,/\,\mu\mathrm{m}$	$N_\mathrm{SPH}/1000$
100	900	5.0	1415	400	100	452.80
100	600	7.5	1415	450	250	374.22
100	400	7.5	1415	450	250	374.22
100	250	7.5	1415	600	250	498.96
100	100	10.0	1415	500	350	248.50
200	900	7.5	1415	500	200	341.90
200	600	7.5	1415	550	300	551.88
200	400	10.0	1415	650	300	276.90
200	250	10.0	1415	600	350	87.40
200	100	10.0	1415	900	500	639.00
350	2000	7.5	1215	605	200	354.29
350	1500	10.0	1215	605	450	329.40
350	900	10.0	1215	605	450	329.40
350	500	10.0	1515	805	360	437.76
350	250	10.0	1215	805	600	600.24
500	2000	7.5	1215	605	200	354.29
500	1500	10.0	1215	605	450	329.40
500	900	10.0	1215	605	450	329.40
500	500	10.0	1515	805	360	437.76
500	250	10.0	1215	805	600	600.24

Table D.3: Domain dimensions, employed spatial discretization as well as total amount of simulated SPH particles as a function of the parameter set given in Tab. 7.1.

set	Δx / µm	L / µm	H / µm	D / µm	$N_{\mathrm{SPH}}/1000$
1	4.0	1415	225	100	938.10
2	10	3415	600	300	615.60
3	7.5	3415	700	250	1 272.24
4	7.5	3415	700	225	1 272.24
5	7.5	3415	600	225	1 272.24
6	5.0	1665	400	175	932.40
7	7.5	1665	500	250	490.84

Table D.4: Investigated wetting forces in the simulations with parameter set 3 ($w_0 = 120\,\mu\mathrm{m}$, $P_0 = 350\,\mathrm{W}$ and $u_1 = 1500\,\mathrm{mm\,s^{-1}}$) and parameter set 4 ($w_0 = 120\,\mu\mathrm{m}$, $P_0 = 500\,\mathrm{W}$ and $u_1 = 1500\,\mathrm{mm\,s^{-1}}$).

Θ_∞ / °	60	65	70	75
$\Theta^{\mathrm{s}}_\infty$ / °	65	70	75	80

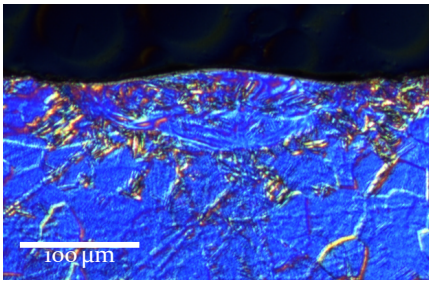

(a) Image of the weld cross section obtained by parameter set 1 in the experiments ($w_0 = 120\,\mu\text{m}$, $P_0 = 100\,\text{W}$, $u_1 = 600\,\text{mm}\,\text{s}^{-1}$).

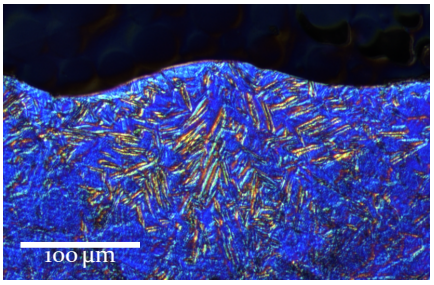

(b) Image of the weld cross section obtained by parameter set 2 in the experiments ($w_0 = 120\,\mu\text{m}$, $P_0 = 350\,\text{W}$, $u_1 = 500\,\text{mm}\,\text{s}^{-1}$).

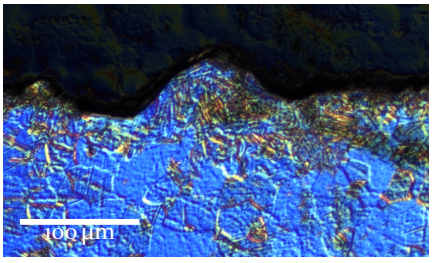

(c) Image of the weld cross section obtained by parameter set 3 in the experiments ($w_0 = 120\,\mu\text{m}$, $P_0 = 350\,\text{W}$, $u_1 = 1500\,\text{mm}\,\text{s}^{-1}$).

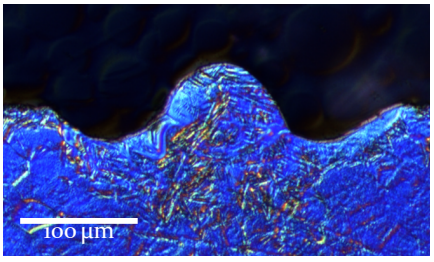

(d) Image of the weld cross section obtained by parameter set 4 in the experiments ($w_0 = 120\,\mu\text{m}$, $P_0 = 500\,\text{W}$, $u_1 = 1500\,\text{mm}\,\text{s}^{-1}$).

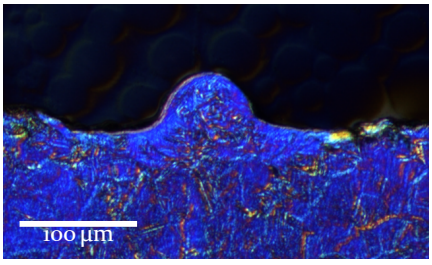

(e) Image of the weld cross section obtained by parameter set 5 in the experiments ($w_0 = 120\,\mu\text{m}$, $P_0 = 600\,\text{W}$, $u_1 = 3000\,\text{mm}\,\text{s}^{-1}$).

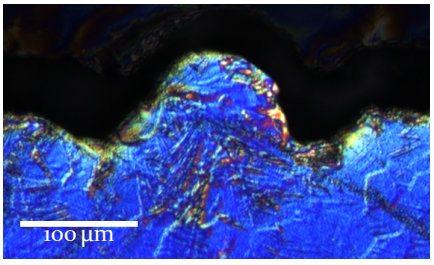

(f) Image of the weld cross section obtained by parameter set 6 in the experiments ($w_0 = 75\,\mu\text{m}$, $P_0 = 350\,\text{W}$, $u_1 = 2000\,\text{mm}\,\text{s}^{-1}$).

Figure D.1: Microscopy images of the welding seam cross-sections obtained by experiments for various laser process parameters. Experimental images provided by Florian Huber, LPT, FAU.

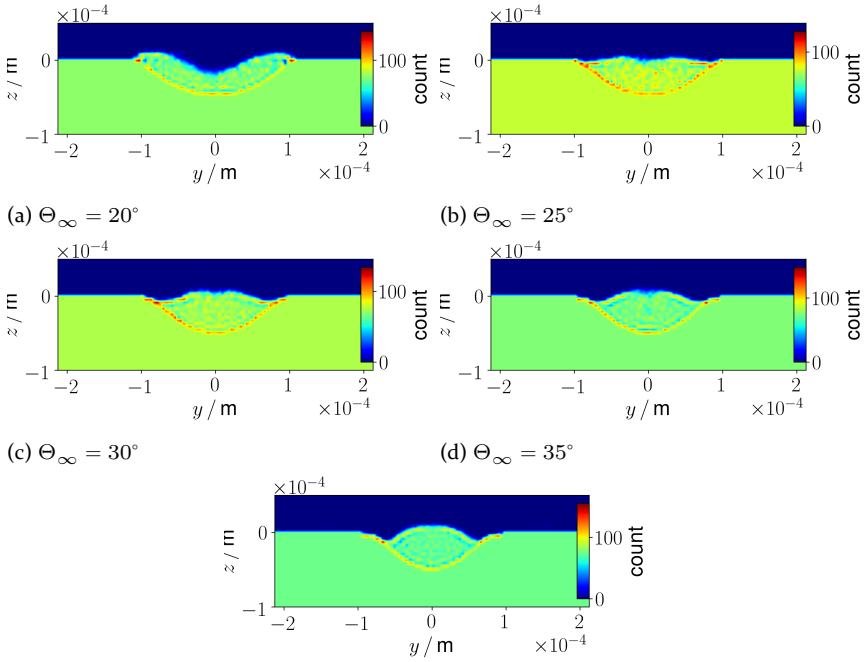

(a) $\Theta_\infty = 20°$

(b) $\Theta_\infty = 25°$

(c) $\Theta_\infty = 30°$

(d) $\Theta_\infty = 35°$

(e) $\Theta_\infty = 40°$

Figure D.2: Histograms of the x- and y-positions of SPH particles that are located within $0.33 \leq x/L \leq 0.54$ for parameter set 1 ($w_0 = 120\,\mu\text{m}$, $P_0 = 100\,\text{W}$, $u_1 = 600\,\text{mm}\,\text{s}^{-1}$) at $t = 1\,\text{ms}$.

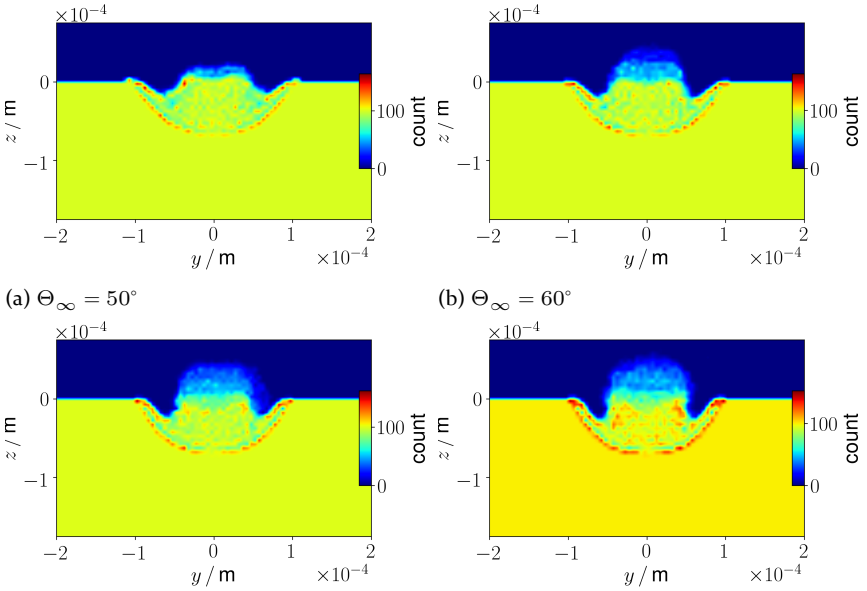

(a) $\Theta_\infty = 50°$ (b) $\Theta_\infty = 60°$

(c) $\Theta_\infty = 70°$ (d) $\Theta_\infty = 80°$

Figure D.3: Histograms of the x- and y-positions of SPH particles that are located within $0.28 \leq x/L \leq 0.58$ for parameter set 6 ($w_0 = 75\,\mu\text{m}$, $P_0 = 350\,\text{W}$, $u_1 = 2000\,\text{mm}\,\text{s}^{-1}$) at $t = 1\,\text{ms}$.

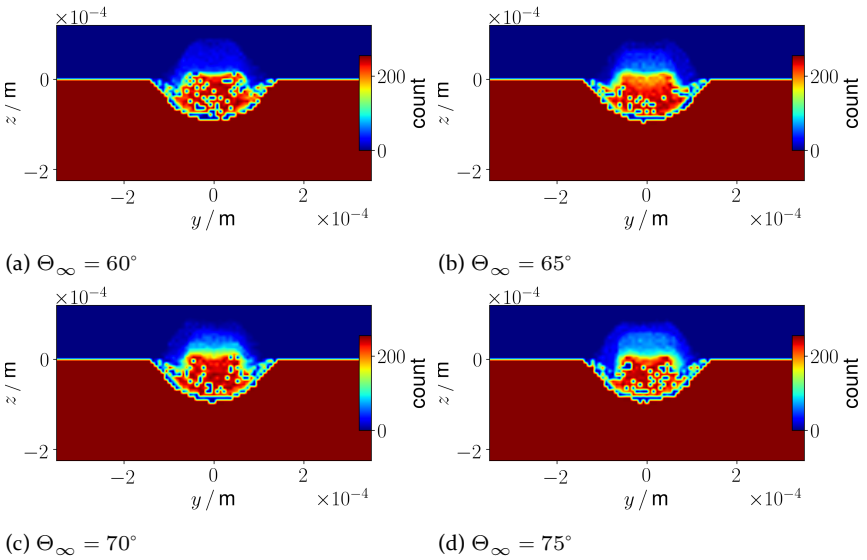

(a) $\Theta_\infty = 60°$ (b) $\Theta_\infty = 65°$

(c) $\Theta_\infty = 70°$ (d) $\Theta_\infty = 75°$

Figure D.4: Histograms of the x- and y-positions of those SPH particles that are located within $0.34 \leq x/L \leq 0.63$ for parameter set 3 ($w_0 = 120\,\mu\text{m}$, $P_0 = 350\,\text{W}$, $u_1 = 1500\,\text{mm}\,\text{s}^{-1}$) at $t = 1\,\text{ms}$.

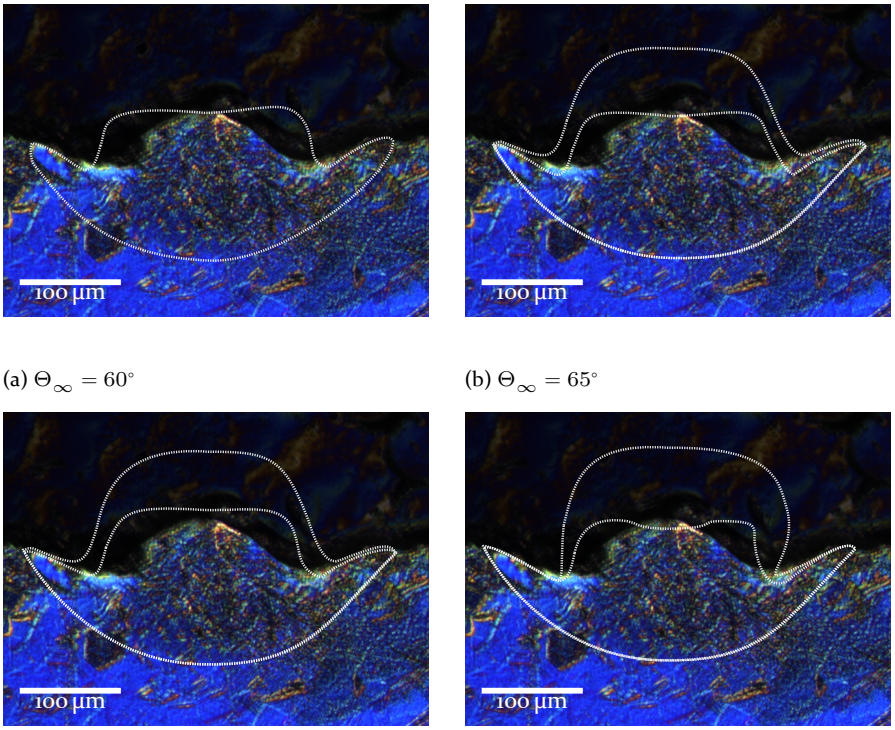

(a) $\Theta_\infty = 60°$

(b) $\Theta_\infty = 65°$

(c) $\Theta_\infty = 70°$

(d) $\Theta_\infty = 75°$

Figure D.5: Comparison of the weld geometries obtained by experiments and simulations with varying wetting forces for parameter set 3 ($w_0 = 120\,\mu\text{m},\ P_0 = 350\,\text{W},\ u_1 = 1500$). Experimental images provided by Florian Huber, LPT, FAU.

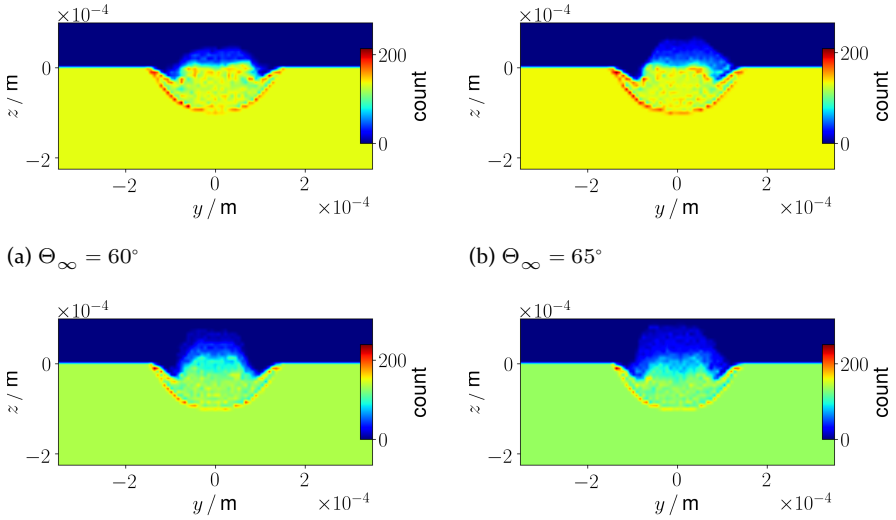

(a) $\Theta_\infty = 60°$

(b) $\Theta_\infty = 65°$

(c) $\Theta_\infty = 70°$

(d) $\Theta_\infty = 75°$

Figure D.6: Histograms of the x- and y-positions of those SPH particles that are located within $0.34 \leq x/L \leq 0.63$ for parameter set 4 ($w_0 = 120\,\mu\text{m}$, $P_0 = 500\,\text{W}$, $u_1 = 1500\,\text{mm}\,\text{s}^{-1}$) at $t = 1\,\text{ms}$.

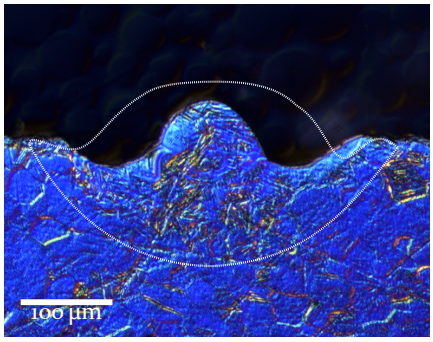

(a) $\Theta_\infty = 60°$

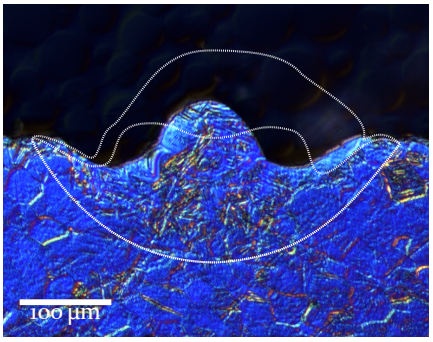

(b) $\Theta_\infty = 65°$

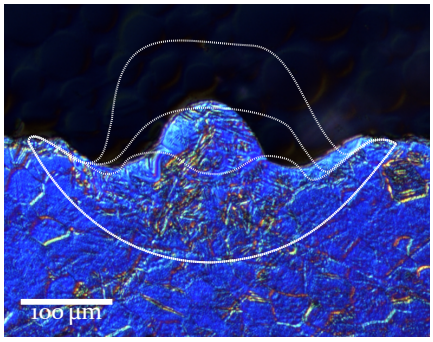

(c) $\Theta_\infty = 70°$

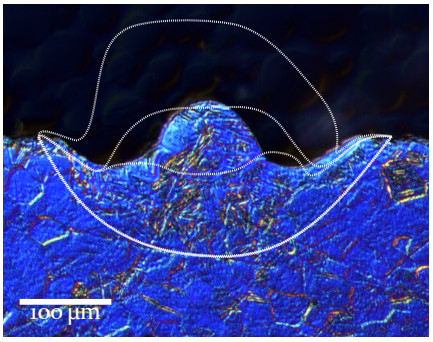

(d) $\Theta_\infty = 75°$

Figure D.7: Comparison of the weld geometries obtained by experiments and simulations with varying wetting forces for parameter set 4 ($w_0 = 120\,\mu\text{m}$, $P_0 = 500\,\text{W}$, $u_1 = 1500\,\text{mm}\,\text{s}^{-1}$). Experimental images provided by Florian Huber, LPT, FAU.

Laser welding, selective laser melting, and wire-based laser metal deposition are joining or additive manufacturing technologies in which a metal is melted by a laser beam. Inappropriate process parameters can lead to defects such as humping or balling, which degrade the mechanical properties of the weld or the manufactured part. In this work, the laser melting process of titanium is investigated by three-dimensional numerical simulations using the Smoothed Particle Hydrodynamics method. The absorption of laser light by the material surface and the emerging vapor is determined using a ray tracing technique. Numerical and mathematical models are developed to predict the interfacial tension and optical properties of titanium. The numerical model is validated with theory and experiments. Among others, single-line laser tracks on titanium have been simulated and compared with experiments. It is shown that the optical properties of titanium used in the experiments differ significantly from atomically clean titanium. Surface roughness, oxidation, or chemical impurities decrease the reflectivity of the titanium surface compared to atomically clean titanium. By assuming an “aged“ surface, quantitative agreement between simulation and experiments can be achieved for a wide range of laser parameters. Furthermore, the numerical tool is used to study the homologous wetting of molten titanium with its solid phase. It is shown that the wetting forces affect the geometry of the resolidified melt. High-temperature gradients at the solid-liquid phase interface lead to weak wetting forces, thus promoting the humping phenomenon. Finally, wire-based laser welding of titanium in zero gravity and selective laser melting of polydisperse titanium powder are investigated using the developed model.

ISBN 978-3-96147-647-3

FAU UNIVERSITY PRESS 2023